Developing Zebrafish Embryos as a Model to Study Host-Material Interactions and Wound Healing

Håkon Høgset

Department of Materials

Imperial College London

Thesis submitted for the degree of
Doctor of Philosophy

September 2020

Abstract

Inappropriate wound healing represents a considerable medical challenge associated with high mortality. However, improving on current wound healing therapies has proven difficult due to the complex and dynamic wound environment. The complexity of the wound healing process also puts high demands on the animal models used in wound research, since ideally such models should encompass the full complexity of the wound healing process, and at the same time be accessible for advanced biomedical analysis methods. In this thesis, the aim was to further develop the use of zebrafish embryos in wound healing research. Key advantages of zebrafish embryo models are the ability to visualize complex biological processes in high detail in intact tissues, as well as highly tractable genetics. The first part of the work describes the development of a zebrafish embryo model for investigating the immunomodulatory properties of hydrogels derived from decellularized extracellular matrix (ECM). The results demonstrate that the hydrogels can be properly injected into the embryos and that the host-materials interactions can be explored in detail inside live zebrafish embryos during wound healing. This constitutes a new *in vivo* model for investigating immunomodulatory materials in a realistic wound healing context. The second part of the work describes the development of a confocal Raman spectrometry imaging (cRSI) method for biomolecular characterization and the study of biological processes in zebrafish. This represents a new imaging modality that enables simultaneous inspection of a multitude of biomolecules in a label-free manner. The use of cRSI was demonstrated for biomolecular discrimination of mycobacteria in a zebrafish infection model, and for live *in vivo* imaging of zebrafish during the early wound response. Taken together, the work in this thesis has provided a new methodologies and insight for the use in zebrafish embryo models in wound healing research.

Table of content

List of figures and tables

Acknowledgments

I would first like to thank my main supervisor Professor Molly Stevens for giving me the great opportunity to work in her group. I am very grateful for the support she has given me for the entire duration of this project and for the encouragement and freedom to pursue my ideas. Working in her group has been a tremendous experience.

I would also like to thank Professor Maggie Dallman for support, help, and insight on the zebrafish work. This project would not have been possible without the facilities and expertise provided by her and the rest of her group.

A huge thanks to Dr. Serge Mostowy for his incredible help and support on enabling the zebrafish research. Without his effort, this project could not have been achieved.

A special thanks to Dr. James Armstrong for his mentoring during my Ph.D. His insight and knowledge have been invaluable to me during this project. A huge thank also to Dr. Conor Horgan and Dr. Mads Bergholt for being outstanding colleagues and for all the input and help provided on the Raman project. A big thanks also to Dr. Tim Keane for help in initiating the project on ECM hydrogels and for teaching and input throughout that project. Also, I am incredibly grateful to Dr. Adrian Najer, Dr. Vincenzo Torraca, Dr. Elena Moroz, Dr. Laurence Bugeon, and Dr. Marie-Christine Ramel for their various input and help on my project.

Thanks to all the past and present members of the Stevens groups. It has been an incredible place to work and I am grateful to everyone for the fantastic atmosphere in the groups. Also, a big thanks to my fellow postgraduate students in the Dallman group, Ralf, Dory, Madina, and Anna. You have all been incredibly supportive and helpful and I have learned a lot from all of you.

I am very grateful to Aker Scholarship for the funding and the opportunity to travel abroad for my Ph.D. Thanks to all the past and current members of the Aker Scholarship team, Bjørn, Hanne, Jakob, Mari Sofie, and Vilde for the support and help during my Ph.D.

A special mention to all past and present members of the Mighty Morags Football Club. The best football club in London south of the Seven Sisters station.

I want to thank my always supportive family, my mom, my dad, and my sister for all their help and effort.

Declaration of Originality

I, Håkon Høgset, declare that the work presented in this thesis is my own. All contributions and assistance received have been acknowledged in the text.

Copyright Declaration

Publications

1. **Håkon Høgset**, Conor C. Horgan, Mads S. Bergholt, James P. K. Armstrong, Vincenzo Torraca, Qu Chen, Timothy J. Keane, Laurence Bugeon, Margaret J. Dallman, Serge Mostowy & Molly M. Stevens – "*In Vivo Biomolecular Imaging of Zebrafish Embryos using Confocal Raman Spectroscopy*" - **Nature Communications** *In revision)

2. Elena V. Moroz-Omori, Dwiantari Satyapertiwi, Marie-Christine Ramel, **Håkon Høgset**, Ilona K. Sunyovszki, Ziqian Liu, Jonathan P. Wojciechowski, Yueyun Zhang, Christopher L. Grigsby, Liliana Brito, Laurence Bugeon, Margaret J. Dallman, and Molly M. Stevens – "*Photoswitchable gRNAs for Spatiotemporally Controlled CRISPR-Cas-Based Genomic Regulation*" - **ACS Central Sciences** 2020, 6, 5, 695–703

3. **Håkon Høgset**, James P. K. Armstrong, Timothy J. Keane, Adrian Najer, Evelyn Spencer, Sirli Treumuth, Ekaterina Pchelintseva, Laurence Bugeon, Margaret J. Dallman, & Molly M. Stevens "*Using Zebrafish Embryos to Study the Effect of ECM Hydrogels on Wound Healing*" – **In prep.**

4. Adam Creamer, **Håkon Høgset**, Lino Pardos, Qu Chen, Adrian Najer, Stephen Turnock, Cristopher S. Wood, Gabriela Kramer-Marek, Daniel Richards, Laurence Bugeon, Margaret J. Dallman, Molly M. Stevens – *"Functionalisation of Semiconducting Polymer Nanoparticle for Cancer Imaging and Therapy"* - **In prep.**

Conference Presentations

1. **UK Zebrafish Infection and Inflammation Conference 2020 Oral Presentation - July 10th, 2020**

   Confocal Raman Spectroscopic Imaging of Zebrafish

   Håkon Høgset, Conor C. Horgan, Mads S. Bergholt, James P. K. Armstrong, Vincenzo Torraca, Qu Chen, Timothy J. Keane, Laurence Bugeon, Margaret J. Dallman, Serge Mostowy & Molly M. Stevens

Abbreviations

3D: three-dimensional

ANOVA: analysis of variance

CARS: coherent anti-Stokes Raman spectroscopy

CCD: charge-coupled device

cDNA: complementary DNA

cfu: colony-forming units

CHT: caudal hematopoietic tissue

CLSM: confocal laser scanning microscopy

cRSI: confocal Raman spectroscopic imaging

DAMP: danger-associated molecular pattern

DNA: deoxynucleic acid

dpf: days post fertilization

dpi: days post-injection

ECM: extracellular matrix

EMT: epithelial-mesenchymal transition

FACS: fluorescence-activated cell sorting

FBGC: foreign body giant cell

FBR: foreign body reaction

FCA: Freund's complete adjuvant

FGF: fibroblast growth factor

FGF-2: fibroblast grow factor-2

GFP: green fluorescent protein

hpf: hours post-fertilization

hpi: hours post-injection

hpw: hours post wounding

HSC: hematopoietic stem cells

IFN-γ: interferon- γ

IL-1β: interleukin-1β

IL-4: interleukin-4

IL-6: interleukin-6

IL-10: interleukin-10

IL-13: interleukin-13

LPS: lipopolysaccharide

LSDRS: light sheet-excited spontaneous Raman spectroscopy

LSRM: light sheet Raman micro-spectroscopy

LV: latent variable

MMP: matrix metalloproteinase

mRNA: messenger ribonucleic acid

NA: numerical aperture

NO: nitric oxide

OD_{600}: optical density at 600 nm

PAA: peracetic acid

PAMP: pathogen-associated molecular pattern

PBS: phosphate-buffered saline

PC: principal component

PCA: principal component analysis

PCR: polymerase chain reaction

PDGF: platelet-derived growth factor

PFA: paraformaldehyde

PLS-DA: partial least square-discriminant analysis

PRR: Pattern recognition receptors

ROI: region-of-interest

ROS: reactive oxygen species

RSI: Raman spectroscopic imaging

SDCM: spinning disk confocal microscopy

SERS: Surface-enhanced Raman spectroscopy

SHG: second harmonic generation

SHIM: second-harmonic imaging microscopy

SIS: small intestinal submucosa

SIS-ECM: SIS derived ECM

SRS: stimulated Raman scattering

TEM: transmission electron microscopy

TGF-β: transforming growth factor-β

THG: third-harmonic generation

THIM: third-harmonic imaging microscopy

TNF-α: tumor necrosis factor-α

TPEM: two-photon excitation microscopy

VCA: vertex component analysis

VEGFA: vascular endothelial growth factor A

WT: wildtype

ZN-staining: Ziehl-Neelsen acid-fast staining

Introduction and preface

Failed wound healing (e.g. excessive scar formation/fibrosis, chronic wounds) constitutes a considerable challenge on modern healthcare, associated with significant morbidity and mortality. Due to a growing number of patients with underlying chronic diseases (e.g. diabetes, obesity) and an aging population, also the occurrence of chronic, non-healing wounds is rising. Chronic wounds are now estimated to affect more than 6.5 million people worldwide[1] moreover, chronic wound mortalities are now on a level with cancer[2]. Despite the burden of non-healing wounds put on patients and the healthcare system, very few new therapeutics have reached the clinics in the last decades[3], meaning treatment options are still falling short of the task. There are several important reasons why the development of new wound healing therapies to be slow. Firstly, introducing a new medical product depends on large time and monetary investment[4] regardless of the disease or condition they are intended for. For wound treatments, this is further exacerbated by the fact that wound healing is an intricate and dynamic process that is unlikely to respond to single factor treatments such as a single drug.

Secondly, because wound healing entails the restoration of complex tissues involving multiple cell types and cellular processes, wound healing research is dependent on the use of living animal models to realistically represent a wound scenario. Zebrafish embryos represent an attractive alternative because they offer the opportunity for tracking wound responses in a live vertebrate species. Moreover, zebrafish is a well-characterized and genetically tractable model that enables close examination of mechanistic details and improved throughput compared to mammalian models[5,6]. These advantages have made zebrafish a popular model organism in biomedical sciences and in particular the link between immunity and wound healing has been well explored[7].

This thesis aimed to exploit and improve the utility of the zebrafish embryo model for applications in biomaterials and wound healing studies. This work involved two distinct sub-projects that have been split into two separate results chapters.

The first result chapter makes use of the ability to track innate immune cells and wound progression in zebrafish embryos to explore the host-material interactions between injectable hydrogels derived from pig extracellular matrix (ECM) and the zebrafish host. ECM hydrogel is a versatile biomaterial that has demonstrated promise for wound healing applications, and that can combine engineered and inherent functionalities with minimally invasive wound introduction. The mechanisms and host interactions exerted by ECM hydrogels are still poorly understood but are thought to involve modulation of host macrophages. By introducing a microinjection protocol for ECM hydrogels in zebrafish embryos, the interactions between the gels and the host innate immune cells can be studied in real-time, enabling a close examination of the effect of the material.

The second result chapter introduces the use of confocal Raman spectroscopic imaging (cRSI) for use in zebrafish embryos. Zebrafish embryos are optically transparent, making them a key tool for the visualization of biological processes using light-based imaging techniques. cRSI is an imaging technique that enables label-free simultaneous visualization of multiple biomolecules and can reveal important information on for instance variations in cells or tissue metabolism during wound healing. In this chapter approaches for both three-dimensional (3D) and live cRSI are outlined, and cRSI is then applied for analyses of intact, infected, and wounded zebrafish tissues.

Although these two sub-projects in the thesis are linked in their aim to apply zebrafish embryos for wound healing research, they are approaching the problem from two quite different angles. For this reason, each chapter comes with its own introduction and discussion, highlighting the key developments and literature relevant to each of the sub-projects.

Chapter 1: Literature review

1.1 The wound healing process – an overview

Wound healing is a comprehensive physiological reaction to tissue damage, which starts directly upon injury and is crucial for the survival of multicellular organisms. Injury puts the organism in an immediate state of emergency and the early phase of the wound healing process has a protective function aimed at restoring enough tissue integrity for the survival of the affected individual[3,8,9]. These protective functions includes minimizing the loss of body fluids such as blood and preventing the entry of pathogens through any broken barriers such as the skin. If these immediate threats can be cleared, the wound healing process will proceed and try to restore the tissues' function through the replacement of lost or damaged tissue. Although wound healing is an evolutionarily conserved process, found across all animal phyla, the outcomes of this process vary greatly from species to species and even from tissue to tissue within the same species[10–12]. Thus, while some groups of animals such as the axolotls can regenerate entire limbs upon amputation, in humans, the most damaged tissue will not regain pre-injury functionality and will, depending on the severity of the injury, affect the individuals for the rest of their lives[3].

Wound healing can be seen as a sequence of four overlapping processes and follows the same pattern in almost all tissues and independent of the type of injury[8,13]. The first of these stages is hemostasis, which follows within minutes after injury. The main aim of hemostasis is to prevent blood and fluid loss and provide a provisional scaffold for infiltrating immune cells. Initially, blood thrombocytes will plug the wound before a fibrin clot is formed to cover the damaged area and form a temporary protein matrix[14,15]. Additionally, blood flow through the wound site will be limited through vasoconstriction[11,16]. Hemostasis is also important in initiating the second stage of the wound healing cascade; the inflammatory response. Degranulating thrombocytes, activated complement proteins and, if present, foreign pathogens all drive recruitment of leukocytes from the host innate immune system to the wound site. Neutrophils are the first leukocytes to arrive at the wound site and are important in clearing the wound of

any potential intruding pathogens. The other important leukocyte in wound healing is the macrophage. While most tissues contain some resident macrophages that will be recruited upon injury, the wound inflammation will also attract an influx of blood circulating monocytes that will mature into macrophages after arriving at the wound site[17,18].

Both neutrophils and macrophages display a collection of pattern recognition receptors (PRR) that can recognize and bind generic molecular patterns associated with threats to the organism[19]. Signaling through the PRR pathways are important in activating the leukocytes and mediate the inflammatory response. In addition to binding exogenous molecular patterns associated with pathogens (i.e. pathogen-associated molecular patterns (PAMPs)), PRRs also recognize and respond to the endogenous danger-associated molecular patterns (DAMPs)[20,21]. Several intracellular and extracellular biomolecules such as ATP, nucleic acids, histones, and fragments from the extracellular matrix (ECM) can act as DAMPs, thus, even a pathogen-free wound environment will elicit a prompt immune reaction[22]. The main role of the inflammatory response is to sterilize the wound and remove any pathogens that have entered the body through the wound site.

Until midway through the last century, when antibiotics became commonplace in the clinics, the main cause of death after injury was bacterial infections[23–25]. Therefore, for most of human existence, survival was dependent on rapid wound sterilization and wound closure rather than precise repair of the tissue[26]. However, if the wound site can be cleaned the inflammation will gradually subside and make way for the first part of the repair process, the proliferation phase[8,27]. The transition from inflammation to proliferation is gradual and partly mediated by the macrophages (this will be discussed in more detail in sub-chapter 3.4). During the proliferation phase, the provisional fibrin matrix will be replaced by granulation tissue, which is a vascularized matrix composed of collagen and fibronectin[8,26,28]. The wound site will attract fibroblasts that help in shaping the granulation tissue through the deposition of matrix proteins[29]. Moreover, fibroblasts and macrophages will release vascular endothelial growth factor A (VEGFA) and fibroblast growth factor 2 (FGF2) to stimulate angiogenesis and

vascularisation of the wound site[30,31]. The early proliferation phase will also initiate the skin repair process by reforming the epithelial cell layer. This re-epithelization begins with the re-programming and migration of epidermal keratinocytes[32,33]. Under the influence of various wound associated molecules (e.g. cytokines, growth factors, matrix metalloproteases (MMPs), integrins), keratinocytes will start migrating across the wound to form an initial epithelial barrier covering the granulation tissue[30,34]. Re-epithelization is vital for successful wound healing, and chronic wound conditions such as diabetic ulcers are characterized by their failed wound epithelialization[32,33].

Depending on the tissue-type the proliferation phase may also lead to stimulation of local progenitor cells populations to expand and contribute to the tissue repair (e.g. epidermal stem cells found in skin follicular niches)[35]. Later in the proliferation phase, some of the recruited fibroblasts will differentiate into myofibroblasts, which are important in shaping and processing the wound ECM matrix[36,37]. The myofibroblasts will start to contract the wound area by pulling the wound edges closer together[38]. Moreover, the myofibroblast will, together with the fibroblasts, produce more protein and in particular, collagen, which eventually will become the scar tissue, and for this reason myofibroblasts have often been associated with fibrosis[38–41].

The proliferation phase will slowly progress into the wound remodeling phase. During this transition, the number of cells in the wound site will drop and many of the macrophages and fibroblasts will become apoptotic or migrate away from the wound[34,42]. After a completed proliferation phase, the tissue that was lost due to wounding has been replaced either through the proliferation of local stem cells or in most cases by a disorganized mass of protein matrix constituting an immature scar[43]. The remodeling phase can typically last for years after the wound introduction and acts to gradually process the wound protein matrix to make a more robust scar[43–45]. Both macrophages and fibroblasts participate in the remodeling phase, which controls this process through the expression of MMPs and their inhibitors "tissue inhibitor of matrix metalloproteases" (TIMP)[46,47]. During the remodeling, the matrix composition will gradually change, and collagen III will be replaced by collagen I to form a firmer tissue scar[44].

The timing and composition of the remodeling phase are also deemed important for the wound healing outcome. Investigations using axolotl regeneration models have identified a low collagen I/collagen III ratio and a high MMP/TIMP ratio to be favorable for regenerating the wound site. Moreover, additional matrix proteins such as hyaluronan, fibronectin, and tenascins may also be important in shaping the final wound matrix[48–50]. It is well established that ECM itself contributes to the wound response both through mechanotransduction and chemical signaling to wound-associated macrophages and fibroblasts[51].

Thus, the wound healing process is a complex cascade of events, requiring tight control and interplay between several cellular processes and tissue components. While all the key steps in the wound healing cascade are shared across the animal phyla, important variations exist, leading to widely differing outcomes. A further understanding of how the differences in the wound healing cascade may lead to different wound healing outcomes is therefore paramount in improving wound healing therapies. Specifically, it is important to understand how the initial acute inflammation is linked to the following repair process to identify therapies that can sufficiently balance the need for an initial wound response without provoking excess fibrosis or chronic wound reactions. A summary of the wound healing cascade can be found in (**Figure 1.1**)
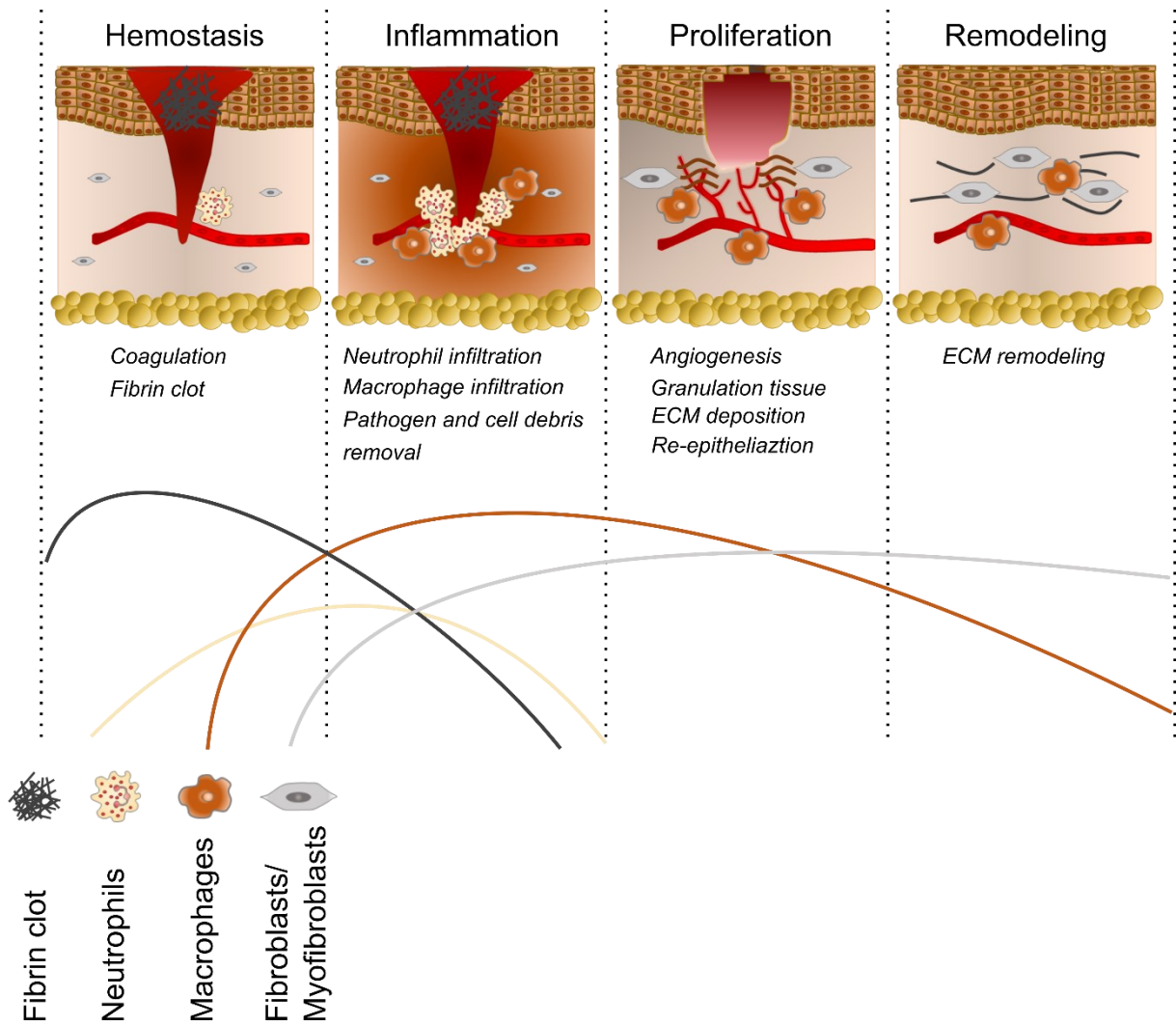
Figure 1.1: The Wound Healing Cascade. *The figure illustrates the main events during the wound healing cascade.*

1.2 Wound repair - types of wound healing outcomes

While the wound healing cascade is highly conserved across the animal phyla it also leads to drastically different outcomes. Broadly, the result of a wound healing process can be categorized into four different outcomes (**Table 1.1**): Chronic wounds, scar formation/fibrotic tissue, constructive repair, and regeneration.

Chronic wounds	*The wound remains unhealed and remains in a chronic state of damaged tissue, often with excessive inflammation*
Fibrosis	*Scars form at the injury site without replacement of damaged tissue. Tissue function may be impaired.*
Constructive repair	*Repair of tissue with minimal scar formation but without replacement of damaged tissue. Some restoration of function can be achieved.*
Regeneration	*The damaged tissue is replaced by de novo healthy tissue. When this occurs, the function and form of the tissue are regenerated and restored to its pre-damage state.*

Table1.1: Wound Healing outcomes

Although chronic wounds constitute a wide range of conditions, they are usually characterized by wound responses that fail to enter the reparative phase of wound healing. Chronic wounds are often associated with underlying conditions such as diabetes, or old age, and are usually classified based on these underlying causes. Among the most common types of chronic wounds are diabetic foot ulcers, pressure ulcers, and venous ulcers[52]. Because the repair process is insufficient in chronic wounds, the wound response is often trapped in a constant state of inflammation[53]. The chronic wound environment is therefore often exposed to excessive levels of pro-inflammatory cytokines, leukocyte infiltration, reactive oxygen species (ROS), and high expression of ECM degrading proteases such MMPs[53–55]. This consistent proinflammatory condition is damaging to the surrounding tissue and excessive levels of ROS are known to damage host proteins and cells needed for the wound repair[56]. Moreover, dysregulation and continual high expression of proteases also lead to a constant breakdown

of ECM further hampering the wound repair[54]. Lastly, chronic wounds often also suffer from senescent cell populations, which display a low capacity for proliferation and are less responsive to pro-repair stimuli[57].

The second major problem in wound healing is the replacement of wounded tissue by excessive scar tissue, known as fibrosis[40,41,58]. Like chronic wounds, fibrosis also encompasses a variety of different conditions ranging from the constantly growing keloid scars to smaller and less severe scars with less impact on the patient. Moreover, fibrosis also has several and often poorly understood causes and different fibrotic conditions may, therefore, vary considerably. However, a common view is that fibrosis arises from a chronic inflammatory environment that is not supportive of tissue repair[39–41,59]. Like the situation observed in chronic wounds, the persistent inflammation preceding fibrosis also leads to a dysregulation of deposition of connective ECM components[60,61]. However, when fibrosis, an excess of non-functional connective tissue is produced at the expense of the original tissue and functional parenchymal tissue, impairing the overall function of the tissue[40,41]. In the most severe cases, fibrosis will compromise entire tissues or organs to a degree such that they become completely dysfunctional and must be replaced for the patient to survive.

The scarring tissue consists mostly of poorly organized collagen deposited by activated wound myofibroblasts[44,62]. These myofibroblasts often develop from epithelial cells at the wound site through the epithelial to mesenchymal transition (EMT) and from recruited fibroblasts under the influence of transforming growth factor-beta (TGF-β) and interleukin-13 (IL-13)[41,63–66]. This information has led to several anti-fibrotic strategies being applied with the aim to reduce the amount of EMT through interfering with for instance TGF-β signaling or increasing the degradation of collagen, e.g. by stimulating proteolysis by matrix-degrading proteases such as MMPs[67,68].

1.3 Wound repair – regeneration and constructive repair

Regeneration involves *de novo* synthesis of healthy tissue and occurs quite commonly occurring in the animal kingdom[10,69]. However, while the human fetus can regenerate and repair tissue without scar formation, in adult humans regeneration is restricted to a few tissues, namely the liver, bone marrow, intestinal epithelium, and the skin epidermis[18,70,71]. Thus, for most injured human tissues, regeneration will not take place and is, therefore, less relevant as a potential clinical outcome for most wound healing scenarios.

Despite chronic wounds and scarring being common outcomes of wound healing, there are also numerous ways damaged tissue can repair itself and regain its previous function[69,72]. Undertsanding these different successful wound healing outcomes are also important for improving current wound healing therapies because they represent alternative routes to achieve constructive wound repair. Successful wound healing and regeneration are phenomena that are poorly understood, and further investigation into their regulation may lead to important insights needed for improving regenerative medicine and clinical wound care.

The replacement of damaged tissue by new functional tissue can arise from several different cellular sources and is generally categorized based on the cell source and the cellular process leading up to new tissue formation[69,73,74]. Broadly, tissue repair can be classified either as epimorphic regeneration which involves *de novo* synthesis of tissue through cell proliferation[75]; or morphallaxis which involves restructuring and remodeling of tissue cells without proliferation[76]. The proliferating cells observed in epimorphic regeneration can arise from different sources and several routes to tissue regeneration have been observed in the animal kingdom. In vertebrates such as zebrafish, salamanders, and newts the appendix can be regenerated through the formation of a blastema[69,77,78]. A blastema is a loosely organized mass of de-differentiated mesenchymal cells surrounded by a layer of epidermal cells that forms at the amputation site[76]. The blastema acts as an organizing center for the regeneration, providing the signaling stimuli necessary for the cell proliferation and regeneration of the tissue. Recent studies have also reported that the blastemas are both tissue specific and mosaic,

which means they often consists of several different cell lineages that are needed to regenerate the tissue[69].

Epimorphic regeneration can also take place without the formation of a blastema and throughout the animal kingdom, several different mechanisms of non-blastemal epimorphic regeneration can be found. Thus, lost tissue can be regenerated either through so-called transdifferentiating cells; dedifferentiation of surviving tissue cells; or by proliferation and differentiation of resident tissue stem cells[79–82]. While there are a few examples of blastemal regeneration in mammals[83–85], most mammalian regeneration, occurs through non-blastemal regeneration. This is for instance the case for human epidermis or gut epithelium where the regeneration is dependent on resident stem cells for tissue renewal[35,86].

Complete tissue regeneration represents the ideal outcome of any wound healing event, however, the process of regeneration is still poorly understood and there are still no clear answers to why some animals and tissues can regenerate well, while others can not[73]. From a treatment perspective, it is important to understand the fundamental biology underlying regeneration, especially because it is now recognized that many of the cellular and molecular events that support regeneration are also important in achieving improved wound healing outcomes in non-regenerating tissues, for instance in the regulation of the immune system[3,17,60,77,87,88].

Most current wound healing therapies aim to stimulate a transition into a tissue repair process without provoking a continued chronic inflammation and to minimize fibrosis. This is often referred to as constructive repair and involves repairing the wound using connective tissue followed by wound contraction by myofibroblasts to minimize the wound area[9,87]. Thus, if successful, constructive repair heals the wounded tissue by forming the smallest possible scar needed for wound closure. Many wounds will heal naturally by constructive repair and this outcome is strongly influenced by the patient immune system.

1.4 Inflammatory regulation of wound healing and regeneration

The inflammatory process is central to wound healing, and it is widely recognized that the type and strength of the wound inflammation play a huge role in the subsequent outcome of the tissue repair. However, the exact role of inflammation in wound healing has confounded scientists for a long time. Immune cells are present in the wound site throughout the entire repair process even if the initial inflammation has been properly resolved suggesting they play a role that goes beyond just sterilizing the wound site[89,90]. However, non-resolved inflammation at the wound site, for instance those caused by wound infections is invariably bad for the healing process. The fact that embryonic and fetal wounds can perform scar-free repair at a stage where the immune system is not fully developed led scientists to hypothesize that the immune reaction may at least partly interfere with wound healing and regeneration[11,61,91–93]. This view has been further supported by wound healing studies in PU.1-knockout mice (which are deficient in myeloid and b-lymphoid formation and therefore fails to produce macrophages and functional neutrophils) that observed both faster re-epithelialization and fibrosis free wound repair[94,95]. However, further investigations into the roles of the different wound leukocytes have challenged the hypothesis that inflammation is having a net negative effect on tissue repair. Referring to sub-chapter 1.2 the two main leukocytes present at the wound site are the neutrophils and the macrophages. While the role of neutrophils during wound healing is still poorly understood, prolonged neutrophil presence is generally considered a sign of a failed resolution of the inflammation[96–98]. Thus, neutrophils are mostly found at the wound site at the early, pro-inflammatory stage and the number of neutrophils normally drops after the recruitment of macrophages[96,99]. Neutrophils are strongly pro-inflammatory and important in combating potential infectious agents that may enter through the wound. Thus, neutrophils possess several important mechanisms for removing pathogens including phagocytic activity, the release of granules containing anti-microbial proteins, matrix modifying enzymes and neutrophil extracellular traps (NETs) which are nucleus derived chromatin complexed with degrading enzymes and proteins[100,101].

The neutrophils' antimicrobial tools can also be harmful to the host tissue, and there are reports of neutrophil activity in sterile wounds being detrimental to the wound healing[20]. However, other studies have reported the opposite effect and found the neutrophil activity to reduce tissue pathology during the healing of sterile wounds[20]. However, being the first immune cell to arrive at the wound site, neutrophils do play an important role in regulating the early phase of inflammation especially by removing inflammatory triggers such as DAMPs or PAMPS through phagocytosis and release of MMPs which is necessary for resolving the inflammation[7,101]. Moreover, it was recently discovered that neutrophils are attracted to ROS gradients in the tissue and that they actively participate in ROS removal, and this may play an important role in protecting the tissue from ROS damage as well as in regulating the inflammation[102,103].

While the neutrophil response during normal wound healing is swift and seems to only be part of the early acute inflammation, macrophages remain associated with the wound even after the repair has been completed and appears to serve a role during the tissue repair that extends beyond the acute inflammation[17,18,28,60,104,105]. Macrophages are therefore thought to take up several different and sometimes opposing roles during the progression of the wound healing process and their effect and contribution during the various wound healing stages have been subject to much debate. While the discussed work in the PU.1 knockdown mouse model, suggested that macrophages are not essential for tissue repair, this view has later come under scrutiny and several investigations have identified important roles for macrophages both in the early and the later stages of wound healing[90,94,106–108]. First, macrophages, like neutrophils play an important role in the pro-inflammatory phase that commences upon tissue damage, and their contribution is essential in the initial sterilization and cleaning of the wound site. The macrophages also have an important regulatory role during the acute inflammation and will reinforce the pro-inflammatory environment at the wound site and recruit more immune cells[8,17,18]. Thus, depletion of macrophages early after injury will reduce the inflammatory response but this may also lead to insufficient wound cleaning and therefore impair the subsequent healing[109].

Interestingly, work over the last decade in several different animal wound models have now identified macrophages as having a key regulating role at all stages of the wound healing response. For instance, whereas depletion of macrophages during the damage phase in mice leads to increased tissue fibrosis, depletion of macrophages at later stages during the repair phase leads to a slower breakdown of the provisional matrix and a slower scar resolution. This indicates that macrophages are needed both for the initiation and for resolution of the scarring process[109]. Moreover, work in adult zebrafish and axolotl wound models has identified macrophage contribution as crucial for proper tissue regeneration[106,107]. Macrophages have also been shown to be critical in driving angiogenesis during wound repair, which is crucial for the vascularization of the repaired or regenerated tissue[110,111].

The different of roles macrophages during wound healing has been attributed to the high degree of phenotypic plasticity observed for these cells. Traditionally macrophages have been divided into two different polarised phenotypes referred to as "pro-inflammatory macrophages" or "M1" and "anti-inflammatory macrophages" also called "M2"[112]. These two phenotypes have been associated with the stimulation of naive monocytes with different factors (i.e. lipopolysaccharide (LPS) and interferon-γ (IFN-γ) for M1: interleukin -4 (IL-4) and interleukin-13 (IL-13) for M2). *In vitro,* this polarisation scheme leads to M1 macrophages that express pro-inflammatory cytokines such as tumor necrosis factor- α (TNF-α), interleukin-6 (IL-6) and IL1-β. The M1 macrophages also produce ROS and NO and have increased phagocytic activities, making this macrophage phenotype a strong pro-inflammatory contributor highly anti-bacterial[89,104,112,113]. The M2 macrophages on the other hand express high levels of TGF-β, arginase I, VEGFA, and IL-10 are thought to stimulate the resolution of inflammation and therefore regulate the inflammatory environment in the opposite direction to M1[114]. In wound healing, the initial wave of macrophages that develops during the acute inflammation is often classified as M1 while the macrophages found at later stages during the proliferation and remodeling phases are M2[55,115]. The shift from M1 towards M2 has therefore been proposed as a predictor for improved wound healing outcomes and reduced wound fibrosis[87].

However, while the M1/M2 dichotomy is conceptually useful it is now considered to be an over-simplification and it is now understood that *in vivo* macrophages exist in a flexible spectrum of various phenotypes, often with overlapping pro-inflammatory and anti-inflammatory functions[17,116,117]. This view has emerged together with an increased appreciation that also outside of inflammation, macrophages are highly versatile cells. Most animal tissues contain tissue-resident macrophages that are present already from early development, and which are important for shaping and maintaining the tissue throughout the lifespan of the animal. Hence macrophages serve important homeostatic functions, such as removal of senescent cells or metabolic regulation also in healthy and non-inflamed tissues[118]. Moreover, macrophages serve important functions during development and tissue patterning, for example the previously discussed macrophage deficient PU.1 mutant mice develop abnormal hindbrain vascularization and hyperproliferative lymphatic vascularization, and in the frog, *Xenopus laevis* macrophage ablation leads to irregular limb metamorphosis during development[119].

Hence, macrophages are not only crucial regulators of inflammatory responses but also for developing and maintaining normal tissue architecture and function - indicating that macrophages potentially can take up several different non-inflammatory phenotypes as well. In line with this view, several authors have identified a wound repair macrophage phenotype that is distinct from the classical anti-inflammatory macrophages and that is important in regulating tissue repair by activating fibroblasts, stimulating tissue stem cells and inducing angiogenesis[17,117,120]. (A schematic of macrophage activation and phenotypes can be found in **Figure 1.2**. Macrophages are therefore vital in regulating the transition from a wounded to a repaired tissue, and a better understanding of macrophage regulation and phenotypes is important for all aspects of wound healing and to identify therapies that can promote constructive tissue repair.

Pro-inflammatory   **Wound Healing**   **Anti-inflammatory**

INF-γ   *Fatty acids / Lipids*   *Resolvins*
DAMPs   *IL-13*   *IL-10*
PAMPs   *IL-4*

TNF-α   *VEGFA*   *IL-10*
IL-1β   *FGF*   *TGF-β*
IL-6   *PDGF*
                         TGF-β

Microbicidal   ECM deposition   Dampens inflammtion
Removal of wound debris   Angiogenesis   Interacts with lymphocytes
Fibroblast activation   Myofibroblast stimulation
Recruitment of immune cell Stimulate tissue progenitor cell

*Figure 1.2: **Macrophage development and phenotypes during wound healing:** Schematic highlighting some of the important differences in the development and characteristics of macrophage phenotypes associated with wound healing. Figure reproduced from*[17]*.*

1.5 Experimental models of wound repair and regeneration

Wound healing research uses a wide array of experimental approaches ranging from pure computational simulations to experiments in human volunteers. This diversity is necessary for several reasons. First, improved wound healing therapies depend on the one hand on realistic representations of human wound healing, but on the other hand on access to the genetic and cellular mechanisms regulating wound healing and regeneration. Moreover, the development of new therapies always comes with economic considerations and the implementation of cost-efficient alternatives is therefore important in progressing wound healing research.

Hence, *in silico* models have been proposed as a possible first step for screening new wound treatments and a computational approach using a set of ordinary differential equations to compute the effect of wound healing variables such as inflammation damage and fibroblast mortality rate demonstrated the potential of this approach[121,122]. However, while computational approaches are likely to be valuable tools in the future, they rely on accurate biological input data to make precise predictions. Most wound healing research is therefore still conducted using biological specimens, and several *in vitro* approaches are frequently used. Cell monocultures offer an affordable approach with the potential for high-throughput screening. One commonly used *in vitro* method is the scratch assay which measures the ability of cells to reform a confluent monolayer after a physical disruption. This method is typically performed by introducing a scratch across the layer of cells and can give information on how migratory cells such as fibroblasts and keratinocytes respond to various surfaces or substances[123]. Moreover, monocultures using leukocytes such as macrophages or neutrophils are repeatedly used to measure the immune responses of wound healing therapies. Monocultures can usually display results relatively fast and typically requires less complicated set-ups, however, a clear limitation is the lack of any interaction between different cell types. Co-cultures using Boyden chambers enables the assessment of interactions between two different cell types (e.g. fibroblasts and macrophages), but still offers too little complexity to realistically represent a human wound, and it has been accepted that data from cell culture models poorly indicate how therapy will respond *in vivo*[124].

Hence, wound healing research is still heavily dependent on *in vivo* models to make precise biological predictions. While the wound healing process is similar among all animals, different species do repair tissue by slightly different mechanisms, something which is important to consider when choosing a model[3,125,126]. The animal model that most closely recapitulates the human wound healing process is pigs[124,127,128]. However, because of the size, husbandry costs, and low genetic tractability, pigs are less useful when investigating wound healing at the genetic or cell molecular level. Also, rodents and specifically mice are commonly used and

offer improved genetic tractability compared to pigs. However, genetic modification of mice is not always straightforward, and is often associated with unexpected side-effects or compensatory mechanisms limiting the genetic and cell molecular details that can be obtained[129]. For pre-clinical studies, an important drawback with mice is that they have a different skin architecture to humans and cutaneous wounds therefore mostly heal by contraction rather than by re-epitheliasation[128]. Moreover, standardizing mice models to ensure reproducible results has been a recurring concern[130].

While a realistic representation of human wounds is important, many of the challenges posed to the field of wound healing arise from a limited understanding of the genetic and cell molecular mechanisms regulating tissue repair. For this reason, several *in vivo* models that offer improved genetic tractability or accessibility to the cellular process have been introduced. Thus, many important clues to how wounded tissues regulate their repair have come from animal phyla that are distantly related to humans. For instance, important insight into stem cell niches in regeneration has come from the planarian model *Schmidtea mediterranea*[73,74,131]. Moreover, several models have been utilized to assess the multicellular aspects of wound healing. For instance, the fruit fly *Drosophila melanogaster* has been used to investigate re-epithelialization and identify links between immunity and regeneration[126,132]. *D. melanogaster* offers a high degree of genetic amenability, which makes them well suited for identifying regulatory pathways involved in wound healing. Moreover, because of their small size and optical clearness, an event such as wound closure can be captured using live microscopy[88,126]. However, the fruit flies have a rudimentary circulatory system, excluding the opportunity to study for instance angiogenesis[133]. Moreover, the innate immune system found in *D. melanogaster* is only distantly related to the human innate immune system and consists of only one cell type, the hemocyte which has a similar function to macrophages[126].

Axolotls and zebrafish are two vertebrate models with increased popularity in wound healing research[134–136]. Axolotls are known for their ability to regenerate amputated digits, while zebrafish can regenerate a range of different organs and tissues including heart, fins, and

spinal cord[137–139]. Axolotls and zebrafish models have also been useful in investigating the link between acute inflammation and wound healing[7,140]. Compared to fruit flies the immune system in axolotls and zebrafish are more closely related to the human immune system and these models, therefore, offer a more realistic representation of wound healing immunity[5,141]. Hence, the dependency on macrophage for tissue regeneration was first demonstrated in axolotls, and zebrafish before being reported in mice[106,107,142]. Zebrafish are particularly well suited because they offer comparatively straight-forward husbandry, are highly genetically amenable, and are well characterized. Also, zebrafish embryos are increasingly used to investigate the role of innate immunity and wound repair, and in the following chapters follows a discussion of the development of the zebrafish model and its benefits and contribution to the wound healing research.

1.6 The zebrafish embryo model of regeneration and inflammation

1.6.1 Advantages of the zebrafish model

Zebrafish was first introduced to the scientific community by Georg Streisinger in the 1970s as a model to study developmental biology[143]. Since then, zebrafish embryos have become a prominent model to investigate innate immunity. These embryos develop a functional innate immune system within the first 48 hours of their life span[144–146]. This immune system has been subject to decades of research and it is therefore well-characterized with many established and important similarities to the human immune system[5,6,147].

Zebrafish embryos have a rapid external development combined with optical transparency, which makes the embryos well suited for various imaging methods, including live imaging[148]. Moreover, the Zebrafish has a sequenced and well-annotated genome that produces a high number of offspring and has a relatively short generation time[149]. This, combined with well-established protocols for genetic manipulation of zebrafish, using, for instance, CRISPR/Cas9 makes zebrafish well suited for genetic manipulations with many immune cell reporter lines or

gene knock-out strains available[7,144,150–152]. Notably, transgenic reporter lines for neutrophils, macrophages as well as important pro-inflammatory markers such as IL-1β and TNF-α exist, meaning inflammatory processes can be monitored with high spatiotemporal precision[153,154].

Due to these advantages, zebrafish embryos have been used for studies of innate immune functions e.g. in disease modeling, and such studies have demonstrated that this model can recapitulate important aspects of human inflammation or pathogenesis. For instance, work on mycobacterial infection in zebrafish identified the formation of macrophage driven granulomas a hallmark of mycobacterial infection which at that point had only been observed in mammalian models[146,155,156].

1.6.2 The zebrafish embryo immune system

Zebrafish is a teleost and when fully developed, it has an immune system consisting of an innate and an adaptive branch similar to what is found in mammalian species[157]. Thus, adult zebrafish produces lymphocytes (e.g. T-cells and B-cells) and antibodies that are critical to their immune function. However, this immune system arises through the developmental process and it is not fully operational at the early stages of the fish life span. Thus, it is necessary to consider the development of the zebrafish immune system in general and in particular the myelopoiesis (the development of the myeloid cells such as macrophages and neutrophils) when interpreting data obtained from the zebrafish embryos.

Similar to other vertebrates the zebrafish hematopoiesis occurs in overlapping waves starting with primitive hematopoiesis early in the embryonic stage which will be gradually replaced by definite hematopoiesis that will supply the fish with the blood cells for the rest of its' life span[158]. The first wave of primitive hematopoiesis occurs in the embryonic mesoderm and is capable of producing myeloid precursor cells that can mature into functional macrophages in the zebrafish yolk. Already at 15 hours post-fertilization (hpf); these macrophages are expressing markers *draculin* and *leukocyte-specific plastin* (*L-plastin*) and are capable of phagocytosing injected bacteria[159]. This first wave of primitive hematopoiesis is only active for the first 48

hours of the embryos' life and supplies the organism with precursor cells of erythrocytes and neutrophils as well as macrophages[160]. During the first day of embryo development the site of hematopoiesis is relocated to the caudal hematopoietic tissue (CHT) near the embryo tail[161,162] (**Figure 1.3**). The CHT becomes the main supplier of hematopoietic cells from 3 days post fertilization (dpf) and the CHT derived leukocytes are at this point thought to outnumber the primitive leukocytes derived from the primitive hematopoiesis of the embryo development and thus constitutes a tissue for intermediary haematopoiesis[161,163]. The definitive hematopoiesis is emerging already at 3 dpf when the thymus and kidney develop. Unlike mammals, fish do not have blood marrow and in the adult fish, the kidney will be the site of myelopoiesis producing the adult leukocytes such as macrophages and neutrophils, while the thymus will be the site of lymphopoiesis and supply the adult fish with the adaptive immune cells. Although the definite hematopoiesis begins already 3 dpf and both precursors B-cells and T-cells can be detected, the adaptive immune system is not functional until around 4 weeks post fertilization[158,164].

The zebrafish relies on the myeloid cells constituting the innate immune system in the earliest stages of its development and a lot of effort has gone into characterizing the myelopoiesis and the leukocytes arising in the CHT. An important discovery was that the myeloid cells produced in the CHT arise from a source of hematopoietic stem cells (HSC) that also seeds the myelopoiesis niche in the kidney. This means that the definitive and intermediate myeloid cells are of the same origin and different from the precursor myeloid cells arising from the primitive haematopoiesis[161,162]. While the distinction between neutrophils and macrophages arising from the primitive hematopoiesis is not fully established, and co-expression of lineage-specific markers has been reported, characterization of the cells found in the CHT strongly points to there being two stable and separate lines of neutrophils and macrophages produced from the intermediate hematopoiesis in the CHT[7,158,165–168]. Moreover, characterization of the CHT macrophages and neutrophils has identified important overlaps in gene expression and immune function between zebrafish and humans[158,169]. Notably, the neutrophils express high

levels of myeloperoxidase (Mpx) and lysozyme C (LyzC), stain positively for Sudan black, and multi-lamellated electron-dense granules can be observed with electron microscopy[170–172]. The CHT macrophages are highly phagocytic, negative for Mpx and LyzC, and display an elongated and dendritic morphology.

Thus, by 3 dpf the zebrafish embryos have developed mature neutrophils and macrophages, closely related to the neutrophils and macrophages found in all adult vertebrates. This has made zebrafish embryos a useful tool for investigating innate immune function during disease progression or wound healing disease. Furthermore, transgenic fluorescent reporter lines have been engineered for neutrophils (e.g. Tg (Mpx:GFP)[173] and Tg(LyZ:GFP))[174]; and macrophages (e.g. Tg(Mpeg:mcherry))[175] enabling tracking of individual myeloid cells in living embryos. This has made zebrafish embryos an excellent tool for visualizing and interrogating the many multicellular interactions taking place during the wound healing process.
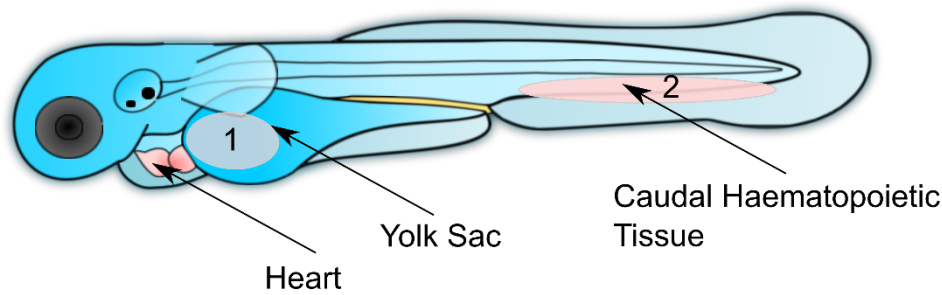
12-48 hpi	2-7 dpi	Adult
Primitive Haematopoiesis	**Intermediary Haematopoiesis**	**Definitive Haematopoiesis**
Primitive macrophages Primitive neutrophils	Mature macrophages Mature neutrophils	Mature macrophages Mature neutrophils
Embryonic mesoderm	Caudal Haematopoietic Tissue	Kidney
Myeloid predcursor cells	Haematopoietic stem cell	Haematopoietic stem cell

Figure 1.3 Zebrafish Myelopoiesis: Schematic of zebrafish embryo at 3 dpf indicating the site where primitive myeloid development (1) and definitive macrophage development occurs in the embryo(2). At 3 dpf, the CHT is the source of the embryo myeloid cell, including macrophages and neutrophils.

1.6.3 Wound healing and inflammation in zebrafish embryos

The features described above indicate that the zebrafish embryo represents a realistic model for studying the role of innate immunity in wound healing and regeneration. Thus, zebrafish embryos are by now a well-established tool in wound healing research, and work in this model over the last decades has provided important insights in this field. Several zebrafish wound models exist, but the commonly used are the stab wound model where a needle is used to cause an incision in the dorsal epaxial myotome[110,176,177]; the tail fold transection model where the tip of the embryonic tail fold is amputated using a needle or scalpel, or laser ablation wounds where a strong laser is focussed on the fish tissue to cause a wound[170,178]. Regardless

of the method, wound introduction causes a rapid response from the innate immune system with the recruitment of macrophages and neutrophil to the wound site. Similar to the canonical wound inflammation (**See sub-chapter 1.3**), the neutrophil response is immediate but short-lived, and the neutrophil number at the wound site will typically peak between 6-12 hours, before gradually diminishing. Macrophages arrive later to the wound but will remain at the wound site for longer time[172,175,179]. As might be expected, the inflammation and subsequent repairs process have been reported to vary according to the size of the wound[110,180].

Zebrafish embryos have robust regenerative properties and can replace damaged or amputated tissue by *de novo* formation of new tissue. Work using a tail fold amputation demonstrated that this tissue regenerates by a process that closely resembles adult tail fin regeneration. Notably, the tail fold seems to regenerate by forming a blastema-like structure consisting of proliferating mesenchymal cells and an epithelial layer[181]. The proliferation following the amputation is restricted in time and is dependent on the expression of fibroblast growth factor[181,182]. Moreover, a gene expression profiling study observed close resemblance in the gene embryonic and adult regeneration transcripts when comparing adult tail fin and embryonic tail fold amputation[183]. Zebrafish embryos also regenerate muscle tissue and the stab wound method has been used to elucidate this process. Muscle tissue regeneration occurs through activation and proliferation of resident muscle stem cells (i.e. satellite cells)[184]. Recent work in zebrafish embryos has demonstrated how the satellite cells coordinate the muscle regeneration through asymmetric cell division to maintain the stem cell niche while simultaneously adding new muscle cells[176]. Moreover, it has been revealed that the satellite cells form a heterogeneous population of muscle precursor cells serving different roles during the formation of new muscle tissue[177].

The most studied part of the wound healing process in zebrafish embryos is the inflammation and the ability to track the inflammatory cells and processes in real-time has enabled several important discoveries on innate immune regulation. Thus, Niethammer *et al.* discovered that the wound inflammation is initiated by an H_2O_2 gradient, which is centered at the wound site

and established within 3 minutes after wounding[185]. This gradient extends up to 200 μm into the tissue and ensures the rapid recruitment of neutrophils to the wound site. Moreover, neutrophils contribute to reducing the H_2O_2 gradient through myeloperoxidase activity and contribute in this way to regulating their own recruitment[103].

Several studies have looked into the link between immune cells and regeneration. Li et al. reported that macrophages were necessary for normal regeneration in zebrafish larvae, while the neutrophils were not[186]. On the contrary, the absence of neutrophils appeared to accelerate the regeneration[187]. Later work demonstrated that macrophages are important for protecting the tail fold blastema from becoming apoptotic by attenuating IL-1β expression from the tail epidermis[188,189]. Recent work has also described macrophage polarisation in zebrafish embryos[153,190,191]. Using the dorsal myotome stab wound model Gurevich et. al demonstrated that macrophages are orchestrating angiogenesis during wound repair. Pro-inflammatory macrophages support new vessel sprouting by associating with endothelial cells, the release of VEGF and removal of anti-angiogenic neutrophils. Later during tissue repair, wound healing macrophages facilitate vessel regression by stimulating apoptosis of redundant endothelial cells[110].

1.7 Aims of the thesis

Zebrafish embryos constitute an opportunity for in-depth investigations of molecular and cellular processes during wound healing. Thus, the last decade has seen many important discoveries in wound healing research coming from the use of zebrafish embryos. The overall aim of this thesis was to make use of the unique opportunities offered by the zebrafish embryo model to further develop its' use in wound healing studies. This aim resulted in two projects, each with their own aims, which will be presented in the following chapters.

The first project aimed to establish a zebrafish embryo model to investigate the host-material interactions between the embryos and injectable hydrogels derived from ECM. ECM hydrogels are frequently used for wound therapy, but their mode of action is poorly understood, although

it appears to involve host macrophages. Zebrafish embryos represent an attractive prospect to investigate these interactions in more detail and provide insight on immunomodulation and during wound healing. This also represents a relatively unexplored model for host-material interactions and the second important aim of this project was to investigate this potential. The background and a separate literature review related to this project will be presented in **Chapter 3** including a small discussion of emerging work investigating host-material interactions in zebrafish.

The second project aimed to develop and use protocols for confocal Raman spectroscopic imaging (cRSI) in zebrafish. The utility of zebrafish embryos in wound research will benefit from the development and adaptation of new technologies, and many of the important advances in zebrafish technology have emerged from new imaging technologies. cRSI enables visualization of a multitude of biomolecules simultaneously, while also providing spectroscopic data suited for multivariate analysis. Thus, cRSI can provide visual interrogation of metabolic and biomolecular niches during disease progression or wound healing. The main aims of this second project were to enable this technology for *in vivo* and 3-dimensional analysis of zebrafish embryos and apply cRSI analysis to wound healing and infection studies. **Chapter 4** contains an introduction discussing important imaging technologies applied to zebrafish and previous applications of Raman spectroscopy in zebrafish to further develop these aims.

Chapter 2: Methods and experimental details

2.1 Zebrafish methodology

2.1.1 Ethics statements

Experiments involving zebrafish were performed in compliance with UK Home Office requirements (Animals Scientific Procedures Act) 1986. All experiments not involving *Mycobacterium marinum* infection were performed under project license P5D71E9B0. Experiments involving *M. marinum* infection were conducted at the London School of Hygiene and Tropical Medicine under Project licenses: PPL P84A89400 and P4E664E3C.

2.1.2 Zebrafish husbandry

All fish were kept in the CBS facility of Imperial College London and were reared and maintained according to standard practices at 28.5°C on a 14-hour light/10-hour dark cycle[192]. Embryos were raised in E2 water supplemented with 0.3 ppm methylene blue[192]. Embryos were kept in Petri dishes at a density of ~50 embryos per dish and E2 water was replaced daily.

2.1.3 Microinjections of zebrafish embryos

Microinjections were conducted on zebrafish embryos using borosilicate capillaries (outer diameter 1.0 mm, inner diameter 0.78 mm length 100 mm; Harvard, Apparatus, Holliston, MA, USA;) in a Flaming/Brown P-97 micropipette-puller (Sutter, Novato, CA, USA) with the settings: heat 855, pull 150, velocity 80 and time 94. The injections were performed using a Narishige IM300 microinjection pressure controller (Naishige-group Tokyo, Japan). The injection volume was controlled using an eyepiece reticule (NE120, Pyser-SGI, Edenbridge, UK) and the needle was controlled using a micromanipulator (M3301 Micromanipulator Right hand World Precision Instruments Ltd. Hitchin, UK) and stereomicroscope (Nikon SMZ-1000).

Prior to injections, the fish were anesthetized in a solution of 4.2% (w/v) tricaine mesylate (MS-222, Sigma-Aldrich, St. Louis, USA)[192]. The fish were then mounted on a 2% agarose gel injection plate and all excess water was removed. Two different injection routes were used: The posterior caudal vein or the dorsal muscle tissue. Immediately after the injections, the fish were transferred to a petri dish with fresh 0.3 ppm methylene blue (v/v) in E2 water.

2.1.4 Stab wound injection in zebrafish embryos

Live zebrafish embryos at 3 days post fertilization (dpf) were anesthetized in a solution of 4.2% (w/v) MS-222 and mounted on a 2% (w/v) agarose gel injection plate. Stab wound injections were performed in the epaxial dorsal myotome using borosilicate capillaries that had their tip manually adjusted to 30 µm diameter. Embryos were injected with either PBS, 5 mg/mL SIS-ECM hydrogels, or Freund's complete adjuvants (Imject™ Freund's Complete Adjuvant, Thermo Scientific™) (FCA) in the somite opposite to the anal pore and immediately transferred to E2 water. The embryos were kept in an incubator at 28.5°C until used for further experiments.

2.1.5 Stab wound model

Zebrafish embryos at 3 days post fertilization (dpf) were anesthetized in 4.2% (w/v) MS-222 and then mounted on a 2% (w/v) agar plate. The embryos were wounded by making an incision in a single somite using a surgical tungsten needle (W20-148-01x2.0, World Precision Instruments Ltd.) in the dorsal epaxial myotome just opposite to the anal pore. Immediately after wounding, the embryo was transferred to a petri dish containing E2 water to allow for recovery. The embryos were then maintained in E2 at 28.5 °C until used for further experiments.

2.1.6 Survival of zebrafish embryos after injection

Zebrafish embryos were injected at 3 dpf with 0.5 nL of either PBS, FCA, or 5 mg/mL of Alexa 546 maleimide labeled SIS-ECM hydrogels in the dorsal muscle tissue. The survival of the embryos was recorded at 6, 24, 48, 72, and 96 hpi, and death was defined by the absence of heartbeat. Survival was analyzed by performing a log-rank test using Origin 2018b (OriginLab Corporation, Northampton, MA 01060, U.S.).

2.1.7 Gel retention after injection

Zebrafish embryos were injected at 3 dpf with 0.5 nL 5 mg/mL of Alexa 488 maleimide labeled SIS-ECM hydrogels in the dorsal muscle tissue. The embryos were kept alive in single wells using 12 well plates to keep track of the individual embryos. Images were captured at 6, 24, 48, 72- and 96-hours post-injection (hpi) using a Leica Stereomicroscope (Leica M165 C, Leica Microsystems, Wetzlar Germany) using with a GFP filter (excitation: 395-455 nm; emission: 480 long pass) and 8x magnification (optical zoom). Images were captures with the gain set to 10x and exposure time at 100 μs. The gel retention was analyzed in Fiji (ImageJ, U.S. National Institutes of Health, Bethesda, Maryland, USA) by applying a threshold and measuring the gel area for each fish at each time point. The data was exported to Origin 2018b and analyzed using a one-way repeated measures ANOVA provided by the software.

2.1.8 RNA isolation from zebrafish embryos

Wild type zebrafish embryos were injected as described above with at 3 dpf with 0.5 nL of either PBS, FCA, or 5 mg/mL SIS-ECM hydrogels and kept alive in the incubator at 28.5°C until used for RNA isolation. For RNA isolation, the zebrafish embryos were anesthetized in a solution of 4.2% (w/v) MS-222 and mounted on a 6% (w/v) agarose plate[192]. An 18-gauge, flat tip needle was then used to stamp out the middle part of the zebrafish embryos to produce mid-section biopsies. Using sterilized forceps (Tweezer, Dumont #55, Dumostar, 11cm, Straight, World Precision Instruments), the mid-section biopsies were immediately transferred

to an Eppendorf tube containing 200 µm RNAlater™ Stabilization Solution, (Invitrogen, Thermo Fischer Scientific, Waltham, MA, USA). For each group (16-20 embryos) biopsies were pooled to ensure enough sample material. After transfer to RNAlater™ the samples were kept at 4°C until further use.

RNA purifications were performed using PureLink™ RNA Micro Scale Kit, (Invitrogen, Thermo Fischer Scientific) RNA purification according to the manufacturer's instructions. Briefly, the RNA later solution was replaced by 200 µL of Trizol (TRIzol™ Reagent, Invitrogen, Thermo Fischer Scientific) and the samples were homogenized using pestles. After the homogenization, the RNA was extracted using neat chloroform and then loaded onto RNA-binding columns (PureLink™ RNA Micro Scale Kit, Invitrogen, Thermo Fischer Scientific) and purified through several washing steps according to the manufacturer's manual. Lastly, the RNA was eluted in a new collection tube, using 12 µm of RNA-free water (PureLink™ RNA Micro Scale Kit, Invitrogen™).

2.1.9 Reverse transcription of RNA

RNA purified from zebrafish embryos were converted to cDNA using the High-Capacity cDNA Reverse Transcription Kit (Applied Biosystems, Foster, CA, USA) and a thermocycler (Veriti™ 96-Well Thermal Cycler, Applied Biosystems) according to the manufacturer's protocol. The RNA concentrations were first estimated using NanoDrop 2000 at 260 nm (Thermo Fisher Scientific) before 250 ng RNA was added to the reverse transcription reagents to make up a reaction volume of 20 µL.

2.1.10 Quantitative PCR

Quantitative PCR was performed on the cDNA obtained, to quantitate the expression of inflammation marker mRNAs in zebrafish midsection biopsies. The TaqMan™ Fast Universal PCR Master Mix (2X), no AmpErase™ UNG assay (Thermo Fisher Scientific) was used and 2 µL of 25 ng of cDNA was added to the Taqman reagents to make up a final reaction volume

of 10 μL. mRNA from two housekeeping genes β-actin (Dr03432460_m1) and 18s (4310893E) and three inflammation markers were analyzed: TNFα (Dr03122586_m1), IL-1β (Dr031144368_m1) and MMP9 (Dr03139879_m1), and a 40 cycle program was run using an Applied Biosystems™ 7500 Fast Real-Time PCR qPCR machine. After completing the reaction, all cycle thresholds were set to 0.2 and the corresponding C_t-values were exported and analyzed using the $\Delta\Delta Ct$ method. The data were exported to Origin 2018b and analyzed using a one-way repeated measures ANOVA provided by the software.

2.1.11 Neutrophil counting in injected zebrafish embryos

Zebrafish embryos from the neutrophil reporter line Tg(MPX:eGFP)[172] were injected at 3 dpf with 0.5 nL of either PBS, FCA, or 5 mg/mL of Alexa 546 maleimide labeled SIS-ECM hydrogels. The embryos were kept alive in single wells in 12 well plates to keep track of the individual embryos and imaged at 6, 24, 48, 72 and 96 hpi. Prior to imaging, the embryos were anesthetized in a solution of 4.2% (w/v) MS222 in E2 water and mounted on a 2% (w/v) agarose imaging plate. The embryos were then imaged using a Leica Stereomicroscope (Leica M165 C) with 2.0x objective (Leica), and a Leica EL6000 external light source and Leica DFC7000 T camera. Images were captured using the following settings: Fluorescent images were captured using 10x gain, at 8x magnification. Neutrophils were captured using a GFP filter and 200 μs exposure time. SIS-ECM hydrogel was captured using 100 μs exposure time and a DSR filter (excitation: 510-560 nm; emission 590-650 nm). Brightfield images were captured at 10x gain and 1 μs exposure time. Immediately after imaging the embryos were put back into fresh E2 water, transferred to the incubator, and kept at 28.5°C until the experiment was terminated at 96 hours post-injection (hpi).

The number of neutrophils was calculated using Fiji. A circular Region-of-interest (ROI) with 200 μm diameter was centered around the injection site to capture the neutrophils in the vicinity of the injection. A built-in Fiji gaussian blur was used to reduce noise with sigma radius put to 4. The number of neutrophils was then identified using a Fiji built-in "find maxima" function with

noise level set to 10. The data were exported to Origin 2018b and analyzed using a two-way repeated-measures ANOVA, including a Tukey post-hoc analysis provided by the software.

2.1.12 Macrophage counting in zebrafish embryos

Zebrafish embryos from the macrophage reporter line Tg(Mpeg:mcherry)[193] were injected at 3 dpf with 0.5 nL of either PBS, FCA, or 5 mg/mL of Alexa 488 maleimide labeled SIS-ECM hydrogels. Embryos were kept and imaging was performed as described above. Images were captured using the settings described above for neutrophils. Immediately after imaging the embryos were put back into fresh E2-water, transferred to the incubator, and kept at 28.5°C until the experiment was terminated at 96 hpi. The number of macrophages was calculated using Fiji as described above for neutrophils. The data were exported to Origin 2018b and analyzed using a two-way repeated-measures ANOVA provided by the software.

2.1.13 Phalloidin staining of zebrafish embryos

Phalloidin staining was performed according to a protocol by Goody *et al.*[194]. Prior to staining the embryos were fixed overnight in 4% (v/v) paraformaldehyde (PFA) at 4°C. The next day, the embryos were washed 3 x 5 min in 0.5 mL 0.1% (v/v) Tween 20 (Sigma-Aldrich, St. Louis, USA) in PBS (Gibco, Thermo Fisher Scientific) and then washed for 90 min at room temperature in 0.5 mL 2% (v/v) Triton X-100 (Sigma) in PBS (Gibco). The Triton X-100 solution was then replaced with 19 µL of fresh 2% (v/v) Triton X-100 with 1 µL of either rhodamine-phalloidin (Thermo Fisher), Alexa Fluor™ 488 Phalloidin or Alexa Fluor™ 555 Phalloidin (Invitrogen). Staining was performed overnight at 4°C with gentle shaking.

2.1.14 Confocal fluorescence imaging of fixed zebrafish embryos

Prior to imaging, the embryos were gradually transferred to 80% glycerol (v/v) through subsequent washing steps of increasing glycerol concentration (20%, 40%, 60%, respectively). After transfer to 80% glycerol, the embryos were mounted on a glass-bottom dish (Cellview

Cell Culture Dish, PS 35/10 MM, glass Bottom, Greiner bio-one, Monroe, NC, USA) and then imaged using an SP5 inverted confocal fluorescence microscopy (Leica) equipped with a 20x/0.5 PL FLUOTAR objective lens (Leica).

2.1.15 Confocal fluorescence imaging of live zebrafish embryos

Injected zebrafish embryos were anesthetized in a solution of 4.2% MS-222 (w/v) and put in a glass-bottom dish (Cellview Cell Culture Dish, PS 35/10 MM, glass Bottom, Greiner bio one). All excess water was removed, and the larvae were embedded in 0.8% (w/v) low melting point agarose (NuSieve™ GTG™ Agarose, Lonza, Basel, Switzerland) heated to melting and cooled to 35°C on a heat block. The embryos were carefully aligned with the side facing upwards using a hairpin loop. After the agarose had gelled, the embryos were covered in 4.2% MS-222 in E2 (w/v). The embryos were then imaged using an SP5 inverted confocal fluorescence microscope (Leica) with a 20x/0.5 PL FLUOTAR objective lens (Leica) and a heat chamber put to 28.5°C.

2.1.16 *Mycobacterium marinum* model in zebrafish

Wild type and ΔRD1 mutant *M. marinum* were cultured and injected into zebrafish embryos as according to previously described protocols[195–197]. Briefly *M. marinum* from frozen glycerol stocks were cultured on Middlebrook 7H10 agar plates (BD Biosciences, San Jose, CA, USA) supplemented with oleate-albumin-dextrose-catalase (OADC) enrichment (BD Biosciences). The bacteria were incubated at 28.5°C in the dark for 7-10 d at which point single, developed colonies were collected to make liquid cultures. The bacteria were resuspended in 10 mL of Middlebrook 7H9 medium (BD Biosciences) supplemented with albumin-dextrose-catalase (ADC) enrichment (BD Biosciences) and the bacteria were added until the liquid culture had reached an optical density at 600 nm (OD_{600}) of 0.1 measured using a 7205 UV/Visible spectrophotometer (Jenway, Cole Palmer, Stone, UK). Cultures were incubated without shaking in the dark at 28.5°C for 24-36 h to reach an OD_{600} of 0.5-0.8. After an appropriate

OD$_{600}$ had been confirmed, the bacteria were spun down, washed in PBS, and resuspended to the desired concentration in 2% (w/v) polyvinylpyrrolidone in phosphate-buffered saline (PVP / PBS, Sigma Aldrich). 0.5 nL of this solution, containing ~50 CFU of wild type *M. marinum* or 150 CFU of ΔRD1 *M. marinum*, was injected into the trunk of zebrafish embryos at 2 dpf. The injected embryos were then kept in 10 cm diameter Petri dishes at a density of 20 embryos per dish at 28°C until 4 days post-injection (dpi) when they were anesthetized in 4.2% (w/v) MS222 and then fixed for histology, electron microscopy or cRSI.

2.1.17 Histology of mycobacterial lesions*

Zebrafish embryos infected with wild type *M. marinum* were fixed overnight in 4% PFA and then embedded in paraffin wax and sectioned onto Thermo Scientific™ SuperFrost Plus™ adhesion slides (Thermo Fisher Scientific) (section thickness of 4 μm). The sections were stained with Ziehl Neelsen stain to visualize the *M. marinum*. Briefly, the sections were dewaxed and rinsed first in ethanol and then in water. The sections were then transferred to a carbol fuchsin solution (at 60 °C for 30 min. Next, the sections were washed in acid alcohol solution containing 1% (v/v) hydrochloric acid in 70% ethanol until there was no stain observed coming off of the sections. The sections were then counterstained for ~1 min in 0.25% methylene blue (v/v) in 1% acetic acid (v/v). The sections were then dehydrated, mounted, and imaged using a Zeiss Axio Observer microscope.

*The histology procedure was performed by Lorraine Lawrence, Senior Technician, South Kensington Campus, Imperial College London.

2.2.18 Electron microscopy of mycobacterial lesions*

Zebrafish embryos infected with wild type *M. marinum* were fixed overnight in 1% glutaraldehyde (w/v) (Electron Microscopy Sciences, Hatfield PA, USA) in 60 mM HEPES (Gibco). The embryos were post-fixed in 2 % (w/v) aqueous osmium tetroxide (Electron

Microscopy Sciences) for 1 h at room temperature, followed by 1 h staining with 1% (w/v) tannic acid (Sigma Aldrich). The embryos were then dehydrated using sequential 2 x 10 min incubations in 70, 80, 90, and 100% (v/v) ethanol. The embryos were embedded in Quetol 651 (TAAB Laboratories Equipment, Aldermaston, UK) in a flat mold and oriented so that the lesion was visible through the resin, which was then cured at 60-65°C for 40 h. The resin block was manually trimmed using a razor blade and then sectioned using an ultramicrotome (RMC PowerTome, Labtech, Heathfield, UK) equipped with a glass knife, with an automatic advancing distance of 1 µm per section. The sections were collected onto a glass slide, stained with Toluidine Blue, and observed under a light microscope. This allowed the identification of sections containing the mycobacterial lesion, which were further sectioned using a 45° diamond knife (Diatome, Hatfield, PA, USA). 60 nm sections were collected onto an ultra-thin Formvar 100 mesh copper grid (Electron microscopy Sciences), stained with UranyLess for 2 min and lead citrate (Electron Microscopy Sciences) for 1 min and then coated with a 4 nm layer of carbon using an evaporation coater (Low Vacuum Coater Leica EM ACE600). These stained sections were used for transmission electron microscopy using a Titan (FEI) 80-300 (Thermo Fisher Scientific) operating at 80 kV.

*The TEM staining and imaging procedure was done collaboratively but led by Dr. Qu Chen, Postdoctoral researcher, Department of materials, South Kensington Campus, Imperial College London.

2.2 ECM hydrogel preparation and characterization

2.2.1 Decellularization of small intestinal mucosa ECM

Porcine small intestines were washed in deionized water and cut into segments of ~40 cm. Each segment was split open with a razor blade to expose the luminal side of the intestine. Using an ice-scraper the submucosa was physically cleansed and released from the mucosa on the luminal side, and thereafter from the smooth muscle tissue on the abluminal side. The resulting small intestinal submucosa (SIS) was rinsed in deionized water.

To disinfect the SIS, 0.1% peracetic acid (PAA) was prepared in a solution of 96% type 1 water and 4% pure ethanol (100%). The SIS was put in the PAA solution overnight, using 20 mL of PAA solution per gram of SIS. After disinfection, the PAA solution was replaced by PBS and the SIS was rinsed with PBS and Type 1 water. The SIS was then used for hydrogel production.

*The decellularization was performed with Dr. Timothy J. Keane at Imperial College London.

2.2.2 Production of ECM hydrogels

To make dry SIS-powder, the SIS was milled and lyophilized overnight. An ECM digest was obtained by adding 1 g of dry ECM to 100 mL of a solution of 0.1% pepsin (w/v) in 0.01 M HCl and kept stirring at room temperature for 24 hours. The ECM digest was stored at -20 $^{\circ}$C until used.

To produce SIS-hydrogels, the ECM digest was neutralized adding 10% (v/v) 0.1 M NaOH and 10% (v/v) 10x PBS. The concentration of the SIS-digest was adjusted by adding 1x PBS to obtain a final concentration of 5 mg/mL.

2.2.3 Ellman assay

Ellman assay (Ellman's reagents, CAS # 69-78-3, Thermo Scientific) was performed on six independent replicates of SIS-ECM hydrogels at 5 mg/mL according to the manufacturer's

instructions. In summary, a standard curve of known cysteine concentration was prepared (0.0 mM – 1.5 mM) alongside the six SIS-ECM hydrogel samples. The 250 µL of each cysteine standard or SIS-ECM samples were then mixed with 50 µL of Ellman's Reagent and 2.5 mL of Reaction buffer as described by the manufacturer. The samples were then left to incubate at room temperature for 15 min before absorbance was measured at 412 nm using a SpectraMax M5 (Molecular Devices) plate reader.

2.2.4 Rheology of ECM hydrogels

5 mg/mL SIS-ECM hydrogel was prepared as outlined above. 1 mL of the hydrogel was then loaded onto a rheometer (AR2000, TA instruments, New Castle, DE) with the Peltier plate cooled to 4 °C. The geometry gap was set to 500 µm and all rheological measurements were conducted using a 40 mm parallel steel plate. After loading, the gel was sealed with mineral oil to prevent the gel from drying during the time sweep. The temperature was then raised to either 28 °C or 37 °C depending on the measurement and an oscillatory time sweep was performed at constant 0.1% strain and a constant frequency of 1 Hz for a duration of 12 h. Following the time sweep, a frequency sweep was performed from 0.1 Hz to 10 Hz at a constant strain of 0.1%. Lastly, the gel was tested using a strain sweep between 0.01% and 100% keeping the frequency constant at 1 Hz.

2.2.5 Maleimide labelling of ECM hydrogels

The hydrogel was labeled by adding 0.6% (v/v) of 10mM of either Alexa Fluor® 488 C5 maleimide, Alexa Fluor® 546 C5 maleimide or Alexa Fluor® 647 C2 maleimide in DMSO to the gel and the hydrogel was left at 4 °C overnight. Fresh gels were produced as described in 2.2.2 for every experiment and kept in dark on ice up until use.

2.3 Confocal Raman spectroscopic imaging*

* cRSI work was performed together with Dr. Conor Horgan, Postgraduate student Department of materials, South Kensington Campus, Imperial College London.

2.3.1 Raman spectroscopic imaging of fixed zebrafish embryos

Confocal Raman spectroscopic imaging of fixed zebrafish embryos was performed using a confocal Raman microscope (alpha300R+, WITec, GmbH, Ulm, Germany). A 532 nm laser light source at 35 mW power output was applied through a 63x/1.0 NA water-immersion microscope objective lens (W Plan-Apochromat, Zeiss, Jena, Germany). Inelastically-scattered light was collected through the objective and directed via a 100 μm diameter silica fiber, acting as a confocal pinhole, to a high-throughput imaging spectrograph (UHTS 300, WITec, GmbH, Germany) with a 600 groove/mm grating and equipped with a thermoelectrically cooled (-60 °C) back-illuminated charge-coupled device (CCD) camera. Raman spectra were acquired in the range from 0 to 3700 cm^{-1} with a spectral resolution of 11 cm^{-1}.

The fixed embryos were mounted on a glass slide in 0.8 % (w/v) low melting point agarose (NuSieve™ GTG™ Agarose, Lonza). During mounting, the embryos were gently aligned to ensure the sagittal plane was parallel with the glass slide. All mounted samples were kept in 10 cm Petri dishes and immersed in ~50 mL of E2 water. This was done to dissipate the heat from the laser to prevent sample damage or melting of the agarose gel. E2 water was used to maintain an osmotic balance and avoid swelling or contraction of the mounted embryo

After imaging, all acquired data were subjected to spectral preprocessing using the WITec ProjectFOUR software. Spectra were first cropped to remove Rayleigh scattered light before a background subtraction was then performed using a 'shape' background filter with a parameter size of 500 and a noise factor of 0 to remove tissue autofluorescence. Finally, each Raman spectrum was normalized to the area under the curve.

Univariate image analysis was then performed by calculating the total area under the curve for different spectral features, namely: protein-rich regions (2940 ± 16 cm^{-1}), lipid-rich regions (2850 ± 5 cm^{-1}) carotenoid-rich regions (1159 ± 16 cm^{-1}), collagen-rich regions (901 ± 170 cm^{-1}), DNA-rich regions (789 ± 10 cm^{-1}), lipid-rich regions (2885 ± 10 cm^{-1}) and cytochrome-rich regions (1579 ± 15 cm^{-1}).

2.3.2 3D and high-resolution cRSI

Zebrafish embryos at 3 dpf were anesthetized in 4.2% (w/v) MS-222 and fixed overnight in 4% PFA as outlined above. 3D whole-embryo Raman images were acquired with a spectral resolution of ~11 cm^{-1}. All 3D images were measured with a 10 µm lateral and 10 µm axial spatial resolution with an integration time of 1 s per spectrum. High-resolution tissue imaging was performed using the same procedure but with a lateral spatial resolution of 0.5 or 1.0 µm. All images were acquired and preprocessed as described above (2.3.1).

2.3.3 Raman spectroscopy of liquid culture *M. marinum*

Samples of mycobacteria were collected at an OD$_{600}$ of 0.6, 0.9 and 2.3, centrifuged and then fixed in 4% PFA overnight at a concentration of OD$_{600}$ = 0.5 per mL of PFA. The mycobacteria were transferred to a magnesium fluoride slide and Raman spectra were collected for 4-8 replicate samples for each mycobacterium, using a 20x/0.4 NA air objective lens (EC Epiplan, Zeiss, Germany) and a 0.5 s integration time. The acquired spectra were exported to Origin 2018b and analyzed using a built-in principal component analysis (PCA).

2.3.4 cRSI of *M. marinum* lesions*

Zebrafish embryos were infected, fixed, and mounted as outlined above. Single plane cRSI images were captured of lesions in the wildtype (WT) group using a 532 nm laser at a spatial resolution of 1 µm and an integration time of 1 s. 3D cRSI images were captured of lesions in both the WT and ΔRD1 injected groups (N = 3) using a 532 nm laser with a lateral resolution of 2 µm, an axial resolution of 2 µm, and an integration time of 1 s.

The volumetric cRSI images were pre-processed as previously described (2.3.1) before being analyzed using a custom MATLAB script*. Briefly, thresholding was performed using the peak intensity between 2844 – 2864 cm^{-1} which was strongly present in the bacterial clusters. Any Raman spectra with a peak intensity below this threshold were discarded. Individual mycobacterial clusters were then identified using blob analysis, with each Raman spectrum assigned to its corresponding blob (bacterial cluster)[198]. Colored blob images were then imported into Icy (Icy – Open Source Image Processing Software) to generate merged images. Raman spectral variation of bacterial clusters was assessed using both PCA and Partial Least Square-discriminant analysis (PLS-DA) of normalized (area under the curve), mean-centered Raman spectra. These analyses were conducted in PLS_Toolbox (Eigenvector Research, Manson, WA, USA) within the MATLAB environment. PLS-DA spectral classification was performed using 3 latent variables and a Venetian blinds cross-validation with 10 data splits. Negative controls were zebrafish embryos had been injected with resuspension buffer alone (2% polyvinylpyrrolidone in PBS) were included and imaged and analyzed using the same parameters as for the two experimental groups.

* The MATLAB script analysis was designed by Dr. Conor Horgan, Postgraduate Department of materials, South Kensington Campus, Imperial College London.

2.3.5 *In vivo* cRSI of live zebrafish embryos

Confocal Raman spectroscopic imaging of live zebrafish embryos was performed using a confocal Raman microscope (alpha300R+, WITec, GmbH, Germany) with a 785 nm laser light source at 85 mW power output. Raman spectra were acquired in the range from 0 to 1825 cm^{-1} with a spectral resolution of 11 cm^{-1}.

Briefly, zebrafish embryos were covered in a droplet of 0.8% (w/v) low melt agarose at 36°C and (added 4.2% of MS-222 for live fish). The embryos were transferred in the agarose droplet onto a glass slide and then aligned flat and with the sagittal plane orthogonal to the incident

laser beam. After gelation, the glass slide was transferred to a 10 cm petri dish containing 4.2% MS-222 in E2 water. All live imaging was performed in a heat chamber set at 28.5 °C and using *TraNac* zebrafish embryos (*mitfaw2/w2*, *mpvb18/b18*) at 3 dpf[199].

2.3.6 Tolerance of living zebrafish embryos to cRSI

To assess laser tolerance, zebrafish embryos at 3 dpf were prepared for live cRSI as outlined above. Three Raman images were measured in sequence using a 1.5 s integration time with a 2 x 2 μm spatial resolution. Before and after each of the three scans, 30 s videos were recorded of the heartbeat and blood circulation using bright-field microscopy attached to the confocal Raman microscope using the screen recording software (Icecream Apps). In parallel, an identical protocol was performed without Raman imaging, as a negative control (N = 4).

The heart rates were manually counted from the videos and compared between the Raman scanned embryo and the unscanned embryo for each experimental repeat and at each time point. Linear regression was performed on the heart rate counts and the slopes of each of these regression lines analyzed individually using a two-sided Wald test to determine significant deviation from zero*. The whole set of slopes were then tested using a Wilcoxon signed-rank test.

*The statistical analysis was designed by Dr. John Goertz at Imperial College London, Postdoctoral researcher, Department of materials, South Kensington Campus, Imperial College London.

2.3.7 cRSI of living zebrafish embryo wound response

The stab wound protocol using surgical tungsten needles were performed as outlined above on live zebrafish embryos at 3 dpf. The stab wounded embryos were then mounted and prepared for live cRSI as outlined above. cRSI was then performed on the living embryos to acquire three planar scans collected for a period of 12 h. Images were collected as before using a spatial resolution of 2 x 2 μm, and 1.5 s integration time.

The Raman spectroscopy images were processed by spectral cropping and background subtraction, as previously described, and then a weighted spectrum subtraction of a background pixel spectrum was used to remove the spectral contribution of the underlying substrate. An exemplar univariate image of the wounded region was then generated *via* a sum filter between 1435 – 1465 cm^{-1}. Processed Raman spectra were analyzed using a custom MATLAB script*. Briefly, sequential Raman spectroscopy images of the wounded region were concatenated for processing before normalization (area under the curve) and removal of spectra containing cosmic peaks. Vertex component analysis (VCA) was performed to identify 10 endmembers. A spectral comparison was made between these endmembers and a live zebrafish control, scanned using a 785 nm laser. This was used to identify the 4 most relevant endmembers, representing water, pigment, and two different tissue signatures. The selected endmembers were then used to perform non-negatively constrained least-squares regression to generate abundance images for each endmember. The abundance images associated with the two tissue components were further analyzed in Fiji software to quantitively compare the relative temporal changes in wound response. A region of interest corresponding to the wounded somite was defined and the area under the curve was measured for the pixel intensity histograms corresponding to the two tissue components.

* The MATLAB script analysis was designed by Dr. Conor Horgan, Postgraduate Department of materials, South Kensington Campus, Imperial College London.

Chapter 3: Developing a zebrafish model for host-material interactions using ECM-hydrogels

3.1 Introduction

3.1.1 Biomaterial modulation of the host immune system

Despite the increasing problem chronic wounds constitutes, therapeutic progress in this area has been slow, and while current clinical treatments (e.g. antibiotics, operative debridement, and hyperbaric oxygen therapy) can alleviate part of the chronic wound condition, they fail to re-program the inflammatory wound milieu and to support constructive tissue repair[200,201]. For this reason, the use of biomaterials to promote wound immunomodulation has gained attention[202,203]. Many of these strategies have aimed at modulating macrophage behavior, both due to the importance of the macrophages in the wound healing process and because macrophages are among the most consistent responders to introduced biomaterials[204–206].

While the use of biomaterials to modulate macrophages into a state promoting wound healing state represents an attractive opportunity, macrophages may also negatively affect the biomaterial strategy. Specifically, biomaterials can induce the foreign-body reaction (FBR) which is an inflammatory reaction that develops on the surface of biomaterials[207–210]. The hallmark of FBR is the formation of the foreign body giant cells (FBGC) which are fused multinucleated macrophages sitting on the material surface[208,209,211]. The presence of FBGC is linked to the formation of a fibrotic capsule around the material, often interfering with the intended function of the material and causing tissue. It is now increasingly accepted that almost any introduction of a biomaterial will induce some form of immune reactions. This has led to increased efforts to understand how these host immune responses can be shaped into a favorable outcome. Thus, macrophages have been demonstrated to respond to many material cues such as shape, stiffness, size, and topography[204,212–215]. For chronic wounds, the desired biomaterial effect would be to stimulate the macrophages to form a less inflammatory environment and to promote the initiation of constructive wound repair.

3.1.2 ECM derived biomaterials – a strategy for wound immunomodulation

One proposed strategy for chronic wound immunomodulation is the application of biomaterials derived from decellularized ECM. These materials are manufactured from animal tissue by the removal of cellular and immunogenic tissue components to produce an extracellular scaffold, and decades of research have associated ECM materials with improved wound healing outcomes[216]. The therapeutic potential of ECM materials was first demonstrated for vascular surgery, but their use has since been expanded to cover almost every tissue in the body[217–220]. Thus, the ECM platform has seen several products achieve clinical approval for use in wound healing treatment (e.g. Surgisis®, MatriStem®, and MatriDerm®)[58,221].

Because decellularized ECM scaffolds require a surgical introduction, the development of injectable ECM hydrogels has expanded the potential applications of the ECM platform. Such hydrogels are formed from soluble mixtures of enzymatically digested and freeze-dried, decellularized ECM[219,222]. The enzymatic digestion is typically performed using pepsin in the water at a pH ~2. When the temperature, pH, and salt concentration of the ECM digests are raised to near-physiological levels the ECM digests can irreversibly form hydrogels. Thus, ECM hydrogels can be injected as a liquid when cool and form gels *in situ*, enabling them to conform to spatial irregularities such as wound cavities. These properties make ECM-hydrogels an attractive option for minimally invasive applications and to date, one product (VentriGel) has reached phase 1 clinical trials for the treatment of myocardial infarction[219,223].

3.1.3 ECM materials and modulation of macrophages

Despite the increased attention ECM materials have received, their interactions with host tissues are still poorly understood, and ECM based therapies have produced drastically varied outcomes in the clinic[224]. Variations in material source and manufacturing protocols are likely culprits for these effects[225,226]. However, the inherent complexity of ECM materials means that identifying the molecular causes underlying the therapeutic variations is very challenging.

Moreover, the ECM modes of action are not satisfactorily characterized, further complicating the interpretation of clinical failures.

However, a significant body of work has implicated the modulation of wound macrophages to be critical for ECM therapies. Hence, it has been demonstrated that decellularized ECM materials can cause a shift in the macrophage population away from the pro-inflammatory phenotypes towards anti-inflammatory phenotypes associated with a constructive wound repair[18,87,227–230]. The underlying mechanisms are still being explored but appear to be dependent on several different mechanisms related to the release of ECM content. Degradation of the implanted decellularized ECM material seems to be a premise for constructive wound healing, and it has been shown that ECM degradation products can alter the macrophage phenotype *in vitro*[231]. Degradation of decellularized ECM is likely to modulate macrophages through several different mechanisms. First, the hydrated part of ECM naturally acts as a reservoir of soluble factors and signaling molecules (i.e. TGFβ). Many of these factors remain intact and stored in the decellularized ECM materials and are slowly released during the material degradation[232]. Moreover, recently it was demonstrated that decellularized ECM retains extracellular vesicles containing unique immunomodulatory microRNAs[233]. Also, the matrix fibrillar network contains bioactive molecules that can stimulate and modulate host cells. These so-called matricryptic molecules are oligopeptide or oligosaccharide derivatives from the matrix and are released during proteolytic cleavage from the matrix parent chains[230,234]. Bioactive matricryptic fragments have been identified from laminins, collagen, elastin hyaluronan, and fibronectin[67,235]. Matricryptic fragments have long been known to influence many important aspects of inflammation including chemotaxis, phagocytosis, and gene expression[235].

Because macrophages are the main contributors to the ECM degradation, it is likely that they are exposed to several of the stored soluble factors, matricryptic fragments, and vesicles and that several of these molecules contribute to the macrophage modulation. However, their relative importance is yet to be understood and the mechanism of ECM immunomodulation is

still elusive. A second important drawback of these investigations is incomplete macrophage profiling. The macrophage characterization performed for ECM materials are usually performed using either quantitative PCR or immunohistochemistry and based on only a few select markers derived from the classical M1/M2 dichotomy (e.g. TNFα, iNOS, CCR7, for pro-inflammatory macrophages; ARG1, TGFβ, CD206, CD163, Fizz1 for anti-inflammatory macrophages)[18,220,231,236]. Moreover, most of the macrophage characterization has been performed *in vitro* with only a few exceptions. This leads to an incomplete picture of the macrophage population. It is now appreciated that *in vivo* macrophages generally are distinctly different from those observed *in vitro*, and in line with this general notion, a recent *in vivo* study using ECM material in a syngeneic mouse tumor model observed a macrophage response that did not conform to the classical M1/M2 paradigm and displayed both anti-inflammatory and tumor-inhibiting activity at the same time[113,237].

Therefore, to further discern the effects of ECM materials on host immune cells such as macrophages during wound healing, there is a need to move towards more realistic wound models where a larger part of the wound inflammatory niche can be recapitulated. While mammalian models are fundamental in such studies, these models often provide limited access to important spatiotemporal parameters such as cell recruitment or material degradation. This limited access constitutes a considerable challenge when considering for instance the important link between the degradation of the ECM and the release of bioactive molecules and fragments that are important for immunomodulation. Hence, the limited data available on ECM degradation has been recognized as an important knowledge gap for improved understanding of ECM functionality[58]. Moreover, the dynamic relationship between material, immune cells, and the surrounding tissue is also challenging to investigate in mammalian models. Hence, intravital imaging of material responses in mice has only been performed using a skin window model combined with multiphoton and non-linear optics (i.e. second and third harmonic optics[238].

3.1.4 Zebrafish as a model organism for host-material interactions

It is acknowledged that many biomaterial investigations are conducted in conditions lacking representative wound healing complexity[52,203,239]. Despite the advantages of the zebrafish model (Discussed in chapter 1.6.1), there has however been very limited use of zebrafish to study host-material interactions or biomaterial mediated immunomodulation. Recently, however, a few studies have made use of the zebrafish model to study host-material interactions.

Using a microinjection approach in zebrafish embryos Zhang *et al.* developed a semi-automated imaging approach to look at the early inflammatory response of polystyrene (PS) and poly(ε-caprolactone) (PCL) microspheres. This study revealed a stronger infiltration of neutrophils and macrophages to the PCL microspheres compared to the same sized PS, indicating a differential immune reaction to different material chemistries in the embryos. Moreover, the authors observed no difference in immune cell infiltration between 10 μm and 15 μm micro-particles[240]. Using a similar microinjection approach Witherel *et al.* demonstrated that adsorption of IL-10 onto 10 μm PS microparticles reduced neutrophil infiltration to the material at 24 hours post-injection in living zebrafish embryos. This further signifies the potential of studying immunomodulation of host-material interactions in real-time using the zebrafish model[241]. During this study these researchers also developed a strategy for surgical suture implantation of adult zebrafish tails, to study the formation of collagen capsules around implanted polypropylene sutures. This set up also enabled live adult imaging using multiphoton microscopy[241].

Further work using the adult tail suture model, compared the FBR of nylon and vicryl sutures and compared them to non-implanted controls. Interestingly, this study identified extensive formation of multinucleated FBGCs around the sutures in both material groups, while none were observed in the non-implant controls. Moreover, the vicryl sutures displayed a higher number of FBGC, a larger non-vascularized wound area, and an elevated number of

neutrophils and macrophages compared to the nylon sutures[242]. Also, the vicryl suture produced a higher level of TNFα expressing macrophages and a larger fibrotic area than the nylon sutures indicating both a stronger FBR and a stronger inflammatory response. Interestingly the authors were able to partly reduce the FBR response observed for vicryl both by treatment with the anti-inflammatory drug hydrocortisone and by using the zebrafish mutant line *panther*[242]. *Panther* mutants lack the colony-stimulating factor 1 receptor (*csf1ra*) and are known to produce a suppressed wound inflammation and these data suggest a strong link between the early inflammatory response to the material and the later development of FBR[242].

While the body of work studying host-material interactions in zebrafish is still very small, the studies discussed above indicate that the material inflammatory responses observed in this model are analogous and highly conserved when compared to mammalian models. Taken together, the ability to use live imaging approaches and the availability of transgenic or mutant lines to track responses with high fidelity, suggests that the zebrafish model can be further developed into a very attractive and informative model for studying host-material interactions.

3.1.5 Aims of the chapter

Following the discussion above, zebrafish embryos could be a useful model for studying host-material interactions caused by ECM hydrogels and specifically to study the interaction between the hydrogels and the innate immune system of the embryos. Thus, the aim of this chapter was to establish a zebrafish embryo model to conduct these studies and investigate the potential of this model.

The chapter describes the development of a zebrafish embryo model for studying host-material interactions using ECM hydrogels derived from porcine small intestinal submucosa (SIS). By using microinjections, fluorescently labeled hydrogels were applied to zebrafish embryos, tracked over time, and correlated with the presence of neutrophils and macrophages at the injection site. Moreover, the inflammatory response of SIS ECM hydrogels was compared to that of the pro-inflammatory agent Freund's complete adjuvants and PBS mock injection.

Lastly, a stab wound injection protocol was established to investigate the role of ECM hydrogels during wound repair.

3.2 Results and Discussion

3.2.1 Establishing ECM Hydrogel Injection in Zebrafish Embryos

3.2.1.1 Establishing an Injection Route

The first challenge to developing a zebrafish embryo model for ECM hydrogels was to establish a protocol for introducing the gels into the embryos. This strategy had to meet several criteria to ensure that the study remained both relevant and reproducible. Specifically, it was necessary to identify a route that enabled a fast, precise, and localized introduction of the gel material, while keeping the ECM concentration high enough for the subsequent transition from ECM liquids into hydrogels. Moreover, to be able to visualize the gel inside the embryos, it was also necessary to determine a labeling strategy for the ECM hydrogels. To this end, a series of optimizations were performed to identify a set of gel and injection parameters where all these criteria could be met (**Figure 3.1**).

Zebrafish Microinjections
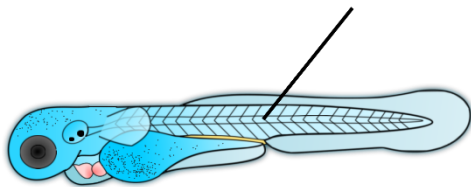
Criteria:
i) Precise and Localized
ii) Close Volume Control
iii) Sufficient Throughput

Material Characterisation
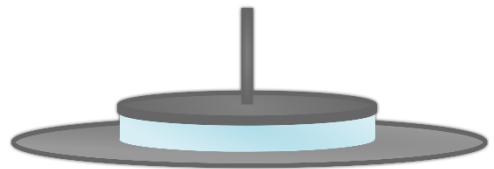
Criteria:
iv) Maintain Gelation Properties
v) Labelling Strategy

Figure 3.1: Schematic of the optimization needed to enable the zebrafish embryo model for ECM-hydrogels.

The first optimization was to identify a route for introducing the ECM hydrogel into the embryos. Given the small size of the zebrafish embryos, we elected to use microinjections through glass capillary needles (See Methods for more details). Although microinjection is a quite common

procedure in zebrafish embryos, there were no described methods for injections of hydrogels and during the initial testing, a few important considerations were identified. First, ECM hydrogels have a concentration-dependent viscosity and at higher concentrations (>5 mg/mL) the gels could not be ejected from the glass capillaries, meaning even when maximum pressure (~400 kPa) was applied[243]. However, at 5 mg/mL the hydrogels could be consistently released from the capillaries, and this was still within the concentration range that has been used in previous studies of ECM-hydrogels[222,243]. Second, while a concentration of 5 mg/mL enabled ejection of the hydrogels, small drifts in the injection volume over time was observed. Thus, to ensure a consistent injection volume the microinjections were performed using a microscope eyepiece reticle (NE120, Pyser-SGI). This enabled direct measurement of the diameter of the injection droplet and assuming a spherical droplet, the injection volume could be estimated. This protocol provided a continuous control over the injection volume, allowing the droplet size to be rapidly inspected before each injection. With these two optimizations, controlled injections of ECM hydrogels at a relevant concentration could be performed.

3.2.1.2 Rheological Characterization of ECM Hydrogels

Having identified a microinjection procedure, it was necessary to characterize the rheological properties of the SIS-ECM hydrogels at 5 mg/mL, and specifically to determine how the ECM-hydrogels responded to the temperature used in the zebrafish model. While zebrafish embryos are reared at 28.5℃, experiments involving ECM hydrogels are normally performed at the human physiological temperature of 37℃. Because ECM hydrogels are thermo-responsive and their gelation mechanism is dependent on an increase in temperature, it was important to determine to what extent the SIS-ECM hydrogel would still form a gel at 28.5℃. In particular, it has been reported that without the formation of a gel, the ECM solution will diffuse out of the injection site diluting the effect of the material. Thus, characterizing the rheological properties was required to ensure proper hydrogel function. Moreover, many of the important features of hydrogels such as degradation time and cell infiltration may be affected by their mechanical properties[244].

To this end, rheology was performed using small-amplitude oscillatory shear (SAOS) which is a well-established method that is commonly used to characterize ECM-derived hydrogels[222,243]. In SOAS, the sample is placed between two parallel plates and subjected to small torsional oscillations caused by an angular displacement between the two plates. This generates shear flow in the sample and the torque associated with this displacement is used to calculate the elastic modulus (G') and the viscous modulus (G'') of the sample. The elastic modulus G' is a measure of the resistance to mechanical deformation and therefore describes the solid-like component of the hydrogel. The viscous modulus G'' is a measure of the liquid-like behavior of the hydrogel. Thus, gelation can be observed by an increase in the G' relative to the G'', and previous rheological characterization of ECM hydrogel has observed G's that are about ten times larger than G''s after gelation[222].

When working with soft materials such as ECM hydrogels the SOAS parameters (e.g. frequency, strain) need to be carefully considered to avoid that the measurements themselves can introduce mechanical perturbations to the hydrogel sample[245]. Thus, these measurements need to happen within the linear viscoelastic range (LVE) where G' is independent of strain and frequency[245]. To this end, strain and frequency sweeps were performed on SIS-ECM hydrogels at 5 mg/mL after 12 h incubation at 28 ℃. These experiments identified linear visco-elastic behavior for the ECM hydrogels at 0.1% strain and 1 Hz frequency (**Figure 3.2**) which is in agreement with previously reported rheology of ECM hydrogels formed at 37 ℃[222]. Hence, 0.1% strain and 1 Hz were chosen for testing the changes in G' and G'' in response to heating at 28 ℃.
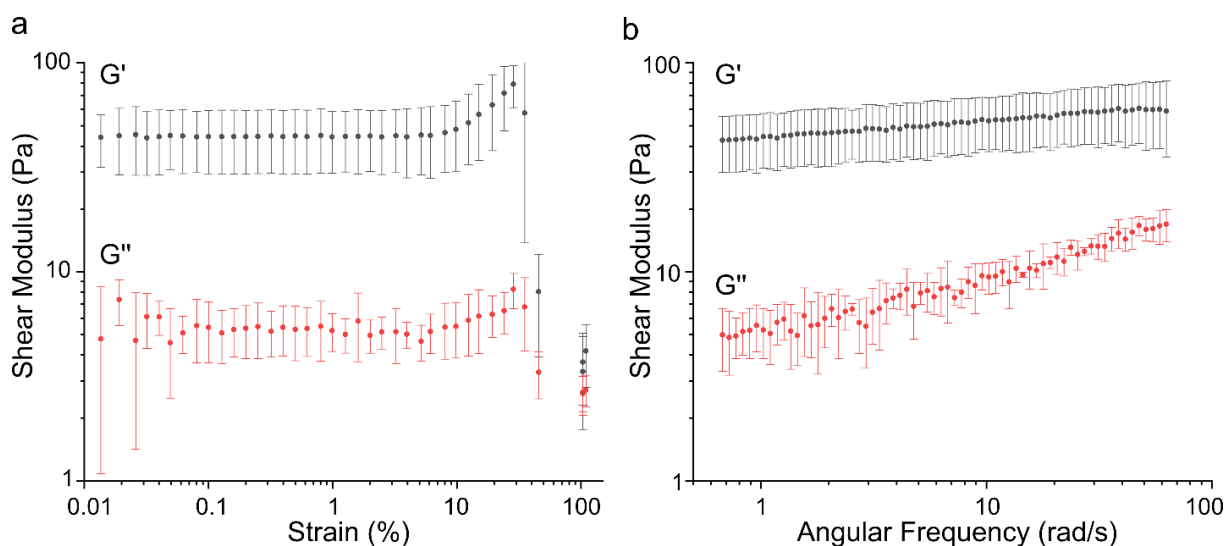
Figure 3.2: Rheological validation of the LVE for 5 mg/mL SIS-ECM hydrogels at 28℃. a) *Strain sweep of 5 mg/mL SIS-ECM hydrogels at 28℃. Grey line shows the mean G'; the red line shows the mean G" of three independent replicates.* **b)** *Frequency sweep of 5 mg/mL SIS-ECM at 28℃. Grey line show the mean G' red line shows the mean G" of three independent replicates.*

To characterize the changes in moduli upon heating to 28℃, 12 h time sweeps were performed on three independent replicates of ECM hydrogels at 5 mg/mL concentration. Fresh hydrogels were prepared on ice and loaded onto the rheometer that had been cooled to 4℃. The temperature was then raised to 28℃ and allowed to equilibrate for 1 min before starting the time sweep. Two control measurements at 37℃ were also included to allow for comparison to the 28℃ samples. The experiments show that the 5 mg/mL SIS-ECM hydrogels respond to heating to 28℃ with a marked increase in the G' relative to the G" over time (**Figure 3.3**) with the mean values at 12 h being 43.2 ±11.0 Pa and 5.2 ± 1.2 Pa respectively. These experiments also indicate that the gelation kinetics is slower at 28℃ than at 37℃. Moreover, the mean G' at 12 h at 37℃ was 60.1 Pa indicating that at the end of these measurements the 37℃ samples were slightly stiffer. The observed difference in gelation kinetics between the SIS-ECM hydrogels at 28℃ and 37℃ may have some important implications affecting the study of ECM hydrogels in zebrafish embryos that should be investigated further. Specifically, because the ECM hydrogels are more liquid at 28℃ than at 37℃, they may also have a slightly altered release kinetics of for instance soluble factors or matrix bound vesicles. Differences in release

kinetics is likely to affect the functionality of the hydrogels and this would be important to consider when interpreting the experiments obtained using the zebrafish embryo model. Thus, it would be valuable to assess the differences in release kinetics between the hydrogels at 28 ℃ and 37 ℃. To this end, the hydrogel samples could be loaded with fluorescently labelled model proteins of different sizes and allowed to gel at either 28 ℃ or 37 ℃. Following the gelation, the hydrogels could be transferred to a buffer solution where the release of fluorescent proteins into the buffer solution could be measured over time to identify and quantitate any differences in protein release kinetics between the two temperatures. However, while the reduction in temperature did change the gelation properties slightly, these experiments demonstrate that at the injectable concentration of 5 mg/mL SIS-ECM hydrogels retain their solid-like properties and still undergoes gel transition at 28 ℃.
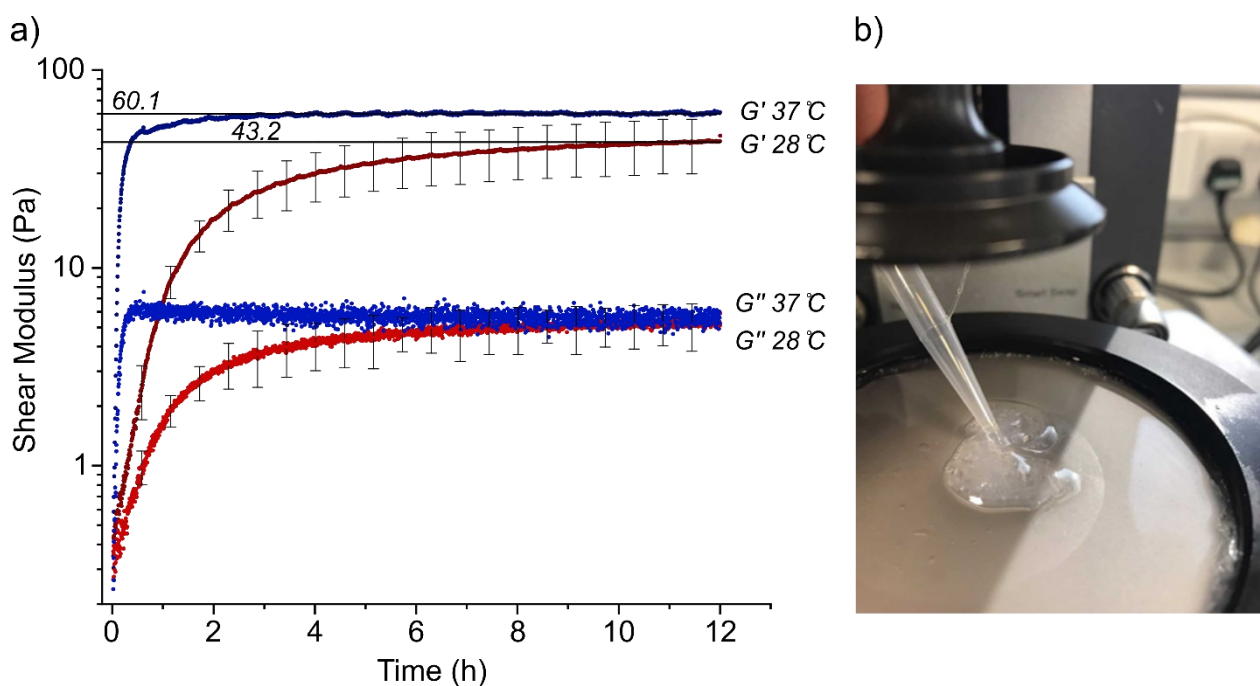
Figure 3.3: Time sweep of SIS-ECM hydrogels to determine gelation properties. a) Time sweeps were performed on 5 mg/mL SIS-ECM using 0.1% strain and 1 Hz angular frequency. The dark red line shows the G' mean of three independent replicates at 28 ℃ with and the error bars indicates the standard deviation. The light red line shows the mean G'' at 28 ℃ from the same three replicates. The dark blue line shows the mean G' of two independent replicates of 5 mg/mL SIS-ECM hydrogel at 37 ℃ and the light blue line indicates the mean G'' from the same two measurements. The G' values are indicated by straight lines and are 60.1 Pa at 37 ℃ and 43.2 at 28 ℃. b) Image of 5 mg/mL SIS-hydrogel just after a completed time sweep at 28 ℃. After the time sweeps. the SIS-ECM hydrogel had transitioned from a liquid into a cohesive gel which could be observed when poking the hydrogels with a pipette tip.

3.2.1.4 Ellman Assay and Maleimide Labelling of ECM hydrogels

The next objective was to identify a method to fluorescently label the ECM hydrogels. One such approach is to use fluorophore coupled maleimides that react through Michael's addition with the thiol groups present on for instance proteins present in the ECM. One important benefit to this approach is that it provides a covalently attached label and therefore reduces artifacts such as label-leaking that may occur if a noncovalently attached label is used. However, to prevent the addition of excess maleimide molecules a stoichiometric assessment of free thiols in the ECM hydrogels was required. Stoichiometric estimation of free thiol groups can be achieved using the Ellman assay[246]. This assay is based on the Ellman reagent 5,5'-dithiobis-(2-nitrobenzoic acid) (DTNB) which is cleaved by reactive thiol groups to release the colored salt 2-nitro-5-thiobenzoate (TNB). This reaction is rapid and happens at a stoichiometric ratio of 1:1, thus releasing 1 mol of TNB per mol of thiol. The concentration of thiols can be estimated from the color change associated with the formation of TNB using a standard curve.

Thus, an Ellman assay was performed on six independent replicates of SIS-ECM hydrogels at 5 mg/mL (**Figure 3.4**). From these measurements, it could be estimated that the ECM hydrogels had a mean thiol concentration of 0.10 ± 0.01 mM at this concentration. Hence, to label the SIS-ECM hydrogels, 0.6% (v/v) of 10 mM Alexa fluorophore maleimides (488, 546, or 647 nm depending on the experiment) was added to the gels. This would bring the final maleimide concentration in the gels to 0.06 mM giving a sub-stoichiometric ratio of 0.6 maleimides relative to the estimated hydrogel thiols and thus ensuring that an excess of maleimide was not added.
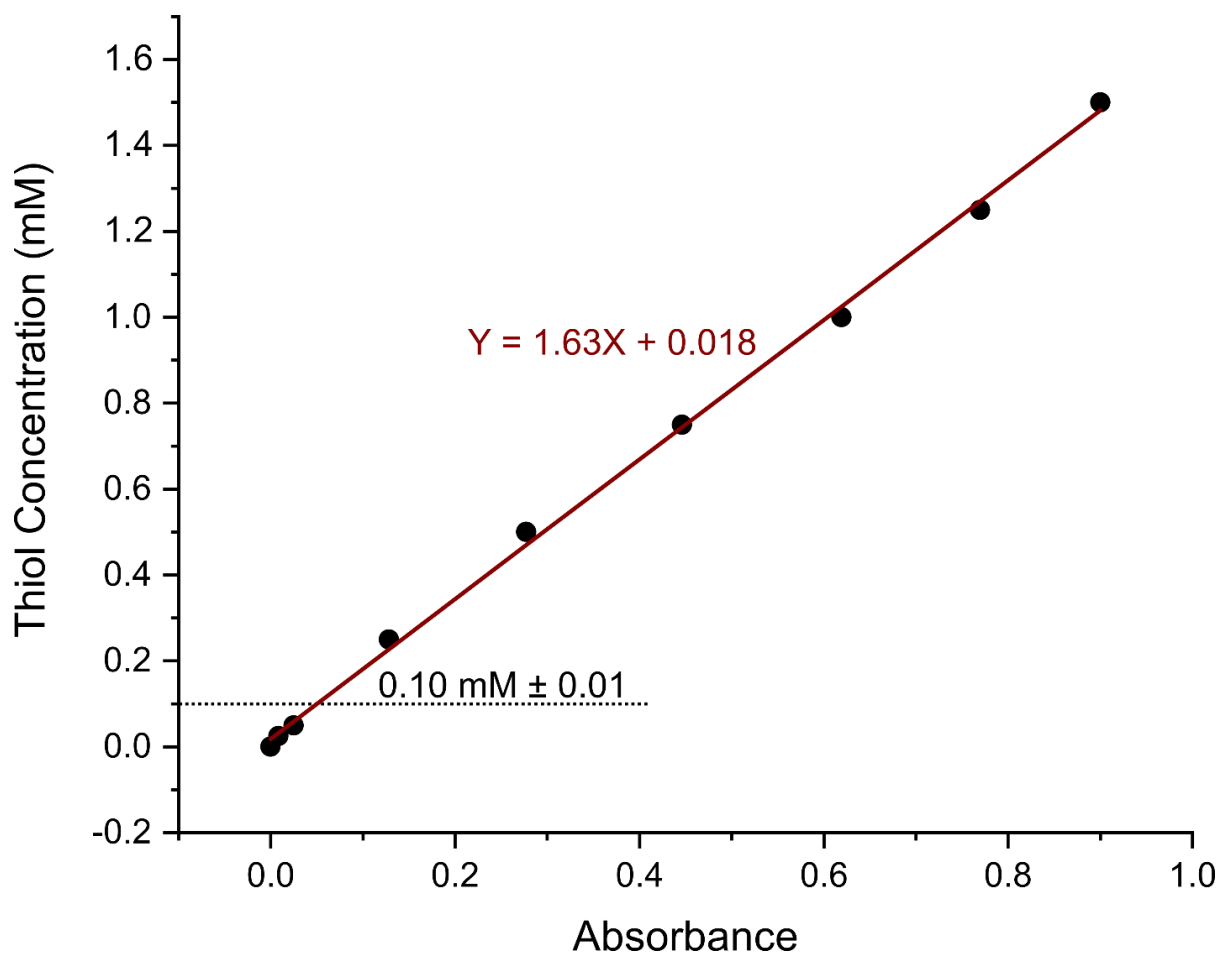
Figure 3.4: Ellman assay performed on SIS-ECM hydrogels to quantitate the concentration of ECM bound thiols. *An Ellman assay was performed on six independent replicates of 5 mg/mL SIS-ECM hydrogels to quantitate the concentration of ECM bound thiols groups that could be used for maleimide labeling of the gels. The black dots indicate the absorbance measured for the cysteine standard and the red line indicates the calculated standard curve with the standard curve equation shown in red letters. The dotted line indicates the mean thiol concentration (0.10 mM) obtained from the six independent ECM measurements with a standard deviation of 0.01 mM.*

3.2.1.4 Experimental Groups and Survival

This project aimed to study the host-material interactions of ECM hydrogels in the zebrafish embryo model with a special emphasis on the innate immune system. However, to better define the immune responses towards the ECM hydrogels, it was important to establish complementary experimental groups. Specifically, the study should include a mock injection group to control for the introduction process for the ECM hydrogel, and ideally also a pro-inflammatory group that would drive the immune response towards chronic inflammation. After testing several potential candidates (data not shown), the use of Freund's complete adjuvants (FCA) was identified as a promising candidate for a pro-inflammatory injection group. FCA consists of mineral oil mixed with mycobacterial cell wall extracts and is therefore a strong pro-inflammatory agent. Moreover, because FCA is an oil mixture it is was also feasible to inject and to visualize in the embryo.

To ensure a localized placement of the ECM hydrogels and FCA the zebrafish embryos were injected with 0.5 nL in the dorsal epaxial myotome just opposite to the anal pore. Also, a group of PBS injected embryos were included as a control group. Using this injection route both the maleimide labeled SIS-ECM hydrogels and the FCA could be observed at the injection site using a stereomicroscope to image live embryos (**Figure 3.5**). Thus, this set up enabled controlled and localized microinjections of both the FCA and SIS-ECM hydrogels followed by tracking of the injected agents.
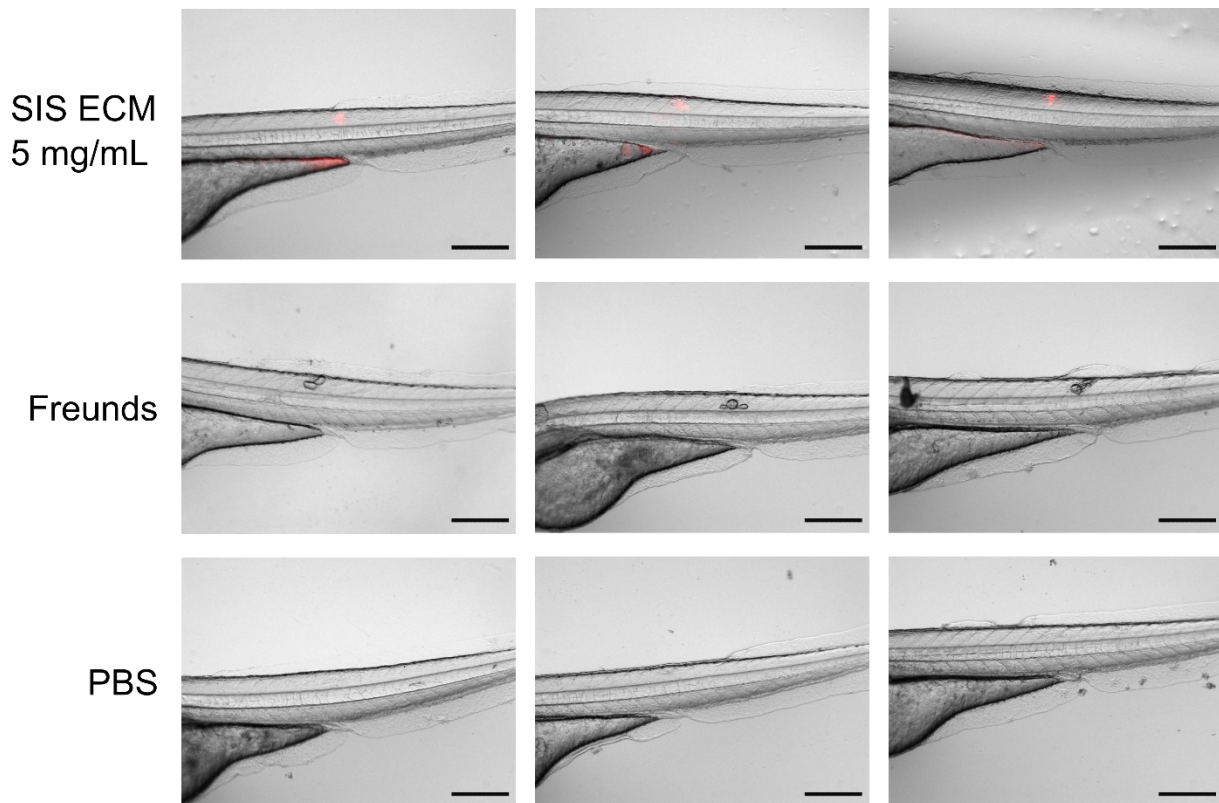
Figure 3.5: Demonstration of microinjections in zebrafish embryos at 3 dpf using labeled 5 mg/mL SIS-ECM, FCA, and PBS. *Exemplars zebrafish embryos injected with 5 mg/mL SIS-ECM hydrogels (red dots, top row), FCS (middle row), and PBS (bottom row). Each row displays three representative embryos at 5 hpi. Scale bars: 300 µm.*

To test the survival of the embryos following the injections, PBS, SIS-ECM of FCA injected embryos were tracked for 96 h and dead embryos were recorded (**Figure 3.6**). Out of a total of 83 embryos used in this assessment two deaths were registered – one in the PBS and one in the SIS-ECM group (both at the first recording time point, 6 hpi). This indicates that within this time frame none of the injections are leading to high mortalities in the embryos. Collectively, the results presented so far demonstrate a feasible microinjection strategy for ECM-hydrogels, providing sufficient control over injection volume and localization. Moreover, the hydrogels can be fluorescently labeled and do undergo a liquid to gel transition. Lastly, two additional experimental groups were included, FCA and PBS, enabling a comparison to the effects of the injected SIS-ECM hydrogels.
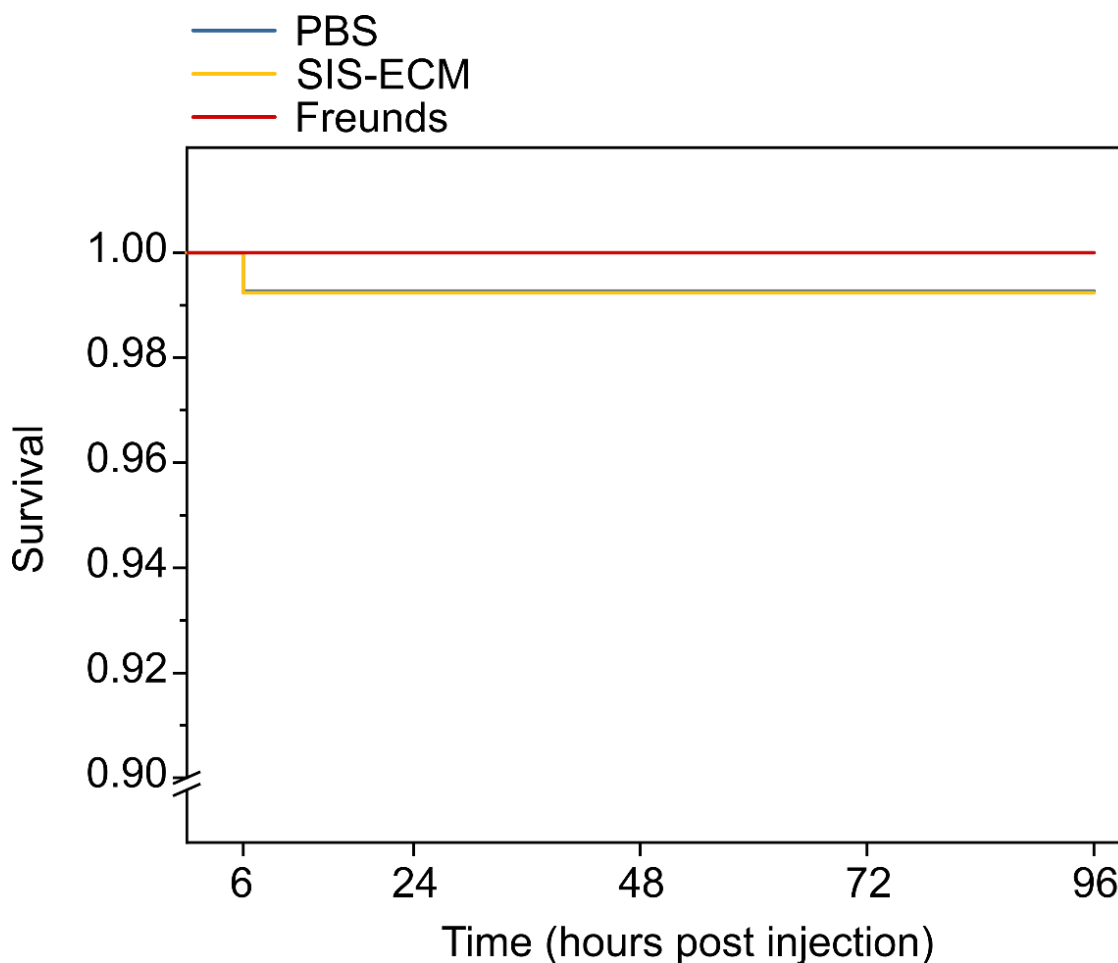
Figure 3.6: Kaplan-Meier plot showing survival of zebrafish embryos following microinjections.
Kaplan-Meier plot of Zebrafish embryos injected with 0.5 nL of either PBS, FCA, or 5 mg/mL SIS-ECM hydrogels. Out of the 83 embryos injected in total, only two did not survive until the end of the experiments (1 embryo in the PBS groups and 1 embryo in the SIS-ECM groups). The graph is a pool of two independent experiments using 11-15 embryos per experimental group. The data were subjected to a Kaplan-Meier test followed by a Log-Rank test and no significant differences were found at significance level 0.05 (Chi-Square = 0.59086).

3.2.1.5 Live Monitoring of Material Retention after Injection

To what extent the hydrogels are retained at the application site is important for their subsequent function. As discussed above, insufficient gelation can lead to leakage of the material out of the wound and thereby diminish their therapeutic effect[243]. However, ECM hydrogels are also biodegradable and previous reports have demonstrated that proper degradation of the ECM material is necessary for their effect on wound healing[222]. Specifically, ECM materials contain bioactive matricryptic molecules that are released upon material degradation, and these molecules may play a key role in the effect of ECM material[234]. Hence,

estimating the retention of the ECM hydrogels after injections into the zebrafish embryos could provide important insights needed for downstream analysis of the effects of the ECM hydrogels.

To this end, zebrafish embryos were injected with 0.5 nL of 5 mg/mL Alexa 546 maleimide labeled SIS-ECM hydrogels at 3 days post fertilization (dpi) using the injection set up described above. The injected embryos were then live-tracked for 96 hours using a stereomicroscope (Leica M165 C) to capture images of the fluorescently labeled ECM-gels. Between the imaging time points, the embryos were kept in an incubator using 24 well plates that were sealed with aluminum foil to reduce the effects of photobleaching. The embryos were kept separate with one embryo per well to enabled tracking of each injected sample individually. After imaging, a threshold was applied to the fluorescent signal before the gel area was measured in ImageJ to estimate the retention rate of the ECM gels *in vivo* (**Figure 3.7 a**). To identify any changes in detected fluorescent area over time, the data was further analyzed using a one-way repeated measures ANOVA[247]. Repeated measures ANOVAs are used to analyze experimental designs that contain dependent variables, for instance in experiments where the same subjects are measured on multiple occasions over a period of time. The one-way repeated measures ANOVA test is similar to the regular one-way independent ANOVA but includes an additional step where the within-subject sum of squares is subtracted from the error sum of squares that is used to calculate the F-distribution and the p-value in the one-way independent ANOVA test. Thus, this step reduces the contribution of subject-to-subject variation and increases the power of the repeated measures ANOVA compared to the independent ANOVA. However, this additional step also introduces a few extra assumptions regarding the data set which needs to be carefully addressed prior to running a repeated measures ANOVA[248].

These assumptions are as follows:

1) The experimental variable should consist of a minimum of two categorical and matched groups of measurements (e.g., repeated measurements of the same subject multiple times)

2) The outcome variable should be continuous.

3) The outcome variable should approximately follow a normal distribution.

4) There should be no significant outliers in the data set.

5) The data needs to fulfil the criteria of sphericity. That means that the variances of the differences between all combinations of matched groups must be equal. If the sphericity is violated, the data should be analysed applying a sphericity correction (e.g., Greenhouse-Geisser, Huynh-Feldt or lower-bound)[249].

In this experiment repeated measurements of gel fluorescence were conducted in the same specimen at different timepoints over the course of 96 hours, leading to a continues outcome variable. This means that assumption 1) and 2) were fulfilled. Furthermore, a Shapiro-Wilk was performed, and no violations of normal distribution were detected (24 hpi: p = 0.73266; 48 hpi: 0.60272; 72 hpi: 0.34872; 96 hpi: 0.47267), and a series Grubbs test was performed with no significant outliers detected. The most crucial criteria to test the sphericity when using a repeated measures ANOVA because violation of this criteria can easily render the test prone to Type 1 errors and thus a false detection of differences between the tested group means[249]. Sphericity was therefore tested using the Mauchly's test which indicated a deviation from sphericity ($\chi^2(5) = 26.34$, $p = 7.68 \cdot 10^{-5}$)[249]. For this reason, a Greenhouse-Geisser epsilon correction was used ($\varepsilon = 0.51626$) yielding an overall significant difference ($F(1.54879, 20.13) = 251.79$, $p < 3.31 \cdot 10^{-14}$).

Given the overall significant difference detected in the experiment the dataset was further analysed using a Bonferroni post-hoc test to test for significant differences in detected fluorescent gel between the successive timepoints. The amount of detected gel was found to be significantly reduced between the 24 hpi and 48 hpi timepoints ($p = 3.69 \cdot 10^{-16}$); the 48 hpi and 72 hpi timepoints ($p = 1.18 \cdot 10^{-8}$); and between the 72 hpi and 96 hpi timepoints ($p = 0.011$). This analysis revealed a gradual decrease in the fluorescent area detected around at the injection site and by 24 hpi the mean normalized fluorescent area had shrunk to 59% as compared to the first measured time point at 6 hpi (**Figure 3.7 b**). At the last time point, 96 hpi,

the mean normalized fluorescent area had been reduced by to 17% of that measured for the first time point at 6 hpi. This estimate indicates that a significant portion of the SIS-ECM hydrogels remains at the injection site at least four days. This could be important because several of the interesting application of ECM gels that could be studied in zebrafish, such as wound healing often happens over this time scale[177,180].

The reduction in the normalized fluorescent area is likely to be caused by several factors. First, some contribution from photobleaching cannot be excluded. To control for photobleaching effects, further experiments should be done to estimate any potential decay in the fluorescent signal caused by the chosen imaging procedure. To this end, SIS-ECM hydrogels should be prepared using the labelling parameters that was determined in section 3.2.1.4. Next, samples of labelled gel should be subjected to repeated imaging using the same microscope and the same imaging parameters that were used for the quantitation of the hydrogels presented in figure 3.7. From these images the mean fluorescence intensity can be calculated to evaluate the effect the imaging procedure contributes to any loss of fluorescent signal. For each hydrogel sample, at least five successive imaging repeats should be included to match the number of repeats that each injected gel was subjected to for the estimate of the gel retention presented in figure 3.7 b. However, to make the experiment more informative the imaging repeats should be extended until a clear photobleaching effect is observed. This information would define the robustness for this procedure with regards to photobleaching and would provide valuable information for future experiments that may include more timepoints than the five that was presented in this thesis. Second, it is likely that also part of the reduction is caused by gel degradation. While the exact degradation mechanisms of ECM hydrogels *in vivo* are not fully understood, it has been demonstrated to involve host immune cells and in particular, macrophages are involved in the reduction of the measured amount of gel at the injection site[250]. Third, although the ECM hydrogels do obtain solid-like properties at 28℃ and this has been shown to reduce gel leakage it is also likely that some of the reduction in fluorescent area is caused by the hydrogels diffusing away from the injection site. Hence further experiments

are needed to determine the relative contributions of these causes on the reduction in the detected hydrogel. However, this data demonstrates how the ECM hydrogel microinjection protocols developed in this study provides an opportunity for tracking the gel retention, and further work using this approach may help to better define retention properties of ECM hydrogels, and also to elucidate possible gel degradation mechanisms.

a)

	6 hpi	24 hpi	48 hpi	72 hpi	96 hpi

Embryo 1

Embryo 2

Embryo 3

Embryo 4

Embryo 5

b)
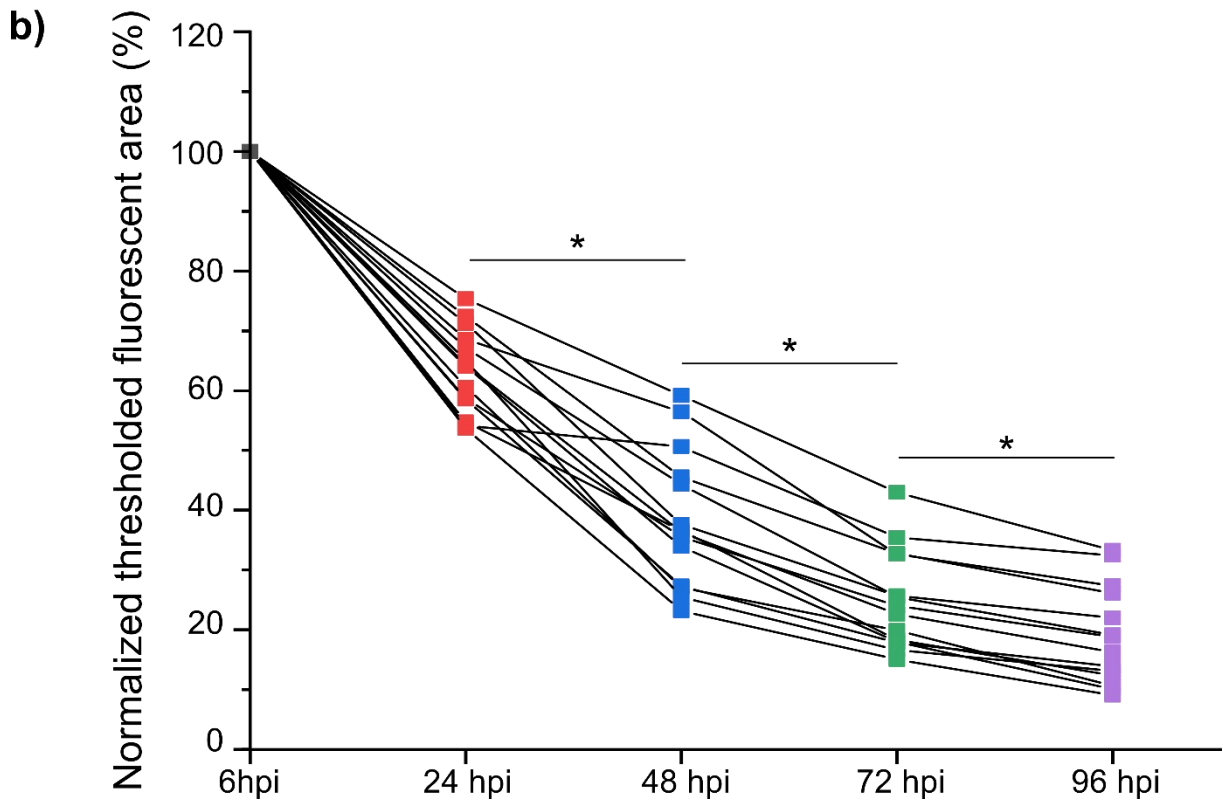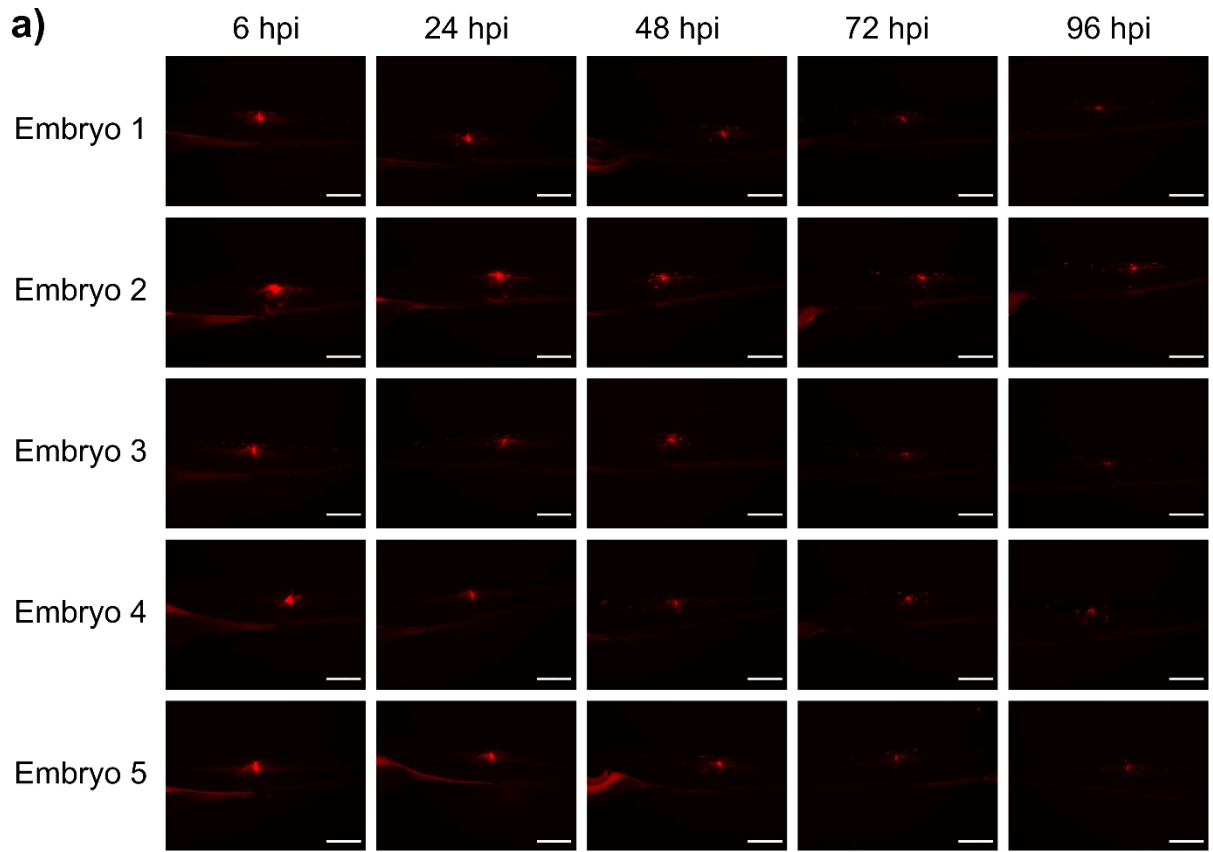
Figure 3.7: Quantitation of in vivo retention of SIS-ECM hydrogels. *The retention of SIS-ECM hydrogels was quantitated by thresholding and measuring the fluorescent area at the injection site at 6, 24, 48, 72, and 96 hpi.* ***a)*** *Exemplar embryos were injected with 5 mg/mL maleimide Alexa-Fluor 488 SIS-ECM hydrogels. Each row shows the same embryo imaged at different time points. Scale bars: 300 μm* ***b)*** *Data plot of showing the measured thresholded fluorescent area normalized to the value at 6 hpi for each embryo. The data is presented as connected trajectories of the embryos that were used in this experiment, (The means ± SD are: 24 hpi = 63 ± 7 %; 48 hpi = 38 ± 11 %; 72 hpi = 25 ± 7 %; 96 hpi = 19 ± 9 %). Statistical analysis was performed using a one-way repeated measures ANOVA followed by Bonferroni post-hoc test. Significant statistical differences are indicated by asterisks and were detected between 24-48 hpi (p = 3.69·10^{-16}); 48-72 hpi (p = 1.18·10^{-8}); and the 72-96 hpi (p = 0.011).*

3.2.2. Live monitoring of leukocyte recruitment after injection

3.2.2.1 Neutrophil Recruitment to Injection Site

The introduction of biomaterials into a living host will usually prompt an acute inflammatory response with the recruitment of innate immune cells such as neutrophils and macrophages[206,209,210]. While this inflammation can be detrimental to the functioning of some biomaterials, ECM derived materials are thought to exert their positive effects through interactions with the immune system. One of the benefits of investigating ECM hydrogels in zebrafish embryos is that it provides an opportunity to visually track the innate immune cells *in vivo*. Moreover, because the adaptive immune system in zebrafish does not develop until around 4 weeks post-fertilization, the zebrafish embryos represent an opportunity to study the innate immune system in isolation and thus uncouple it from the adaptive immune responses[251].

To analyze the neutrophil recruitment, the transgenic zebrafish line Tg(MPX:eGFP) was used. In these embryos (N = 14-16), the neutrophils can be tracked due to the expression of eGFP under the zebrafish myeloperoxidase promoter[172]. ECM hydrogel injections were performed as described above and the ECM injected embryos were compared to embryos injected with either FCA or PBS to compare the neutrophil recruitment profiles. Again, the embryos were imaged for 96 hours using a stereomicroscope (Leica M165 C). As before the embryos were kept separately using 24 well plates to enable tracking of single embryos. The images were then analyzed in ImageJ. For the analysis, a circular region of interest with a diameter of 200 μm was centered at the injection site. A gaussian blur filter was then applied to reduce the noise before the number of neutrophils was counted using the 'find maxima' function available in ImageJ (see methods for more details).

 For statistical analysis of the cell recruitment experiments a mixed two-way ANOVA design was chosen. The mixed two-way ANOVA is used for experimental designs that contain two factors where one of the factors is a within-subject factor (e.g., repeated measurements over

time) and the other factor is a between-subjects factor (e.g., subjects receiving different treatments). Thus, the two-way mixed ANOVA can be used when the effects of more than one treatment is studied and where the data includes repeated measurements on the same subjects over time. However, the two-way mixed ANOVA requires several assumptions to be fulfilled and these needs to be carefully checked prior to the analysis.

1) The within-subjects factor should consist of a minimum of two categorical and matched groups of measurements (e.g., repeated measurements of the same subject multiple times).

2) The between-subjects factor should consist of a minimum of two categorical and independent groups of measurements (e.g., different treatment).

3) The outcome variable should be continuous (i.e., quantitative, and non-categorical).

4) The outcome variable should approximately follow a normal distribution for every of the groups for the two factors.

5) There should be no significant outliers in the data set.

6) The variances for each combination of the groups of the two factors needs to be homogeneous.

7) The data needs to fulfil the criteria of sphericity. That means that the variances of the differences between all combinations of matched groups must be equal. If the sphericity is violated, the data should be analysed applying a sphericity correction (e.g., Greenhouse-Geisser, Huynh-Feldt or lower-bound).

Prior to running the test, the data set was checked against the seven assumptions required to run a two-way mixed ANOVA. While assumption 1), 2) and 3) could be verified directly by inspecting the data set, the four other assumptions required further statistical testing before they could be sufficiently verified. First, a Grubbs test was conducted for every single level of the factors. This test identified two significant outliers; one of these outliers was detected in the PBS 96 hpi (number of cells = 9, $p < 0.005$) and another one was detected in the FCA 96 hpi (number of cells = 17, $p < 0.01$). Moreover, Shapiro-Wilk tests were performed to test for normal distribution. These tests found that all of the three treatment the groups deviated from a normal distribution at the 96 hpi timepoint (PBS 96 hpi: $p = 0.005$; SIS-ECM 96 hpi: $p = 0.02$ and FCA 96 hpi: $p = 0.04$). For the rest of the groups, no deviations were detected. Thus, the data set did not perfectly match the assumption for the two-way mixed ANOVA model,

however, small deviations from the assumptions are not uncommon and may not severely affect the ANOVA analysis. Thus, before discarding this approach completely the effect of the nonconformity on the ANOVA analysis should be inspected in more detail. Further inspection of the data set revealed three important features of the data set:

i) when the two identified outliers were removed, the PBS 96 hpi and the FCA 96 hpi became normally distributed.

ii) removing the two outliers in the PBS 96 hpi and the FCA 96 hpi groups did not significantly change the means when compared using a two-sided two-sample t-test: (PBS 96 hpi: $p = 0.517$; FCA 96 hpi: $p = 0.508$).

iii) Comparing the results from two-way mixed ANOVAs run both with and without the outliers produced identical conclusions.

This indicates that the deviation from assumption 4) and 5) is mostly caused by the presence of two outliers in the dataset and importantly that the presence of these outliers does not change the conclusion the two-way mixed ANOVA analysis. Hence, because the two-way mixed ANOVA is generally considered to be robust towards deviations from normal distribution and because the identified outliers were few (2 out of 225 data points) and did not affect the overall analysis in any important way, analysing the data set using a two-way mixed ANOVA with the outliers included were considered to be the most appropriate statistical approach that was available for this data.

Next, the data was tested for sphericity using Mauchly's test which signified a deviation from sphericity ($\chi^2(9) = 37.98$, $p < 2.0 \ 10\text{-}5$). Thus, a Greenhouse-Geisser epsilon correction was used ($\varepsilon = 0.67294$) and a significant interaction between the two factors 'time' and 'treatments' were found ($F(5.38355, 113.05454) = 2.77833$, $p < 0.01828$). A significant interaction implies that further analysis of the data to identify any simple main effects (that is the effects of the two factors 'time' and 'treatment' independent of each other) must be performed by analysing each

factor separately for all factor levels. In other words, five separate one-way tests must be run for each time point separately to compare the effect to compare the effect of the treatments within that single timepoint. Moreover, three separate repeated one-way tests must be run for each of the treatments across the timepoint to identify if any of the three treatments groups changed over time.

Following the same line of reasoning as above, three one-way repeated measures ANOVA were used to assess the changes for each injection group over time and five one-way ANOVAs were used to compare the three injection groups for each time point separately (**Figure 3.8**). All groups where the ANOVAs indicated statistical differences were subjected to post-hoc analysis using the Tukey test. These analyses showed that for all three injection groups, the highest number of neutrophils was detected at 6 hpi and moreover for all three groups a significant reduction in the neutrophil number between the 6 and 24 hpi was observed (PBS: p = $2.99682 \cdot 10^{-8}$; SIS-ECM: p = 0.0066; FCA: p = $8.22949 \cdot 10^{-6}$). However, no significant changes in neutrophil numbers were found between any of the other subsequent timepoints. This analysis indicates that regardless of the injection group the highest neutrophil activity is found at the early time point, and also previous studies have identified the time points between 4 and 8 hpi to be the peak of neutrophil activity[172].

Further analysis using the Tukey test, comparing the number of counted neutrophils between the injected groups within single time points identified a significantly higher number of neutrophils in the FCA injected embryos compared to both the SIS-ECM and the PBS at 6 hpi (PBS vs. FCA: p $6.71438 \cdot 10^{-5}$; SIS-ECM vs. FCA: p = $3.68779 \cdot 10^{-4}$) and between all three groups at 24 hpi (SIS-ECM vs. PBS: p = 0.02412; PBS vs. FCA: p = $6.00178 \cdot 10^{-7}$; SIS-ECM vs. FCA: p = 0.00375). Importantly, at the last time point, 96 hpi statistically significant differences were detected between the PBS and the FCA (p = $1.45537 \cdot 10^{-4}$), and the FCA and SIS-ECM (p = 0.03831) but not PBS and SIS-ECM (p = 0.13224).

Neutrophils are mostly pro-inflammatory cells involved in the early stages of the inflammation. They are particularly important in sterilizing wounds, such as an injection site, but do normally not remain in the wound site beyond the early stages of the inflammation[98,252]. Therefore, differences in the number of neutrophils could indicate differences in the inflammatory environment at the injection site. The number of neutrophils observed around the injection site at 6 hpi in the PBS group is likely to be caused by the injection procedure and the subsequent decrease in neutrophil numbers indicates that the PBS injection for the most part does not induce a prolonged inflammation. The FCA on the other hand had a significantly high number of neutrophils compared to the PBS throughout the experiments suggesting that FCA does cause a pro-inflammatory environment, which was not unexpected given that FCA contains bacterial cell wall extract that should induce inflammation.

In line with this argument, these data also suggest a somewhat more inflammatory environment around the SIS-ECM hydrogels compared to PBS. Interestingly, statistically significant differences between PBS and SIS-ECM is first detected at the 48 hpi time point ($p = 4.31 \cdot 10^{-4}$). Thus, from these data, it seems that while the SIS-ECM does not cause a stronger neutrophil response initially compared to the PBS. However, the SIS-ECM seems to either retain or recruit neutrophils to the injection site for a longer time than PBS injection, which suggests a prolonged inflammation around the ECM-material.

a)

	6 hpi	48 hpi	96 hpi
SIS ECM			
PBS			
FCA			

b)
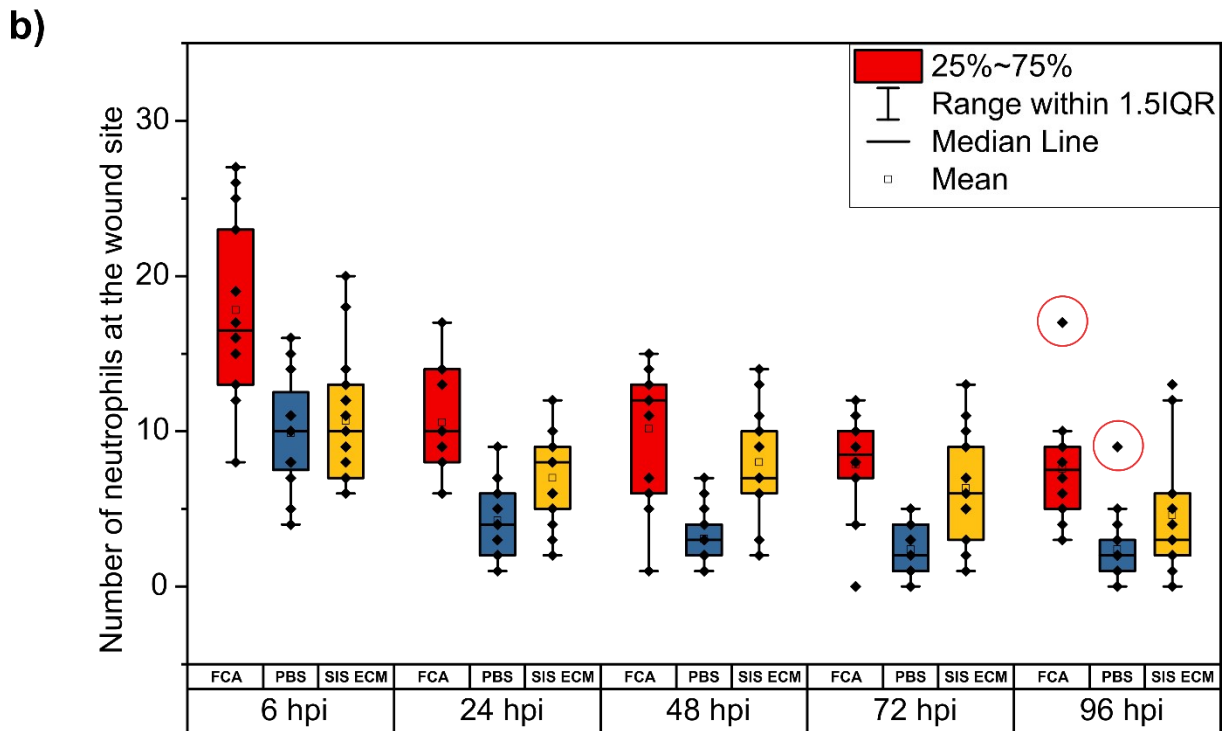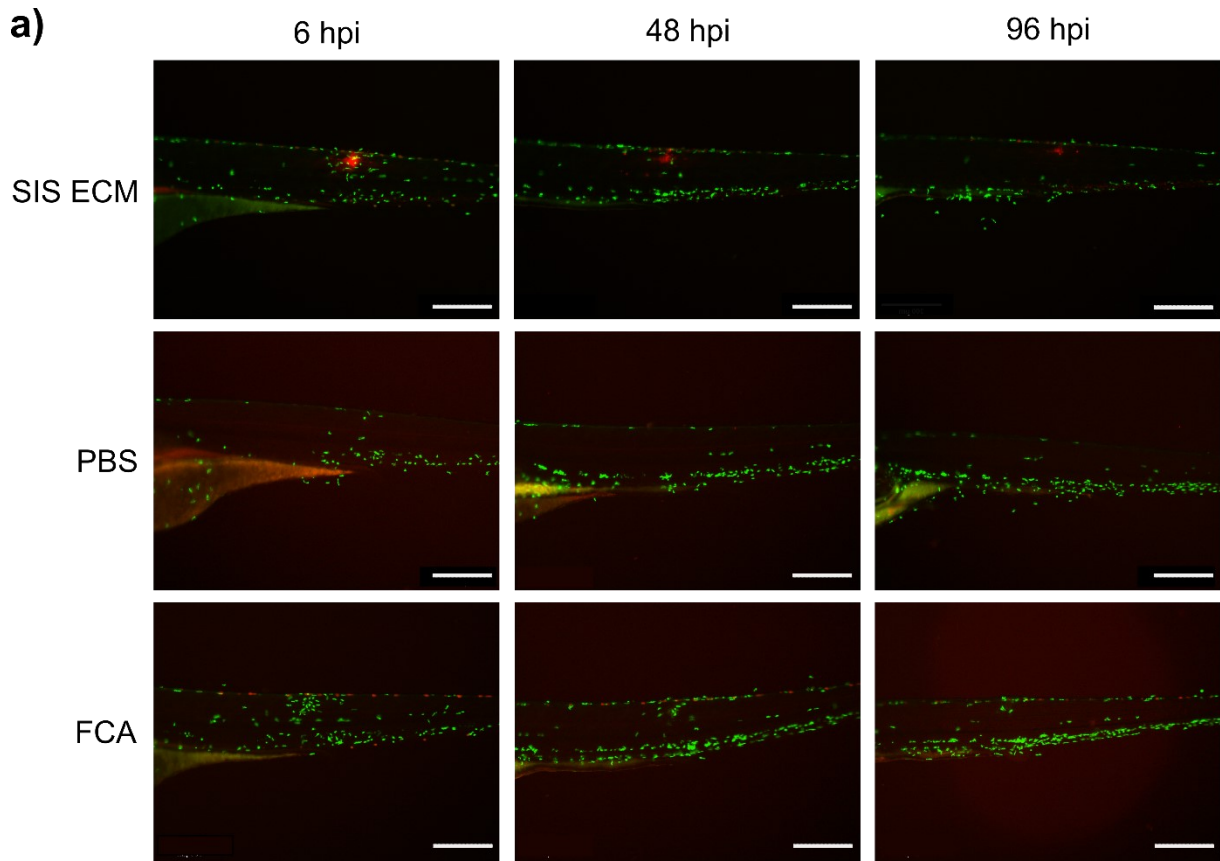
Figure 3.8: *Neutrophil count of microinjected zebrafish embryos. Tg(MPX:eGFP) embryos were injected with 0.5 nL of PBS, FCA or 5 mg/mL SIS-ECM hydrogels. **a)** Exemplar images showing a PBS injected embryo (left row), an FCA injected embryo (middle row), and a SIS-ECM injected embryo (right row) at 6, 48, and 96 hpi. The same embryo was used throughout the rows. Scale bars: 300 µm **b)** Box plot showing the number of neutrophils counted at each time point. Single counts are indicated by diamonds, the means are indicated by the hollow squares, the medians are indicated by the horizontal lines, the upper and lower quartiles are indicated by the boxes while the 1.5 quartile ranges are indicated by the vertical lines. Detected outliers are indicated by red circle.*

3.2.2.2 Macrophage Recruitment to the injection Site

To study the recruitment of macrophages to the injection site an injection experiment was conducted using the transgenic macrophage reporter line Tg(Mpeg:mcherry)[175]. The injections were performed as outlined before and with single injected embryos being live tracked over time using a stereomicroscope (Leica M165 C). The images were processed and analyzed using the same approach as for the neutrophil analysis, and the number of macrophages was counted inside a circular region of interest with a diameter of 200 μm centered at the injection site. For statistical analysis of the counted macrophages, a two-way mixed ANOVA designed was used, after the data had been tested against the two-way mixed ANOVA assumptions (page 79). While assumptions 1), 2) and 3) could be verified without further testing, the other assumptions required the performance of several statistical tests on the dataset. To this end, a series of Grubbs tests were conducted, and one significant outlier was detected (PBS 96 hpi, 14). Furthermore, Shapiro-Wilk tests were performed to test for normal distribution. Of the 15 data columns analysed 13 followed a normal distribution while two of the groups had slight deviations from the normal distribution (PBS 96 hpi, $p = 0.006$ and SIS-ECM 72 hpi, $p = 0.02$). However, the two-way mixed ANOVA is quite robust towards slight deviations from normal distribution and for this reason and because the majority of the groups conformed to a normal distribution, the two-way mixed ANOVA were considered to be the most appropriate statistical test that was available for this data. Furthermore, to test whether the detected outlier had any severe impact on the statistical analysis the two-way mixed ANOVA were performed both with and without the outlier included, but this did not change the outcome of the test. Therefore, the two-way mixed ANOVA was performed with the outlier included. Sphericity using Mauchly's test which indicated a significant deviation from sphericity ($\chi2(9) = 20.70$, $p = 0.01417$). To correct for this, a Greenhouse-Geisser epsilon correction was used ($\varepsilon = 0.80391$) when analysing the outcome of the two-way mixed ANOVA. Using the Greenhouse-Geisser corrections two-way mixed ANOVA analysis showed a significant interaction between the two factors 'time' and 'treatments' $F(6.43126, 106.11583) = 9.21402$, $p < 1.9038 \ 10^{-8}$. A significant

interaction implies that further analysis of the data to look for simple main effects (that is the effects of the two factors 'time' and 'treatment' separately) must be performed by analysing each level of the two factors separately. In other words, three separate one-way repeated measures ANOVAs had to be performed for the three treatments groups to identify any changes over time, and five one-way ANOVAs had to be performed for each of the timepoints to identify any differences between the injection groups (FCA, PBS and SIS-ECM) for each time-point. All ANOVA tests were then followed by a Tukey post-hoc test.

Interestingly, when counting the number of macrophages there was a clear difference between the PBS and the two other groups (**Figure 3.9**). This difference first appears from the 48 hpi time point. Thus, the one-way ANOVAs and subsequent Tukey tests (α = 0.05) identified no significant differences between the three groups at the 24 hpi time point (PBS vs. SIS-ECM: p = 0,97957; PBS vs. FCA: p = 0.64868; FCA vs. SIS-ECM: p = 0.77222). However, at 48 hpi the analysis detected significantly fewer macrophages in the PBS injected embryos compared to SIS-ECM (p = $8.91784 \cdot 10^{-6}$) and FCA (p = $4,05712 \cdot 10^{-5}$). The analysis also showed that the PBS group had significantly fewer macrophages also at the last two time points (i.e. 72 and 96 hpi) (p values not shown). Interestingly although FCA and SIS-ECM had a similar number of macrophages at all later time points, the statistical analyses detected a difference between FCA and SIS-ECM at the first time point (6 hpi), with more macrophages being recruited to the FCA compared to the SIS-ECM (6 hpi; p = 0.00594). However, for all the later time points, the Tukey test indicated no differences between FCA and SIS-ECM (p values not shown).

The macrophage count profile observed in the PBS injected embryos most likely is an effect of the injection procedure and the reduction in macrophages observed from 48 hpi and onwards suggests a resolution to the small wound response caused by the injections. It is, therefore, reasonable to conclude that the presence of FCA or SIS-ECM either retains or recruits macrophages to the injection site. However, while neutrophils are considered mostly pro-inflammatory, macrophages have a more nuanced and varied role in inflammation. Specifically, macrophages are key regulators of the inflammation and can exist in both pro-

inflammatory and pro-wound healing phenotypes[117,120]. Thus, while the number of macrophages at the injection site indicates an effect of the injected agents, this count alone is not enough to conclude that the macrophage response to FCA and SIS-ECM is identical. Previous work has identified macrophages as an important contributor to the degradation of ECM materials, and the macrophages may be associated with the injection site until the gel has been completely removed[250].

a)

24 hpi   48 hpi   96 hpi

SIS ECM

FCA

PBS

b)

89
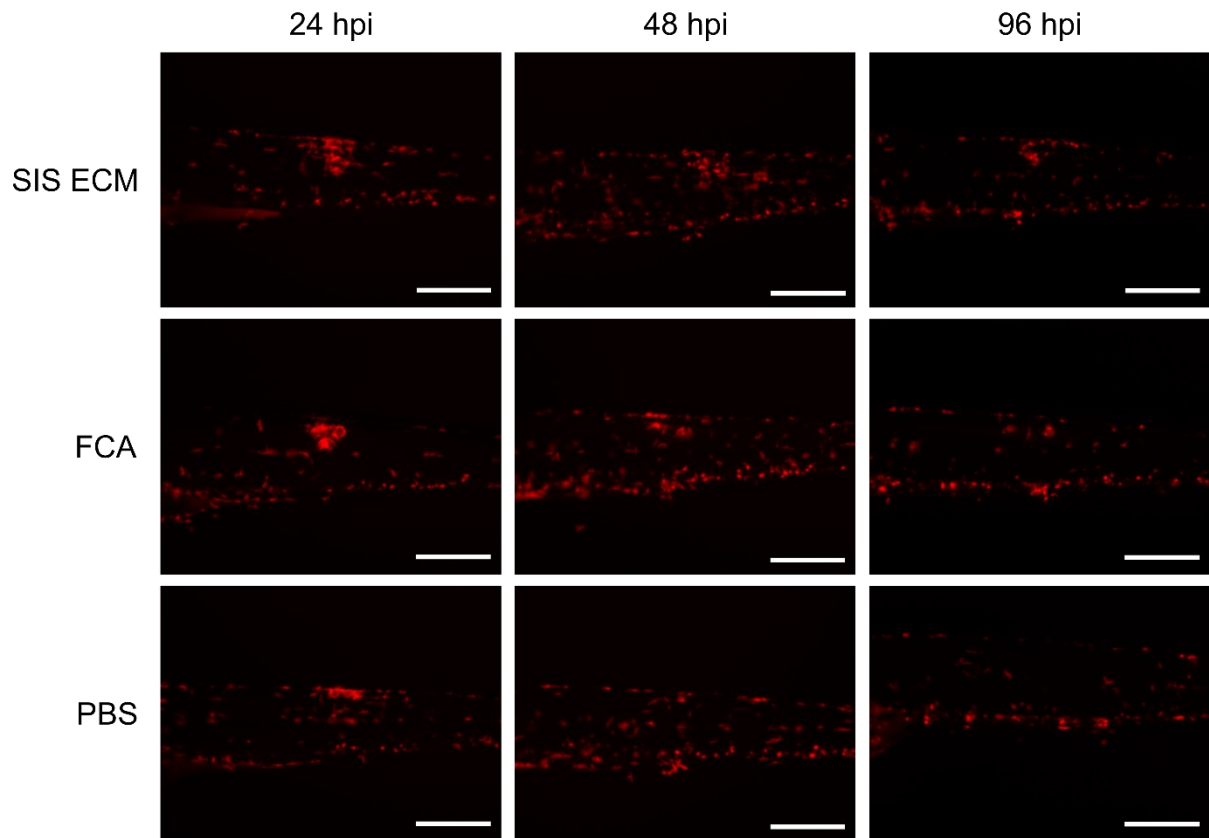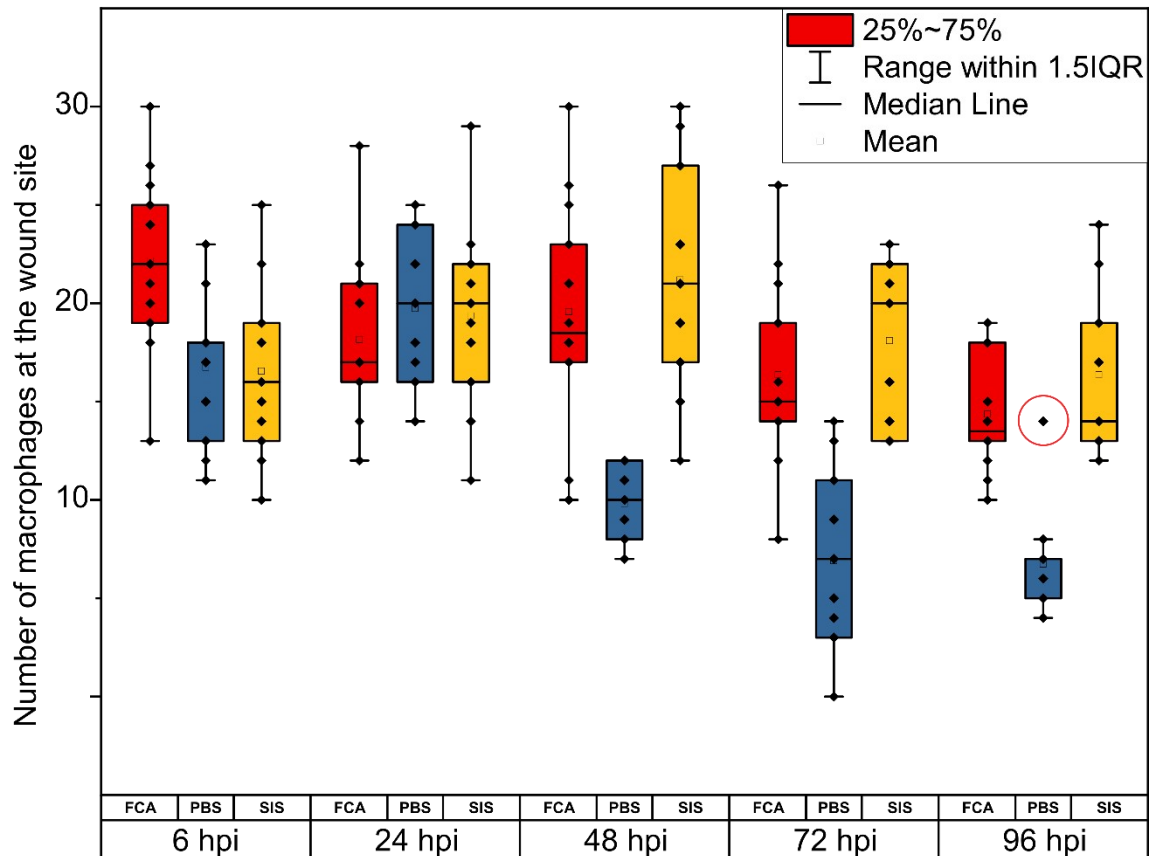
Figure 3.9: Macrophage count of microinjected zebrafish embryos. Macrophage count of microinjected zebrafish embryos. Tg(Mpeg:MCherry) embryos were injected with 0.5 nL of PBS, FCA or 5 mg/mL SIS-ECM hydrogels. **a)** Exemplar images showing a PBS injected embryo (bottom row), an FCA injected embryo (middle row), and a SIS-ECM injected embryo (top row) at 6, 48, and 96 hpi. The same embryo was used throughout the rows. Scale bars: 300 µm **b)** Box plot showing the number of macrophages counted at each time point. Single counts are indicated by diamonds, the means are indicated by the hollow squares, the medians are indicated by the horizontal lines, the upper and lower quartiles are indicated by the boxes, while the 1.5 quartile range is indicated by the vertical lines. Detected outlier is indicated by red circle.

3.2.3 Differential Gene Expression after Biomaterial Injection

3.2.3.1 qPCR to analyze Inflammation Marker Expression after Biomaterial Injection

A current limitation with the zebrafish model is that there are few antibodies available. Changes in the inflammatory processes is therefore often studied at the gene expression level using quantitative Polymerase Chain Reaction (qPCR) or in situ hybridization rather than at the protein level using for instance antibody staining or Enzyme-linked immunosorbent assay (ELISA) which is the preferred method in other animal models such as mice. However, the zebrafish genome is well annotated and there are many well-established primers and probes available for gene expression analysis. Hence, several recent studies have used gene expression analyses (e.g., qPCR, RNAseq) to investigate macrophage polarization in zebrafish embryos during wound healing and bacterial infection[110,153,191]. Given the several demonstrations in literature that qPCR could be used for this purpose, qPCR was a natural starting point for the analysis of inflammatory progression after the microinjections. The first set of experiments were aimed at testing the hypothesis that the three injection groups (PBS, FCA and SIS-ECM hydrogels) produced different wound environments and that these differences could be reliably detected at the gene expression level in the zebrafish embryos. The first set of experiments were designed to analyze the wound response at the tissue level using isolated midsection samples, containing the injection site and the surrounding tissue. To analyze the mRNA expression levels of inflammatory marker genes (e.g. IL-1β, TNF-α, and MMP-9) qPCR were performed. To this end, a protocol was developed to cut out the midsection of zebrafish embryos to remove the head and tail regions prior to RNA extraction (**Figure 2.10 a**). To achieve this, live embryos were mounted on a 6% (w/v) agarose plate, and an 18-gauge flat tip needle was used to punch out the injected midsection of the embryos. To preserve the RNA, the midsections were transferred directly into 'RNA later' (RNAlater™ Stabilization Solution, Invitrogen™) before the RNA was isolated using standard procedures as described under methods (See 2.1.9). To ensure enough RNA, 20 embryos were pooled per group and this gave RNA yields of 300 - 1000 ng with purity values (260/280 ratio) of 1.80-

2.00. Using this RNA isolation protocol, qPCR experiments were performed on zebrafish embryos injected with PBS, PCA, or SIS-ECM hydrogels as outlined before. Initial testing identified IL-1β, TNF-α, MMP9 as the most promising markers and for this reason, the experiments focused on the expression of these three genes, and three-time points (6 hpi, 48 hpi, and 96 hpi) were chosen for the analysis. The gene expression analysis was performed on three biological replicates, with each of these replicates containing all experimental groups (i.e. FCA, PBS, and SIS-ECM) in addition to an noninjected control group.

Inspection of the data showed that there were clear signs of batch-to-batch variations between the three biological replicates. While this was expected, it had to be taken into account when determining a suitable statistical model for analysis of the data. The experiments were designed so that each biological replicate always contained the complete set of all four experimental groups (i.e., SIS-ECM, PBS, FCA, and noninjected controls). However, the different biological replicates were performed at different days, meaning that different fish batches were used for each biological replicate. It is therefore reasonable to assume that the observed batch-to-batch variations were due to background differences between the different fish batches. To account for the presence of fish batch variations and to reduce effect this variation had on the analysis of the gene expression between the treatment groups, a repeated measures statistical model was chosen. This design means that the gene expression is treated as a dependent variable and that the gene expression is analyzed within each batch separately, rather than across all batches at once. However, the data set only contained three replicates which are too few to assume a normal distribution and therefore the non-parametric repeated measures procedure Friedman test was used[253]. Thus, for each gene and time point a separate Friedman test was used with three repeat levels, one for each fish batch. For the groups where the Friedman test indicated significant differences, post-hoc analyses were performed using a paired Wilcoxon signed rank test with a Bonferroni correction. These analyses identified statistically different mRNA levels for TNFα at 48 hpi ($p < 0.05$) and 96 hpi

(p < 0.05). MMP9 at 6 hpi and 96 hpi (p < 0.05) and for IL-1β at 96 hpi (p < 0.05). However, none of the post-hoc tests returned a significant value.

Despite the lack of significant differences detected by the Wilcoxon signed rank test, there are clear trends in the data set that could indicate differences in gene expression. Especially at the 96 hpi where the detected levels TNF-α and MMP9 are mRNA are apparently higher for FCA compared to SIS-ECM. An important limitation of the current data set is that it contains only three replicates which was not sufficient to draw any strong conclusions on the differences in the data. For experiments such as qPCR, where the expected variance is high, more replicates are needed to derive robust estimates of the means and data spread. Ideally, the experimental design should include enough data points to test for normal distribution and use a parametric test design, if the data are normal distributed. The non-parametric tests such as the Wilcoxon signed rank test, that are used when normal distribution cannot be assumed, suffer from lower statistical power than their parametric counterparts and are therefore less able to detect real differences in the data. This limitation could play a role in the statistical analysis that was performed on these data, that due to the few data points had to be performed using non-parametric tests. Thus, although the Friedman tests identified different expression levels in several for several of the tested genes at several timepoints, the post-hoc paired Wilcoxon signed rank tests could not determine between which treatments groups these differences occurred which meant that the experiment was partly inconclusive. For this reason, a future priority should be to add more repeats to conclusively assess whether the different injection materials lead to differences in inflammatory gene expression.
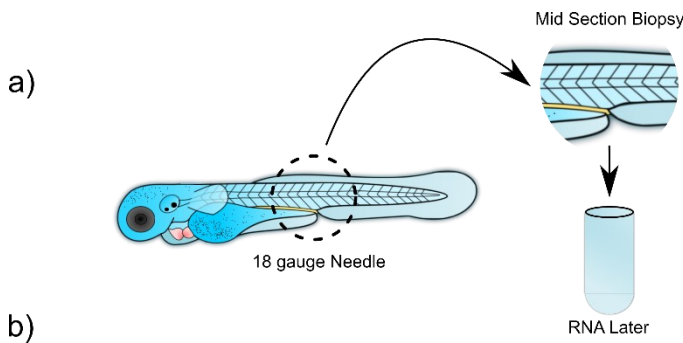
Figure 3.10: Gene expression of inflammatory cytokines in microinjected zebrafish embryos.

a) Schematic of the procedure developed to obtain RNA from mid-section biopsies containing the injection site from the zebrafish embryos. b), c) and d) Column chart showing the relative mRNA expression at 6, 48 and 96 hpi respectively. All data are expression levels relative to un-injected control embryos. Columns indicate mean and error bars show the SEM. Statistical significance were detected is indicated by asterisk. All mRNA expression levels were tested using a One-way repeated measures ANOVA followed by a Tukey post-hoc test. b) At 6 hpi no significant differences were detected in mRNA levels for IL1-β, TNFα, while a significant difference was found between for MMP9 (p < 0.05). c) At 48 hpi no statistically significant differences were detected for IL1-β or MMP9 while a significant difference was found between for TNF-α (p <0.05). d) At 96 hpi significant differences were detected in the expression of all of the three tested genes (p < 0.05).
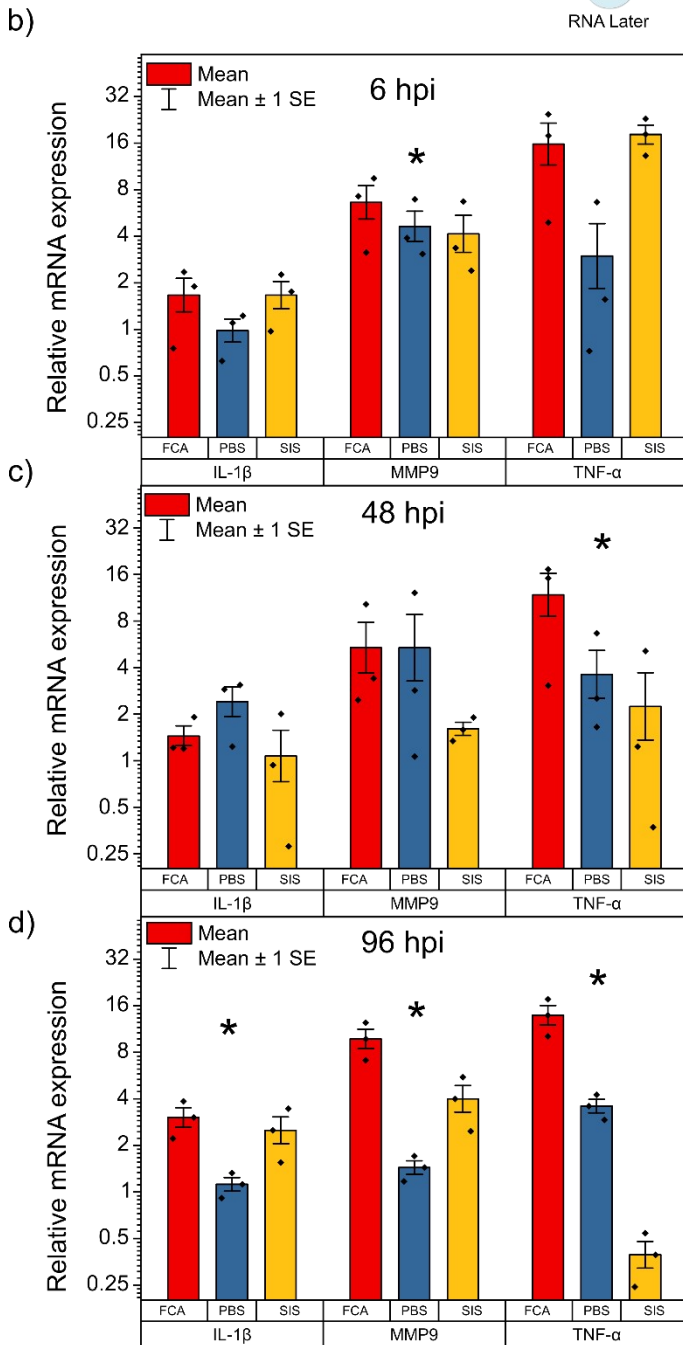
3.2.4 Summary of Host - Material Interaction experiments

Taken together the data acquired so far presents evidence that the three injected agents are causing different inflammatory environments at the injection site (Summary of the data are found in **Figure 3.11**). PBS injections appear to cause a transient, acute inflammation. Thus by 48 hpi, both macrophage and neutrophil numbers had dropped, and TNF-α mRNA expression levels were detected at a low level throughout these experiments. Moreover, at 96 hpi lower levels of *il-1β* and *mmp9* mRNAs were detected relative to FCA and SIS-ECM, further indicating a milder response. FCA on the other hand appears to induce a stronger and longer-lasting inflammation. Notably, at 6 hpi FCA injection embryos had a higher number of both neutrophils and macrophages and the overall number of neutrophils was higher compared to the two other groups throughout these experiments. In line with these findings, at 96 hpi increased levels of TNF-α and *mmp9* mRNA were detected in FCA relative to both PBS and SIS-ECM indicating a more pro-inflammatory environment at this time point.

SIS-ECM hydrogels seem to cause an inflammation that is somewhat stronger than the response caused by PBS injections, but milder than the response caused by FCA injections. Thus, while SIS-ECM displayed an overall lower number of neutrophils compared to FCA, SIS-ECM injections also caused a consistently higher number of neutrophils compared to PBS. Moreover, SIS-ECM injected embryos had the same number of macrophages associated with the wound site as FCA and the number of macrophages was consistently higher in SIS-ECM injected embryos than in the PBS injected group. However, the expression levels MMP9 and TNF-α mRNA appears to be lower in SIS-ECM relative to the FCA at the 96 hpi. This could suggest a less pro-inflammatory environment. Interestingly at this point, the TNF-α expression in the SIS-ECM was negative relative to the un-injected control and lower than what was observed in the PBS groups. Downregulation of TNF-α is one of the observed effects of SIS-ECM hydrogels on macrophages *in vitro* and that effect could be what was observed here. It is important to emphasize that this result needs to be corroborated by additional experiments (e.g. in-situ hybridization, transgenic TNF-α reporter lines).

Hence, one important question to address in the following experiments would be to what extent the macrophages observed at the FCA, SIS-ECM and PBS injection sites represent different macrophage phenotypes and what impact that would have on the surrounding tissue.
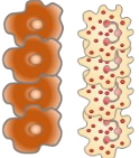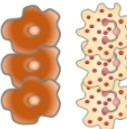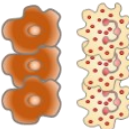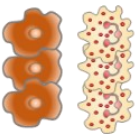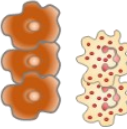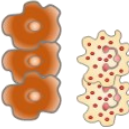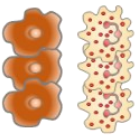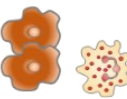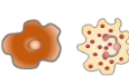
	6 hpi	48 hpi	96 hpi
FCA	TNFα MMP9 IL-1β	TNFα MMP9 IL-1β	TNFα MMP9 IL-1β
SIS	TNFα MMP9 IL-1β	TNFα MMP9 IL-1β	TNFα MMP9 IL-1β
PBS	TNFα MMP9 IL-1β	TNFα MMP9 IL-1β	TNFα MMP9 IL-1β

Figure 3.11: Summary of host-material interaction in zebrafish embryos. *Differences in macrophages and neutrophils counted at the injection site are indicated for each group and timepoint by the number of cell schematics. Differences in mRNA expression are indicated by font size with larger font indicating higher detected mRNA expression.*

3.3 Towards a Wound Healing Assay for ECM-Hydrogels in Zebrafish Embryos

An important aim of this study was to investigate the effects of SIS-ECM hydrogels during wound healing and regeneration. Thus, the last part of this chapter describes the design and initial experiments conducted towards this aim, with the initial results that were obtained. During the previous experiments, the injected embryos were also inspected using a brightfield stereomicroscope to identify if there were any visible effects on the injected host tissue. In the PBS injected groups, no visible effects of the injections could be seen in the embryos at 96 hpi. However, some effects were observed in both the FCA and the SIS-ECM injected groups (**Figure 3.12**). In the SIS-ECM injected embryos this effect took the shape of small hunchback formations at the injection site which was observed in several but not all of the embryos. In FCA injected embryos signs of tissue damage and debris formation were observed around the FCA droplets. Given the differences observed in the inflammatory response between the PBS, FCA and SIS-ECM injected groups it would interesting to also include the effects on the host tissue in the continuation of these studies and specifically to investigate if there are any important links between the immune reactions and the subsequent tissue responses.
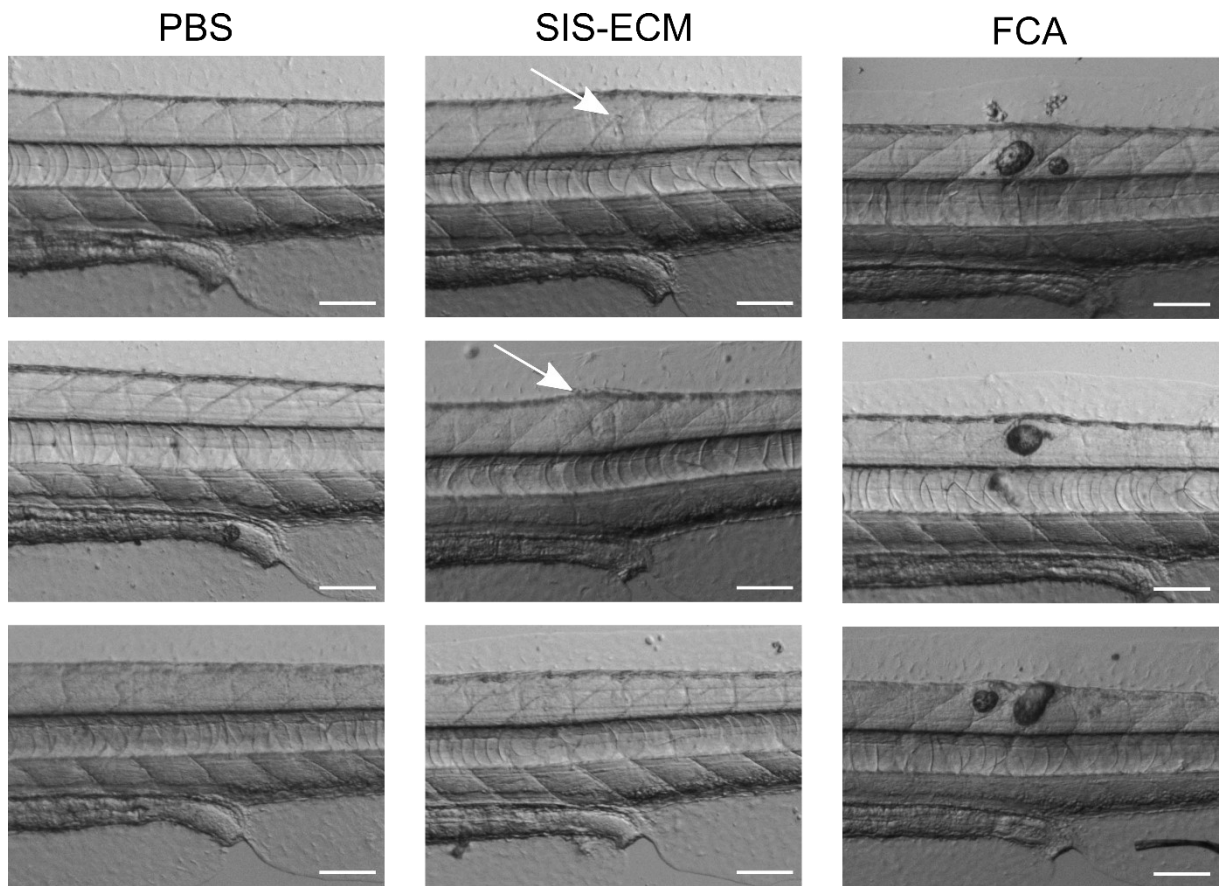
Figure 3.12: Brightfield image panel of injected embryos at 96 hpi. *Brightfield images captured at 96 hpi. The left column shows three exemplar PBS injected embryos. There are no clear signs of the injection sites in the PBS injected embryos at this timepoint. The middle column shows three SIS-ECM injected embryos. The two top embryos display the hunchback formation (indicated by white arrows) observed in several of the ECM-injected embryos at this timepoint. The right column shows three FCA injected embryos debris and tissue damage can be observed around the FCA droplets that are still intact in the injection site at this timepoint. Scale bars: 100 µm.*

3.3.1.1 Establishing Wound Injection in Zebrafish Embryos

The first consideration was to establish a suitable protocol for combined tissue wounding and material injections in the zebrafish embryos. To this end, the tip of injection glass capillaries was adjusted to an outer diameter of 30 µm using fine forceps and a stereomicroscope. This needle diameter was sufficient to cause single somite wounds in the embryos while injecting a small amount of SIS-ECM hydrogel (**Figure 3.13 a**). Further testing this approach with maleimide labeled SIS-ECM hydrogel demonstrated that the wound injection caused a visible stab wound, centered in the injected somite and that the injected gels were consistently placed at the wound site (**Figure 3.13 b**).

a)

Injected somite

45°

Anal pore

b)

24 hpi

48 hpi

72 hpi
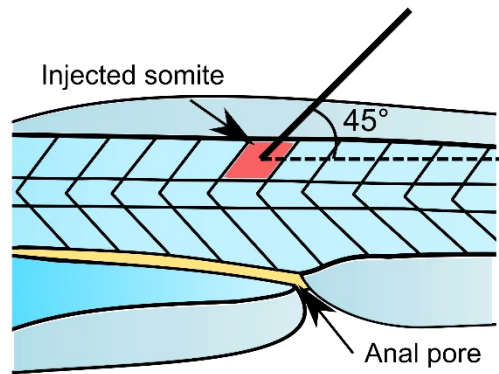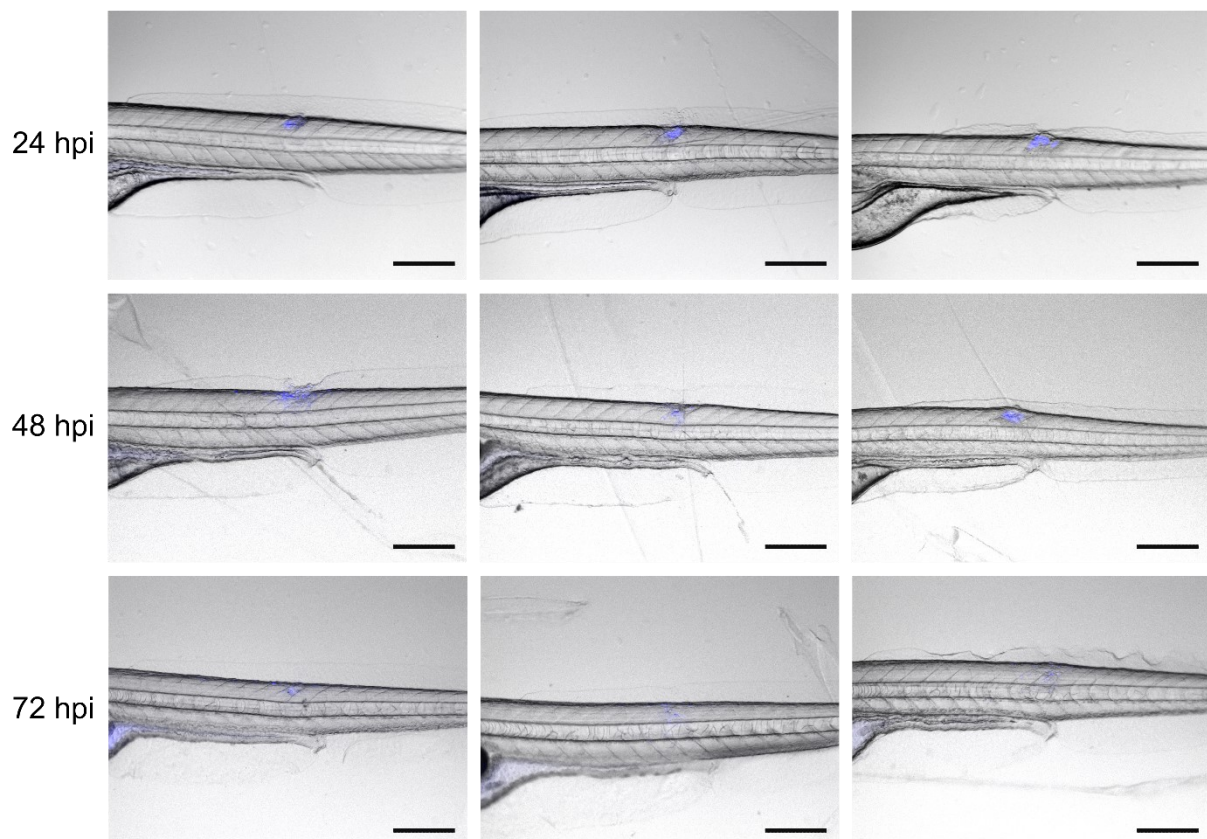
Figure 3.13: Establishing a stab wound injection in zebrafish embryos. a) Schematic demonstrating the stab wound injection procedure. Glass capillaries with a tip diameter adjusted to 30 μm were used to simultaneously stab and inject the zebrafish embryos in the dorsal epaxial myotome with the needle being held at a 45° angle **b)** Representative images showing stab wound injected zebrafish embryos at 24 hpi (top row), 48 hpi (middle row) and 72 hpi (bottom row). The embryos were injected with 0.5 nL of 5 mg/mL maleimide labeled SIS-ECM which can be seen in blue at the injection site. Scale bars: 300 μm.

3.3.1.2 Wound Healing and Regeneration in the Presence of ECM Gels

Using the wound injection approach, initial experiments applying confocal fluorescence microscopic imaging (CFLM) were performed to inspect the wound injection site in more detail. These experiments had two aims: i) to track the interaction between the injected material and the host immune cells in live embryos and ii) use phalloidin staining of muscle tissue to track the wound progression and gel progression in the days following the wound injections.

To this end, a video of a double-transgenic embryo Tg(Mpeg:Mcherry/MPX:eGFP) injected with Alexa 647 maleimide labeled SIS-ECM hydrogels were obtained using CFLM. The wound injection causes immediate recruitment of immune cells to the wound with both macrophages and neutrophils migrating towards the wound site within 20 minutes after the injection (**Supplementary Video 2.1**). Further CFLM of live zebrafish embryos 24 hours after injection with SIS-ECM hydrogels demonstrated a close association between the immune cells and the injected material and instances of macrophages covering the ECM hydrogels were observed (**Figure 3.14 a**). Moreover, a few examples of macrophages containing ingested hydrogel were also observed, which could imply macrophages involved in the degradation of the material. Hence continued CFLM experiments including more time points should be performed to further investigate the interaction between the host immune cells and the ECM hydrogels at the wound site.

Next, a phalloidin staining procedure was performed on embryos injected with maleimide labeled SIS-ECM, to investigate the effect of the presence of the hydrogels had on the surrounding wounded muscle tissue (see Methods for more details). One time point was inspected (24 hpi), and at this time point, the gels were localized in the center of the wounds where an absence of intact muscle tissue could be observed (**Figure 3.14 b**).
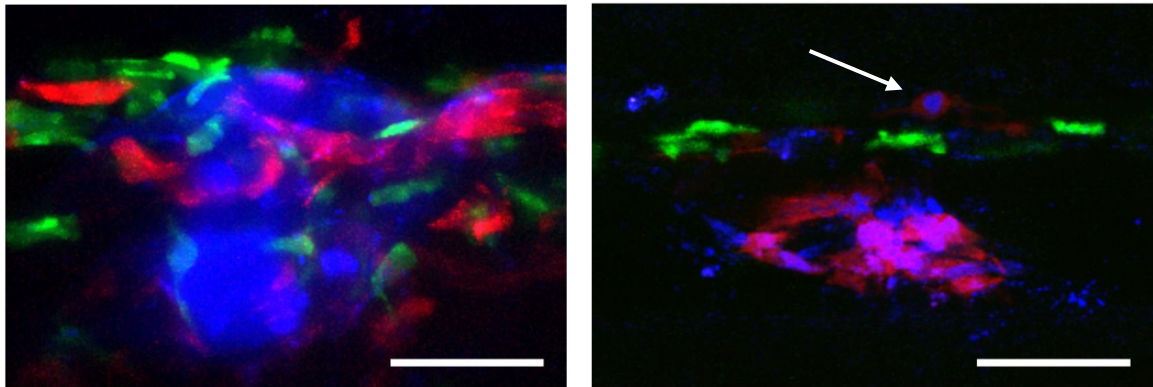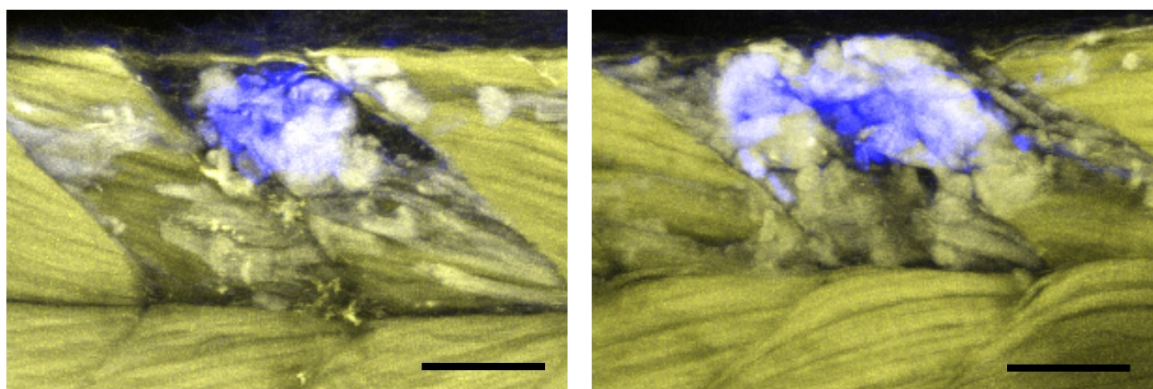
Figure 3.14: *Confocal microscopy imaging of stab wound injected embryos. a) Demonstration of live confocal imaging of TG(Mpeg:Mcherry/MPX:eGFP) embryos stab wound injected with 5 mg/mL of SIS-ECM hydrogel at 24 hpi. The two images are from two different representative embryos. Neutrophils can be observed in green; macrophages can be observed in red and the hydrogel can be observed in blue. The white arrow indicates a macrophage containing ingested gel material. Scale bars: 50 µm b) Examples of two zebrafish embryos at 24 hours post stab wound injection with 5 mg/mL of maleimide labeled SIS-ECM subjected to fixation and phalloidin staining to simultaneously visualize the injected gel and the damaged muscle tissue. The two images show two different representative embryos. The hydrogel can be seen in blue and the phalloidin stained muscle tissue can be seen in yellow. Scale bars: 50 µm.*

Lastly, a wound tracking experiment was planned to compare the effect of PBS, FCA, and SIS-ECM on the reformation of muscle tissue following the wound injections described above. To also enable fluorescent tracking of the FCA, a small volume of Bodipy630-NHS was mixed into the FCA solution prior to injections. Moreover, in this experiment, the transgenic fluorescent reporter line Tg(MPX:eGFP/TraNac) was used to allow tracking of neutrophils in addition to the injected agents and the wounds. To observe the wounds, the embryos were stained with phalloidin as described above. One timepoint was tested and at 6 hpi the injected agents were

found in close proximity to the wounds which could be observed by the damaged muscle fibers (**Figure 3.15**). Moreover, neutrophils were observed around the wound site in agreement with previous observations in this study.

a)
b)
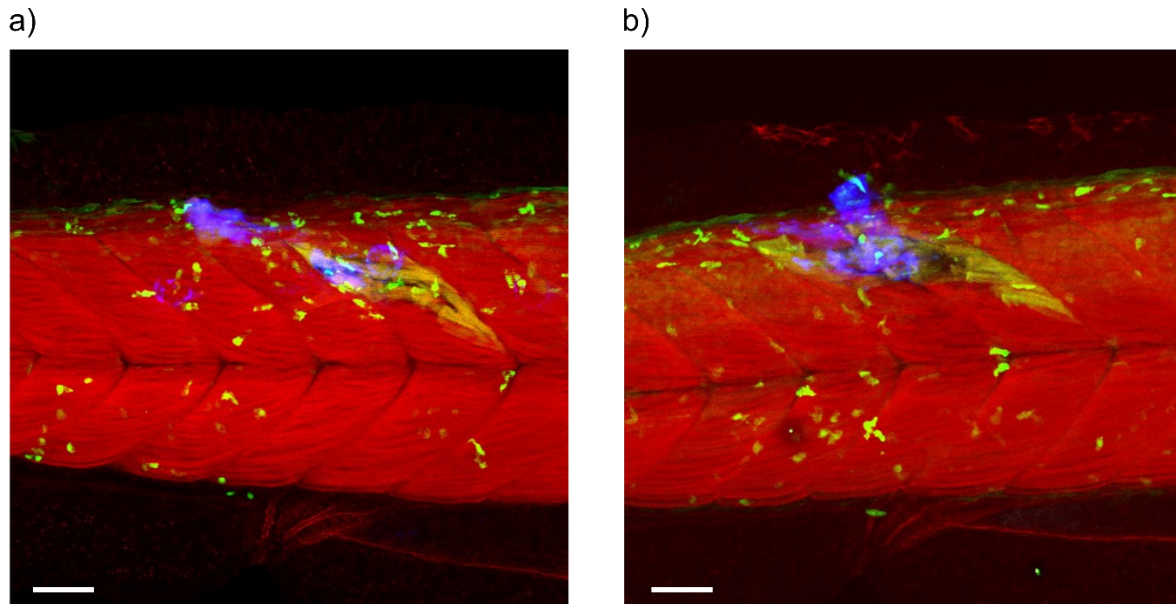
Figure 3.15: *Wound tracking experiment of stab wound injected embryos at 6 hpi. Representative confocal images of stab wound injected embryos at 6 hpi with a) Bodipy630-NHS-FCA and b) maleimide-labeled SIS-ECM. The embryos were fixed and stained with phalloidin to visualize the wound. The muscle tissue can be observed in red; the neutrophils can be observed in green and the FCA and SIS-ECM can be observed in blue. Also, a green auto-fluorescent area can be observed around the stab wounded tissue (for further discussion of the autofluorescence see chapters 3.3.4 and 3.3.5. Scale bars: 50 μm.*

Unexpectedly, the muscle tissue also displayed a high degree of green autofluorescence localized around the wounded area which partly interfered with the neutrophil GFP signal. The source of the autofluorescence was not identified, but one possible explanation is that it could stem from the endogenous xanthophore pigments found in zebrafish embryos. While the TraNacs mutants used in this experiment lack the two other types of pigments naturally found in wild type zebrafish (i.e. melanophores and iridophores) they still contain the yellow-colored xanthophore pigments. (A similar effect was observed when conducting stab wound for Raman spectroscopic imaging and a further discussion of this observation is found in Chapter 3.3.4.)

Finally, the wound areas observed using the phalloidin staining were measured in ImageJ by drawing an area around the damaged muscle tissue and then measuring the sizes of these areas (**Figure 3.16 a**). In this analysis, the FCA and PBS wounds were found to be significantly different (p = 0.01615, one-way ANOVA followed by Tukey test, α = 0.05), while no statistically significant differences were detected between SIS-ECM and PBS (p = 0.06977) or SIS-ECM and FCA (p = 0.69576) (N = 5) (**Figure 3.16 b**). While this constitutes the first measurement of the wound progressions, both more time points and repeats are needed to work out the effect of the injections on the wounds. Importantly, adding later timepoint would enable the comparison of wound progression over time rather than the absolute wound size which was analyzed here. These experiments and analyses are planned in the continuation of this study.

a)

Freunds   Mock   SIS
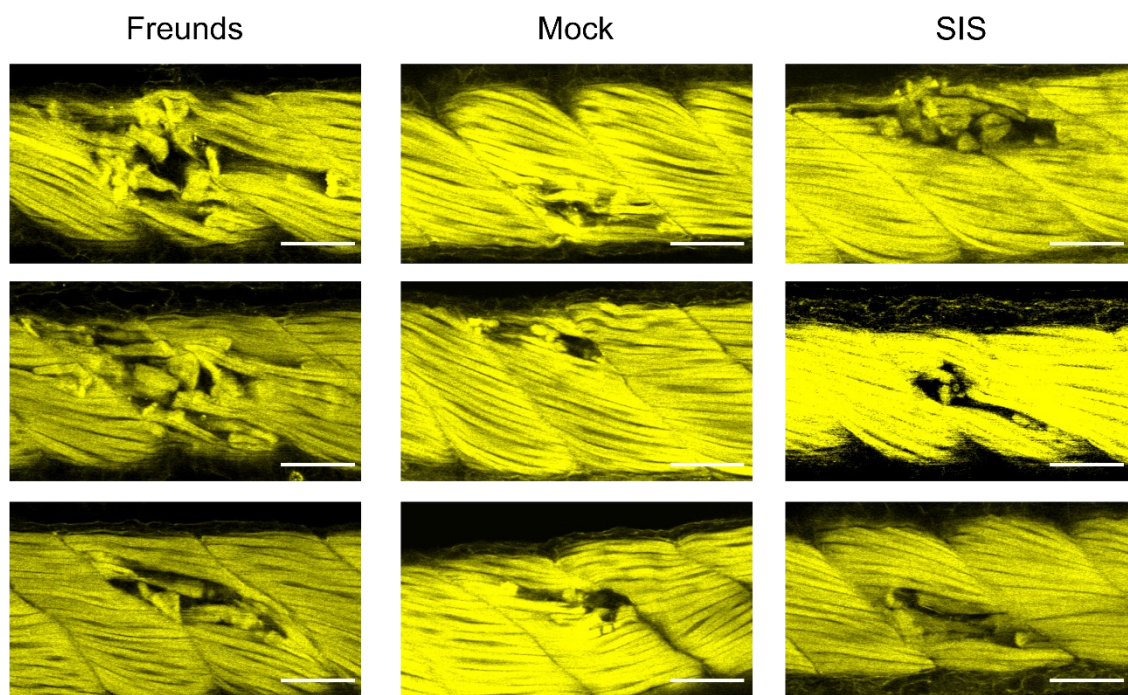
b)
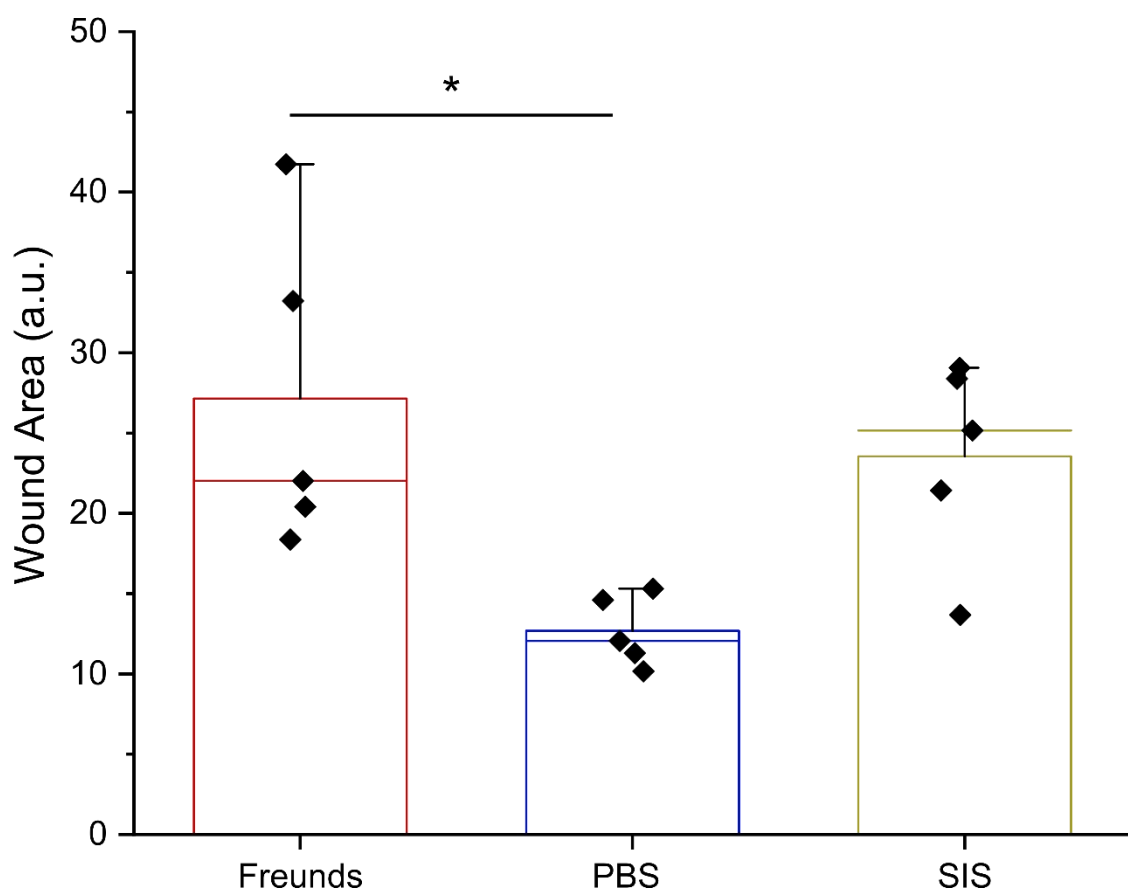
Figure 3.16: **Wound quantitation of stab wound injected embryos at 6 hpi.** *Zebrafish embryos (5 per group) were stab wound injected with either FCA, PBS, or SIS-ECM hydrogels. The embryos were fixed at 6 hpi and stained with phalloidin to visualize the wound areas.* ***a)*** *Representative images of stab wound injected embryos were used for the quantitation. FCA is the left column, Mock in the central column, and SIS-ECM in the right column.* ***b)*** *Histogram plot of measured wound areas at 6 hpi comparing stab wound injected embryos. The wound sizes were measured by drawing an area around the damaged tissue and these areas were measured and compared. The individual wound areas are represented by diamonds, the mean areas are represented by the bars, the vertical lines indicate the median and the standard deviation is indicated by the vertical capped lines. Statistical testing was performed using a one-way ANOVA followed by a Tukey post-hoc test. At a significance level of 0.05 Mock vs., FCA was significantly different; Mock vs. SIS-ECM was significantly different, while FCA vs. SIS-ECM was not significantly different. (N=5 per group). Scale bars: 50 μm.*

3.4 Concluding remarks

In this chapter, a zebrafish embryo model for host-material interactions using SIS-ECM hydrogels was established. The presented results demonstrate how ECM hydrogels can be controllably introduced and studied in zebrafish embryos without impairing important mechanical properties such as liquid to gel transition. The presented work demonstrates that the ECM hydrogels are retained at the injection site for at least 4 days following the injections. Moreover, the data indicate that the introduction of SIS-ECM hydrogels causes an inflammation that differs from the inflammation observed for PBS injection and the pro-inflammatory agent FCA. Specifically, the SIS-ECM mediated inflammation seems to be dominated by macrophages rather than by neutrophils and compared to FCA a lower level of inflammatory mRNA encoding inflammatory markers were detected. This could indicate that ECM material follows a specific inflammatory trajectory and identifying this inflammatory route might be important in designing future ECM mediated therapeutic strategies. The model established here thus represents a novel research strategy for close monitoring of the ECM induced inflammation. A wound-healing assay was also developed to study the effect of SIS-ECM hydrogels on the host tissue during wound healing. Thus, a combined stab wound injection was established producing consistent and highly localized hydrogel injected wounds. Moreover, confocal microscopic protocols were optimized to track the wound progression following stab wound injections. This effort provided ready-to-go procedures for both live imaging of host cell-material interactions and muscle wound tracking using phalloidin staining on fixed embryos.

This model represents a new approach for exploring immunomodulation using ECM, with several added benefits to the field. The zebrafish embryos are already a well-characterized model organism that enables the interrogation of the ECM-hydrogels in a realistic biological context and with a developed innate immune system. Moreover, zebrafish embryos are optically transparent, facilitating live visual inspection of the host-material interactions. Furthermore, zebrafish are highly genetically amenable and combined these features make

zebrafish a powerful candidate model for investigating the involvement of individual cell types and genes on host-material interactions. Hence, these important attributes have recently also been demonstrated in a few articles exploring zebrafish as a model for FBR[240–242]. In all these articles the materials studied were however synthetic microparticles, without the molecular and structural complexity of the ECM material employed in the present work, E.g. the issue of gel formation after injection was not a challenge in work with the synthetic materials used in these studies.

The development of a method for introducing ECM material into zebrafish embryos could potentially meet the need for a model for achieving a more in-depth understanding of e.g. macrophage reactions towards decellularized ECM materials in a complex wound healing system. So far, the majority of the investigations on immunomodulation using decellularized ECM-materials have been conducted *in vitro* or *in vivo* by using just a few selected macrophage markers. This has limited the interpretation of the macrophage response to the classical M1/M2 dichotomy possibly leading to a loss of important nuances. This was recently addressed in a mouse tumor model where decellularized-ECM induced a wound-healing macrophage phenotype that also displayed tumor-inhibiting properties[237].

While the work presented here clearly demonstrates the potential of the zebrafish embryo model for elucidating host-material interactions and biomaterial mediated immunomodulation there are a few important limitations to this model. Specifically, while the experiments presented here detected differences in mRNA levels for important inflammatory markers, suggesting different host responses to different injected agents. However, the zebrafish embryo model has the potential to be used for obtaining much more detailed data on the macrophage response to the injected SIS-ECM hydrogels (a further discussion is found in chapter 4 on the future perspectives).

Importantly, Witherel *et al.* identified a more severe FBR in adult zebrafish compared to embryos. FBR develops under the influence of the adaptive immune system with cytokines

such as IL-4 and IL-13 being important in creating FBGCs[208,209,241]. Similarly, it has been reported that immune modulation using decellularized ECM requires input from T helper 2 cells[254]. Thus, identifying how the embryonic immune responses correlate with those of the adult fish is an important future question to address. Also, the small size of the embryo means that not all types of materials can be introduced. Thus, while this model should facilitate the inspection of different types of ECM hydrogels (e.g. urinary bladder, heart), it excludes the use of decellularized scaffolds that require surgical host introductions.

However, the zebrafish embryo model can represent an important tool for investigating host-material interactions, and especially the acute inflammatory phase before the onset of adaptive immune responses. Also, importantly, several cancer models and bacterial infection models are already established in zebrafish embryos, and reports from Wolf *et al.* that decellularized ECM can influence the cancer environment indicates that the applicability of a zebrafish model for ECM hydrogels can be extended beyond the wound healing study that was presented in this chapter[197,237,255,256].

Chapter 4: Live and 3D biomolecular imaging of zebrafish embryos using Raman spectroscopy

4.1 Introduction

4.1.1 Optical imaging of zebrafish

Zebrafish embryos are a well-characterized organism having a rapid external development and high optical transparency which enables direct, visual access to biological processes. Moreover, the small size of zebrafish embryos (i.e. 2 - 5 mm) allows for whole-mount and live sample imaging - providing the researcher with unique spatiotemporal access when conducting imaging experiments[148]. These properties make zebrafish embryos a well-suited model organism for imaging-based approaches and this model has gained a prominent place both in the development and applications of new imaging technologies. Moreover, zebrafish embryos are a versatile vertebrate model that is used extensively in different branches of biology such as cancer research, infection biology, developmental biology, and, of interest here, wound healing, and regeneration[197,255,256]. Combined with innovative imaging approaches highly dynamic and intricate biological processes can be monitored on a single-cell level with real-time temporal resolution. Thus, the development and application of new imaging methods to zebrafish embryos has permitted a deeper visual and molecular interrogation of vertebrate biology.

The currently available imaging technologies used for zebrafish research vary extensively both in terms of the optical phenomena they make use of to visualize the sample and in the optical design of light pathways and illumination. Importantly, these optical considerations will eventually determine the information that can be extracted from the experiments and thus set the boundaries for the visual interrogation of the zebrafish model. Especially effective are imaging methods that can facilitate either live or 3D-imaging of the embryos and some of the important advances in this regard will be discussed in the following sections.

4.1.2 Fluorescence imaging of zebrafish

Zebrafish are highly genetically amenable, they naturally lend themselves to the introduction of genetically expressed fluorescent protein markers (e.g. green fluorescent protein (GFP) and it is, therefore, no surprise that the majority of imaging applications in zebrafish are based on fluorescence microscopy[151,257,258]. Perhaps the most common technique for fluorescent zebrafish microscopy is Confocal Laser Scanning Microscopy (CLSM). CLSM provides high spatial resolution because the excitation light is spatially filtered through a pinhole before entering the photodetector. This improves the contrast because it reduces the contribution from out-of-focus information. Thus, CLSM provides excellent optical sectioning abilities which are important in a 3-dimensional specimen such as zebrafish. Several new developments have extended the applicability of fluorescent microscopy in zebrafish. Notably, the invention of Spinning Disk Confocal Microscopy (SDCM) has improved the temporal resolution by which confocal images can be acquired[259,260]. This is achieved by splitting the incoming excitation light through a series of multiple micro-lenses connected on a spinning disk array. This means that the sample can be illuminated simultaneously by more than a thousand parallel laser beams. Next, the fluorescent emission light is guided through a spinning pinhole disk providing the same spatial filtering used in conventional CLSM before the emission light is directed to the photosensors. By applying a plane of more than a thousand parallel confocal pathways at the same time rather than a single point as in CLSM the temporal resolution is vastly increased. This is especially useful in for instance cell tracking experiments in zebrafish where temporal resolution is critical[261]. However, placing multiple pinholes close to each other comes at a cost because this design leads to pinhole crosstalk. Pinhole crosstalk occurs because fluorescent emission from distant focal planes and out-of-focus scattering can pass through adjacent pinholes and obscure the image. This limits the applications for SDCM in thick samples such as animals and tissue[260,262].

Another important fluorescent microscopy development that has had a huge impact on zebrafish imaging is the advent of fluorescent light-sheet microscopy techniques and in

particular, Selective Plane Illumination Microscopy (SPIM) which has enabled long term fluorescent imaging of live transgenic zebrafish[263–266]. Light-sheet differs from CLSM and SDCM in two important ways. First, the excitation plane does not consist of focused point/s, but rather on a focused sheet of light meaning the specimen is subjected to a continuous excitation plane rather than separated illumination points. Second, most CLSM and SDCM systems are based on episcopic illumination meaning that the excitation and emission light travels antiparallel along the same axis and through the same objective. In light-sheet however, the detection plane is oriented perpendicular to the excitation plane necessitating a second and perpendicular oriented objective. The main effect of this set-up is that it reduces the illumination of out-of-focus objects which would anyway be filtered out by the pinholes in the CLSM and SDCM set-ups. This reduces photobleaching and also reduces photodamaging and phototoxic effects enabling long term imaging. For this reason, light sheet approaches have typically been used for long term imaging approaches for instance in developmental biology in zebrafish[259].

In addition to the above-mentioned approaches also two-photon excitation microscopy (TPEM) has found important applications in zebrafish embryos. In contrast to conventional fluorescence microscopy, where the signal is created by the conversion of a single photon of shorter wavelength into another single photon of longer wavelength; two-photon excitation occurs by combining two photons of longer wavelength into a single photon with a wavelength half of that of the two incoming photons[267]. Because two-photon excitation events are rare, they occur almost exclusively in the focal plane where the photon density is highest. This limits the out-of-focus excitation, something which provides TPEM with sharp axial resolution. Moreover, the two-photon excitation means that TPEM can use excitation lasers with near-infrared wavelength. These lasers have a greater tissue penetration depth compared to the shorter wavelength lasers used in conventional fluorescent microscopy and can, therefore, be used to image features in deeper tissue. Thus, TPEM has been particularly useful for imaging

of the embryo brain where low tissue light scattering and high axial resolution are important requirements[268–270].

4.1.3 Label-free imaging of zebrafish embryos

While all these fluorescent microscopy techniques form a highly complementary set of imaging approaches that can be applied to zebrafish experiments, they are all based on detecting introduced fluorescent labels. While this allows certain biomolecules to be probed with high specificity, fluorescent sample labeling has several important drawbacks. Specifically, only a few biomolecules can be visualized at the same time giving only limited information about the biomolecular complexity of the sample. Moreover, while quantitative data can be extracted from fluorescent images, photobleaching and variable fluorescent intensities between different labels make exact and comparative quantitation hard to achieve. For these reasons, label-free imaging approaches have gained attention. Several microscopy techniques use label-free modes of visualization that can be applied to zebrafish. One such technique is Second-Harmonic Imaging Microscopy (SHIM). SHIM exploits an optical phenomenon called second harmonic generation (SHG) which is a non-linear process where two photons of the same wavelength combine to produce a new photon with exactly half the wavelength of the original photons. SHG occurs exclusively when the photons interact with a material that is non-centrosymmetric (i.e. lacks inversion symmetry) and can, therefore, be used to visualize this special class of biomolecules without the introduction of labels. The requirement of non-centrosymmetric materials is however quite restrictive and limits its application in animal tissues (collagen and myosin are two of the few biomolecules that satisfy this criterium). For this reason, SHIM has mostly been applied to study collagen in zebrafish[271,272]. Another label-free imaging approach based on harmonic generation is Third-Harmonic Imaging Microscopy (THIM). Third harmonic generation (THG) occurs when three photons of the same wavelength combine to form a new photon with a wavelength a third of the original photons. As opposed to SHG, THG does not require any specific asymmetry in the material but instead takes place on structural interfaces such as local transitions in the refractive index[273]. In biological samples,

this will typically be interfaces found between aqueous body fluids and either lipid or protein structures such as cell membranes or protein aggregates. Moreover, THG can occur on interfaces between aqueous fluids and inorganic structures such as calcified bone[273]. Because THIM visualizes interfaces it has been used to delineate boundaries of cells, yolk plates, and nuclei in zebrafish embryos[274,275].

4.1.4 Raman spectroscopic imaging

While SHIM and THIM remove the requirement of labeling, both SHG and THG are too restricted optical phenomena to visualize a broad spectrum of biomolecules simultaneously. Thus, these imaging techniques are not suitable for probing biomolecular complexity either. The inability of the imaging technologies discussed so far to address biomolecular complexity constitutes a limitation in zebrafish technology. For instance, diseases frequently studied in zebrafish such as cancer and bacterial infections are known to display phenotypical heterogeneity with subtle but important variations in their biomolecular composition. It is therefore evident that there is an unmet need for a high-resolution imaging technique capable of visualizing and analyzing local biomolecular heterogeneity in different zebrafish embryo models.
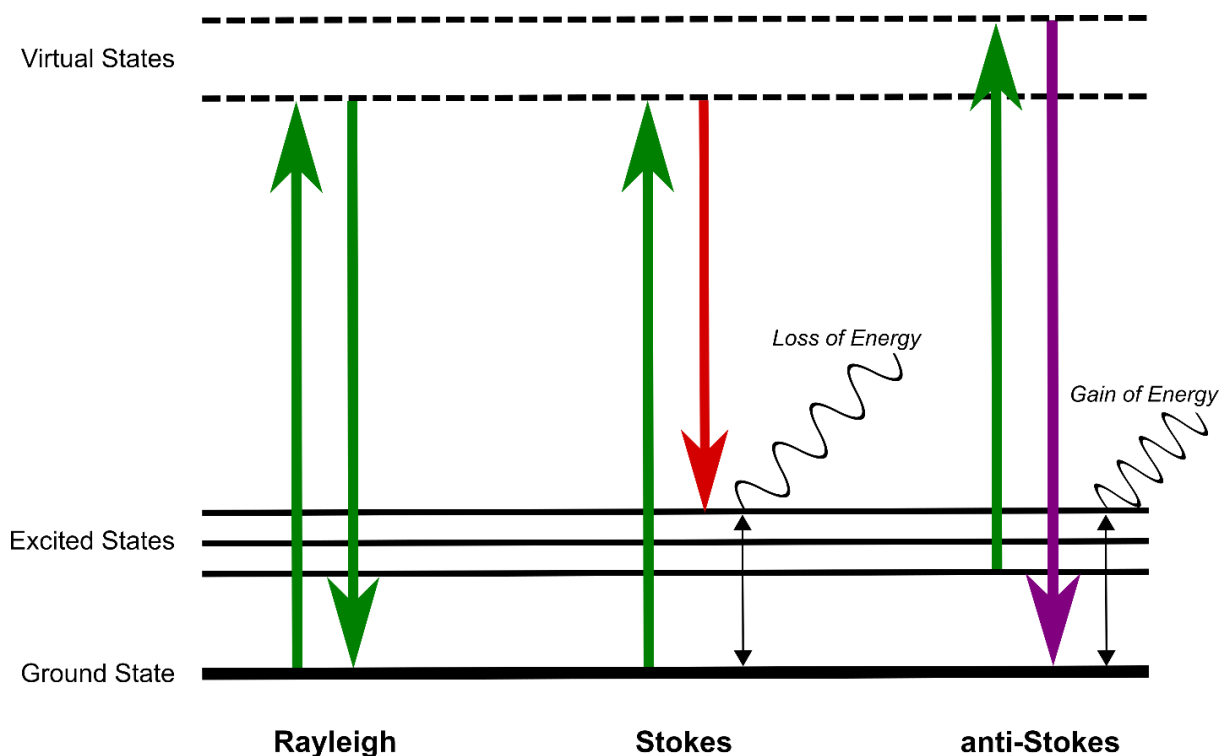
Figure 4.1: *Jablonski diagram comparing Rayleigh, Stokes, and anti-Stokes scattering. Rayleigh scattering is an elastic scattering event without any transfer of energy between the photon and the illuminated sample, meaning the incident light and the scattered light having the same energy. Stokes and anti-Stokes scattering are the two types of inelastic Raman scattering were energy is transferred through the Raman effect between the photons and the illuminated sample. In the case of Stokes scattering, the photon transfers energy to the sample, and the scattered light has a higher wavelength (i.e. red-shifted) than the incident light beam. In anti-Stokes, the sample transfers energy to the photon meaning the scattered photon has a lower wavelength (i.e. blue shifted) than the incident light beam.*

One potential candidate of interest here is Raman spectroscopic imaging (RSI)[276,277]. RSI is a spectroscopic imaging technique based on an optical phenomenon known as the Raman effect, which is due to inelastic scattering events caused by photons interacting with molecular bonds having a polarizable dipole moment (i.e. Raman active molecules)[278,279]. When light hits a sample, the vast majority of the photons will be elastically scattered without any change in wavelength (i.e. Rayleigh scattering). However, during Raman scattering, energy will be transferred between the photon and the polarizable molecular bond - causing a shift in the photon's wavelength[280] (**Figure 4.1**). These wavelength shifts are highly specific for the molecular bonds causing them, meaning they can serve as a signature of these molecular bonds. Thus, the Raman effect can be used spectroscopically to analyze sample chemistry

simply by shining a focused, monochromatic laser onto a sample and subsequently collect spectra of Raman scattered wavelength shifts. This constitutes the foundation for RSI where Raman spectroscopy is coupled to a microscopy set-up to collect positional and Raman spectroscopic information providing molecular signature maps of the samples (**Figure 4.2**).
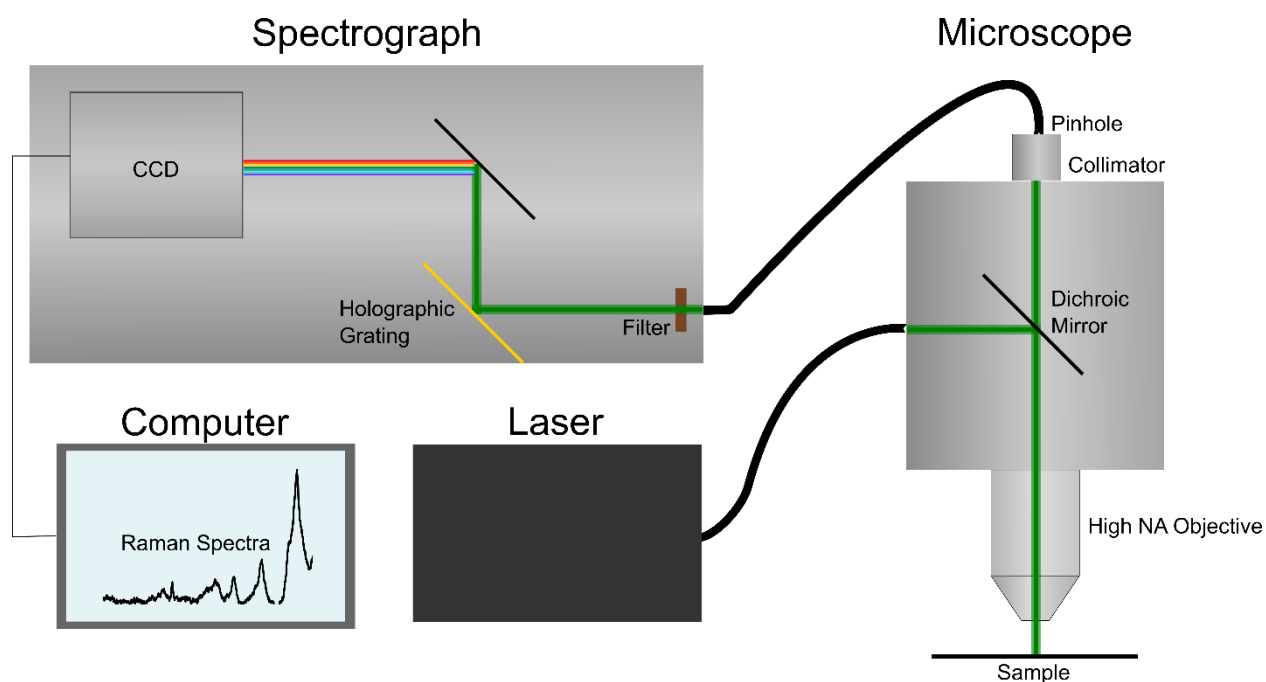
Figure 4.2: *Schematic of a confocal Raman spectroscopic microscope set up. Monochromatic laser light is focused onto the sample through a high NA objective. The scattered light is guided back into the objective before passing through a collimator and a pinhole ensuring confocal optical sectioning. The light is then transferred through optical fibers to the spectrograph where the light first passes through a filter before entering a holographic grating and mirror which ensures separation of the different wave shifts. This separated light is then transferred to a charge-coupled device detector (CCD) where the different wavelength intensities are counted. These counts are then transferred electronically to a computer producing graphical Raman spectra.*

There are several important considerations when applying Raman spectroscopy for imaging purposes. Because Raman scattering is a rare event – a Raman scattering event occurs for every 10^6-10^8 photon – RSI is typically dependent on quite strong lasers[278,281]. Moreover, the Raman signal is proportional to λ^{-4} meaning that the use of low wavelength lasers will give a significant increase in Raman signal. However, RSI has several important advantages that make it a useful tool for biological sciences. The application of Raman spectroscopy to living

biological specimens was first demonstrated in 1990 and has since been a valuable tool in biology[278,282]. Many of the most common biomolecules such as DNA, proteins, and lipids have Raman active bonds, meaning that RSI can be readily applied for biomolecular analysis (**Figure 4.3**) shows an example of a biological Raman spectrum with important wavelength shifts annotated[278,280,283]. Another important benefit of RSI is that water molecules scatter most strongly in an area of the spectrum that does not overlap with the major biomolecules[284]. Importantly, because of the specificity of the wavelength shifts caused by Raman scattering and because Raman scattering is caused by direct interactions between the laser and the sample biomolecules, RSI can provide information about multiple biomolecules simultaneously without the need for introducing any label. Furthermore, because RSI uses monochromatic laser light it can achieve a theoretical spatial resolution defined by Abbe's diffraction limit, meaning that RSI can achieve a high spatial resolution. Moreover, since RSI is also based on lasers, several of the optical inventions that have improved fluorescent microscopy are also applicable to RSI including confocal and light-sheet technologies[285–287].
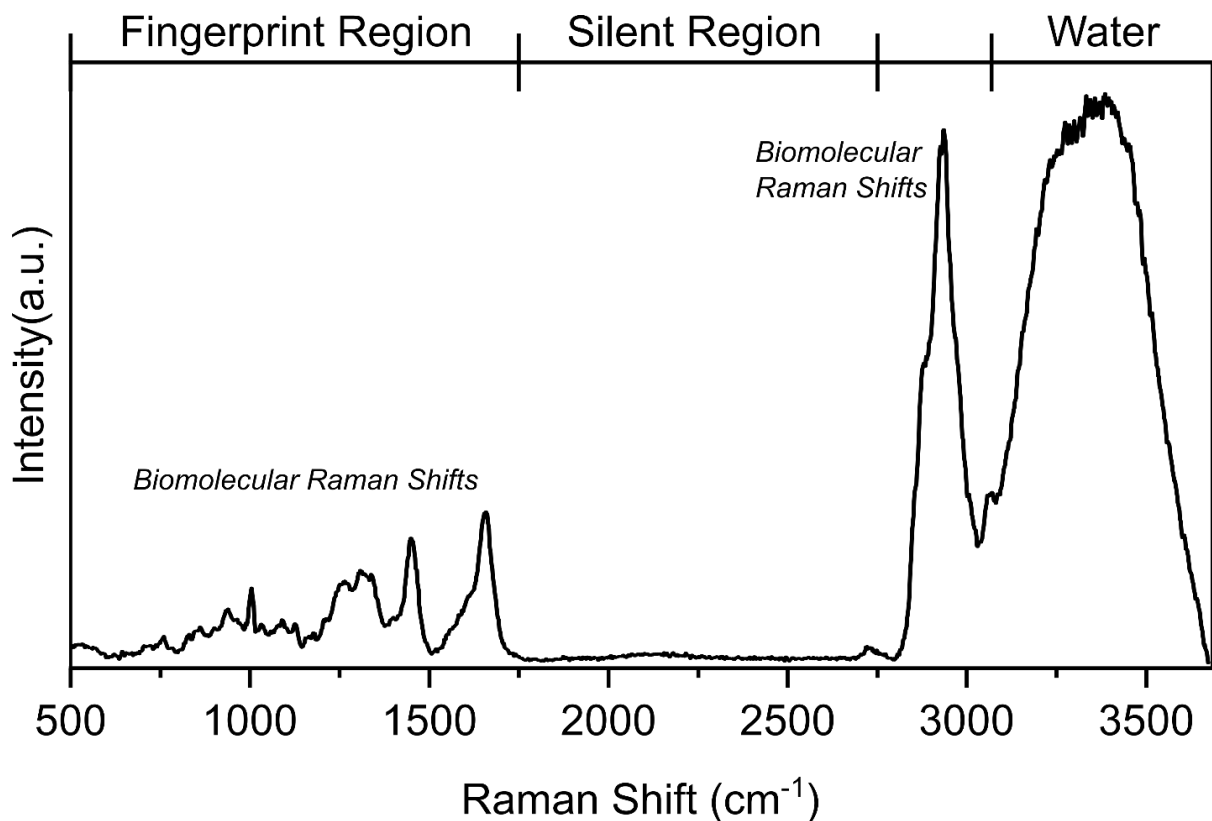
Figure 4.3: *Exemplar Raman spectrum of a biological specimen (zebrafish embryo tissue acquired using a 532 nm laser). A biological spectrum can be broadly divided into 4 different regions. The fingerprint region (~500-1800 cm^{-1}) contains a range of biomolecular information and most Raman active biomolecules have vibrational shifts in this part of the spectrum (e.g. DNA, lipids, proteins, polysaccharides). The silent region (1800-2800) is a part of the Raman spectrum without any biomolecular vibrations, making this to a virtually flat part of the spectrum. The region between 2800-3000 is another area containing biomolecular information, mostly from proteins and lipids. The water region (3050-3500) is a part of the spectrum that is mostly dominated by the molecular vibrations of water.*

RSI technologies have been used both for studies of prokaryotic and eukaryotic cells as well as for larger biological samples such as tissue explants and tissue-engineered samples[288289]. For instance, RSI has been applied to describe the intracellular lipid distribution of single bacteria[290] and to distinguish between cancerous and non-cancerous human breast tissue[277]. Moreover, RSI has enabled the tracking of low-density lipoprotein in single human macrophages and to define biomolecular responses in stem-cells when grown on different micro-pattern platforms[291,292]. Notably, developments within Raman technology has allowed implementation of 3D Raman spectroscopy and enabled quantitative volumetric Raman spectroscopic imaging[293].

4.1.5 Raman spectroscopy for zebrafish research

Despite the apparent advantages Raman spectroscopy adds to biomolecular analysis, there are only a limited number of examples where this technology has been applied to zebrafish embryos. A few studies have reported the collection of individual point spectra to analyze bone maturation in zebrafish embryos[294,295]. While this method is rapid and demonstrated the utility of Raman spectroscopy in zebrafish, this approach does not provide any spatial information, while also necessitating a high degree of pre-knowledge about the sample. Furthermore, several different approaches using nonlinear Raman methods have been used for imaging of zebrafish embryos such as Coherent anti-Stokes Raman spectroscopy (CARS), Stimulated Raman spectroscopy (SRS), Surface-enhanced Raman spectroscopy (SERS)[296–298]. Nonlinear Raman techniques can increase the efficiency of Raman imaging by stimulating more Raman scattering either by the use of secondary or tertiary lasers (in the case of SERS and CARS) or by exploiting material surfaces that enhance the Raman signal, e.g. in the case of SERS[299]. However, each of these approaches can only amplify the signal in a narrow range of the Raman shifted wavelengths, which means that they cannot provide full spectral coverage leading to a significant loss of biomolecular information[300].

To obtain complete biomolecular information linear or spontaneous Raman imaging approaches are needed. Two microscopy techniques are particularly suited for spatially resolved hyperspectral imaging of zebrafish embryos: those employing either light sheet or confocal-based microscopic designs. Oshima *et al*. demonstrated the first use of light sheet-excited spontaneous Raman spectroscopy (LSDRS) to image in live Medaka (*Oryzias latipes*) fish embryos (which is another transparent fish embryo model)[287]. However, this technique was limited by a low spatial resolution and weak signal, which limited the analysis to the medaka eye. Muller et al. used a light sheet Raman micro-spectroscopy (LSRM) with significantly improved resolution and signal-to-noise to image the eye of a fixed zebrafish embryo[286]. Furthermore, light-sheet RSI has been applied to address toxicological effects on cryosections of zebrafish eyes[301,302].

4.1.6 Aims of chapter

Despite the promises of these Raman imaging approaches, linear RSI has found only limited applications in zebrafish. Notably, the abovementioned examples have all been restricted to analysis of the zebrafish eyes with no demonstration of applicability to the rest of the embryo. Moreover, none of the techniques have demonstrated time-lapse imaging or multivariate analysis on living zebrafish embryos. Also, none of the discussed techniques have demonstrated comparative biomolecular analysis in whole-mount embryos. Confocal RSI (cRSI) has yet to be fully tested in zebrafish despite offering several potential advantages. Importantly, a confocal set up achieves slightly better lateral resolution, but significantly better axial resolution and signal-to-noise ratio compared to light-sheet set-ups[286].

The aim of the work presented in this chapter was first to develop a methodology for the employment of high-resolution cRSI in the analysis of zebrafish embryos and to show that the method could enable access to the full complement of biomolecular information in whole-mounted zebrafish embryos. A further aim was to investigate whether the developed methods could be used for 3D biomolecular profiling and comparison of zebrafish embryo infections by two different strains of mycobacteria. A third aim was to develop a method for cRSI imaging of liver zebrafish embryos that could be used to follow biological processes over time in the same embryo. Lastly, it was a goal do use such methods to explore differences between wounded and unwounded zebrafish embryo tissue.

4.2 Results and discussion

4.2.1 Establishing confocal Raman spectroscopic imaging in zebrafish embryos

4.2.1.1 Sample preparation and cRSI procedure

The first challenge to implement cRSI in zebrafish embryos was to establish a practical experimental set-up that could ensure high-quality data acquisition with minimal imaging artifacts or interference. First, wild type zebrafish naturally develop three types of pigments, melanophores, iridophores, and xanthophores, all of which can interfere with the image acquisition by causing increased light absorption, increased fluorescence, or light scattering. To minimize pigment interference, the optically transparent mutant line *TraNac* (*mitfa*$_{w2/w2}$, *mpv*$_{b18/b18}$) was used, which lacks iridophore and melanophore pigments[199]. Second, to reduce background signal and sample drift the embryos were embedded in 0.8% (w/v) low melting point agarose on glass slides. The glass slides were then put into 10 cm Petri dishes containing ~50 mL E2 water. This agarose concentration was high enough to immobilize the embryos while still being below the detection limit for Raman spectroscopy. Adding an excess of E2-water also helped to dissipate the heat caused by the laser. This is important not only because heating from the laser can damage the samples directly (i.e. burning), but also because heating of the agarose gel may cause it to melt and this would lead to sample displacement. Third, to maximize the Raman signal and the resolution, imaging was performed using a 532 nm laser and a 63x/1.0 NA water objective lens. Because the Raman signal intensity is inversely proportional to λ^4, a green shifted laser such as 532 nm will give a significantly stronger signal than red-shifted laser such as 785 nm[303]. Combined, this sample preparation and cRSI procedure enabled the acquisition of high-quality Raman spectra with minimal interference from either endogenous pigments or out-of-plane background signal.

4.2.1.2 3D confocal Raman spectroscopic imaging of whole embryos

Previous work using Raman spectroscopy on zebrafish has focused on imaging of small and well-defined regions of interests mainly the eye or the developing bones and it was therefore not clear how well Raman imaging could be translated to the remaining zebrafish tissues[286,294]. Moreover, since cRSI could be applied for 3D-imaging, it was necessary to inspect any effects in the axial planes, such as increased tissue scattering or fluorescence. To gain experience for subsequent experiment designs, a 3D cRSI scan of the whole embryo was performed using 10 µm lateral and 10 µm axial resolution.

Hence, the first observation from the 3D-scan was that the yolk sac, vasculature, and outer surface of the embryo exhibited a degree of autofluorescence. Moreover, a reduced Raman signal was obtained in the head region. This could be due to light scattering; because the head is significantly thicker than the rest of the embryo it will also scatter more light compared to the thinner regions of the embryo. However, cRSI enabled the extraction of well-resolved biomolecular information from the rest of the embryo (**Figure 4.4**). Univariate analysis recognized that the dominating features detected were proteins at 2940 cm^{-1} (v_{as} CH$_3$), lipids at 2885 cm^{-1} (v_{as} CH$_2$), and carotenoids at 1159 and 1528 cm^{-1} (conjugated C-C=C-C stretch). The protein and lipid signals were visible throughout the embryo and were demarcating the individual somites (i.e. body segments) of the embryo. In the somites, the protein signal was the most prominent, while lipids could be observed separating the somites (**Figure 4.5**).
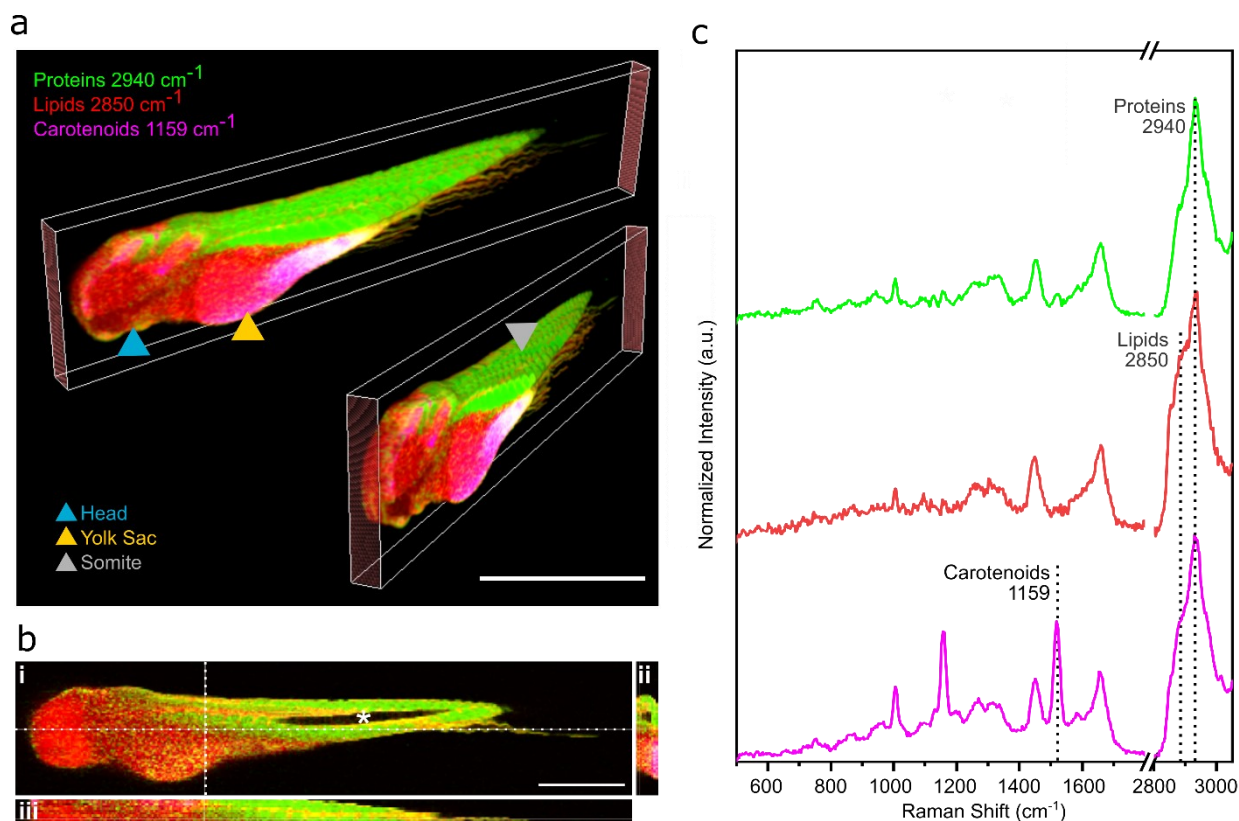
Figure 4.4: 3D confocal Raman spectroscopic imaging of whole zebrafish embryos: *cRSI of fixed zebrafish embryo at 3 dpf. The images were acquired using 10 µm lateral resolution and 10 µm axial resolution.* ***a)*** *Multichannel 3D reconstruction with 10 x 10 x 10 µm³ voxel resolution. Scale bar: 1 mm* ***b)*** *Z-projections showing the (i) the sagittal plane, (ii) the frontal plane, and (iii) the transverse plane. The asterisk in the sagittal plane denotes the hollow notochord. Scale bar: 500 µm* ***c)*** *Representative spectra collected from volumetric cRSI performed on whole zebrafish embryos. The annotated peak centers used for univariate analysis are indicated by dotted lines.*

Further inspection of the 3D stack demonstrated that the proteins and lipids signals were evenly distributed throughout the axial planes. However, a stronger carotenoid signal was detected on the outer surface of the embryo and in the yolk sac. The carotenoid signal is caused by characteristic resonant vibrations by conjugated C-C=C-C stretches found in carotenoid pigment molecules[304]. There are two likely sources of this signal in the zebrafish embryo. First, although the *TraNac* embryos used are deficient in iridophores and melanophores, they do produce the third class of zebrafish pigments, known as xanthophores, and their presence is likely to contribute to the observed pigment signal. Secondly, zebrafish embryos contain maternally derived β-carotene in the yolk sac, which is used in the biosynthesis of retinoic acid[199,305–308]. The presence of β-carotene would also contribute to the

observed carotenoid signal and it is, therefore, possible that the sharp pigment peaks observed in the cRSI arise from a combination of xanthophores and β-carotene molecules.
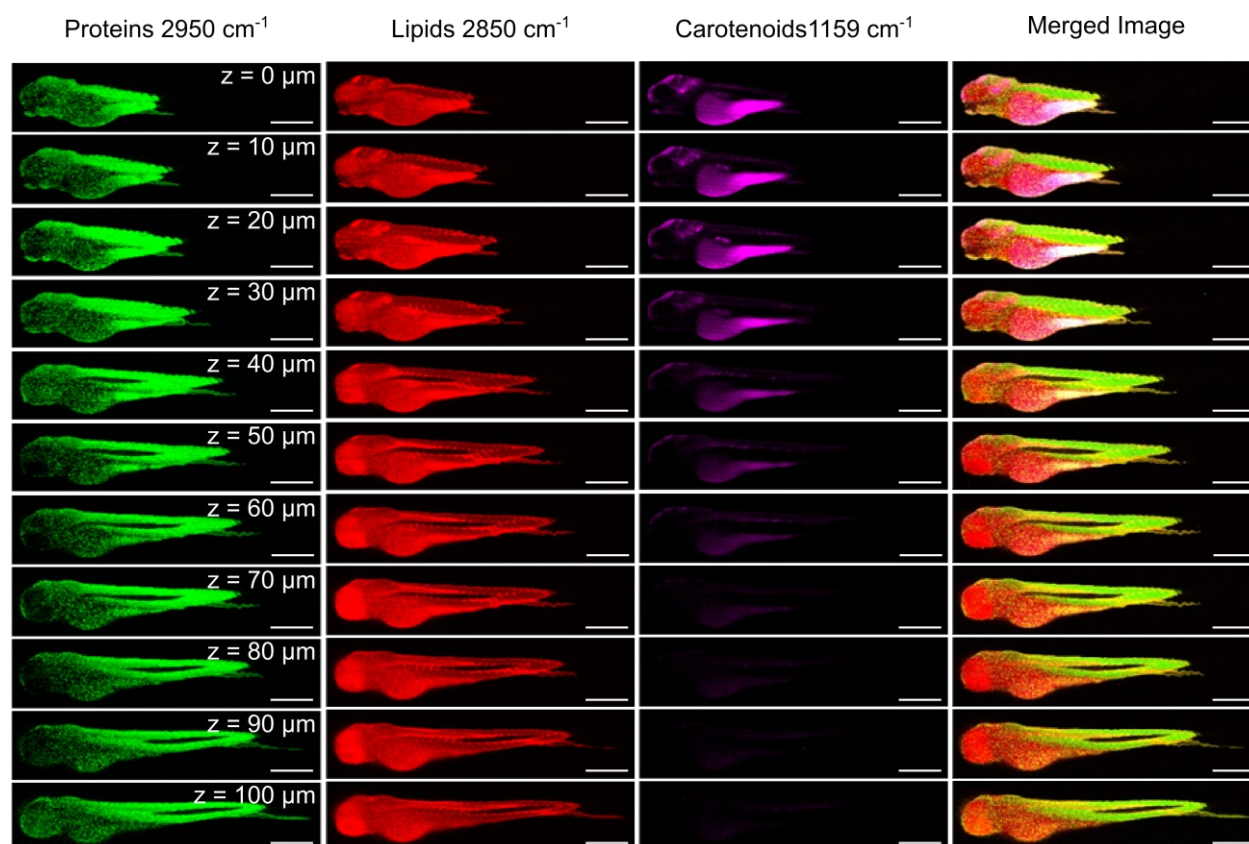
Figure 4.5: Full confocal stack of whole zebrafish embryos imaged with cRSI: *This figure shows the entire stack collected from 3D the cRSI scan with univariate normalized peak intensity. Scale bars: 500 μm.*

4.2.1.3 High-resolution Raman spectroscopic imaging of embryo tissue

While the 3D-scan provided an overview of the entire zebrafish, the 10 x 10 μm resolution meant that smaller sized biomolecular features (e.g. cell nuclei) could not be resolved during this experiment. This limited the amount of tissue-specific information that could be obtained from this scan. Hence, to investigate to what extent cRSI could be applied to resolve biomolecular features on a cellular level a series of high-resolution cRSI scans were conducted.

To this end, cRSI was performed using 1 µm lateral resolution followed by univariate analysis to image embryonic muscle tissue. At this resolution, the fine stratification of myofibers and muscle cells running along the anteroposterior axis could be visualized by applying a univariate filter to a collagen-rich region of the Raman spectra (filter center at 901 cm^{-1}, contributions from hydroxyproline at 852 cm^{-1} and C-C stretching at 935 cm^{-1}). The muscle bundles were separated by elongated regions of lipids at 2885 cm^{-1} (v_{as} CH$_2$), which matches the features of the membrane phospholipids of muscle cells[177]. Moreover, univariate analysis using a nucleic acid signal at 795 cm^{-1} (O-P-O stretching) identified regions of dense nucleic acids possibly corresponding to cell nuclei (**Figure 4.6 a**).

A second high-resolution scan from the tail tissue also revealed collagen fibers but, in the tail, they displayed a radial orientation (**Figure 4.6 b**). Moreover, this cRSI scan also identified individual nuclei that were clearly dispersed throughout the tail 795 cm^{-1} (O-P-O stretching). Lastly, cRSI was used to examine the gut of a zebrafish embryos at 3 days post fertilization dpf (**Figure 4.6 c**). The zebrafish gut develops rapidly for the first 5 days after fertilization which is point where the embryo begins of external feeding[309,310]. Again, cRSI could readily discriminate between the different tissue features and resolve biomolecular details. The tract lining of the gut could be observed using a lipid peak signal centered at 2885 cm^{-1} (v_{as} CH$_2$). Moreover, the interior of the tract was abundant in DNA, cytochrome, and collagen (**Figure 4.6 d**).

Together, these three experiments demonstrate that cRSI can be used to obtain sub-micron scale biomolecular maps of zebrafish embryos and that univariate analysis can be used to highlight clear distinctions between the different tissues.
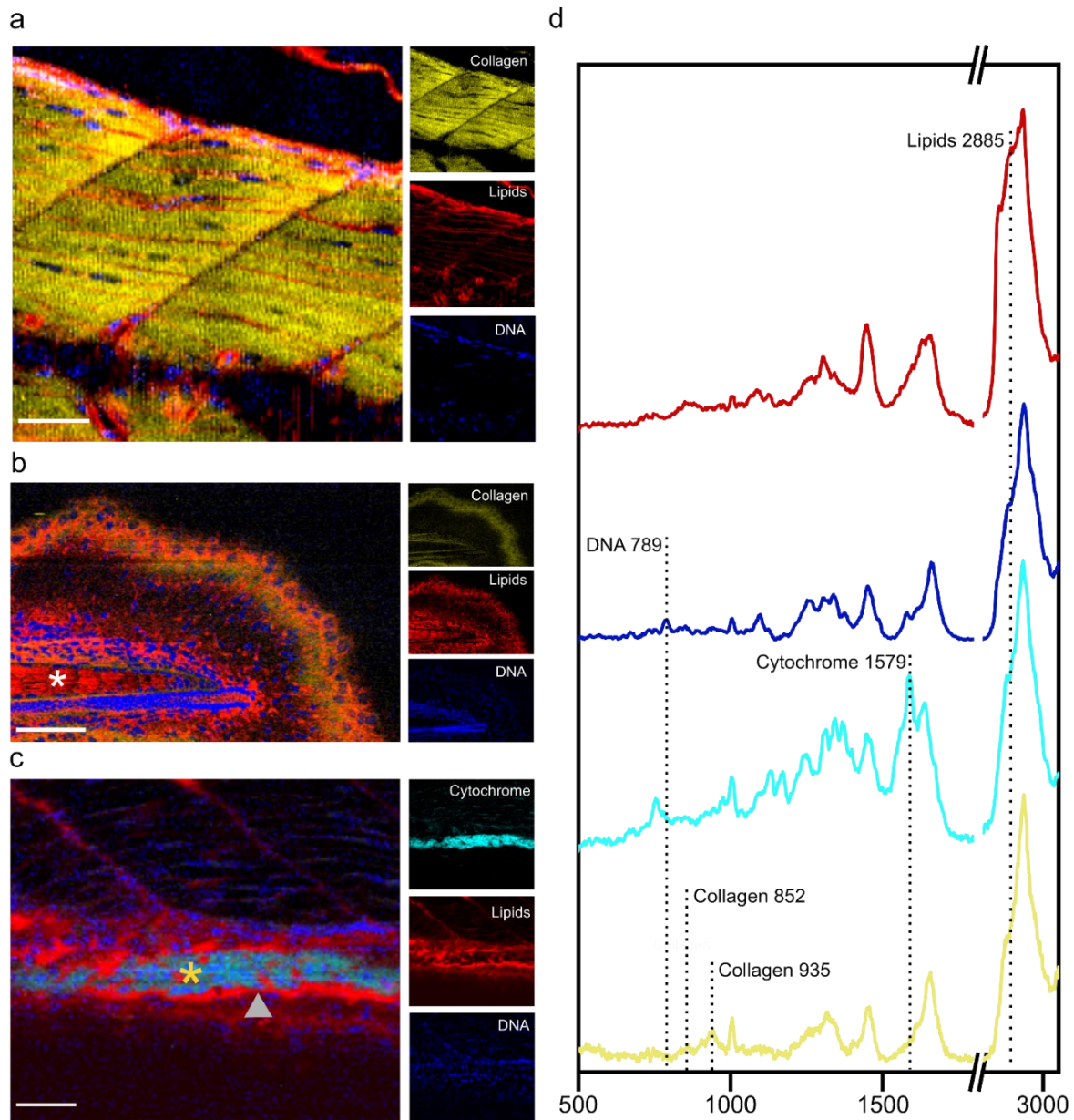
Figure 4.6: High-resolution cRSI characterization of zebrafish tissue: *Univariate analysis performed on cRSI images obtained from regions of interest in zebrafish embryos at 3 dpf. Collagen rich regions (901 cm⁻¹) are shown in yellow, lipids (2885 cm⁻¹) in red, DNA (795 cm⁻¹) in blue, and cytochrome (1574 cm⁻¹) in cyan. Regions of interest shown are **a)** The dorsal muscle tissue, scale bar: 40 µm **b)** the tail tissue. The white asterisk marks the notochord (scale bar: 50 µm) and **c)** the developing gut. The orange asterisk marks the gut lumen and the grey triangle points to the gut lining. Scale bar: 40 µm **d)** Exemplar Raman spectra obtained from regions of intense univariate signal, with the labeled peaks used for univariate analysis*

Biomolecule	Anatomical Region	Peak Center (cm^{-1})	Molecular Vibration	Reference
DNA	Whole Embryo	789	O-P-O stretching	[311]
Collagen	Muscle segments	852	Hydroxyproline	[312]
Collagen	Muscle segments	918	Hydroxyproline	[312]
Collagen	Muscle segments	935	C-C stretching	[313]
Proteins	Whole Embryo	1004	Ring breathing phenylalanine v_s(C-C)	[312]
Proteins Carbohydrates	Gut	1128	v(C-C)	[312]
Carotenoids	Surface/Blood	1159	C-C=C-C Conjugation	[304]
Proteins	Gut	1170	Tyrosine	[312,314]
Amide III (Collagen)	Gut	1246	v_s(C-N)	[312]
Lipids Collagen		1305	CH$_2$Twisting δ(CH$_2$)	[315,316]
Collagen	Gut	1312	CH$_3$CH$_2$ twisting modes of collagen	[317,318]
Phospholipids	Gut	1366	v_s(CH$_3$)	[314]
Lipids	Whole Embryo	1450	(CH$_2$ bending)	[315]
Carotenoids	Surface/Blood	1528	C-C=C-C Conjugation	[280,304]
Cytochrome	Gut	1579	v(C=C)	[319]
Collagen	Gut	1587	Hydroxyproline	[312]
Collagen	Gut	1636	Amide I Band	[314]
Amide I	Whole Embryo	1665	Amide I	[312]
Lipids, Fatty Acids	Whole Embryo	1748	v(C=O)	[315,319]
Lipid	Whole Embryo	2850/2	v_s(CH$_2$)	[315,319]
Lipid	Whole Embryo	2885	v_s(CH$_3$)	[315,319]
Protein	Whole Embryo	2940	v_{as}(CH$_2$)	[319]

Table 3.1: Library of annotated Raman shifts observed in zebrafish embryos

During these characterization experiments, many different peaks were observed in the Raman spectra obtained from the embryos. Several of these peaks have previously been assigned to specific biomolecules making it possible to identify the source of that peak. **Table 3.1** presents a complete list of all the biomolecules that were identified and where in the embryos these biomolecules were detected. This table constituted a peak library that could be used throughout the study to analyze Raman spectra obtained from the embryos.

4.2.2 Raman spectroscopic imaging of mycobacterial infection

4.2.2.1 Infection procedure and characterization of the mycobacterial infection site

Zebrafish embryos are commonly used in disease modeling and have become popular in infectious biology because they provide an opportunity to visualize host-pathogen interaction

in a vertebrate host. Thus, zebrafish disease models can often deliver more details on the disease progression compared to mammalian models and are particularly useful for uncovering cellular mechanisms. Raman spectroscopy is a popular tool in disease modeling too. Specifically, the extensive biomolecular information contained in the Raman spectra can be used to both discriminate between diseased and healthy tissue and inform on the disease progression[277,280]. For this reason, Raman spectroscopy has been proposed as a tool in diagnosis in both infectious diseases as well as cancers[320–322]. Hence, one key potential application of cRSI in zebrafish would be disease modeling. For instance, cRSI could be used image and analyze different metabolic niches or changes associated with disease progression.

To develop this concept an established zebrafish infection model was set up, using the natural aquatic pathogen *Mycobacterium marinum* (*M. marinum*). After initial testing, an infection route was the zebrafish were injected with ~50 cfu of *M. marinum* in the neural tube at 2 dpf was chosen because this procedure consistently produced localized bacterial lesions that were easy to identify (**Figure 4.7 a**). At 4 days post-infection (dpi), all embryos had developed clear bacterial lesions around the injection site, which could be identified by visible tissue protrusions. These lesions were further characterized using Ziehl-Neelsen acid-fast staining (ZN-staining) on zebrafish tissue sections (**Figure 4.7 b**). This procedure specifically stains mycobacteria, due to the acid-fastness caused by the high content of mycolic acid in mycobacterial cell walls. Mycolic acids are a group of fatty acids unique to mycobacteria which contains long hydrocarbon chains consisting of 60-90 carbon atoms[323]. The ZN-stain revealed that the tissue protrusions seen at the injection site contained dense clusters of rod-shaped mycobacteria. Moreover, the highly localized lesions appearing at the injection site constituted a natural and reproducible region of interests for cRSI analysis of infecting *M. marinum*.
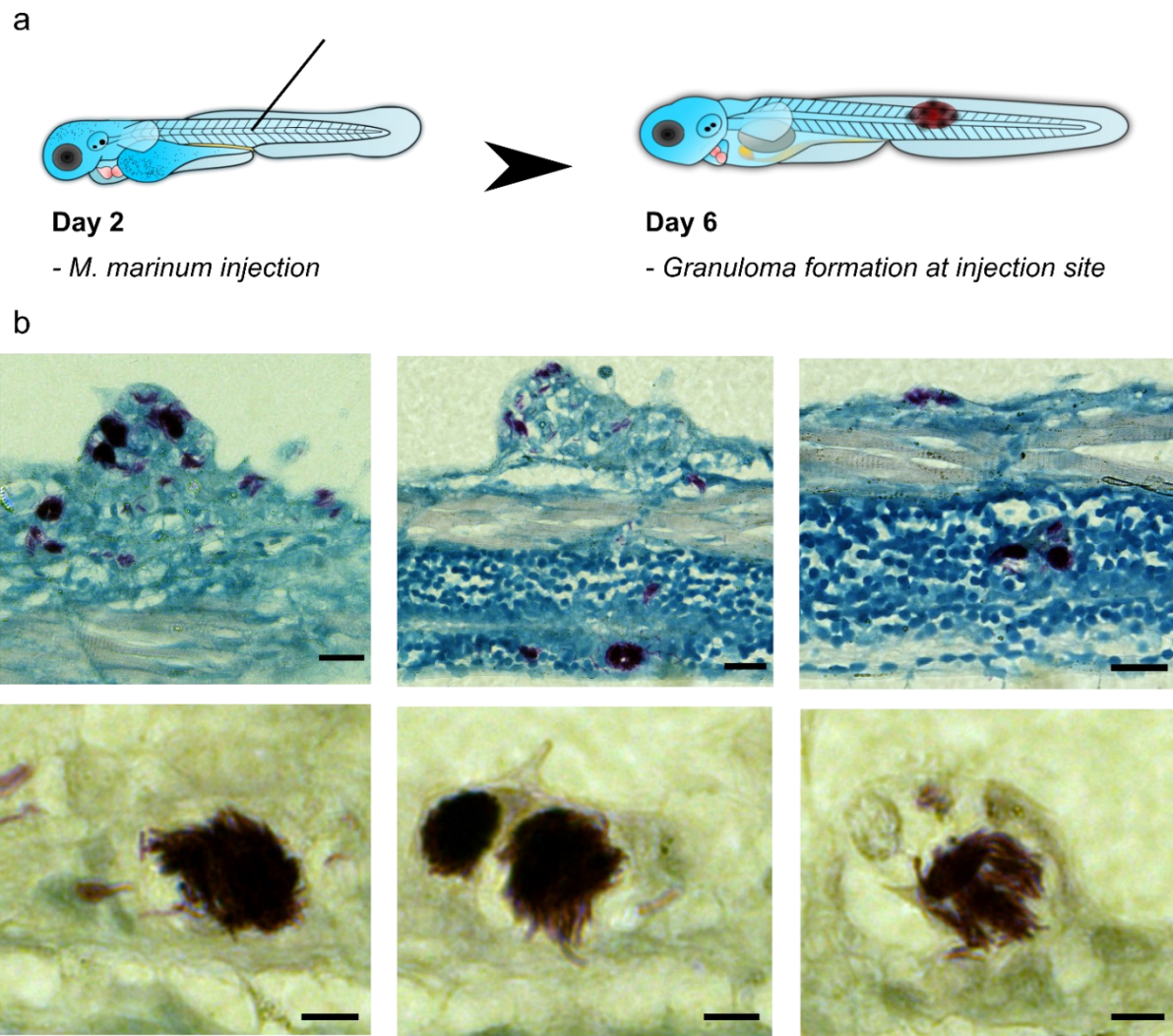
Figure 4.7: Infection Procedure and Characterisation a) *Outline of M. marinum infection in Zebrafish embryos. The embryos were injected with 50 cfu of M. marinum in the neural tube at 2 days post-fertilization. 4 days post-injection the infection site was visible, and the embryos were fixed and processed for further analysis of the infection (i.e. cRSI, histology, or TEM).* **b)** *Ziehl-Neelsen stained histology sections of M. marinum infected zebrafish at 4 days post-infection. The M. marinum bacteria can be seen from the strong purple color caused by the Ziehl-Neelsen staining. The bacteria form dense clusters and are typically found in tissue protrusion formed around the bacterial lesion. The top row shows three different bacterial lesions obtained from three different embryos. Scale bar: 50 µm. The bottom row shows three different bacterial clusters found in the same embryo at higher magnification. Scale bar: 5 µm.*

The bacterial lesions were further characterized using transmission electron microscopy (TEM). Again, this analysis was performed on *M. marinum* lesions identified in infected zebrafish embryos at 4 dpi (**Figure 4.8**). This analysis identified clusters of intracellular bacteria in the lesions. *M. marinum* begin their infection cycle inside host macrophages, a feature they share with the more human pathogen *Mycobacterium tuberculosis*, which is the causative agent of tuberculosis. This

analysis means that the dense bacterial clusters observed on the ZN-stained sections likely correspond to intracellular bacterial clusters. Another interesting observation that can be made from the TEM images is the presence of dark, circular spots within the bacteria. This feature has been reported before and corresponds to intra-bacterial lipid droplets[324,325]. Because these lipid droplets stain strongly with uranyl-acetate they can be visualized with electron microscopy.
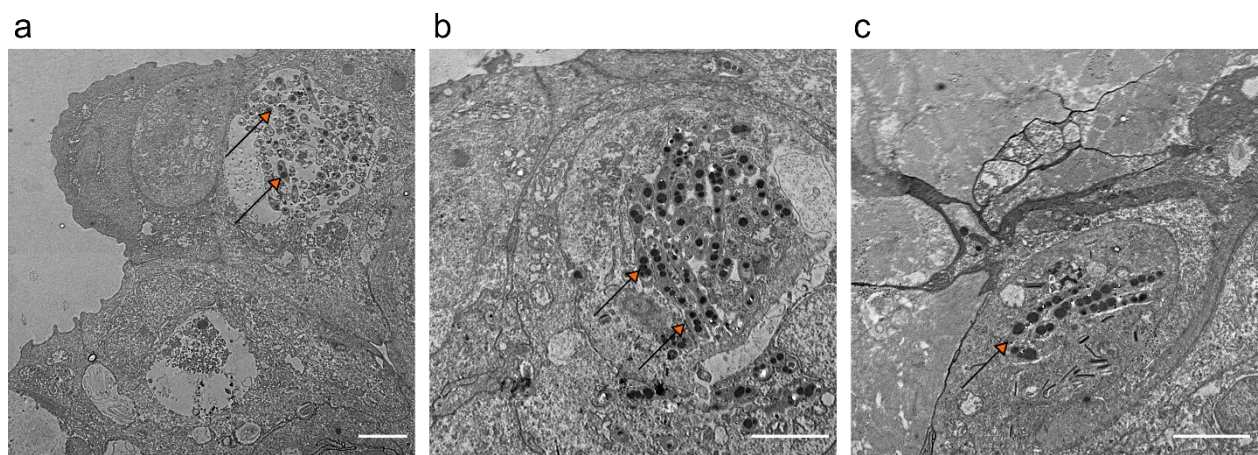
Figure 4.8: Transmission electron micrographs of M. marinum lesions found in zebrafish embryos at 4 days post-injection. The M. marinum bacteria are elongated and rod-shaped and can be easily observed due to the presence of lipid droplets inside the bacteria. These droplets can be seen as circular black spots due to their strong staining with uranyl-acetate. The bacteria are clustered together and are mostly intracellular. Orange arrows point to the bacteria. Scale bars: 2 μm.

This characterization demonstrated that the injection procedure chosen produced consistent and reproducible lesions that were localized at the injection site. These lesions contained clusters of intracellular *M. marinum* that stained strongly with ZN-staining and contained intracellular lipid droplets.

4.2.2.2 *in vitro* biomolecular profiling of mycobacteria

The unique cell wall possessed by mycobacteria gives them a distinct Raman spectroscopic profile. In particular, the presence of the long fatty acids chains found in the mycolic acids leads to very strong vibrational intensities in regions associated with common lipid feature, for instance 1081 cm^{-1} (v(C-O) and v(C-C))[313], 1305 cm^{-1} (CH$_2$ twisting), 1450 cm^{-1} (δ CH$_2$/CH$_3$),

2852 and 2885 cm^{-1} (v_s CH$_2$)[315]. This unique Raman spectral profile has previously been reported for 26 mycobacterial species and it has been demonstrated that these Raman feature can be exploited to discriminate mycobacterial species from other bacterial genera[320]. Moreover, *in vitro* experiments have demonstrated that Raman spectroscopy can be used to ascertain the growth stage of mycobacteria in liquid culture and separate bacteria in the logarithmic growth stage from bacteria in the stationary growth stage[326].

To thoroughly characterize the Raman spectroscopic profile of *M. marinum*, Raman spectra were obtained from liquid cultured *M. marinum* at three different stages of its' growth curve. The three growth stages measured were the early logarithmic growth stage, the late logarithmic growth stage, and the stationary growth stage, and each stage was verified by measuring the optical density at 600 nm (OD$_{600}$) of the liquid cultures (**Figure 4.9**).
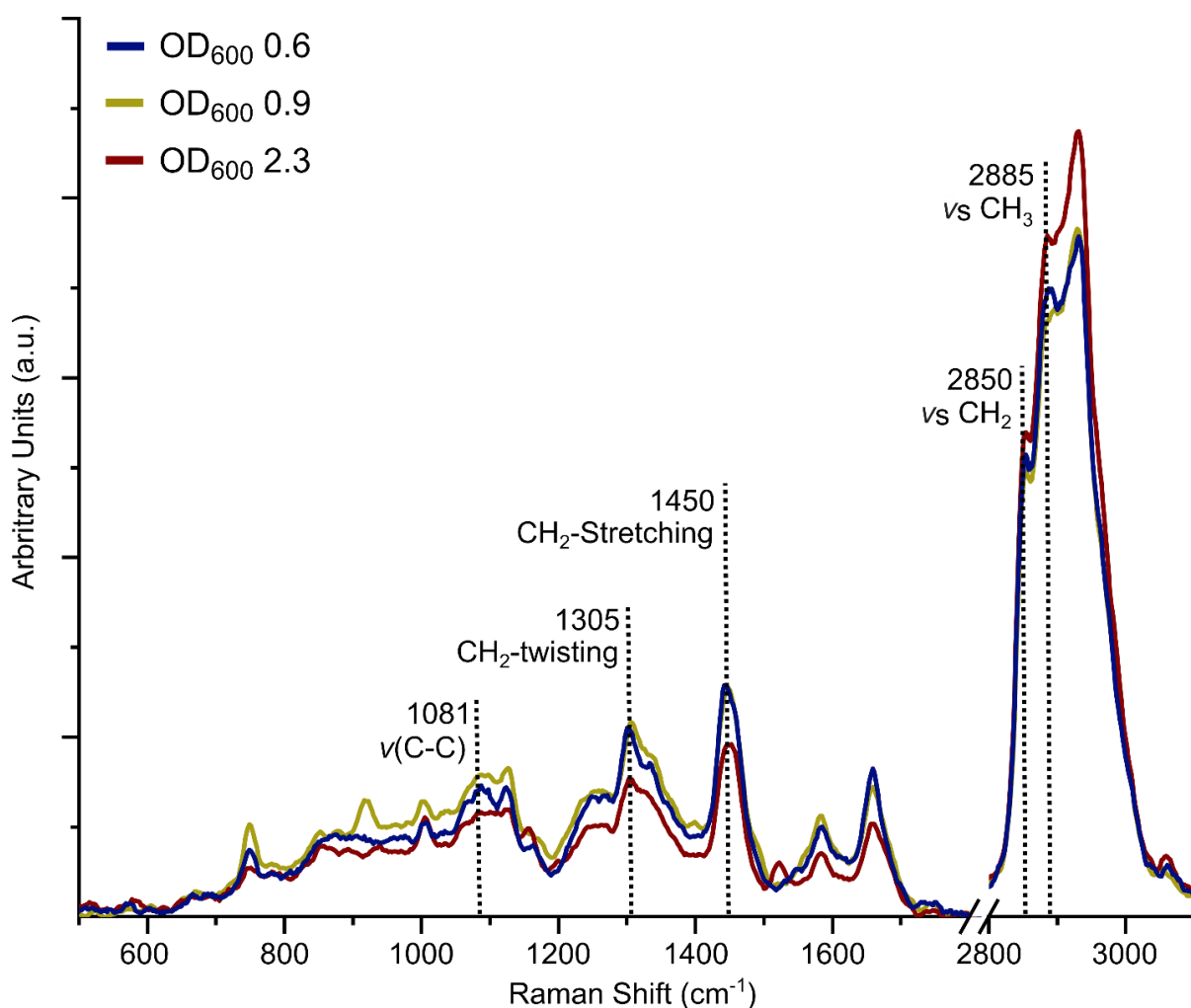
Figure 4.9: Raman spectroscopic analysis of in vitro M. marinum liquid cultures with annotated peaks. Early logarithmic growth stage (OD_{600}: 0.6) is shown in blue, late logarithmic growth stage (OD_{600}: 0.9) is shown in yellow, and stationary growth stage (OD_{600}: 2.3) is shown in red.

These spectra displayed the reported, unique mycobacterial Raman profile with strong intensities in the lipid-associated regions such as 1081 cm^{-1} (v(C-C)), 1305 cm^{-1} (CH_2 twisting), 1450 cm^{-1} (CH_2-stretching), 2852 (v_s CH_2) and 2885 cm^{-1} (v_s CH_3). However, the spectra were not identical and these differences could be observed when conducting a principal component analysis (PCA) on the fingerprint region of the spectra (**Figure 4.10**). In this analysis, the main variation is explained by PC 1 (91.79%) which has an overall shape that is very similar to the three average fingerprints regions observed in Figure 4.10 b. Also, PC 1 is mostly separating the late logarithmic stage from the early logarithmic and stationary stages but is less able to separate the two latter stages from each other. Clearer separation is achieved when

132

introducing PC 3 which causes a complete separation between the stationary growth stage and the logarithmic growth stages and almost complete separation between the two logarithmic growth stages. PC 3 explains less of the overall variation (1.00%) than PC 1, but PC 3 identifies a few critical differences between the liquid cultures that are not as apparent in PC 1. Notably, the spectra obtained from the late logarithmic growth stage displayed much higher intensity in nucleic acid associated regions (e.g. 795 cm^{-1} and 916 cm^{-1}) while the stationary phase bacteria displayed higher content of carotenoid pigments (1159 cm^{-1} and 1528 cm^{-1}).

By collecting Raman spectra from liquid culture, key Raman indicators of *M. marinum* could be identified prior to infection studies in zebrafish. Moreover, the comparison of liquid cultures at different growth stages corroborates previous studies and further demonstrates how Raman spectra can be used to probe fine biomolecular changes in bacteria.
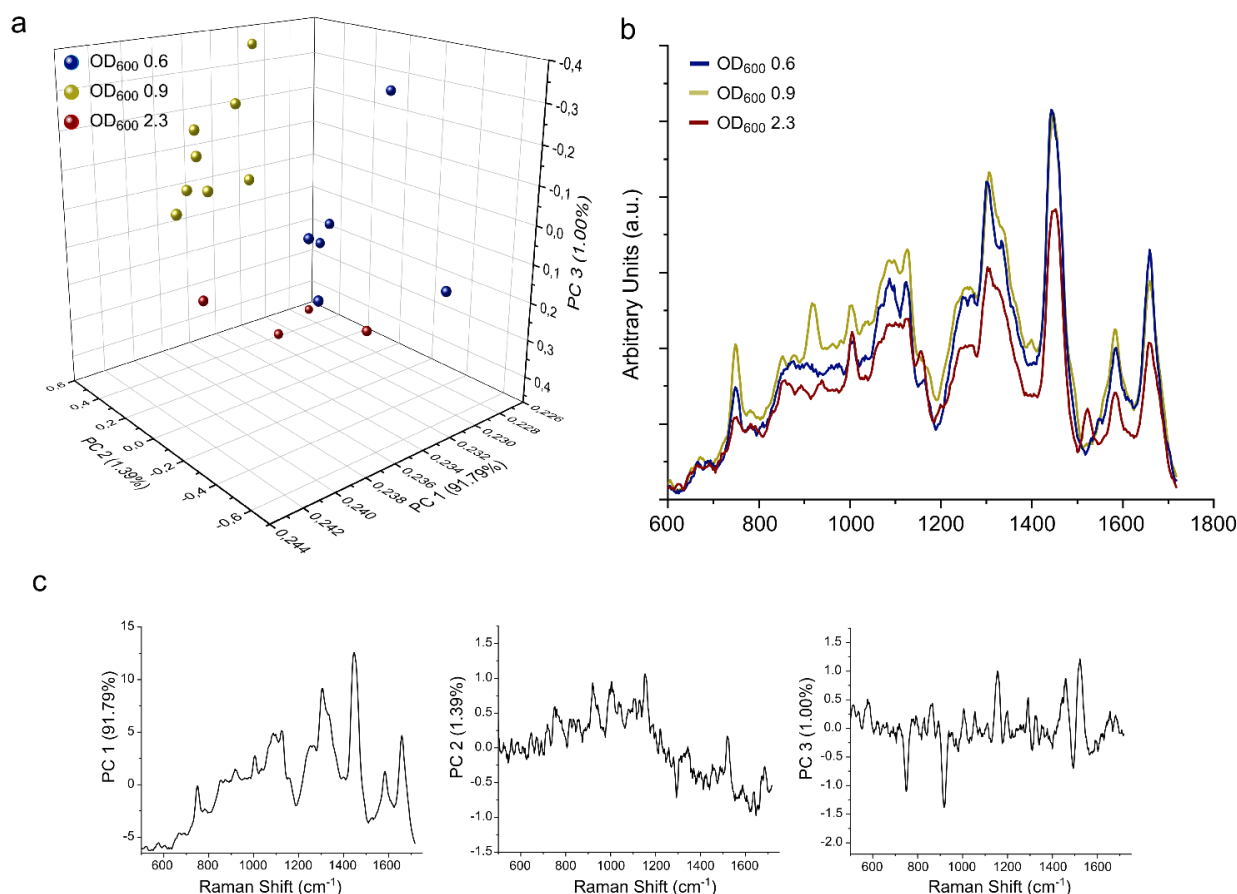
Figure 4.10: *Principal component analysis of in vitro bacterial cultures. **a)** 3D scatterplot of the scores obtained from the PCA performed on the three different liquid M. marinum cultures at OD_{600} at 0.6 (blue), 0.9 (yellow), and 2.3 (red). **b)** Average spectra of the fingerprint regions used for the PCA from the three different liquid M. marinum cultures. OD_{600}: 0.6 (blue), 0.9 (yellow) and 2.3 (red). **c)** The three principal components identified in the PCA performed on liquid M. marinum cultures.*

4.2.2.3 High-resolution confocal Raman spectroscopic imaging of mycobacterial infection

Having characterized the infection model and identified key indicators for M. marinum, the next step was to perform high-resolution cRSI scans across the infection site to provide clear, high-contrast images of mycobacterial lesions. The same infection set-up as described above was used and bacterial lesions were imaged at 4 dpi when clearly visible protrusions could be observed at the injection site. The cRSI could readily detect distinct mycobacterial clusters similar to the ones observed with the ZN staining (**Figure 4.11 a**). Univariate analysis could readily identify the bacterial cluster due to strongly elevated intensity in several of the lipid associated regions of the Raman spectra (e.g. 1081 cm^{-1} (v(C-O) and v(C-C))[313], 1305 cm^{-1}

(CH$_2$ twisting), 1450 cm^{-1} (δ CH$_2$/CH$_3$), 2852 cm^{-1} (v$_s$ CH$_2$) and 2885 cm^{-1} (v$_s$ CH$_3$)) (**Figure 4.11 b**). This was expected since this pattern had already been observed in the measurements of liquid culture bacteria (see above). This lipid rich profile gave the bacteria a different Raman profile clearly contrasting it to the surrounding zebrafish tissue. However, the bacterial clusters observed inside the embryos were not solely lipid rich but also displayed high levels of protein at 1004 and 1665 cm^{-1} (vs(C-C) and v(C=O) respectively), as well as DNA at 795 cm^{-1} (O-P-O stretching) and 1581 cm^{-1} (pyrimidine ring)[317,318], reflecting the comprehensive biomolecular information that could be extracted from the infecting bacteria.
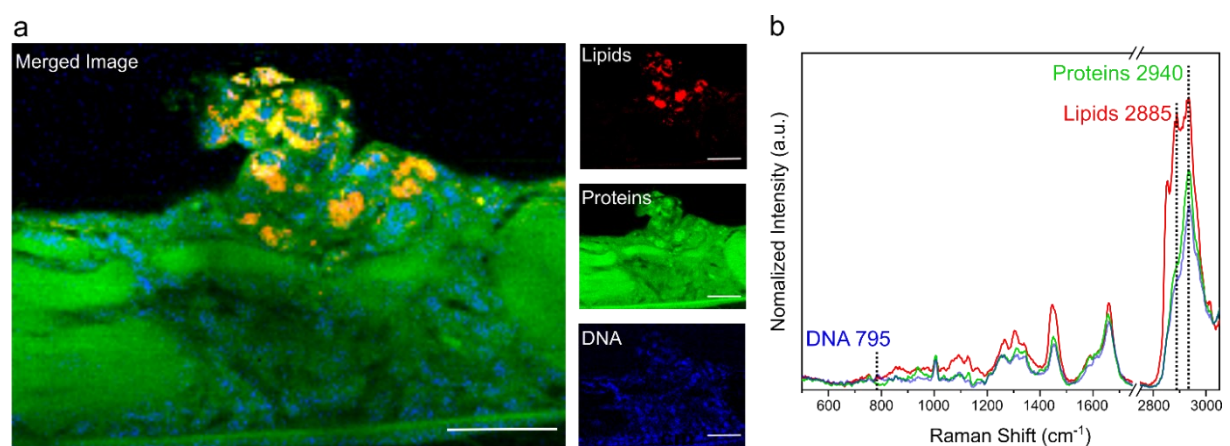
Figure 4.11: ***High-resolution cRSI of M. marinum lesion in zebrafish embryo at 4 days post injection. a)*** *Univariate analysis of cRSI image of a M. marinum lesion. The analyses displays lipids (v$_s$ (CH$_3$)) 2885 ± 10 cm^{-1}, proteins (v$_{as}$(CH$_3$)) 2940 ± 10 cm^{-1} (green), and DNA (O-P-O stretching) 789 ± 10 cm^{-1}. Scale bar: 40 μm* ***b)*** *Exemplar spectra obtained during the univariate analysis. The peak centers used in the univariate analysis are indicated by the dotted lines.*

Also, despite the overall similarity observed in the Raman spectra extracted from liquid cultures and the *M. marinum* in the zebrafish embryo they were not identical. These observed differences can potentially reflect the bacterial response to two vastly different environments, namely a nutrient-rich medium and a hostile host immune cell. This experiment demonstrated how cRSI can be used to identify *M. marinum* infecting bacteria inside a zebrafish host using their unique lipid-rich Raman signature. Furthermore, cRSI could also extract comprehensive biomolecular profiles from the identified bacterial cluster including Raman peaks for nucleic acids and proteins as well as the abovementioned lipids.

4.2.2.4 3D biomolecular profiling of mycobacteria in infected zebrafish

The results presented so far demonstrate that Raman spectroscopy can extract biomolecular profiles from *M. marinum in vitro* to ascertain their metabolic state and that cRSI can be used to detect mycobacterial clusters in infected zebrafish embryos. Moreover, the Raman spectra obtained from the identified mycobacterial clusters contained comprehensive biomolecular information and were well suited for further biomolecular analysis.

The next challenge in implementing cRSI as a technology to be used in zebrafish infection models was to investigate whether cRSI could be used to probe biomolecular differences from two different bacterial strains during zebrafish injections. To this end, cRSI was applied wasto compare the biomolecular profiles of wild type *M. marinum* to that of a mutant strain containing a deletion in a locus called region of difference 1 (RD1) during zebrafish infection. RD1 is one of the most studied loci in mycobacterial research and its' deletion mutants (ΔRD1) display several infection deficiencies. Notably, ΔRD1 *M. marinum* has been shown to have reduced growth and granuloma formation in zebrafish[327]. Moreover, ΔRD1 mutants cause less necrosis and are less able to escape from the host endosomes or cause angiogenesis[325,328]. Together, these deficiencies are likely to restrict the bacteria's access to nutrients and thereby alter their metabolism.

Using the same infection model as above, zebrafish embryos were injected with either wild type or a 3.5-fold dose of ΔRD1 mutant *M. marinum*. At 4 dpi the bacterial lesions were identified and scanned using volumetric cRSI. However, to further analyze the data, it was necessary to find a method for identifying and extract the bacterial spectra specifically. This was achieved by exploiting the uniquely lipid-rich Raman spectra caused by the bacterial cell wall, with several lipid-associated peaks displaying much higher intensity than the surrounding zebrafish tissue. By applying a threshold based on the peak intensity between 2844 – 2864 cm^{-1}, the bacterial pixels were identified and the spectral information from each of these pixels extracted for further biomolecular profiling using multivariate analysis (**Figure 4.12**).

Volumetric Imaging of Bacterial Lesions

Extract all Bacterial Pixels

1 pixel = 1 spectrum

Wild Type Bacteria   Mutant Bacteria

Principal Component Analysis
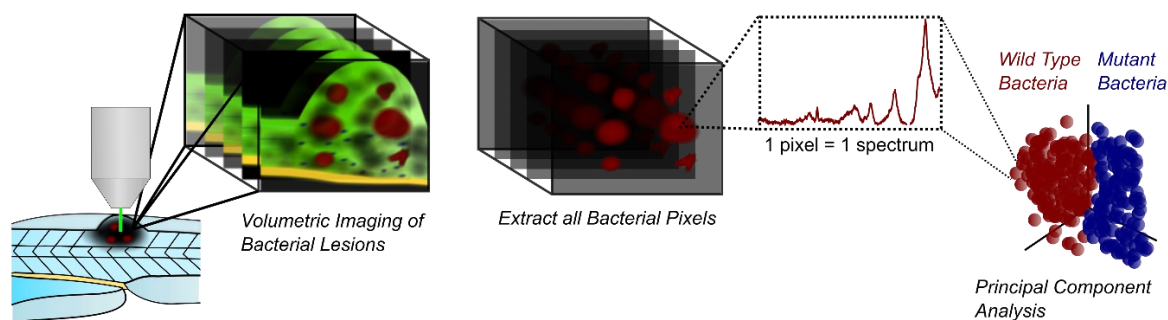
Figure 4.12: Schematic of workflow for the biomolecular analysis of infecting M. marinum in zebrafish.

Notably, this procedure could identify the bacteria in the wild type, as well as the ΔRD1, injected embryos, while the PBS injected controls remained completely bacteria negative (**Figure 4.13 a**). To further compare the wild type and ΔRD1 bacteria a principal component analysis (PCA) was conducted on the fingerprint region (400-1800 cm^{-1}) of all the spectra identified using the abovementioned thresholding. (**Figure 4.13 b** and **c**). This analysis suggested that the wild type and ΔRD1 bacteria could be separated based on their biomolecular differences and identified three principal components corresponding to the main biomolecular variation in the bacteria.

Inspection of the principal components revealed that the main variation between the two bacterial strains was caused by vibrations corresponding lipids with sharpened peaks at 1065 cm^{-1} ((C-C)-stretching), 1128 cm^{-1} (v(C-C)), 1298 cm^{-1} (acyl chains), 1439 cm^{-1} ((C-C)-bending) 1450 cm^{-1} (CH$_2$-stretching). Notably, PC 1 has a strong contribution from saturated fatty acids (e.g. stearic acids or palmitic acids) which is seen from the strong contribution of molecular vibrations caused by C-C motifs (e.g. 1065 cm^{-1} ((C-C)-stretching), 1128 cm^{-1} (v(C-C)), 1298 cm^{-1} (acyl chains), 1439 cm^{-1} ((CH$_2$)-bending). From the matrix plot, it is also clear that PC 1 is the principal component that best separates the two samples, with ΔRD1 mutant bacteria displaying higher scores on PC 1. This indicates that the ΔRD1 contains a higher amount of saturated fatty acids compared to the wild type during the infection. This is an intriguing observation because it is well established that mycobacterial lipid metabolism has a major impact on the course of infection[329]. Moreover, PC 1 also displays that there are clear variations

137

in nucleic acids 795 cm^{-1} (O-P-O stretching) suggesting a higher presence of DNA or RNA in wild type bacteria. PC 2 also displays a clear sign of nucleic acids 795 cm^{-1} (O-P-O stretching) and a strong protein vibration 1661 cm^{-1} (Amide I). However, this component separates the two bacterial strains less well and is more likely to reflect sample variation. PC 3 like PC 1, has a strong presence of saturated fatty acids with strong vibrations in the C-C motifs (e.g. 1065 cm^{-1} ((C-C)-stretching), 1128 cm^{-1} (v(C-C)), 1298 cm^{-1} (acyl chains), 1439 cm^{-1} ((CH$_2$)-bending). PC 3 seems to detect the ratio between saturated and unsaturated fatty acids. This can be observed from the strong vibration centered at 1653 cm^{-1} which runs in the opposite direction to the C-C motifs described above. 1653 cm^{-1} corresponds to C=C stretching (v(C=C)), and the ratio between the CH$_2$ at 1065 cm^{-1} and the C=C stretching at 1653 cm^{-1} can be used to determine the saturated to the unsaturated ratio in lipid samples[315,330].
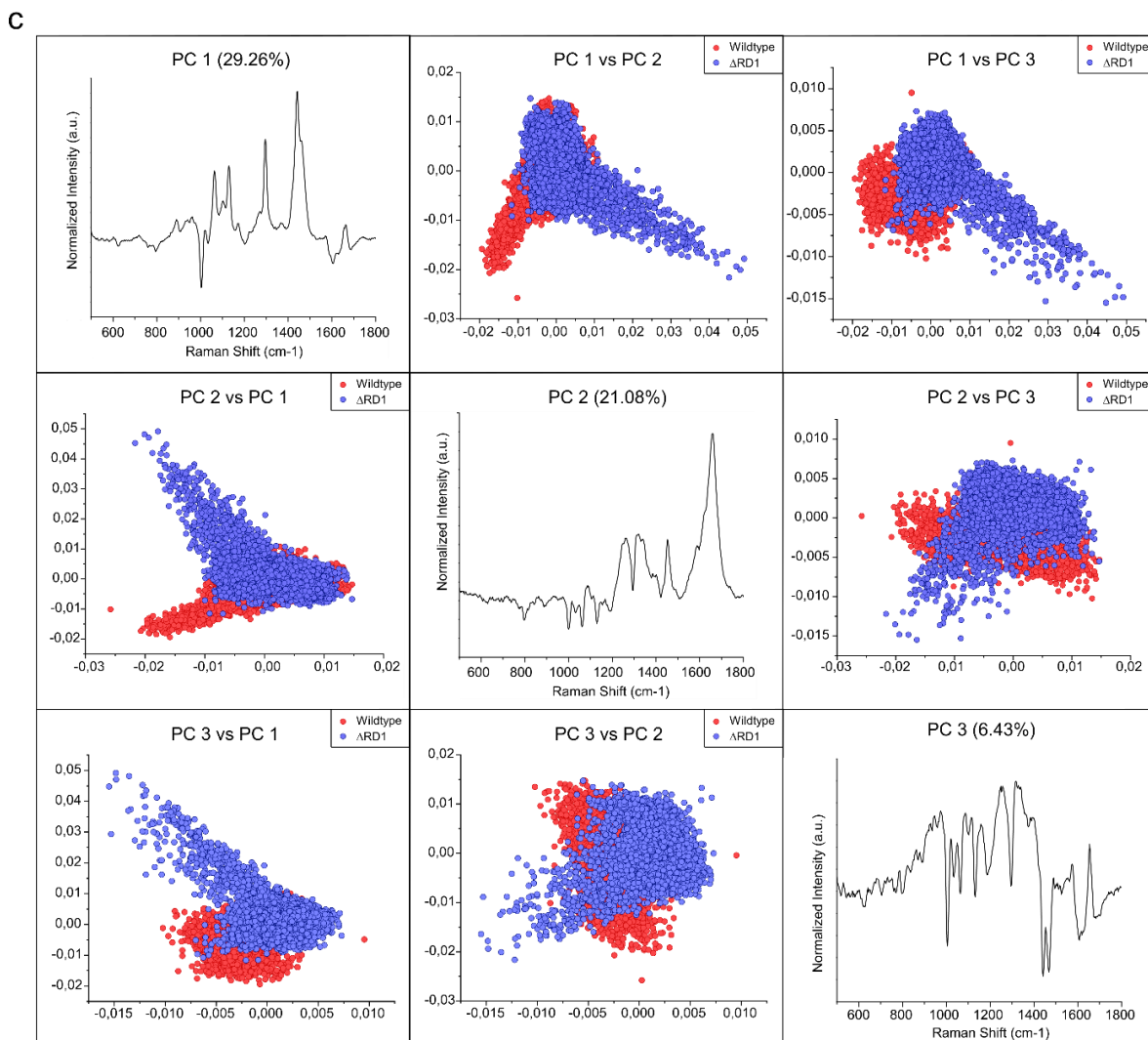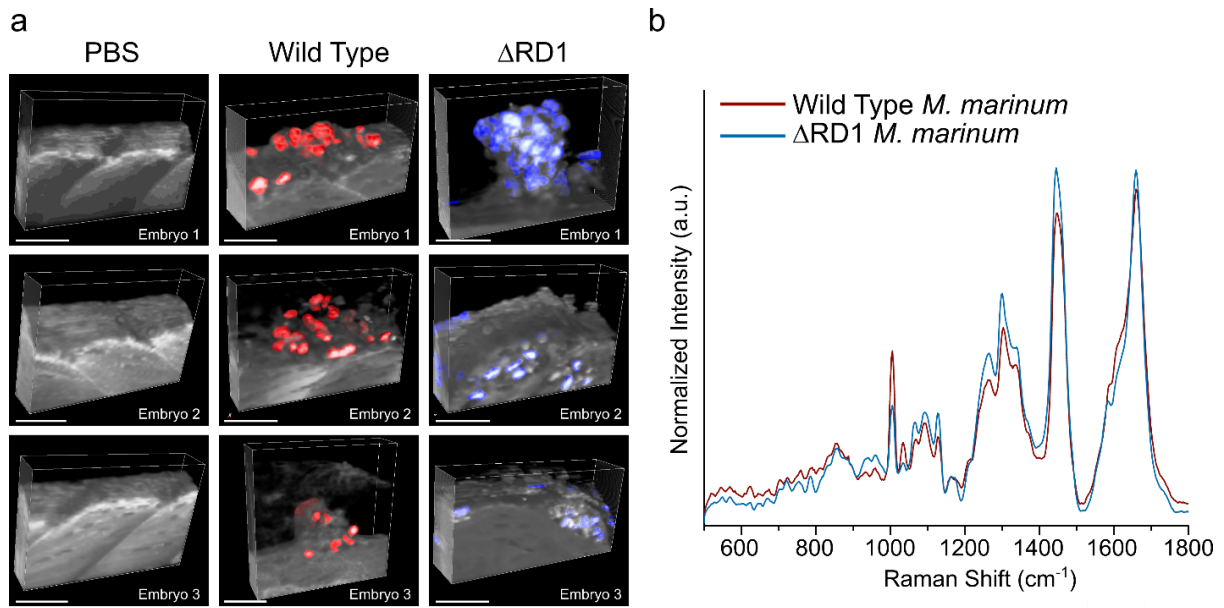
Figure 4.13: Biomolecular profiling and comparison of wild type and ∆RD1 bacteria using 3-dimensional cRSI coupled to PCA. a) 3D cRSI images displaying the identified bacterial clusters using the threshold established for the biomolecular profiling. The images show the result of running the threshold on three biological replicates of PBS, wild type, and ∆RD1 injected embryos. b) Average spectra obtained from the M. marinum positive pixels in the wild type and ∆RD1 injected embryos. c) Matrix plot of PCA performed on M. marinum identified in wild type and ∆RD1 injected zebrafish embryos.

Thus, the PCA indicated a clear separation between the wild type and the ∆RD1 bacteria. To test how well the two populations could be separated the data set was analyzed using a partial least squares discriminant analysis (PLS-DA) (**Figure 4.14**). The PLS-DA achieved a near-complete separation (99.7%) between the wild type and ∆RD1 mutant groups and identified three latent variables (LV) with very similar shapes to three PCs identified with the PCA. Notably, LV 1 is almost identical to PC 1, displaying the same spectral features with strong contribution from saturated fatty acids C-C motifs (e.g. 1065 cm^{-1} ((C-C)-stretching), 1128 cm^{-1} (v(C-C)), 1298 cm^{-1} (acyl chains), 1439 cm^{-1} ((CH$_2$)-bending). Moreover, LV 2 is very similar to PC 3, and LV 3 is very similar to PC 2. Thus, the biomolecular features that best explain the variation in the data set, are also the biomolecular features that best separates the two different bacterial strains.

These results demonstrate how cRSI can be used to extract positional and compositional data to generate biomolecular profiles and use this information to discriminate infections arising from different *M. marinum* strains.
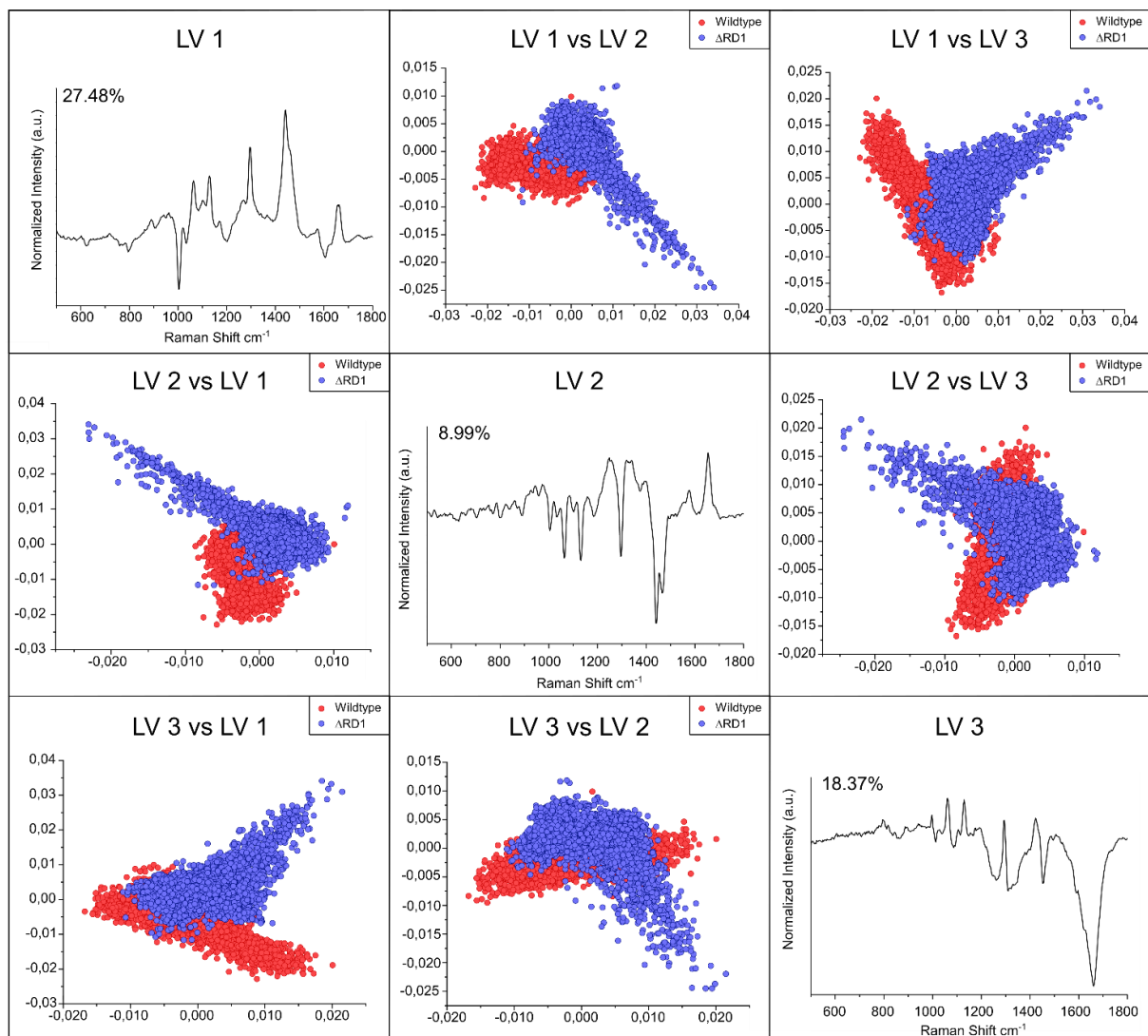
Figure 4.14: *Matrix plot of PLS-DA performed on M. marinum identified in wild type and ∆RD1 and M. marinum injected zebrafish embryos.*

4.2.3 Live imaging

<u>4.2.3.1 Live imaging method and validation</u>

Up to this point, all experiments had been performed in fixed zebrafish embryos. However, an important feature of zebrafish embryos is that they enable live imaging in a vertebrate specimen. While live imaging of zebrafish is commonplace in fluorescent microscopy approaches, there are very few examples of live Raman imaging of zebrafish. Typically, long acquisition time, background interference, and phototoxic effect on the embryos are all challenges that have limited the use of Raman spectroscopy in living zebrafish embryos. However, the cRSI approach outlined here can typically perform imaging with significantly lower pixel integration time than previously tested approaches. Moreover, this cRSI method also achieves thin optical slices and is, therefore, less susceptible to background interference. This meant that the cRSI approach should overcome some of the obstacles to living Raman spectroscopic imaging in zebrafish. However, phototoxicity could still potentially be an issue. Raman spectroscopic imaging typically uses very powerful lasers to generate sufficient Raman signal and these lasers can cause damages in living tissue. For example, sample burning or photothermal damages caused by laser interactions with endogenous chromophores (e.g. heme groups in the blood) are putative damages often observed when strong lasers are applied to living tissue. These issues can be quite severe when using lasers in lower wavelength region (i.e. 532 nm) but are significantly reduced with higher wavelengths such as infrared and near-infrared laser (e.g. 785 nm). Near-infrared Raman spectroscopy is frequently used *in vivo* and has also found applications in diagnostics of human patients. Hence, cRSI using a near-infrared laser should minimize any of the potential laser damages[303].

To test this, a series of cRSI experiments with living zebrafish embryos were conducted using a 785 nm near-infrared laser. First, these experiments were used to identify set of imaging parameters (1.5 s integration time and 2 μm lateral resolution) that could compromise between sufficient Raman signal and spatial resolution on one hand, and the total image acquisition time on the other hand. These imaging parameters are demonstrated in **Figure 4.15 a** and **b**. This imaging set-up provided a clear visualization of the zebrafish tissue where the gut, the notochord, and the individual somites can be observed. Moreover, the spectra obtained with this imaging set-up gives full coverage of the fingerprint region with easily identifiable peaks (e.g. DNA at 795 cm^{-1} (O-P-O stretching), lipids at 1450 cm^{-1} (CH$_2$-stretching), and protein at 1004 and 1665 cm^{-1} (vs(C-C) and v(C=O) respectively.

a

b
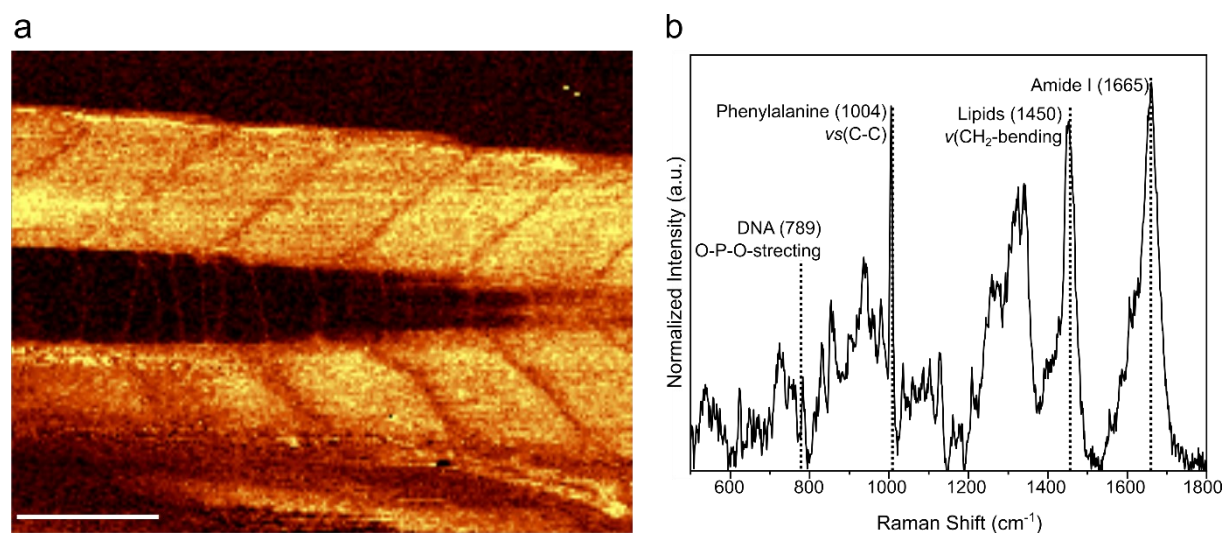
Figure 4.15: Live cRSI imaging of zebrafish embryo 3 dpf using 785 nm laser. a) *Univariate analysis of live Raman cRSI scan. Image display amide I by integrating over the area 1665 ± 10 cm^{-1}. Scale bar: 100 μm.* ***b)*** *Exemplar spectrum obtained during the live cRSI scan. Some of the most used Raman peaks are highlighted to demonstrate the information that can be obtained using live cRSI in zebrafish embryos.*

4.2.3.2 Live imaging tolerance

Having established a set of cRSI parameters that could provide biomolecular information the next task was to determine if this cRSI method was biocompatible. To this end, a series of three cross-sectional cRSI scans were performed on living zebrafish embryos at 3 dpf, which we then compared to unexposed controls. For each experiment, a pair of embryos were embedded together and one of the embryos was subjected to three consecutive cRSI scans, while the other was kept as an unscanned control (**Figure 4.16 a**). The cRSI scans were set up to traverse across the dorsoventral axis of the embryos including the muscle tissue and caudal artery and vein (**Figure 4.16 b** and **c**). After each scan, the scanned embryo and the unscanned control were compared carefully using the bright field microscope connected to the Raman instrument. Careful inspection of the scanned area revealed no visible difference in the scanned tissue and there were no clear signs of tissue damage. Also, upon inspection no clear signs of tissue damage, (i.e. increased tissue fluorescence or the presence of carbon peaks) were observed in the Raman spectra collected during these live cRSI scans (**Figure 4.16 d**).

To further assess the effect of the live cRSI on the zebrafish embryos, 30 s videos were obtained of the heart of the scanned and unscanned control embryos during the experiment. First, one video was taken of both the scanned and the unscanned control embryo prior to the live cRSI scans. Then, after each completed scan a new 30 s video was recorded from both scanned and control embryos to track any changes in the heart rate. No changes in the heart rate were detected between the scanned and unscanned control embryos at the different time points. Moreover, no changes were observed between the different time points either, indicating that repeated cRSI scanning did not affect the heart rate (**Figure 4.16 e**). Also, the mean heart rate across all groups was 140 ± 6 beats per minute which is within the reported range of healthy zebrafish embryos[331].
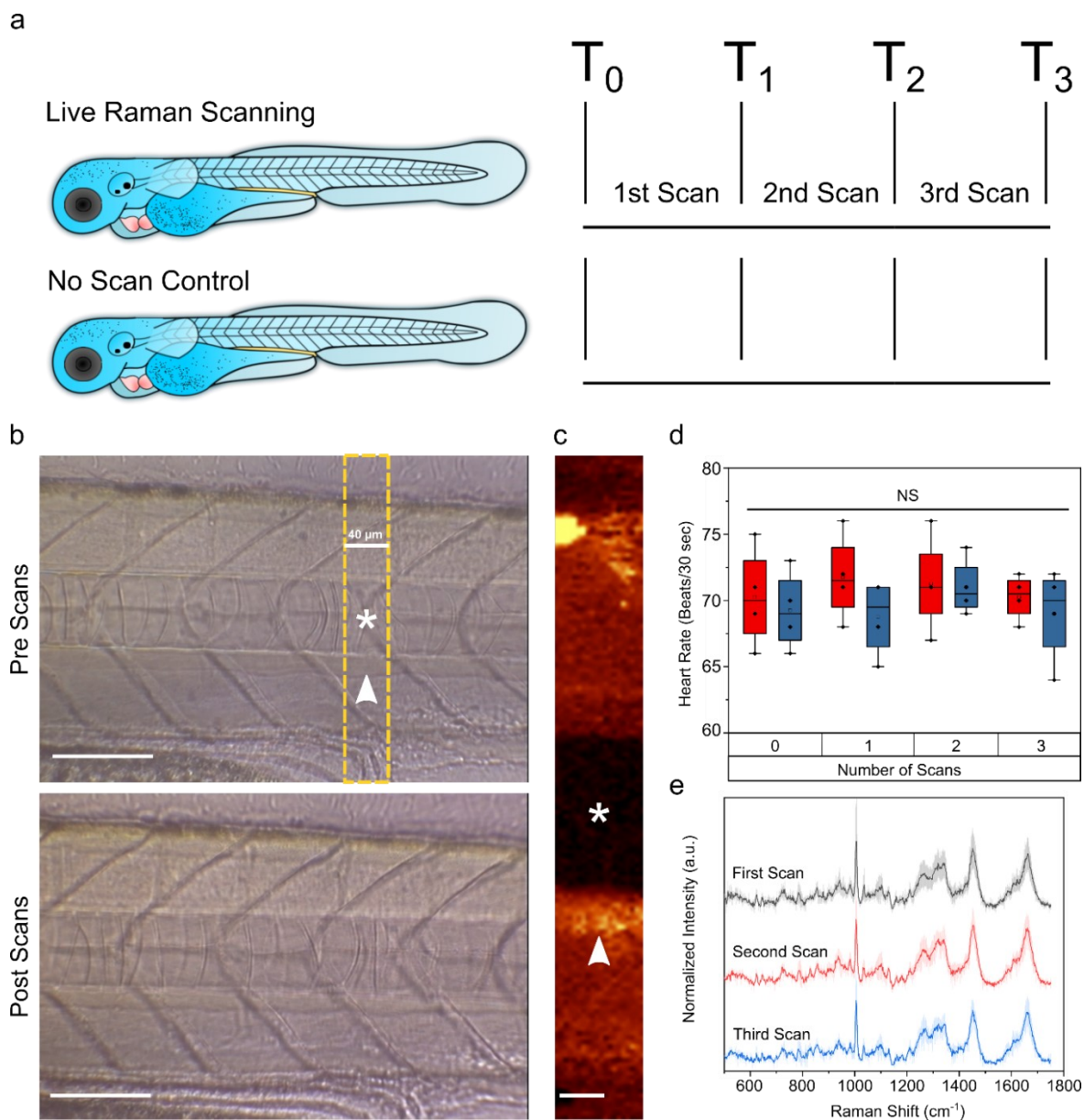
Figure 4.16*: **Live cRSI tolerance experiments using 785 nm laser. a)** Schematic outline of the experimental design. A pair of zebrafish embryos were embedded together at 3 days post-fertilization. One of the embryos were imaged using the live cRSI set up (1.5 s integration time 2 µm lateral resolution). A total of three consecutive scans were performed on the same area of the cRSI scanned embryo (1st, 2nd and 3rd scan), before the first scan and after each scan, short 30 s videos were obtained of the hearts and blood flow of both the cRSI scanned and the unscanned control embryos. **b)** Brightfield images of live Raman scanned zebrafish embryo before (top image) and after (bottom image) the three Raman scans. The scanned area is indicated with a yellow dotted box, the notochord is indicated by a white asterisk and the caudal artery is indicated by a white arrowhead. Scale bars: 100 µm. **c)** Example of a cross-section scan performed during live cRSI tolerance experiments. The zebrafish was visualized by a univariate analysis integrating over a wavenumber range of 1665 ± 20 cm^{-1} (amide I). The asterisk indicates the notochord and the arrowhead indicates the caudal artery. Scale bar: 20 µm. **d)** Mean Raman spectra collected from four zebrafish embryos scanned with cRSI. Data shown are mean ± standard deviation. **e)** The mean heart rate of four zebrafish embryos measured before the study and after each cRSI scan (blue), which showed no significant difference with unscanned controls (red). Lines indicate median, box boundaries indicate 1st and 3rd quartile, and whiskers indicate maximum and minimum values. A statistical analysis was performed by using a regression analysis between cRSI scanned and unscanned control fish followed by a Wilcoxon signed-rank test to test for divergence over time. No significant divergence was observed (p = 0.715).

Apart from burning, the most likely cause of laser damage would be photothermal damage caused by laser interactions with endogenous chromophores such as porphyrins found in the heme-groups of erythrocytes. Thus, the blood constitutes a weak point for photodamage in the embryos. For this reason, 30 s videos were obtained of the blood circulation of both scanned and unscanned control embryos. The same procedure that was used for the heart videos was followed and videos were recorded of both the scanned and of the unscanned control embryos before and after each completed scan. The videos were then inspected for any changes in blood and particularly for any loss in erythrocytes, but no qualitative differences were observed.

Lastly, to fully analyze the effect of the cRSI on the zebrafish embryos, a PCA was performed on all the spectra collected throughout the live scan to look for potential changes in the Raman spectra that could indicate an effect on the scanned tissue. However, no such changes were observed, and the three consecutive scans were indistinguishable from one another in all the cRSI scanned embryos (**Figure 4.17**). Hence, there were no clear, systematic changes associated with repeated cRSI scans in live embryos. Taken together, these results suggested that under the tested conditions, the laser did not affect the heartbeat, blood flow, and tissue biochemistry in the embryos, indicating that these cRSI scans should have minimal impact on the measurements performed.
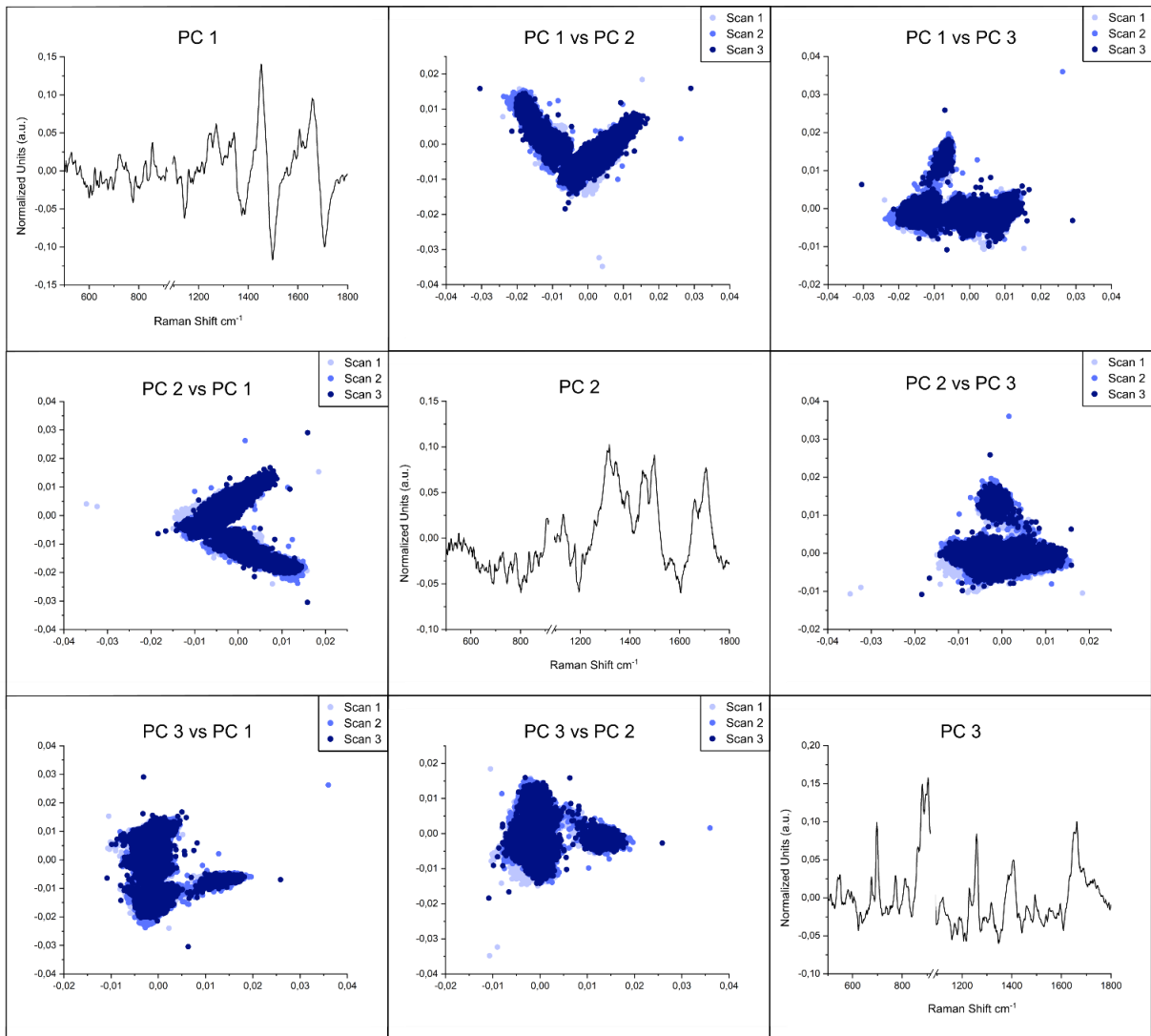
Figure 4.17: PCA analysis of all Raman spectra collected during the live cRSI tolerance scans.

4.2.4 Live Raman spectroscopic imaging of wound response

4.2.4.1 Establishing and verifying stab wounds in zebrafish embryos

Having identified a biocompatible cRSI method for live zebrafish embryos, the next challenge was to apply this method in an embryo model to demonstrate how live cRSI could be used to probe and track biomolecular changes over time. One potentially important application of live cRSI would be to track biomolecular changes caused by tissue damage. Most, instances of tissue damage lead to a wound healing response and encompass gross changes in tissue structure and composition. Many of these changes will also be manifested on the biomolecular

147

level which could be accessed by live cRSI. Moreover, the wound response is rapid, and changes were likely to occur on a time scale that was suitable for live tracking using cRSI.

To this end, a wound assay in zebrafish embryos was established. Stab wounds were performed using a surgical tungsten needle to make a single somite incision in the dorsal myotome of the zebrafish embryos[110]. To verify this approach, stab wounded embryos were stained with phalloidin and imaged using confocal fluorescence microscopy (**Figure 4.18**). The wounds could be clearly observed as a gap in the muscle tissue of the wounded somite already at 3 hours post wounding (hpw). This indicated that the stab wound procedure was successfully set up and that the wounds introduced were well suited for live cRSI.
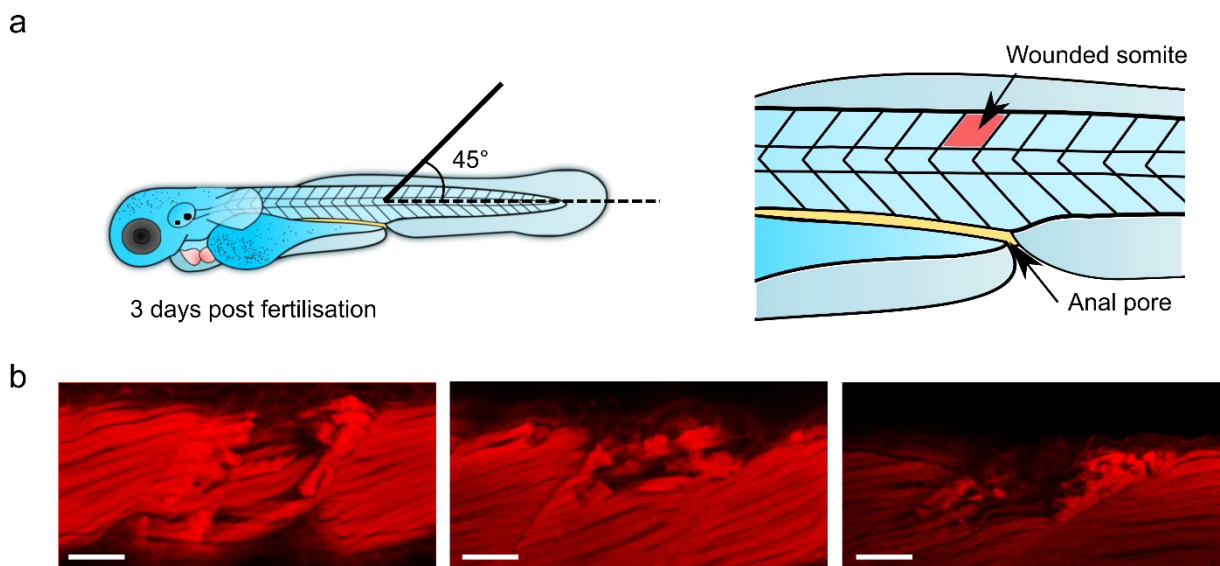
***Figure 4.18: Zebrafish embryo stab wound model. a)** Schematic of the wounding procedure. The zebrafish embryos were stab wounded in a single somite using a surgical tungsten needle at 3 days post-fertilization. The needle was kept at a 45° angle and the wounds were placed in the dorsal myotome just opposite to the anal pore. **b)** Three exemplar confocal fluorescent images of phalloidin stained zebrafish embryos 6 hpw. Scale bars: 50 μm.*

4.2.4.2 Raman spectroscopic characterization of wound response

Before imaging the wound response using live cRSI with the 785 nm laser, further characterization of biomolecular changes caused by the wound response was needed. To this end, zebrafish embryos at 3 dpf were stab wounded as above and the wound response was

characterized using cRSI with a 532 laser in fixed samples at 6, 24, and 48 hpw. This achieved high-resolution imaging across the wound and allowed for identification and annotation of wound specific biomolecular changes. Using univariate analysis, the wound site could be visualized. Markedly, the wounds had a high presence of lipids (2885 cm^{-1}) and carotenoid-like pigments (1159 cm^{-1}) and these two components were segmented to the wounded somite (**Figure 4.19**). Also, the wounded areas often displayed a marked reduction in collagen (901 cm^{-1}). Notably, the collagen signal mimicked the phalloidin staining observed in Figure 4.18 b and most of the wound sites showed the gap in the muscle tissue, marking the area of the tissue that had been damaged by the needle impact. The wound site was visible throughout the experiment but expectedly at 48 hpw, the wounds were harder to identify and displayed a weaker contrast to the surrounding healthy tissue. Moreover, the carotenoid signal seemed to be mostly associated with the early time points and was greatly reduced at 48 hpw.

While further complementary analysis is needed to fully determine the biological meaning of these changes, this data demonstrates that there are several important biomolecular changes associated with the wound response that can be detected by Raman spectroscopy making it an interesting model for testing of live cRSI.

a

| Proteins and Lipids 2800 - 3000 cm⁻¹ | Lipids 2885 cm⁻¹ | Proteins 2940 cm⁻¹ | Collagen 901 cm⁻¹ | Carotenoids 1528 cm⁻¹ |

6 hpi

24 hpi

48 hpi

b

Normalized Intensity (A.U.)

Collagen 901

Carotenoids 1528

Lipids 2850

Proteins 2940

Raman Shift (cm⁻¹)
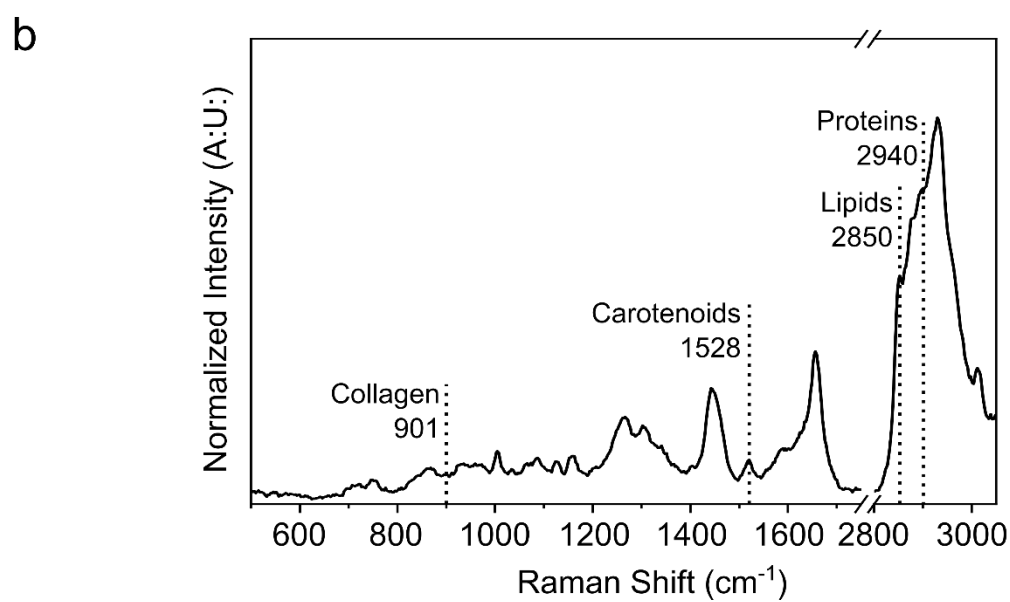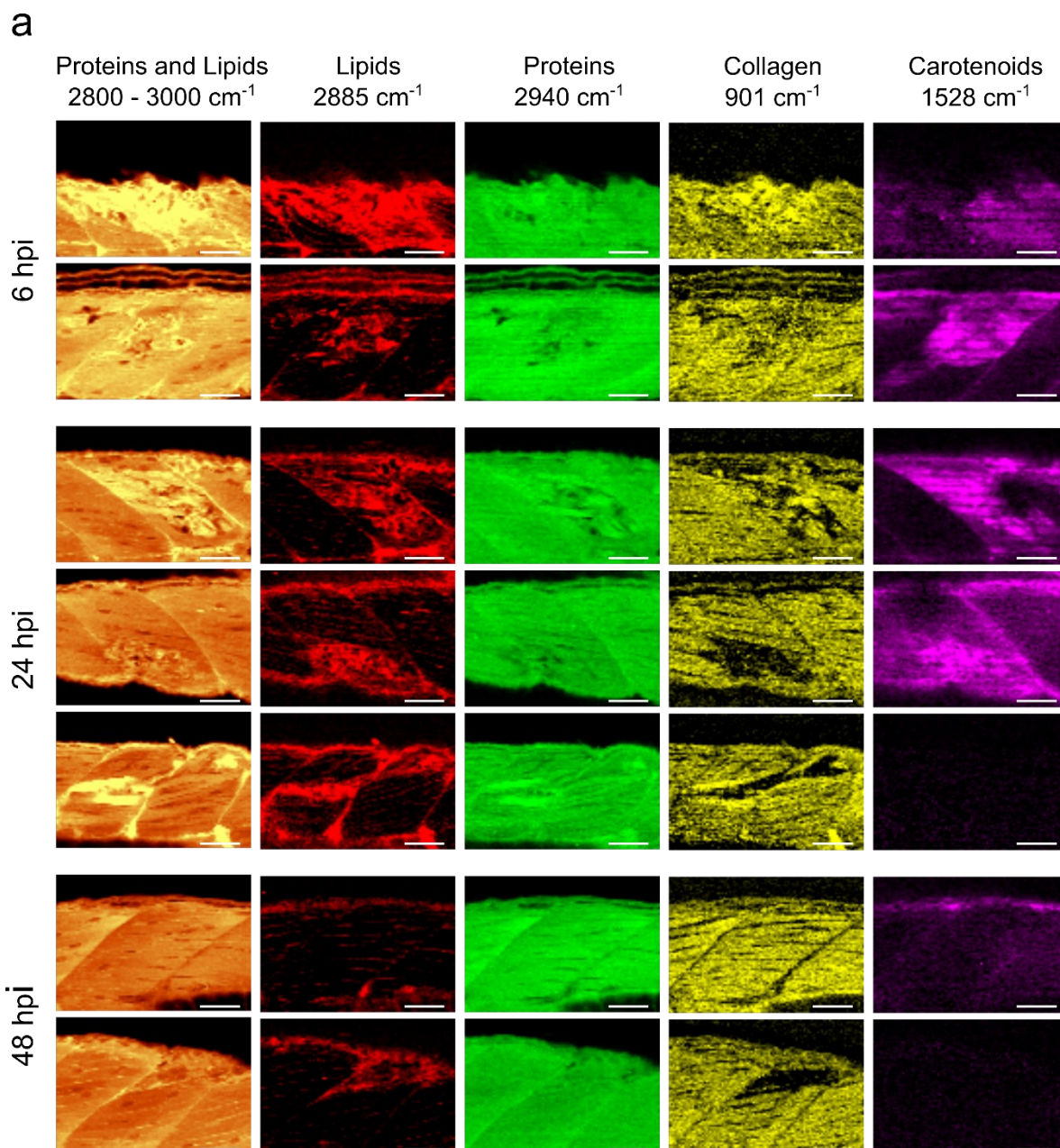
Figure 4.19: *cRSI characterization of wound response in fixed zebrafish embryos.* ***a)*** *Univariate analysis images of zebrafish embryos at 6, 24- and 48-hours post wounding (hpw). Univariate analysis was performed by integrating over a wavenumber range corresponding to relevant biomolecules: protein and lipid-rich area 2900 ± 100 cm^{-1} (shown in orange), lipid-rich regions at 2885 ± 10 cm^{-1} (shown in red), proteins regions at 2940 ± 16 cm^{-1} (shown in green), collagen-rich region 901±170 cm^{-1} (shown in yellow), carotenoid-rich regions at 1528 ± 16 cm^{-1} (shown in magenta). Scale bars: 40 µm.* ***b)*** *Exemplar Raman spectra obtained from a wounded zebrafish embryo with the center of the integrated regions indicated by annotated dotted lines.*

4.2.5 Live tracking of wound response

4.2.5.1 Live, continuous Raman imaging of wound response

Having verified the compatibility and effectiveness of the 785 nm laser and established and characterized the wound healing model using cRSI, the next step was to demonstrate live cRSI in the wound healing model. To this end, a single living zebrafish embryo at 3 dpf was subjected to the stab wound procedure and mounted for cRSI at 1-hour post wounding (hpw). The live cRSI scan was set up to cover the entire wounded somite and part of the adjacent unwounded somites on either side. Scanning this area took about 2 h using the identified live cRSI parameters and three consecutive scans were performed at the 1-3 hpw, 4-6 hpw, and 10-12 hpw time intervals (**Figure 4.20 a**). This allowed for time-lapse cRSI of the wound response in the living zebrafish embryo. The wounded somite could be visualized using univariate analysis of the lipid-associated peak at 1453 cm^{-1} (**Figure 4.20 b**). However, the contrast to the neighboring unwounded somites was a lot weaker when compared to the cRSI images obtained from fixed embryos using the 532 nm laser. This was expected because the Raman signal is inversely proportional to λ^4, meaning that the live cRSI, which is using the 785 nm lasers would obtain significantly lower signals compared to the fixed samples imaged using the 523 nm laser.
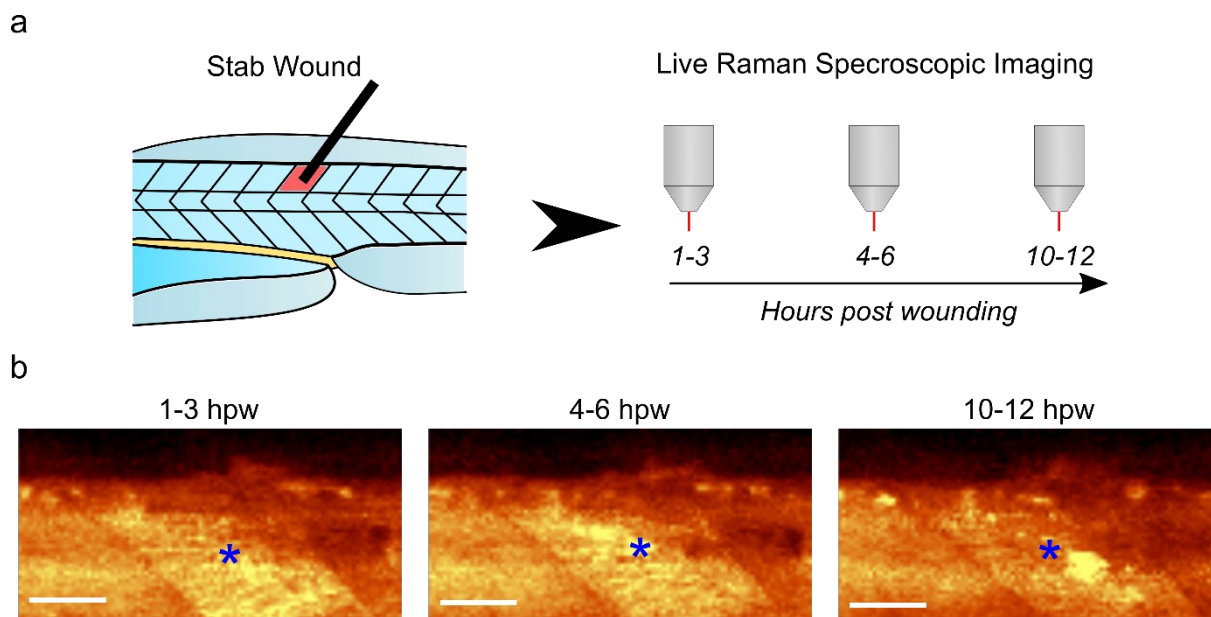
Figure 4.20: Live time-lapse cRSI of stab wounded zebrafish embryo. a) *Schematic of live cRSI experiment. The embryo was wounded in a single somite in the dorsal myotome at 3 days post-fertilization. The live wound response was tracked using the 785 nm laser 2 μm lateral resolution and 1.5 s integration time. Images were recorded in the time intervals 1-3, 4-6 and 10-12 hpw.* **b)** *Univariate analysis of cRSI scans of a living zebrafish embryo at 1-3, 4-6 and 10-12 hpw. The asterisks indicate the center of the wounded somite. Univariate analysis was performed by integrating over a wavenumber range at 1450 ± 30 cm^{-1}. Scale bars: 40 μm.*

However, the differences between the wounded somite and the unwounded somites were clear, and to further analyze the live cRSI time-lapse scans a vertex component analysis (VCA) was performed. VCA is a multivariate analysis technique that aims to identify a set of vectoral endmembers through linear unmixing[332]. Through the VCA, three tissue endmembers were identified in the live cRSI images. The first endmember was highly associated with the stab wounded somite, the second endmember was highly associated with the adjacent unwounded somites and the third endmember was mostly localized on the edge of the embryo and seems to correspond to pigmented structures often found on the embryo surface (**Figure 4.21**). Compared to the univariate analysis the VCA is more suited for distinguishing the wounded and the unwounded somites and the VCA again identified the clear wound segmentation observed in the fixed samples. By comparing the distribution of the wounded and the unwounded endmembers it is clear that the wounded endmember is mostly restricted to the

impacted somite and the boundaries between the wounded and unwounded endmembers follow the natural boundary between the somites.
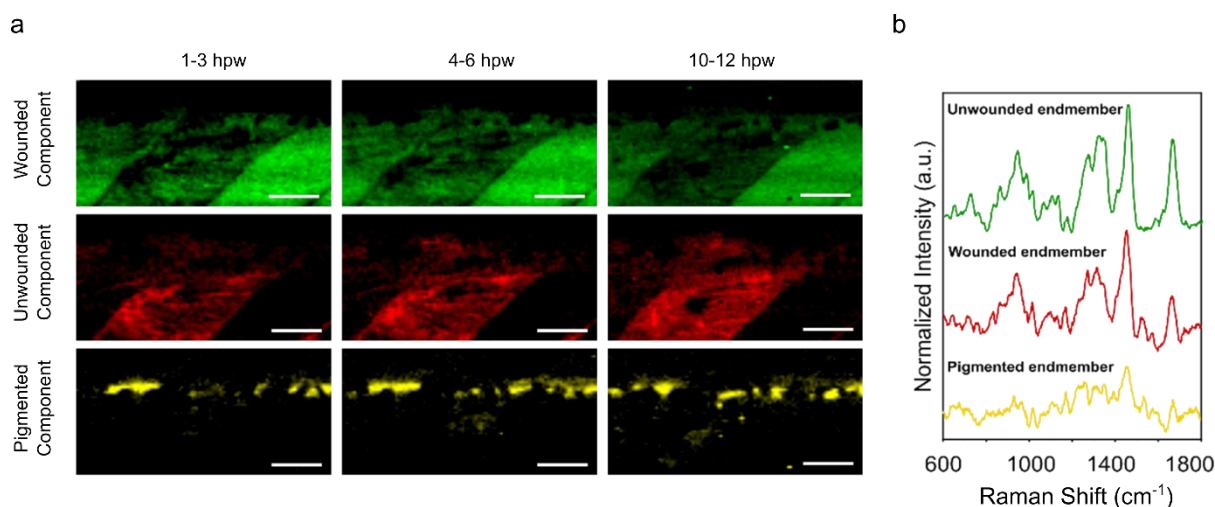
Figure 4.21: Vertex component analysis (VCA) of live cRSI scanned stab wounded zebrafish embryo. a) The VCA could discriminate the wounded somite from the adjacent unwounded somites and identified three tissue endmembers: A wounded endmember (shown in red), an unwounded endmember (shown in green), and a pigment-containing endmember (shown in yellow). Scale bars: 40 μm. b) The three endmembers were identified by VCA. The wounded endmember is shown in red; the unwounded endmember is shown in green and the pigment-containing endmember is shown in yellow.

Further comparing the wounded and unwounded endmember revealed several biomolecular changes associated with the wound response (**Figure 4.22 a**). Similar to what was observed for the fixed embryos the wounded component exhibited an increased presence of carotenoid pigments at 1159 and 1528 cm^{-1} (conjugated C-C and C=C stretch) and lipids at 1435 cm^{-1} (CH$_2$-scissoring), as well as reduced collagen content at 852 cm^{-1} (hydroxyproline) and 1665 cm^{-1} (amide I) (**Figure 4.22 b**). Moreover, the wounded tissue endmember increased in area and intensity over time to become the dominant component in the wounded somite after 12 h (**Figure 4.22 c**). Previous reports have observed that the wound tends to increase in size during the first 24 hours before eventually starting to heal[180]. The observation made here, with a slow expansion of the wounded endmember corroborates those reports. The most likely explanation for the early wound expansion is a slow loss of damaged muscle tissue needed before the wound healing. This hypothesis also fits well with the reduced collagen content

observed in wounded endmember. The presence of carotenoid pigments at the wound site is prominent and has not been reported before; and further investigations are needed to define their possible role in the wound response.

However, while the precise biomolecular progression of the wound response is still unclear, this demonstration illustrates how cRSI can be used for *in vivo* time-lapse biomolecular imaging in living zebrafish embryos, establishing a new tool for biomolecular analysis in this model.

a
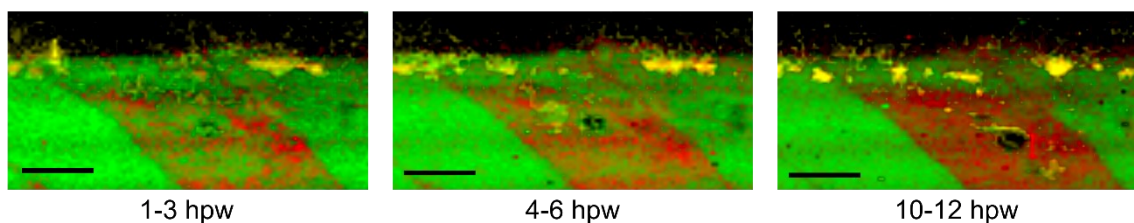
b
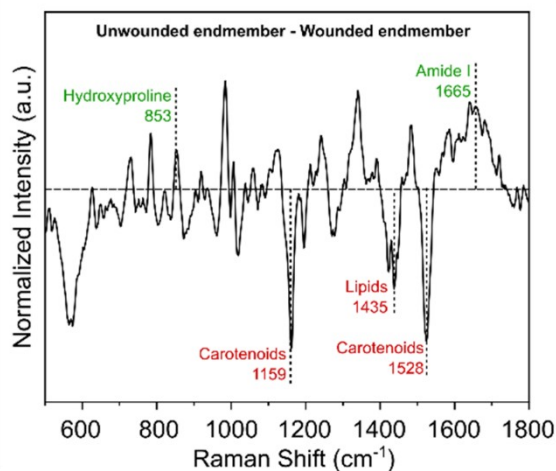
c
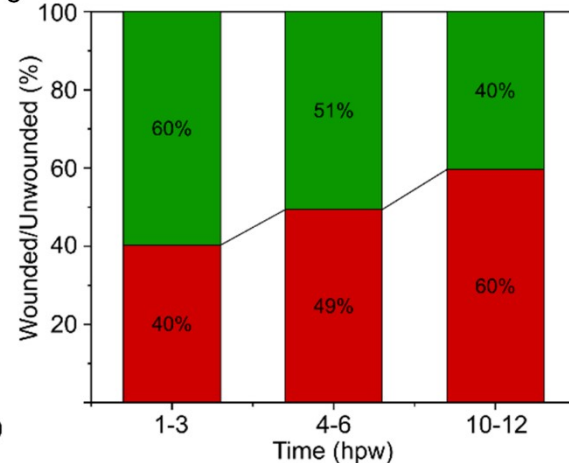
Figure 4.22 Biomolecular analysis of wound response in zebrafish embryos using live cRSI a) *Overlay of VCA generated images. The wounded endmember is shown in red; the unwounded endmember is shown in green and the pigment-containing endmember is shown in yellow. Scale bars: 40 μm.* ***b)*** *Analysis of the unwounded and wounded endmembers identified by the VCA. The black spectrum is the difference spectra when the wounded endmember is subtracted from the unwounded endmember. The horizontal dashed line indicates zero difference between the two endmembers. The dotted vertical lines indicate the center of the annotated peaks that were different between wounded and unwounded tissue, with the color-coding indicating in which component they were dominant.* ***c)*** *The relative abundance of the wounded and the unwounded component in the injured somite at the three time points extracted from pixel intensity histograms produced by the VCA. The wounded component is shown in red and the unwounded component is shown in green.*

4.2.6 Live cRSI limitations and applicability

While the presented live cRSI method offers some attractive opportunities for biomolecular analysis, the method also has a few important limitations that needs consideration. A general limitation concerning the use of non-stimulated Raman spectroscopy is that the occurrence rate of spontaneous Raman scattering is low (10^{-6} - 10^{-8}). This affects both the sensitivity that can be obtained, and the acquisition time needed to perform RSI. For biological material in aqueous solution the lower detection limit for spontaneous Raman spectroscopy is usually around 10-20 mg/mL. This restricts spontaneous RS analyses to relatively abundant biomolecules meaning that important biomolecular information may remain undetected. This is an important limitation to consider for cRSI and means that many biological questions cannot be addressed by using this method, simply because they occur at biomolecular concentrations that are below the detection limit of RS. Moreover, because the occurrence rate of spontaneous Raman scattering is low, the integration time required to collect sufficient Raman signal is typically on the order of seconds (200 ms - 2 s) per sampled pixel. Specifically, in the presented live cRSI method the integration time was set to 1.5 s per pixel meaning that it took close to two hours to complete a full live 2D scan using cRSI. This means that live cRSI obtains poor temporal resolution restricting the use of this method to biological processes that occurs over long timescales. Lastly, in order to generate sufficient Raman signal, powerful lasers are required. For this reason, adverse effects such as phototoxicity or sample heating is often a problem in RS of live samples and in cRSI specifically because cRSI involves lengthy exposures to a point scanning laser moving across the zebrafish tissue.

These limitations had to be carefully considered for the live cRSI analysis of the wound response that is presented in this thesis. Potential phototoxic effects on the embryos caused by laser exposure were investigate and is presented in figure 4.16 and 4.17. However, local heating and potential melting of the agarose gel could still be an issue. For this reason, the embryos were always kept in ~50 mL of E2-water which helps dissipate the heat and the laser shutter was closed between the different measurements to avoid unnecessary laser exposure

and heating. Moreover, the limitations in the time resolution of the live cRSI means that the analysis deviates significantly from real-time and important temporal aspects of the wound response may therefore be lost with this approach.

Despite these disadvantages the ability to perform live cRSI still provide some important advantages. The main advantage is the direct access to live tracking of biomolecules and biomolecular profiles that would otherwise be inaccessible using conventional labelling strategies. The live cRSI experiments showed in this chapter provide one such example namely the detected carotenoid pigments. The role of carotenoid pigments in zebrafish wound healing is poorly described in the literature which could be due to a lack of experimental access to the pigment dynamics. Another important advantage of live cRSI in zebrafish is that it enables access to multivariate inspection of biological processes. This can for instance be used for time-resolved biomolecular profiling of disease progression and serve as an important complementary tool to assess phenotypic and metabolic variability in live specimen. In this work, a proof of concept for disease profiling was done in fixed specimen and without any time resolution, however, this concept should be within reach also for the live cRSI approach and this is something that should be a focus of future research.

4.3 Discussion and concluding remarks

The work presented here demonstrates how high-resolution cRSI can be employed for analysis zebrafish embryos. cRSI offers an attractive combination of axial-resolution and signal-to-noise ratio, features that are highly advantageous for the biomolecular analysis of zebrafish embryos. Thus, cRSI can obtain well-resolved Raman spectra with minimal imaging artifacts from most of the zebrafish embryo. This ability extends to the axial planes and cRSI can readily be applied for 3-dimensional analysis as well. cRSI also achieves good lateral resolution and can readily resolve fine tissue details, such as muscle fiber membranes, or individual cell nuclei, in a single plane.

However, the most influential aspect of cRSI is that it is a method that enables direct and label-free access to a wide array of biomolecules simultaneously. This constitutes a unique opportunity for multivariate interrogations of biomolecular changes associated with for instance metabolic or phenotypic changes, without any spatial interruption of the embryo samples. In the present work, this ability is demonstrated in both a 3D profiling of bacterial infections and in a time-lapse experiment of the early wound response *in vivo.* These two examples display the versatility of cRSI and the potential impact this method could have on imaging complex biological processes. Zebrafish embryos have become a widespread tool for disease modeling and there are several cancer and bacterial infection models available. Common to almost all of these diseases is that they display a varied and heterogeneous mix of phenotypical profiles, often having an important impact on both disease progression and treatment. These phenotypical changes are hard to access and are consequently often poorly understood. The ability of cRSI to probe these phenotypes by inspecting a multitude of biomolecules simultaneously, while upholding complete sample integrity, represents a novel opportunity to investigate these processes with increased spatiotemporal resolution. This arguably represents the most immediate impact of cRSI on zebrafish research and the study of complex biological processes in general. Notably, there are currently more than 240 different bacterial infection models for zebrafish embryos and also several xenograft cancer models, most of which could benefit from a tool that can perform multivariate biomolecular analyses in three dimensions[197,255,256].

A second important advance in this work is the demonstration of a robust *in vivo* platform, compatible with time-lapse imaging. The ability to perform repeated cRSI scans over the same ROI without causing adverse effects represents the first step towards time-resolved cRSI in zebrafish. It should however be mentioned that this *in vivo* cRSI method is time-consuming and cannot achieve video-rate temporal resolution. Still, this *in vivo* cRSI method also provided Raman spectra of sufficient quality for multivariate analysis, enabling 2-dimensional multivariate time-lapse biomolecular tracking in living zebrafish embryos. Also, this application

is likely to have its most immediate impact on zebrafish disease modeling. One important potential application could be tracking of biomolecular changes in a tumor or an infection site during drug treatment.

To further enhance the potential of cRSI in zebrafish research, several important aspects should be considered. First, cRSI does not have the high specificity of immunostaining and has lengthy scan times necessitating both pre-knowledge of the sample and careful corroborations of the RSI data using complementary methods. Methods to perform correlative fluorescence and Raman spectroscopic imaging would considerably improve the utility of RSI methods such as cRSI. The general challenge in achieving a correlative imaging platform is that the fluorescence signal is generally much stronger than the Raman signal and will therefore often overwhelm the Raman signal. While being a clear challenge this does not, however, mean that fluorescence and Raman imaging are incompatible. E.g., a correlated approach was described by Bennet *et. al.*, who performed fluorescence imaging and collection of single confocal Raman point spectra on the same embryo[294]. Extending this correlative platform to include both fluorescence microscopy and cRSI would not only enable more targeted cRSI but also allow for more refined biomolecular profiling. One possibility could be to combine the biomolecular profiling demonstrated in this thesis with the analyses of specific fluorescent expression markers. For instance, in tuberculosis research, such expression markers have been deployed to assess the bacterial replication cycle in mouse explants[333].

Furthermore, cRSI can also complement other biomolecular analyses, such as transcriptomics, proteomics, lipidomics, and metabolomics, to decipher the significance of biomolecular variations in development and disease. Serio *et al.* demonstrated one such approach in a mouse model for multiple sclerosis, where cRSI was combined with desorption electrospray ionization mass spectrometry (DESI-MS) to perform correlated lipidomics[334]. Similar approaches may prove useful for correlative analysis in zebrafish disease models using cRSI.

Also, cRSI is not the only method for Raman imaging, and it is very likely that also other RSI methods will have a significant role to play in zebrafish research. While cRSI has its main strengths in the spatial resolution and signal-to-noise ratio it is also a relatively slow approach with a relatively low temporal resolution. Thus, cRSI is likely to be the preferred RSI tool for experiments were spatial resolution or signal-to-noise ratio is the main challenge. Thus, the overall applicability of RSI in zebrafish research using complementary RSI methods will probably be advantageous, and specifically, RSI methods that can improve the temporal resolution. Important technologies to consider in this respect are light-sheet RSI and the non-linear RSI approaches using Stimulated Raman Scattering (SRS) or Coherent anti-Stokes Raman microscopy (CARS)[335,336]. Light-Sheet RSI has already been demonstrated in zebrafish embryos and represents an alternative for linear Raman that provides faster RSI in exchange for reduced signal-to-noise ration and axial resolution. This enables faster imaging of zebrafish embryos than what can be achieved by cRSI and could be a good alternative in time-sensitive experiments. However, light-sheet Raman cannot achieve video rate acquisition either and will still face the time-limiting step in all linear Raman approaches which is the low rate of Raman events in an unstimulated sample. Thus, while the Light Sheet Raman Micro-spectroscopy approach of Müller *et al.* does obtain higher imaging speed using a 577 nm laser on fixed zebrafish, questions remain over how this approach would perform in a live imaging scenario where using a 785 nm laser that would further lower the Raman signal.

To increase the temporal resolution of RSI, moving to non-linear methods is necessary. Video-rate RSI acquisition has been reported for both CARS and SRS and both have impressively been applied *in vivo*[337–340]. The main drawback of these approaches is that they cannot provide the same spectral coverage as linear Raman such as the cRSI approach presented in this thesis, and thus provide much less biomolecular information. They are therefore likely to find their main application in experimental scenarios where acquisition speed is more important than biomolecular composition – for instance, studies of the temporal dynamics of a specific biomolecule (e.g. DNA or a drug). However, non-linear RSI methodologies are likely to become

important tools in zebrafish imaging and will together with cRSI and LSR-RSI form a comprehensive toolset for studies of biomolecular complexity and dynamics in zebrafish embryos.

Given the unique opportunity, zebrafish offers for *in vivo* vertebrate imaging, further developments in the RSI toolbox, such as the cRSI methodology demonstrated in this work, could further improve the use of zebrafish as a prime model for studying complex biomolecular patterns and dynamics otherwise inaccessible. This could be to the benefit of many branches of biosciences.

Chapter 5: Conclusions and future perspectives

Improper wound healing is a significant challenge in modern health, care affecting millions of people worldwide[341]. However, the progress in this area has been slow so far leading to only minor improvements for the patients. A recurring problem for developing wound healing technologies is the complex and dynamic nature of the wound environment, and to devise strategies that will function properly within this environment. the complex and dynamic wound environment. Therefore, the development of successful new therapeutic strategies will depend on increased knowledge of the wound healing process both on the genetic, biomolecular, cellular, metabolic, and tissue levels. Zebrafish embryos have emerged as an important *in vivo* model for wound repair because it enables close visual examination of the wound healing process in a genetically tractable model that recapitulates many important features of mammalian wound repair[7]. Thus, zebrafish embryos represent an attractive opportunity to study the integrated biological processes underlying the wound repair process, both in the absence and in the presence of therapeutic agents or materials.

The work presented in this thesis has aimed at expanding the applicability of the zebrafish embryo model to gain insight into cellular and tissue changes associated with wound damage and repair. This work was divided into two sub-projects:

> 1) Development of the zebrafish embryo model for host-material interaction of ECM hydrogels.

> 2) Development of a confocal Raman spectroscopic imaging methodology for the biomolecular analysis of zebrafish embryos.

In the rest of this chapter, the key findings from these two sub-projects will be discussed, and potential future directions will be outlined.

5.1 Developing a zebrafish embryo model for studying host-material interactions with ECM hydrogels

5.1.1 Main findings in chapter 3

In chapter 3 a zebrafish model to study host-material interactions caused by the introduction of SIS-ECM hydrogels was developed and characterized. During this work, it was demonstrated that fluorescently labeled SIS-ECM hydrogels could be injected and traced over several days, while neutrophil and macrophage recruitment to and retention at the hydrogel injection site could be monitored. The cell recruitment profiles of SIS-ECM hydrogels were compared to that of two controls, PBS injections and the injection of the pro-inflammatory adjuvant FCA. These experiments identified differences in neutrophil and macrophage numbers at the injection site depending on the injected agent indicating that differences in the immune reaction caused by different agents could be traced. Moreover, analysis of the mRNA expression revealed significant differences in the expression of three inflammation markers genes (*tnf-α*, *il1-β,* and *mmp9*) between SIS-ECM hydrogel injected tissue as compared to mock and FCA injected controls. This further demonstrates that differences in the host reaction towards different injected materials can be studied in this model. Lastly, an approach to produce single somite wound ECM injections was devised, to facilitate future studies of the effect of ECM materials during wound repair in zebrafish embryos.

Taken together, these results demonstrate how the zebrafish embryo model can be used to approach host-material interactions and highlights some of the key advantages this model offers, such as the ability to live-monitor the host-material interaction over several days with minimally invasive imaging procedures. However, future investigations are needed to fully develop the zebrafish model for host-material interactions and to further elucidate the potential immunomodulatory properties of ECM hydrogels. Moreover, during the work with this thesis, several related investigations were published highlighting important insights that should be part of future investigations of ECM hydrogels in zebrafish[240,242,342]. This will be discussed in the following sub-chapters.

5.1.2 Analysis of wound healing

An important continuation of this project would be continuing the investigation of ECM hydrogels during the repair process following the stab wound injections. While this project so far has mostly investigated the immune reactions caused by the injection of the hydrogels, zebrafish can also be used for studying the repair and regeneration process following the initial inflammation, and it would be important to also assess the effect of the ECM hydrogel on the further repair process, and also to try to compare this to what can be observed with other materials with possible wound healing properties. While the phalloidin staining performed so far in this project can indicate the overall repair outcome, several other approaches should be considered for further work in this model.

Using a very similar stab wound approach to the one that was used in this thesis, recent work by other groups have identified how muscle regeneration in zebrafish depends on migration into the wound site by muscle satellite cells[180]. These cells further associate with severed muscle fibers to initiate and guide the regeneration through asymmetric cell division[180]. Hence, it would be very interesting to elucidate if the presence of ECM hydrogels at the wound site can support the migration of muscle satellite cells and the eventual regeneration of muscle fibers. For instance, a transgenic reporter line for the zebrafish satellite cell marker *pax7a* exists (i.e. (Pax7a:GFP) and Morris *et. al* developed a transgenic marker for collagen I (i.e. Tg(Krt19:col1a2-GFP)) to study the collagen deposition and remodeling following stab wounds[343,344]. Including this transgenic reporter line marker would be very informative and allow for live tracking of host ECM around the injected SIS-ECM gels and potentially elucidate the effects of injected ECM on reforming the host ECM after wounding.

A second important factor in the wound healing process is the role of macrophages in regulating angiogenesis during wound repair. In the experiments presented in this thesis, it has been shown that the ECM material attracts and sustains a high number of macrophages after injection[242]. Using an endothelial reporter line such as Tg(fli:GFP)[345] to investigate

whether the ECM gels and its associated macrophages can also support angiogenesis would be another key assessment of the effect ECM hydrogels on the regeneration process.

5.1.3 Macrophage polarization

While the limited gene expression analysis conducted in this investigation is indicative of different immune reactions between the three groups tested (i.e. PBS, FCA, and SIS-ECM hydrogels) the data presented are not conclusive regarding the immunomodulatory properties of the SIS-ECM hydrogels. E.g., the link between ECM immunomodulation and macrophage phenotypes remains to be investigated. Thus, to further probe the macrophage response to the injected ECM gels would constitute an important future line of investigation. Notably, recent evidence suggests that ECM materials induce their own slightly altered macrophage phenotype[231,237]. Studying the effect of, SIS-ECM associated macrophage phenotypes in more detail could give information on whether these observations also translate to zebrafish and start to link the macrophage response to the wound repair responses, as discussed above (4.1.2). Recently, a transgenic zebrafish reporter cell line for TNFα Tg(tnfa:GFP); was introduced, and has been used to assess macrophage polarization. Implementing this cell line could provide a suitable readout for the activation state of the macrophages[153]. However, also RNAseq on flow cytometry sorted (FACS) zebrafish macrophage populations expressing pro- and anti-inflammatory macrophages has been performed, and a similar approach could give valuable input into the ECM-hydrogel associated macrophages[191,346].

5.1.4 Therapeutic agents and complementary models

A further future aim of this project would be to incorporate therapeutic agents and possibly more biomaterials. A few recent studies have taken this approach and notably, Witherel *et al.* demonstrated reduced inflammation following microparticle injection into zebrafish embryos after adsorption of IL-10 to the micro-particles and Gurevich *et al.* observed reduction of foreign body response in adult zebrafish when the fish were treated with hydrocortisone[241,242]. In future investigations it would therefore be very interesting to also look at the host reaction and wound

repair when combining the ECM hydrogels with other therapeutic agents. Moreover, future work could also make use of the recently developed adult zebrafish model for biomaterials and correlate any potential fining in the embryo with experiments in adult fish.

In summary this project has established a zebrafish embryo model to study host-material interactions using SIS-ECM hydrogels. This model constitutes a solid platform for future investigation of the effects of ECM hydrogels on the surrounding tissue and especially on wound repair, with several potential future avenues to investigate.

5.2 Developing confocal Raman spectroscopic imaging for zebrafish embryo research

5.2.1 Main findings in chapter 4

In chapter 4 a cRSI methodology for zebrafish embryos was developed and demonstrated for several applications. Notably, cRSI was used for 3D and high-resolution, label-free imaging of zebrafish embryos, and it was demonstrated that this method provides high-quality Raman spectra from most of the zebrafish tissues. This could be used to resolve fine biomolecular details such as muscle fiber stratification or cell nuclei in intact embryos. Moreover, cRSI with multivariate analysis was used to analyze biomolecular differences between wildtype and mutant *M. marinum* during infection, demonstrating how cRSI can be used to interrogate metabolic differences associated with different bacteria. This biomolecular profiling constitutes a new approach for analyzing pathogens in zebrafish disease modeling. Lastly, a method for conducting cRSI in live zebrafish embryos was devised and performed to track the development of wound response in a living zebrafish embryo. Subsequent multivariate analysis demonstrated that the *in vivo* cRSI could detect differences between unwounded and wounded zebrafish tissue and identify important biomolecular differences between the two.

Hence, cRSI constitutes a promising new tool for zebrafish research. However, there are several future opportunities for improving and expanding the applicability of cRSI in zebrafish that will be discussed in the following part of the thesis.

5.2.2 Disease modeling using cRSI

The key advantage of the cRSI approach presented here is that it enables multivariate analysis of biomolecular differences that can be used for profiling of for instance metabolic niches. This ability could be especially impactful in zebrafish disease models e.g. to detect biomolecular differences observed in bacterial infection models, cancer models, or associated with developmental diseases. This proof-of-concept was demonstrated in chapter 4.2.2, comparing wildtype and mutant bacteria in an *M. marinum* model. Future work, including drug treatment of bacteria, as well as using other disease models available for zebrafish should further explore the potential of this strategy. Thus, more than 240 different bacterial infection models exist for zebrafish embryos[197]. Also, several zebrafish cancer models are emerging, and given the importance of the tissue microenvironment and metabolism in cancer development expanding the use of cRSI to such models would be a very interesting future use of this technology[255,256].

Another important future development would be to implement live imaging in the disease models to perform biomolecular profiling in live zebrafish specimens. This would for instance allow for monitoring of biomolecular changes occurring live, during drug treatments.

5.2.3 Correlative cRSI

A key future development for zebrafish cRSI methodology would be the development of correlative imaging approaches, especially including fluorescent microscopy. Work in this direction was reported by Bennet et al. although their methodology was restricted to collecting single point Raman spectra[294]. However, building on the work presented in this thesis and the approach devised by Bennet *et al.* could potentially enable correlative fluorescent cRSI microscopy. As discussed throughout this thesis the zebrafish community has developed many transgenic reporter lines that facilitate tracking and identification of for instance cell populations with high specificity. By developing correlative fluorescent cRSI techniques, Raman spectroscopic analysis could be connected to this library of reporter lines. This would improve the specificity of the Raman analysis and facilitate more targeted cRSI approaches.

One of the recurring debates in the wound healing field is the phenotype of the wound associated macrophages, and much is yet to be learned about their possible effect on the healing process. Macrophages have often been profiled using a few selected markers, but this may give an incomplete view of the phenotypic differences. One interesting future application using correlative fluorescent and cRSI microscopy, which is especially relevant to this thesis, would be to use cRSI to profile macrophage during wound healing. As discussed above, transgenic fluorescent reporter lines exist both for macrophages, as well as for TNF-α expressing macrophages[153]. cRSI could potentially elucidate the macrophage phenotypes by obtaining biomolecular profiles during wound healing in zebrafish and provide a more robust description of the phenotypic variation observed during the wound healing process.

5.3 Overall concluding remarks

Zebrafish embryos constitute an important model for many aspects of biomedical research, including infectious biology, cancer, and wound healing. One of the key advantages of zebrafish embryos is the ability to visualize and inspect intricate biological processes in high detail in an intact organism. This thesis was divided into two parts; the first developing the use of zebrafish embryos to investigate host-material interactions and the second developing a cRSI methodology for the biomolecular analysis of zebrafish embryos.

The demonstration that the host-material interactions of ECM hydrogels can be explored inside live zebrafish embryos represents an advancement in the study of these materials. Thus, this model provides a tool to study the effect of these materials in great detail in the presence of a developed innate immune system, and further work in this model can bring new insight into the immune interactions of ECM hydrogels and potentially improve their therapeutic effect in wound healing applications. The implementation and demonstration of cRSI for biomolecular analysis of zebrafish embryos constitutes a new imaging modality for zebrafish embryos that enables simultaneous inspection of a multitude of biomolecules. Thus, cRSI can be used together with other methods to obtain integrated knowledge of complex biological processes

in zebrafish models. This includes wound healing models that have been the focus of this thesis, but it also extends to models e.g. for infectious diseases and cancer. Taken together, the work in this thesis has contributed to the use of zebrafish embryos for use in biomedical sciences and wound healing research.

Bibliography

1. Sen, C. K. *et al.* Human Skin Wounds: A Major and Snowballing Threat to Public Health and the Economy. *Wound repair and regeneration : official publication of the Wound Healing Society [and] the European Tissue Repair Society* **17**, 763 (2009).

2. Armstrong, D. G., Wrobel, J. & Robbins, J. M. Guest Editorial: are diabetes-related wounds and amputations worse than cancer? *International Wound Journal* **4**, 286–287 (2007).

3. Eming, S. A., Martin, P. & Tomic-Canic, M. Wound repair and regeneration: Mechanisms, signaling, and translation. *Science Translational Medicine* **6**, (2014).

4. Avorn, J. The $2.6 Billion Pill — Methodologic and Policy Considerations. *New England Journal of Medicine* **372**, 1877–1879 (2015).

5. Meeker, N. D. & Trede, N. S. Immunology and zebrafish: Spawning new models of human disease. *Developmental and Comparative Immunology* **32**, 745–757 (2008).

6. Traver, D. *et al.* The Zebrafish as a Model Organism to Study Development of the Immune System. *Advances in Immunology* **81**, 253–330 (2003).

7. Keightley, M. C., Wang, C. H., Pazhakh, V. & Lieschke, G. J. Delineating the roles of neutrophils and macrophages in zebrafish regeneration models. *International Journal of Biochemistry and Cell Biology* **56**, 92–106 (2014).

8. Gurtner, G. C., Werner, S., Barrandon, Y. & Longaker, M. T. Wound repair and regeneration. *Nature* **453**, 314–321 (2008).

9. Krafts, K. P. Tissue repair: The hidden drama. *Organogenesis* **6**, 225–233 (2010).

10. Murawala, P., Tanaka, E. M. & Currie, J. D. Regeneration: The ultimate example of wound healing. *Seminars in Cell & Developmental Biology* **23**, 954–962 (2012).

11. Harty, M., Neff, A. W., King, M. W. & Mescher, A. L. Regeneration or scarring: An immunologic perspective. *Developmental Dynamics* **226**, 268–279 (2003).

12. Ud-Din, S., Volk, S. W. & Bayat, A. Regenerative healing, scar-free healing and scar formation across the species: current concepts and future perspectives. *Experimental*

Dermatology **23**, 615–619 (2014).

13. Guo, S. & DiPietro, L. A. Critical review in oral biology & medicine: Factors affecting wound healing. *Journal of Dental Research* **89**, 219–229 (2010).

14. Martin, P. Wound healing - Aiming for perfect skin regeneration. *Science* **276**, 75–81 (1997).

15. Weisel, J. W. Fibrinogen and fibrin. *Advances in Protein Chemistry* **70**, 247–299 (2005).

16. Metcalfe, A. D., Willis, H., Beare, A. & Ferguson, M. W. J. Characterizing regeneration in the mammalian external ear. *Journal of Anatomy* **209**, 439–446 (2006).

17. Wynn, T. A. & Vannella, K. M. Macrophages in Tissue Repair, Regeneration, and Fibrosis. *Immunity* **44**, 450–462 (2016).

18. Brown, B. N., Ratner, B. D., Goodman, S. B., Amar, S. & Badylak, S. F. Macrophage polarization: An opportunity for improved outcomes in biomaterials and regenerative medicine. *Biomaterials* **33**, 3792–3802 (2012).

19. Thomas, C. J. & Schroder, K. Pattern recognition receptor function in neutrophils. *Trends in immunology* **34**, 317–28 (2013).

20. Chen, G. Y. & Nuñez, G. Sterile inflammation: sensing and reacting to damage. *Nature reviews Immunology* **10**, 826–837 (2010).

21. Pittman, K. & Kubes, P. Damage-associated molecular patterns control neutrophil recruitment. *Journal of Innate Immunity* **5**, 315–323 (2013).

22. Rock, K. L., Latz, E., Ontiveros, F. & Kono, H. The sterile inflammatory response. *Annual Review of Immunology* **28**, 321–342 (2010).

23. Forrest, R. D. Development of wound therapy from the Dark Ages to the present. *Journal of the Royal Society of Medicine* **75**, 268–73 (1982).

24. Shah, J. B. The history of wound care. *Journal of the American College of Certified Wound Specialists* **3**, 65–66 (2011).

25. Bhattacharya, S. Wound healing through the ages. *Indian Journal of Plastic Surgery* **45**, 177–179 (2012).

26. Atala, A., Irvine, D. J., Moses, M. & Shaunak, S. Wound healing versus regeneration: Role of the tissue environment in regenerative medicine. *MRS Bulletin* **35**, 597–606 (2010).

27. Martin, P. & Nunan, R. Cellular and molecular mechanisms of repair in acute and chronic wound healing. *The British journal of dermatology* **173**, 370–8 (2015).

28. Martin, P. & Leibovich, S. J. Inflammatory cells during wound repair: The good, the bad and the ugly. *Trends in Cell Biology* **15**, 599–607 (2005).

29. Darby, I. A., Laverdet, B., Bonté, F. & Desmoulière, A. Fibroblasts and myofibroblasts in wound healing. *Clinical, Cosmetic and Investigational Dermatology* **7**, 301–311 (2014).

30. Werner, S. & Grose, R. Regulation of wound healing by growth factors and cytokines. *Physiological Reviews* **83**, 835–870 (2003).

31. Galiano, R. D. *et al.* Topical vascular endothelial growth factor accelerates diabetic wound healing through increased angiogenesis and by mobilizing and recruiting bone marrow-derived cells. *American Journal of Pathology* **164**, 1935–1947 (2004).

32. Rousselle, P., Braye, F. & Dayan, G. Re-epithelialization of adult skin wounds: Cellular mechanisms and therapeutic strategies. *Advanced Drug Delivery Reviews* **146**, 344–365 (2019).

33. Pastar, I. *et al.* Epithelialization in Wound Healing: A Comprehensive Review. *Advances in wound care* **3**, 445–464 (2014).

34. Midwood, K. S., Williams, L. V. & Schwarzbauer, J. E. Tissue repair and the dynamics of the extracellular matrix. *The International Journal of Biochemistry & Cell Biology* **36**, 1031–1037 (2004).

35. Levy, V., Lindon, C., Harfe, B. D. & Morgan, B. A. Distinct stem cell populations regenerate the follicle and interfollicular epidermis. *Developmental Cell* **9**, 855–861 (2005).

36. Barisic-Dujmovic, T., Boban, I. & Clark, S. H. Fibroblasts/myofibroblasts that participate in cutaneous wound healing are not derived from circulating progenitor cells. *Journal of Cellular Physiology* **222**, 703–712 (2010).

37.   Opalenik, S. R. & Davidson, J. M. Fibroblast differentiation of bone marrow-derived cells during wound repair. *The FASEB Journal* **19**, 1561–1563 (2005).

38.   Pakshir, P. *et al.* The myofibroblast at a glance. *Journal of cell science* **133**, (2020).

39.   Wynn, T. A. Fibrotic disease and the TH1/TH2 paradigm. *Nature Reviews Immunology* **4**, 583–594 (2004).

40.   Wynn, T. A. & Ramalingam, T. R. Mechanisms of fibrosis: therapeutic translation for fibrotic disease. *Nat Med* **18**, 1028–1040 (2012).

41.   Wynn, T. Cellular and molecular mechanisms of fibrosis. *The Journal of pathology* **214**, 199 (2008).

42.   Gabbiani, G. The myofibroblast in wound healing and fibrocontractive diseases. *Journal of Pathology* **200**, 500–503 (2003).

43.   Profyris, C., Tziotzios, C. & Do Vale, I. Cutaneous scarring: Pathophysiology, molecular mechanisms, and scar reduction therapeutics: Part I. the molecular basis of scar formation. *Journal of the American Academy of Dermatology* **66**, 1–10 (2012).

44.   Xue, M. & Jackson, C. J. Extracellular Matrix Reorganization During Wound Healing and Its Impact on Abnormal Scarring. *Advances in Wound Care* **4**, 119–136 (2015).

45.   Gonzalez, A. C. D. O., Andrade, Z. D. A., Costa, T. F. & Medrado, A. R. A. P. Wound healing - A literature review. *Anais Brasileiros de Dermatologia* **91**, 614–620 (2016).

46.   Gill, S. E. & Parks, W. C. Metalloproteinases and their inhibitors: Regulators of wound healing. *International Journal of Biochemistry and Cell Biology* **40**, 1334–1347 (2008).

47.   Murphy, G. & Nagase, H. Progress in matrix metalloproteinase research. *Molecular Aspects of Medicine* **29**, 290–308 (2009).

48.   Godwin, J. & Kuraitis, D. Extracellular matrix considerations for scar-free repair and regeneration: Insights from regenerative diversity among vertebrates. *The International Journal of Biochemistry & Cell Biology* **56**, 47–55 (2014).

49.   Seifert, A. W., Monaghan, J. R., Voss, S. R. & Maden, M. Skin Regeneration in Adult Axolotls: A Blueprint for Scar-Free Healing in Vertebrates. *PLoS ONE* **7**, e32875 (2012).

50. Lévesque, M., Villiard, É. & Roy, S. Skin wound healing in axolotls: a scarless process. *Journal of Experimental Zoology Part B: Molecular and Developmental Evolution* **314B**, 684–697 (2010).

51. Dingal, P. C. D. P. *et al.* Fractal heterogeneity in minimal matrix models of scars modulates stiff-niche stem-cell responses via nuclear exit of a mechanorepressor. *Nature Materials* **14**, 951–960 (2015).

52. Frykberg, R. G. & Banks, J. Challenges in the Treatment of Chronic Wounds. *Advances in Wound Care* **4**, 560 (2015).

53. Zhao, R., Liang, H., Clarke, E., Jackson, C. & Xue, M. Inflammation in chronic wounds. *International Journal of Molecular Sciences* **17**, (2016).

54. McCarty, S. M. & Percival, S. L. Proteases and Delayed Wound Healing. *Advances in Wound Care* **2**, 438–447 (2013).

55. Krzyszczyk, P., Schloss, R., Palmer, A. & Berthiaume, F. The Role of Macrophages in Acute and Chronic Wound Healing and Interventions to Promote Pro-wound Healing Phenotypes. *Frontiers in physiology* **9**, 419 (2018).

56. Schreml, S. *et al.* Oxygen in acute and chronic wound healing. *British Journal of Dermatology* **163**, 257–268 (2010).

57. Schultz, G. S. *et al.* Wound bed preparation and a brief history of TIME. *International Wound Journal* **1**, 19–32 (2004).

58. Keane, T. J., Horejs, C. M. & Stevens, M. M. Scarring vs. functional healing: Matrix-based strategies to regulate tissue repair. *Advanced Drug Delivery Reviews* **129**, 407–419 (2018).

59. Wynn, T. A. & Ramalingam, T. R. Mechanisms of fibrosis: Therapeutic translation for fibrotic disease. *Nature Medicine* **18**, 1028–1040 (2012).

60. White, E. S. & Mantovani, A. R. Inflammation, wound repair, and fibrosis: Reassessing the spectrum of tissue injury and resolution. *Journal of Pathology* **229**, 141–144 (2013).

61. Stramer, B. M., Mori, R. & Martin, P. The inflammation-fibrosis link? A Jekyll and Hyde role for blood cells during wound repair. *Journal of Investigative Dermatology* **127**, 1009–1017 (2007).

62. Rhett, J. M. *et al.* Novel therapies for scar reduction and regenerative healing of skin wounds. *Trends in Biotechnology* **26**, 173–180 (2008).

63. Barrientos, S., Stojadinovic, O., Golinko, M. S., Brem, H. & Tomic-Canic, M. Growth factors and cytokines in wound healing. *Wound Repair and Regeneration* **16**, 585–601 (2008).

64. Haensel, D. & Dai, X. Epithelial-to-mesenchymal transition in cutaneous wound healing: Where we are and where we are heading. *Developmental Dynamics* **247**, 473–480 (2018).

65. Wipff, P. J., Rifkin, D. B., Meister, J. J. & Hinz, B. Myofibroblast contraction activates latent TGF-β1 from the extracellular matrix. *Journal of Cell Biology* **179**, 1311–1323 (2007).

66. Darby, I. A. & Hewitson, T. D. Fibroblast Differentiation in Wound Healing and Fibrosis. *International Review of Cytology* **257**, 143–179 (2007).

67. Horejs, C. M. *et al.* Biologically-active laminin-111 fragment that modulates the epithelial-to-mesenchymal transition in embryonic stem cells. *Proceedings of the National Academy of Sciences of the United States of America* **111**, 5908–5913 (2014).

68. Horejs, C. M. *et al.* Preventing tissue fibrosis by local biomaterials interfacing of specific cryptic extracellular matrix information. *Nature Communications* **8**, 1–15 (2017).

69. Tanaka, E. & Reddien, P. W. The cellular basis for animal regeneration. *Developmental cell* **21**, 172 (2011).

70. Larson, B. J., Longaker, M. T. & Lorenz, H. P. Scarless fetal wound healing: A basic science review. *Plastic and Reconstructive Surgery* **126**, 1172–1180 (2010).

71. Ilancheran, S., Moodley, Y. & Manuelpillai, U. Human Fetal Membranes: A Source of Stem Cells for Tissue Regeneration and Repair? *Placenta* **30**, 2–10 (2009).

72. Naranjo, J. D. *et al.* Regenerative Medicine: lessons from Mother Nature. *Regenerative Medicine* **11**, 767 (2016).

73. Sánchez Alvarado, A. Planarian regeneration: Its end is its beginning. *Cell* **124**, 241–245 (2006).

74. Sánchez Alvarado, A. & Yamanaka, S. Rethinking differentiation: Stem cells, regeneration, and plasticity. *Cell* **157**, 110–119 (2014).

75. Morgan, T. H. *Regeneration*. (New York: The Macmillian Company, 1901).

76. Seifert, A. W. & Muneoka, K. The blastema and epimorphic regeneration in mammals. *Developmental Biology* **433**, 190–199 (2018).

77. Londono, R., Sun, A. X., Tuan, R. S. & Lozito, T. P. Tissue Repair and Epimorphic Regeneration: an Overview. *Current Pathobiology Reports* **6**, 61–69 (2018).

78. Thornton, C. S. & Steen, T. P. Eccentric blastema formation in aneurogenic limbs of Ambystoma larvae following epidermal cap deviation. *Developmental Biology* **5**, 328–343 (1962).

79. Jopling, C. *et al.* Zebrafish heart regeneration occurs by cardiomyocyte dedifferentiation and proliferation. *Nature* **464**, 606–609 (2010).

80. Selman, K. & Kafatos, F. C. Transdifferentiation in the labial gland of silk moths: is DNA required for cellular metamorphosis? *Cell Differentiation* **3**, 81–94 (1974).

81. Eguchi, G. Instability in Cell Commitment of Vertebrate Pigmented Epithelial Cells and their Transdifferentiation into Lens Cells. *Current Topics in Developmental Biology* **20**, 21–37 (1986).

82. Sánchez Alvarado, A. S. Y. Rethinking differentiation: Stem cells, regeneration, and plasticity. *Cell* **34**, 474–476 (2015).

83. Simkin, J. *et al.* The mammalian blastema: regeneration at our fingertips. *Regeneration* **2**, 93–105 (2015).

84. Muneoka, K., Allan, C. H., Yang, X., Lee, J. & Han, M. Mammalian regeneration and regenerative medicine. *Birth Defects Research Part C - Embryo Today: Reviews* **84**, 265–280 (2008).

85. Gawriluk, T. R. *et al.* Comparative analysis of ear-hole closure identifies epimorphic regeneration as a discrete trait in mammals. *Nature Communications* **7**, (2016).

86. Beumer, J. & Clevers, H. Regulation and plasticity of intestinal stem cells during homeostasis and regeneration. *Development (Cambridge)* **143**, 3639–3649 (2016).

87.   Brown, B. N. *et al.* Macrophage phenotype as a predictor of constructive remodeling following the implantation of biologically derived surgical mesh materials. *Acta Biomaterialia* **8**, 978–987 (2012).

88.   Redd, M. J., Cooper, L., Wood, W., Stramer, B. & Martin, P. Wound healing and inflammation: Embryos reveal the way to perfect repair. in *Philosophical Transactions of the Royal Society B: Biological Sciences* **359**, 777–784 (2004).

89.   Mantovani, A. *et al.* The chemokine system in diverse forms of macrophage activation and polarization. *Trends in Immunology* **25**, 677–686 (2004).

90.   Chazaud, B. Macrophages: Supportive cells for tissue repair and regeneration. *Immunobiology* **219**, 172–178 (2014).

91.   Nodder, S. & Martin, P. Wound healing in embryos: A review. *Anatomy and Embryology* **195**, 215–228 (1997).

92.   Martin, P. & Parkhurst, S. M. Parallels between tissue repair and embryo morphogenesis. *Development* **131**, 3021–3034 (2004).

93.   Lo, D. D., Zimmermann, A. S., Nauta, A., Longaker, M. T. & Lorenz, H. P. Scarless fetal skin wound healing update. *Birth Defects Research Part C: Embryo Today: Reviews* **96**, 237–247 (2012).

94.   Martin, P. *et al.* Wound healing in the PU.1 null mouse--tissue repair is not dependent on inflammatory cells. *Current biology : CB* **13**, 1122–8 (2003).

95.   Hopkinson-Woolley, J., Hughes, D., Gordon, S. & Martin, P. Macrophage recruitment during limb development and wound healing in the embryonic and foetal mouse. *Journal of Cell Science* **107**, 1159–1167 (1994).

96.   Savill, J. S. *et al.* Macrophage phagocytosis of aging neutrophils in inflammation. Programmed cell death in the neutrophil leads to its recognition by macrophages. *Journal of Clinical Investigation* **83**, 865–875 (1989).

97.   Mathias, J. R. *et al.* Resolution of inflammation by retrograde chemotaxis of neutrophils in transgenic zebrafish flammation is a critical process during normal im-. *Journal of leukocyte biology* **80**, 1281–1288 (2006).

98.   Phillipson, M. & Kubes, P. The Healing Power of Neutrophils. *Trends in Immunology* **40**,

635–647 (2019).

99. Kolaczkowska, E. & Kubes, P. Neutrophil recruitment and function in health and inflammation. *Nat Rev Immunol* **13**, 159–175 (2013).

100. Brinkmann, V. *et al.* Neutrophil Extracellular Traps Kill Bacteria. *Science* **303**, 1532–1535 (2004).

101. Wang, J. Neutrophils in tissue injury and repair. *Cell and Tissue Research* **371**, 531–539 (2018).

102. Niethammer, P., Grabher, C., Look, A. T. & Mitchison, T. J. A tissue-scale gradient of hydrogen peroxide mediates rapid wound detection in zebrafish. *Nature* **459**, 996–999 (2009).

103. Pase, L. *et al.* Neutrophil-Delivered Myeloperoxidase Dampens the Hydrogen Peroxide Burst after Tissue Wounding in Zebrafish. *Current Biology* **22**, 1818–1824 (2012).

104. Mosser, D. M. & Edwards, J. P. Exploring the full spectrum of macrophage activation. *Nat Rev Immunol* **8**, 958–969 (2008).

105. Chazaud, B. *et al.* Dual and beneficial roles of macrophages during skeletal muscle regeneration. *Exercise and Sport Sciences Reviews* **37**, 18–22 (2009).

106. Petrie, T. A., Strand, N. S., Tsung-Yang, C., Rabinowitz, J. S. & Moon, R. T. Macrophages modulate adult zebrafish tail fin regeneration. *Development (Cambridge, England)* **141**, 2581–2591 (2014).

107. Godwin, J. W., Pinto, A. R. & Rosenthal, N. A. Macrophages are required for adult salamander limb regeneration. *Proceedings of the National Academy of Sciences of the United States of America* **110**, 9415–9420 (2013).

108. Arnold, L. *et al.* Inflammatory monocytes recruited after skeletal muscle injury switch into antiinflammatory macrophages to support myogenesis. *Journal of Experimental Medicine* **204**, 1057–1069 (2007).

109. Duffield, J. S. *et al.* Selective depletion of macrophages reveals distinct, opposing roles during liver injury and repair. *Journal of Clinical Investigation* **115**, 56–65 (2005).

110. Gurevich, D. B. *et al.* Live imaging of wound angiogenesis reveals macrophage

orchestrated vessel sprouting and regression. *The EMBO Journal* **37**, (2018).

111. Aurora, A. B. *et al.* Macrophages are required for neonatal heart regeneration. *Journal of Clinical Investigation* **124**, 1382–1392 (2014).

112. Mills, C. D., Kincaid, K., Alt, J. M., Heilman, M. J. & Hill, A. M. M-1/M-2 Macrophages and the Th1/Th2 Paradigm. *The Journal of Immunology* **164**, 6166–6173 (2000).

113. Orecchioni, M., Ghosheh, Y., Pramod, A. B. & Ley, K. Macrophage Polarization: Different Gene Signatures in M1(LPS+) vs. Classically and M2(LPS–) vs. Alternatively Activated Macrophages. *Frontiers in Immunology* **10**, 1084 (2019).

114. Rőszer, T. *et al.* Understanding the Mysterious M2 Macrophage through Activation Markers and Effector Mechanisms. *Mediators of Inflammation* **2015**, 1–16 (2015).

115. Ferrante, C. J. & Leibovich, S. J. Regulation of Macrophage Polarization and Wound Healing. *Advances in Wound Care* **1**, 10–16 (2012).

116. Martinez, F. O. & Gordon, S. The M1 and M2 paradigm of macrophage activation: time for reassessment. *F1000Prime Reports* **6**, 13 (2014).

117. Mosser, D. M. & Edwards, J. P. Exploring the full spectrum of macrophage activation. *Nature Publishing Group* **8**, 958–969 (2008).

118. Stefater, J. A., Ren, S., Lang, R. A. & Duffield, J. S. Metchnikoff's policemen: Macrophages in development, homeostasis and regeneration. *Trends in Molecular Medicine* **17**, 743–752 (2011).

119. Smith, S. J., Kotecha, S., Towers, N. & Mohun, T. J. Targeted cell-ablation in Xenopus embryos using the conditional, toxic viral protein M2(H37A). *Developmental Dynamics* **236**, 2159–2171 (2007).

120. Brancato, S. K. & Albina, J. E. Wound Macrophages as Key Regulators of Repair: Origin, Phenotype, and Function. *The American Journal of Pathology* **178**, 19–25 (2011).

121. Ud-Din, S. & Bayat, A. Non-animal models of wound healing in cutaneous repair: In silico, in vitro, ex vivo, and in vivo models of wounds and scars in human skin. *Wound Repair and Regeneration* **25**, 164–176 (2017).

122. Menke, N. B. *et al.* An in silico approach to the analysis of acute wound healing. *Wound Repair and Regeneration* **18**, 105–113 (2010).

123. Liang, C.-C., Park, A. Y. & Guan, J.-L. In vitro scratch assay: a convenient and inexpensive method for analysis of cell migration in vitro. *Nature Protocols* **2**, 329–333 (2007).

124. Wilhelm, K. P., Wilhelm, D. & Bielfeldt, S. Models of wound healing: an emphasis on clinical studies. *Skin Research and Technology* **23**, 3–12 (2017).

125. Parnell, L. K. S. & Volk, S. W. The Evolution of Animal Models in Wound Healing Research: 1993-2017. *Advances in wound care* **8**, 692–702 (2019).

126. Razzell, W., Wood, W. & Martin, P. Swatting flies: modelling wound healing and inflammation in Drosophila. *Disease models & mechanisms* **4**, 569–74 (2011).

127. Montagna, W. & Yun, J. S. The Skin of the Domestic Pig. *Journal of Investigative Dermatology* **43**, 11–21 (1964).

128. Grada, A., Mervis, J. & Falanga, V. Research Techniques Made Simple: Animal Models of Wound Healing. *Journal of Investigative Dermatology* **138**, 2095-2105.e1 (2018).

129. Fang, R. C. & Mustoe, T. A. Animal models of wound healing: uility in transgenic mice. *Journal of Biomaterials Science, Polymer Edition* **19**, 989–1005 (2008).

130. Elliot, S., Wikramanayake, T. C., Jozic, I. & Tomic-Canic, M. A Modeling Conundrum: Murine Models for Cutaneous Wound Healing. *Journal of Investigative Dermatology* **138**, 736–740 (2018).

131. Scimone, M. L., Kravarik, K. M., Lapan, S. W. & Reddien, P. W. Neoblast specialization in regeneration of the planarian schmidtea mediterranea. *Stem Cell Reports* **3**, 339–352 (2014).

132. Karin, M. & Clevers, H. Reparative inflammation takes charge of tissue regeneration. *Nature* **529**, 307–315 (2016).

133. Evans, C. J., Hartenstein, V. & Banerjee, U. Thicker Than Blood: Conserved Mechanisms in Drosophila and Vertebrate Hematopoiesis. *Developmental Cell* **5**, 673–690 (2003).

134. Goessling, W. & North, T. E. Repairing quite swimmingly: advances in regenerative medicine using zebrafish. *Disease Models & Mechanisms* **7**, 769–776 (2014).

135. Gemberling, M., Bailey, T. J., Hyde, D. R. & Poss, K. D. The zebrafish as a model for complex tissue regeneration. *Trends in Genetics* **29**, 611–620 (2013).

136. Seifert, A., Monaghan, J., Voss, R. & Maden, M. Skin regeneration in adult axolotls: A blueprint for scar-free healing in vertebrates. *PLoS ONE* **7**, e32875 (2012).

137. Poss, K. D., Wilson, L. G. & Keating, M. T. Heart regeneration in zebrafish. *Science* **298**, 2188–2190 (2002).

138. O'Reilly-Pol, T. & Johnson, S. L. Melanocyte regeneration reveals mechanisms of adult stem cell regulation. *Seminars in Cell and Developmental Biology* **20**, 117–124 (2009).

139. Goldshmit, Y. *et al.* Fgf-dependent glial cell bridges facilitate spinal cord regeneration in Zebrafish. *Journal of Neuroscience* **32**, 7477–7492 (2012).

140. King, M. W., Neff, A. W. & Mescher, A. L. The Developing Xenopus Limb as a Model for Studies on the Balance between Inflammation and Regeneration. *Anatomical Record* **295**, 1552–1561 (2012).

141. Buchon, N., Silverman, N. & Cherry, S. Immunity in Drosophila melanogaster — from microbial recognition to whole-organism physiology. *Nature Reviews Immunology* **14**, 796–810 (2014).

142. Simkin, J. *et al.* Macrophages are required to coordinate mouse digit tip regeneration. *Development (Cambridge)* **144**, 3907–3916 (2017).

143. Streisinger, G., Walker, C., Dower, N., Knauber, D. & Singer, F. Production of clones of homozygous diploid zebra fish (Brachydanio rerio). *Nature* **291**, 293–296 (1981).

144. Lieschke, G. J. & Currie, P. D. Animal models of human disease: Zebrafish swim into view. *Nature Reviews Genetics* **8**, 353–367 (2007).

145. Herbomel, P., Thisse, B. & Thisse, C. Ontogeny and behaviour of early macrophages in the zebrafish embryo. *Development* **126**, 3735–3745 (1999).

146. Davis, J. M. *et al.* Real-Time Visualization of Mycobacterium -Macrophage Interactions Leading to Initiation of Granuloma Formation in Zebrafish Embryos. **17**, 693–702 (2002).

147. Brittijn, S. A. *et al.* Zebrafish development and regeneration: New tools for biomedical research. *International Journal of Developmental Biology* **53**, 835–850 (2009).

148. Kimmel, C. B., Ballard, W. W., Kimmel, S. R., Ullmann, B. & Schilling, T. F. Stages of embryonic development of the zebrafish. *Developmental Dynamics* **203**, 253–310 (1995).

149. Howe, K. *et al.* The zebrafish reference genome sequence and its relationship to the human genome. *Nature* **496**, 498–503 (2013).

150. Cade, L. *et al.* Highly efficient generation of heritable zebrafish gene mutations using homo- and heterodimeric TALENs. *Nucleic acids research* **40**, 8001–10 (2012).

151. Irion, U., Krauss, J. & Nüsslein-Volhard, C. Precise and efficient genome editing in zebrafish using the CRISPR/Cas9 system. *Development (Cambridge, England)* **141**, 4827–30 (2014).

152. Moroz-Omori, E. V. *et al.* Photoswitchable gRNAs for Spatiotemporally Controlled CRISPR-Cas-Based Genomic Regulation. *ACS Central Science* **6**, 695–703 (2020).

153. Nguyen-Chi, M. *et al.* Identification of polarized macrophage subsets in zebrafish. *eLife* **4**, 1–14 (2015).

154. Nguyen-Chi, M. *et al.* Transient infection of the zebrafish notochord with E. coli induces chronic inflammation. *DMM Disease Models and Mechanisms* **7**, 871–882 (2014).

155. Davis, J. M. & Ramakrishnan, L. The Role of the Granuloma in Expansion and Dissemination of Early Tuberculous Infection. *Cell* **136**, 37–49 (2009).

156. Clay, H. *et al.* Dichotomous Role of the Macrophage in Early Mycobacterium marinum Infection of the Zebrafish. *Cell Host and Microbe* **2**, 29–39 (2007).

157. Press, C. M. & Evensen, Ø. The morphology of the immune system in teleost fishes. *Fish & Shellfish Immunology* **9**, 309–318 (1999).

158. Ellett, F. & Lieschke, G. J. Zebrafish as a model for vertebrate hematopoiesis. *Current Opinion in Pharmacology* **10**, 563–570 (2010).

159. Herbomel, P., Thisse, B. & Thisse, C. Ontogeny and behaviour of early macrophages in the zebrafish embryo. **3745**, 3735–3745 (1999).

160. Willett, C. E., Cortes, A., Zuasti, A. & Zapata, A. G. Early hematopoiesis and developing lymphoid organs in the zebrafish. *Developmental Dynamics* **214**, 323–336 (1999).

161. Murayama, E. *et al.* Tracing Hematopoietic Precursor Migration to Successive Hematopoietic Organs during Zebrafish Development. *Immunity* **25**, 963–975 (2006).

162. Bertrand, J. Y. *et al.* Definitive hematopoiesis initiates through a committed erythromyeloid progenitor in the zebrafish embryo. *Development* **134**, 4147–4156 (2007).

163. Le Guyader, D. *et al.* Origins and unconventional behavior of neutrophils in developing zebrafish. *Blood* **111**, 132–141 (2008).

164. Langenau, D. M. *et al.* In vivo tracking of T cell development , ablation , and engraftment in transgenic zebrafish. **101**, 7369–7374 (2004).

165. Le Guyader, D. *et al.* Origins and unconventional behavior of neutrophils in developing zebrafish. *Blood* **111**, 132–141 (2008).

166. Wittamer, V., Bertrand, J. Y., Gutschow, P. W. & Traver, D. Characterization of the mononuclear phagocyte system in zebrafish. *Blood* **117**, 7126–7135 (2011).

167. Mathias, J. R. *et al.* Characterization of Zebrafish Larval Inflammatory Macrophages. *Developmental and comparative immunology* **33**, 1212–1217 (2009).

168. Lieschke, G. J., Oates, A. C., Crowhurst, M. O., Ward, A. C. & Layton, J. E. Morphologic and functional characterization of granulocytes and macrophages in embryonic and adult zebrafish. **98**, 3087–3096 (2008).

169. Traver, D., Herbomel, P., Patton, E. E. & Murphey, R. D. The Zebrafish as a Model Organism to Study Development of the Immune System. **81**, (2003).

170. Lieschke, G. J., Oates, A. C., Crowhurst, M. O., Ward, A. C. & Layton, J. E. Morphologic and functional characterization of granulocytes and macrophages in embryonic and adult zebrafish. *Blood* **98**, 3087–3096 (2001).

171. Bennett, C. M. *et al.* Myelopoiesis in the zebrafish, Danio rerio. *Blood* **98**, 643–651 (2001).

172. Renshaw, S. A. *et al.* Atransgenic zebrafish model of neutrophilic inflammation. *Blood*

108, 3976–3978 (2006).

173. Renshaw, S. A. *et al.* Atransgenic zebrafish model of neutrophilic inflammation. *Blood* **108**, 3976–3978 (2006).

174. Liu, F. & Wen, Z. Cloning and expression pattern of the lysozyme C gene in zebrafish. *Mechanisms of Development* **113**, 69–72 (2002).

175. Ellett, F., Pase, L., Hayman, J. W., Andrianopoulos, A. & Lieschke, G. J. Phagocytes, Granulocytes, and Myelopoiesis mpeg1 promoter transgenes direct macrophage-lineage expression in zebrafish. *Blood* **27**, e49–e56 (2011).

176. Gurevich, D. B. *et al.* Asymmetric division of clonal muscle stem cells coordinates muscle regeneration in vivo. *Science* **353**, (2016).

177. Pipalia, T. G. *et al.* Cellular dynamics of regeneration reveals role of two distinct Pax7 stem cell populations in larval zebrafish muscle repair. *DMM Disease Models and Mechanisms* **9**, 671–684 (2016).

178. Otten, C. & Abdelilah-Seyfried, S. Laser-inflicted injury of zebrafish embryonic skeletal muscle. *Journal of Visualized Experiments* 4351 (2013). doi:10.3791/4351

179. Redd, M. J., Kelly, G., Dunn, G., Way, M. & Martin, P. Imaging macrophage chemotaxis in vivo: Studies of microtubule function in zebrafish wound inflammation. *Cell Motility and the Cytoskeleton* **63**, 415–422 (2006).

180. Gurevich, D. B. *et al.* Asymmetric division of clonal muscle stem cells coordinates muscle regeneration in vivo. *Science* **353**, (2016).

181. Kawakami, A., Fukazawa, T. & Takeda, H. Early fin primordia of zebrafish larvae regenerate by a similar growth control mechanism with adult regeneration. *Developmental Dynamics* **231**, 693–699 (2004).

182. Mateus, R. *et al.* In Vivo Cell and Tissue Dynamics Underlying Zebrafish Fin Fold Regeneration. *PLOS ONE* **7**, e51766 (2012).

183. Yoshinari, N., Ishida, T., Kudo, A. & Kawakami, A. Gene expression and functional analysis of zebrafish larval fin fold regeneration. *Developmental Biology* **325**, 71–81 (2009).

184. MAURO, A. Satellite cell of skeletal muscle fibers. *The Journal of biophysical and biochemical cytology* **9**, 493–495 (1961).

185. Niethammer, P., Grabher, C., Look, A. T. & Mitchison, T. J. A tissue-scale gradient of hydrogen peroxide mediates rapid wound detection in zebrafish. *Nature* **459**, 996–999 (2009).

186. Li, L., Yan, B., Shi, Y. Q., Zhang, W. Q. & Wen, Z. L. Live imaging reveals differing roles of macrophages and neutrophils during zebrafish tail fin regeneration. *Journal of Biological Chemistry* **287**, 25353–25360 (2012).

187. Li, L., Yan, B., Shi, Y.-Q., Zhang, W.-Q. & Wen, Z.-L. Live Imaging Reveals Differing Roles of Macrophages and Neutrophils during Zebrafish Tail Fin Regeneration. *The Journal of Biological Chemistry* **287**, 25353–25360 (2012).

188. Hasegawa, T. *et al.* Transient inflammatory response mediated by interleukin-1β is required for proper regeneration in zebrafish fin fold. *eLife* **6**, e22716 (2017).

189. Hasegawa, T., Nakajima, T., Ishida, T., Kudo, A. & Kawakami, A. A diffusible signal derived from hematopoietic cells supports the survival and proliferation of regenerative cells during zebrafish fin fold regeneration. *Developmental Biology* **399**, 80–90 (2015).

190. Sanderson, L. E. *et al.* An inducible transgene reports activation of macrophages in live zebrafish larvae. *Developmental and Comparative Immunology* **53**, 63–69 (2015).

191. Wang, T. *et al.* RNAseq Profiling of Leukocyte Populations in Zebrafish Larvae Reveals a cxcl11 Chemokine Gene as a Marker of Macrophage Polarization During Mycobacterial Infection. *Frontiers in Immunology | wwwfrontiersinorg* **1**, 832 (2019).

192. Westerfield, M. *The zebrafish book. A guide for the laboratory use of zebrafish (Danio rerio). 4th Edition*. (University of Oregon Press, Eugene, 2000).

193. Ellett, F. *et al.* mpeg1 promoter transgenes direct macrophage-lineage expression in zebrafish. (2014). doi:10.1182/blood-2010-10-314120

194. Goody, M. & Henry, C. Phalloidin Staining and Immunohistochemistry of Zebrafish Embryos. *Bio-protocol* **3**, (2013).

195. Benard, E. L. *et al.* Infection of zebrafish embryos with intracellular bacterial pathogens. *Journal of visualized experiments : JoVE* 1–8 (2012). doi:10.3791/3781

196. Torraca, V., Tulotta, C., Snaar-Jagalska, B. E. & Meijer, A. H. The chemokine receptor CXCR4 promotes granuloma formation by sustaining a mycobacteria-induced angiogenesis programme. *Scientific Reports* **7**, 45061 (2017).

197. Torraca, V. & Mostowy, S. Zebrafish Infection: From Pathogenesis to Cell Biology. *Trends in Cell Biology* **28**, 143–156 (2018).

198. Danker, A. J. & Rosenfeld, A. Blob Detection by Relaxation. *IEEE Transactions on Pattern Analysis and Machine Intelligence* **PAMI-3**, 79–92 (1981).

199. White, R. M. *et al.* Transparent Adult Zebrafish as a Tool for In Vivo Transplantation Analysis. *Cell Stem Cell* **2**, 183–189 (2008).

200. Harding, K. Innovation and wound healing. in *Journal of Wound Care* **24**, 7–13 (MA Healthcare Ltd, 2015).

201. Zhang, X. *et al.* Functional Biomaterials for Treatment of Chronic Wound. *Frontiers in bioengineering and biotechnology* **8**, 516 (2020).

202. Pop, M. A. & Almquist, B. D. Biomaterials: A potential pathway to healing chronic wounds? *Experimental Dermatology* **26**, 760–763 (2017).

203. Stejskalová, A. & Almquist, B. D. Using biomaterials to rewire the process of wound repair. *Biomaterials science* **5**, 1421 (2017).

204. Andorko, J. I. & Jewell, C. M. Designing biomaterials with immunomodulatory properties for tissue engineering and regenerative medicine. *Bioengineering & Translational Medicine* **2**, 139 (2017).

205. Anderson, J. M. Future challenges in the in vitro and in vivo evaluation of biomaterial biocompatibility. *Regenerative Biomaterials* **3**, 73–77 (2016).

206. Klopfleisch, R. Macrophage reaction against biomaterials in the mouse model - Phenotypes, functions and markers. *Acta biomaterialia* **43**, 3–13 (2016).

207. Christo, S. N., Diener, K. R., Bachhuka, A., Vasilev, K. & Hayball, J. D. Innate Immunity and Biomaterials at the Nexus: Friends or Foes. *BioMed Research International* **2015**, (2015).

208. Klopfleisch, R. & Jung, F. The pathology of the foreign body reaction against

biomaterials. *Journal of Biomedical Materials Research Part A* **105**, 927–940 (2017).

209. Anderson, J. M., Rodriguez, A. & Chang, D. T. Foreign body reaction to biomaterials. *Seminars in Immunology* **20**, 86–100 (2008).

210. Hu, W. J., Eaton, J. W. & Tang, L. Molecular basis of biomaterial-mediated foreign body reactions. *Blood* **98**, 1231–1238 (2001).

211. McNally, A. K. & Anderson, J. M. Interleukin-4 induces foreign body giant cells from human monocytes/macrophages. Differential lymphokine regulation of macrophage fusion leads to morphological variants of multinucleated giant cells. *The American Journal of Pathology* **147**, 1487–1499 (1995).

212. Ogle, M. E., Segar, C. E., Sridhar, S. & Botchwey, E. A. Monocytes and macrophages in tissue repair: Implications for immunoregenerative biomaterial design. *Experimental Biology and Medicine* **241**, 1084–1097 (2016).

213. McWhorter, F. Y., Wang, T., Nguyen, P., Chung, T. & Liu, W. F. Modulation of macrophage phenotype by cell shape. *Proceedings of the National Academy of Sciences of the United States of America* **110**, 17253–17258 (2013).

214. Da Silva, C. A. *et al.* Chitin Is a Size-Dependent Regulator of Macrophage TNF and IL-10 Production. *The Journal of Immunology* **182**, 3573–3582 (2009).

215. Champion, J. A. & Mitragotri, S. Role of target geometry in phagocytosis. *Proceedings of the National Academy of Sciences of the United States of America* **103**, 4930–4934 (2006).

216. Heath, D. E. A Review of Decellularized Extracellular Matrix Biomaterials for Regenerative Engineering Applications. *Regenerative Engineering and Translational Medicine* **5**, 155–166 (2019).

217. Badylak, S. F., Lantz, G. C., Coffey, A. & Geddes, L. A. Small intestinal submucosa as a large diameter vascular graft in the dog. *The Journal of surgical research* **47**, 74–80 (1989).

218. Keane, T. J., Swinehart, I. T. & Badylak, S. F. Methods of tissue decellularization used for preparation of biologic scaffolds and in vivo relevance. *Methods* **84**, 25–34 (2015).

219. Saldin, L. T., Cramer, M. C., Velankar, S. S., White, L. J. & Badylak, S. F. Extracellular

matrix hydrogels from decellularized tissues: Structure and function. *Acta Biomaterialia* **49**, 1–15 (2017).

220. Dziki, J. *et al.* An acellular biologic scaffold treatment for volumetric muscle loss: results of a 13-patient cohort study. *npj Regenerative Medicine* **1**, 16008 (2016).

221. Min, J. H., Yun, I. S., Lew, D. H., Roh, T. S. & Lee, W. J. The use of Matriderm and autologous skin graft in the treatment of full thickness skin defects. *Archives of Plastic Surgery* **41**, 330–336 (2014).

222. Wolf, M. T. *et al.* A hydrogel derived from decellularized dermal extracellular matrix. *Biomaterials* **33**, 7028–38 (2012).

223. Spang, M. T. & Christman, K. L. Extracellular matrix hydrogel therapies: In vivo applications and development. *Acta Biomaterialia* **68**, 1–14 (2018).

224. Badylak, S. F. Decellularized allogeneic and xenogeneic tissue as a bioscaffold for regenerative medicine: Factors that influence the host response. *Annals of Biomedical Engineering* **42**, 1517–1527 (2014).

225. Johnson, T. D. *et al.* Quantification of decellularized human myocardial matrix: A comparison of six patients. *PROTEOMICS - Clinical Applications* **10**, 75–83 (2016).

226. Keane, T. J., Londono, R., Turner, N. J. & Badylak, S. F. Consequences of ineffective decellularization of biologic scaffolds on the host response. *Biomaterials* **33**, 1771–1781 (2012).

227. Spiller, K. L. *et al.* Sequential delivery of immunomodulatory cytokines to facilitate the M1-to-M2 transition of macrophages and enhance vascularization of bone scaffolds. *Biomaterials* **37**, 194–207 (2015).

228. Spiller, K. L. *et al.* The role of macrophage phenotype in vascularization of tissue engineering scaffolds. *Biomaterials* **35**, 4477–4488 (2014).

229. Wolf, M. T. *et al.* A biologic scaffold-associated type 2 immune microenvironment inhibits tumor formation and synergizes with checkpoint immunotherapy. *Science Translational Medicine* **11**, 7973 (2019).

230. Meng, F. W., Slivka, P. F., Dearth, C. L. & Badylak, S. F. Solubilized extracellular matrix from brain and urinary bladder elicits distinct functional and phenotypic responses in

macrophages. *Biomaterials* **46**, 131–140 (2015).

231. Huleihel, L. *et al.* Macrophage phenotype in response to ECM bioscaffolds. *Seminars in immunology* **29**, 2–13 (2017).

232. Hodde, J. P. & Johnson, C. E. Extracellular matrix as a strategy for treating chronic wounds. *American Journal of Clinical Dermatology* **8**, 61–66 (2007).

233. Huleihel, L. *et al.* Matrix-bound nanovesicles within ECM bioscaffolds. *Science Advances* **2**, (2016).

234. Davis, G. E., Bayless, K. J., Davis, M. J. & Meininger, G. A. Regulation of tissue injury responses by the exposure of matricryptic sites within extracellular matrix molecules. *American Journal of Pathology* **156**, 1489–1498 (2000).

235. Adair-Kirk, T. L. & Senior, R. M. Fragments of extracellular matrix as mediators of inflammation. *International Journal of Biochemistry and Cell Biology* **40**, 1101–1110 (2008).

236. Wolf, M. T. *et al.* A hydrogel derived from decellularized dermal extracellular matrix. *Biomaterials* **33**, 7028–7038 (2012).

237. Wolf, M. T. *et al. A biologic scaffold-associated type 2 immune microenvironment inhibits tumor formation and synergizes with checkpoint immunotherapy. Sci. Transl. Med* **11**, (2019).

238. Dondossola, E. *et al.* Examination of the foreign body response to biomaterials by nonlinear intravital microscopy. *Nature Biomedical Engineering* **1**, (2017).

239. Nunan, R., Harding, K. G. & Martin, P. Clinical challenges of chronic wounds: Searching for an optimal animal model to recapitulate their complexity. *DMM Disease Models and Mechanisms* **7**, 1205–1213 (2014).

240. Zhang, X. *et al.* The zebrafish embryo as a model to quantify early inflammatory cell responses to biomaterials. *Journal of Biomedical Materials Research Part A* **105**, 2522–2532 (2017).

241. Witherel, C. E., Gurevich, D., Collin, J. D., Martin, P. & Spiller, K. L. Host–Biomaterial Interactions in Zebrafish. *ACS Biomaterials Science & Engineering* **4**, 1233–1240 (2018).

242. Gurevich, D. B., French, K. E., Collin, J. D., Cross, S. J. & Martin, P. Live imaging the foreign body response in zebrafish reveals how dampening inflammation reduces fibrosis. *Journal of cell science* **133**, (2019).

243. Massensini, A. R. *et al.* Concentration-dependent rheological properties of ECM hydrogel for intracerebral delivery to a stroke cavity. *Acta biomaterialia* **27**, 116–130 (2015).

244. Leipzig, N. D. & Shoichet, M. S. The effect of substrate stiffness on adult neural stem cell behavior. *Biomaterials* **30**, 6867–6878 (2009).

245. Zuidema, J. M., Rivet, C. J., Gilbert, R. J. & Morrison, F. A. A protocol for rheological characterization of hydrogels for tissue engineering strategies. *Journal of Biomedical Materials Research - Part B Applied Biomaterials* **102**, 1063–1073 (2014).

246. Ellman, G. L., Courtney, K. D., Andres, V. & Featherstone, R. M. A new and rapid colorimetric determination of acetylcholinesterase activity. *Biochemical Pharmacology* **7**, 88–95 (1961).

247. Repeated Measures ANOVA - Understanding a Repeated Measures ANOVA | Laerd Statistics. Available at: https://statistics.laerd.com/statistical-guides/repeated-measures-anova-statistical-guide.php. (Accessed: 1st March 2021)

248. One-way ANOVA with repeated measures in SPSS Statistics - Step-by-step procedure including assumptions. Available at: https://statistics.laerd.com/spss-tutorials/one-way-anova-repeated-measures-using-spss-statistics.php. (Accessed: 1st March 2021)

249. Understanding Sphericity - An introduction to, testing for, and interpreting sphericity | Laerd Statistics. Available at: https://statistics.laerd.com/statistical-guides/sphericity-statistical-guide.php. (Accessed: 1st March 2021)

250. Valentin, J. E., Stewart-Akers, A. M., Gilbert, T. W. & Badylak, S. F. Macrophage participation in the degradation and remodeling of extracellular matrix scaffolds. *Tissue Engineering - Part A* **15**, 1687–1694 (2009).

251. Lam, S. H., Chua, H. L., Gong, Z., Lam, T. J. & Sin, Y. M. Development and maturation of the immune system in zebrafish, Danio rerio: A gene expression profiling, in situ hybridization and immunological study. *Developmental and Comparative Immunology* **28**, 9–28 (2004).

252. Kolaczkowska, E. & Kubes, P. Neutrophil recruitment and function in health and inflammation. *Nature Reviews Immunology* **13**, 159–175 (2013).

253. Friedman Test in SPSS Statistics - How to run the procedure, understand the output using a relevant example | Laerd Statistics. Available at: https://statistics.laerd.com/spss-tutorials/friedman-test-using-spss-statistics.php. (Accessed: 1st March 2021)

254. Sadtler, K. *et al.* Developing a pro-regenerative biomaterial scaffold microenvironment requires T helper 2 cells. *Science* **352**, 366–370 (2016).

255. White, R., Rose, K. & Zon, L. Zebrafish cancer : the state of the art and the path forward. *Nature Publishing Group* **13**, 624–636 (2013).

256. Brown, H. K., Schiavone, K., Tazzyman, S., Heymann, D. & Chico, T. J. A. Zebrafish xenograft models of cancer and metastasis for drug discovery. *Expert Opinion on Drug Discovery* **12**, 379–389 (2017).

257. Varshney, G. K. *et al.* High-throughput gene targeting and phenotyping in zebrafish using CRISPR/Cas9. *Genome research* **25**, 1030–42 (2015).

258. Varshney, G. K. *et al.* A large-scale zebrafish gene knockout resource for the genome-wide study of gene function. *Genome Research* **23**, 727–735 (2013).

259. Fischer, R. S., Wu, Y., Kanchanawong, P., Shroff, H. & Waterman, C. M. Microscopy in 3D: A biologist's toolbox. *Trends in Cell Biology* **21**, 682–691 (2011).

260. Gräf, R., Rietdorf, J. & Zimmermann, T. Live cell spinning disk microscopy. *Advances in Biochemical Engineering/Biotechnology* **95**, 57–75 (2005).

261. Lam, P. Y., Fischer, R. S., Shin, W. D., Waterman, C. M. & Huttenlocher, A. Spinning disk confocal imaging of neutrophil migration in Zebrafish. *Methods in Molecular Biology* **1124**, 219–233 (2014).

262. Shimozawa, T. *et al.* Improving spinning disk confocal microscopy by preventing pinhole cross-talk for intravital imaging. *Proceedings of the National Academy of Sciences of the United States of America* **110**, 3399–3404 (2013).

263. Huisken, J., Swoger, J., Del Bene, F., Wittbrodt, J. & Stelzer, E. H. K. Optical sectioning deep inside live embryos by selective plane illumination microscopy. *Science* **305**,

1007–1009 (2004).

264. Keller, P. J., Schmidt, A. D., Wittbrodt, J. & Stelzer, E. H. K. Reconstruction of zebrafish early embryonic development by scanned light sheet microscopy. *Science* **322**, 1065–1069 (2008).

265. Reynaud, E. G., Krzic, U., Greger, K. & Stelzer, E. H. K. Light sheet-based fluorescence microscopy: more dimensions, more photons, and less photodamage. *HFSP journal* **2**, 266–75 (2008).

266. Reynaud, E. G., Peychl, J., Huisken, J. & Tomancak, P. Guide to light-sheet microscopy for adventurous biologists. *Nature Methods* **12**, 30–34 (2014).

267. Benninger, R. K. P. & Piston, D. W. Two-photon excitation microscopy for unit 4.11 the study of living cells and tissues. *Current Protocols in Cell Biology* **0 4**, Unit (2013).

268. Ahrens, M. B., Huang, K. H., Narayan, S., Mensh, B. D. & Engert, F. Two-photon calcium imaging during fictive navigation in virtual environments. *Frontiers in Neural Circuits* **7**, (2013).

269. Carvalho, L. & Heisenberg, C. P. Imaging zebrafish embryos by two-photon excitation time-lapse microscopy. *Methods in molecular biology (Clifton, NJ)* **546**, 273–287 (2009).

270. Renninger, S. L. & Orger, M. B. Two-photon imaging of neural population activity in zebrafish. *Methods* **62**, 255–267 (2013).

271. LeBert, D. C., Squirrell, J. M., Huttenlocher, A. & Eliceiri, K. W. Second harmonic generation microscopy in zebrafish. *Methods in Cell Biology* **133**, 55–68 (2016).

272. LeBert, D. C. *et al.* Matrix metalloproteinase 9 modulates collagen matrices and wound repair. *Development (Cambridge)* **142**, 2136–2146 (2015).

273. Weigelin, B., Bakker, G.-J. & Friedl, P. Third harmonic generation microscopy of cells and tissue organization. *Journal of cell science* **129**, 245–55 (2016).

274. Sun, C. K. *et al.* Higher harmonic generation microscopy for developmental biology. *Journal of Structural Biology* **147**, 19–30 (2004).

275. Olivier, N. *et al.* Cell lineage reconstruction of early zebrafish embryos using label-free nonlinear microscopy. *Science* **329**, 967–971 (2010).

276. Lorico, A., Rappa, G., Corbeil, D. & Le, T. T. Observation-driven inquiry: Raman spectroscopic imaging illuminates cancer lipid metabolism. *Stem Cell Investigation* **4**, 42–42 (2017).

277. Brozek-Pluska, B. *et al.* Raman spectroscopy and imaging: Applications in human breast cancer diagnosis. *Analyst* **137**, 3773–3780 (2012).

278. Butler, H. J. *et al.* Using Raman spectroscopy to characterize biological materials. *Nature Protocols* **11**, 664–687 (2016).

279. Huser, T. & Chan, J. Raman spectroscopy for physiological investigations of tissues and cells. *Advanced Drug Delivery Reviews* **89**, 57–70 (2015).

280. Mahadevan-Jansen, A. & Richards-Kortum, R. Raman spectroscopy for cancer detection: a review. *Annual International Conference of the IEEE Engineering in Medicine and Biology - Proceedings* **6**, 2722–2728 (1997).

281. Smith, G. P. S., McGoverin, C. M., Fraser, S. J. & Gordon, K. C. Raman imaging of drug delivery systems. *Advanced Drug Delivery Reviews* **89**, 21–41 (2015).

282. Puppels, G. J. *et al.* Studying single living cells and chromosomes by confocal Raman microspectroscopy. *Nature* **347**, 301–303 (1990).

283. Talari, A. C. S., Movasaghi, Z., Rehman, S. & Rehman, I. ur. Raman Spectroscopy of Biological Tissues. *Applied Spectroscopy Reviews* **50**, 46–111 (2015).

284. Swain, R. J. & Stevens, M. M. Raman microspectroscopy for non-invasive biochemical analysis of single cells. in *Biochemical Society Transactions* **35**, 544–549 (Biochem Soc Trans, 2007).

285. Opilik, L., Schmid, T. & Zenobi, R. Modern raman imaging: Vibrational spectroscopy on the micrometer and nanometer scales. *Annual Review of Analytical Chemistry* **6**, 379–398 (2013).

286. Müller, W., Kielhorn, M., Schmitt, M., Popp, J. & Heintzmann, R. Light sheet Raman micro-spectroscopy. *Optica* **3**, 452 (2016).

287. Oshima, Y. *et al.* Light sheet-excited spontaneous Raman imaging of a living fish by optical sectioning in a wide field Raman microscope. *Optics Express* **20**, 16195 (2012).

288. Zhang, Y., Hong, H. & Cai, W. Imaging with Raman spectroscopy. *Current pharmaceutical biotechnology* **11**, 654–61 (2010).

289. Bergholt, M. S., Albro, M. B. & Stevens, M. M. Online quantitative monitoring of live cell engineered cartilage growth using diffuse fiber-optic Raman spectroscopy. *Biomaterials* **140**, 128–137 (2017).

290. Walter, A. *et al.* From bulk to single-cell classification of the filamentous growing streptomyces bacteria by means of raman spectroscopy. *Applied Spectroscopy* **65**, 1116–1125 (2011).

291. Stiebing, C. *et al.* Raman imaging of macrophages incubated with triglyceride-enriched oxLDL visualizes translocation of lipids between endocytic vesicles and lipid droplets. *Journal of Lipid Research* **58**, 876–883 (2017).

292. Von Erlach, T. C., Hedegaard, M. A. B. & Stevens, M. M. High resolution Raman spectroscopy mapping of stem cell micropatterns. *Analyst* **140**, 1798–1803 (2015).

293. Kallepitis, C. *et al.* Quantitative volumetric Raman imaging of three dimensional cell cultures. *Nature Communications* **8**, (2017).

294. Bennet, M. *et al.* Simultaneous Raman Microspectroscopy and Fluorescence Imaging of Bone Mineralization in Living Zebrafish Larvae. *Biophysical Journal* **106**, L17–L19 (2014).

295. Akiva, A. *et al.* Mineral Formation in the Larval Zebrafish Tail Bone Occurs via an Acidic Disordered Calcium Phosphate Phase. *Journal of the American Chemical Society* **138**, 14481–14487 (2016).

296. Osborne, O. J. *et al.* Effects of particle size and coating on nanoscale Ag and TiO 2 exposure in zebrafish (Danio rerio) embryos. *Online) Journal* **7**, 1315–1324 (2013).

297. Wang, Y., Seebald, J. L., Szeto, D. P. & Irudayaraj, J. Biocompatibility and Biodistribution of Surface-Enhanced Raman Scattering Nanoprobes in Zebrafish Embryos: In vivo and Multiplex Imaging. *ACS Nano* **4**, 4039–4053 (2010).

298. den Broeder, M. *et al.* Altered Adipogenesis in Zebrafish Larvae Following High Fat Diet and Chemical Exposure Is Visualised by Stimulated Raman Scattering Microscopy. *International Journal of Molecular Sciences* **18**, 894 (2017).

299. Pang, S., Yang, T. & He, L. Review of surface enhanced Raman spectroscopic (SERS) detection of synthetic chemical pesticides. *TrAC - Trends in Analytical Chemistry* **85**, 73–82 (2016).

300. Prince, R. C., Frontiera, R. R. & Potma, E. O. Stimulated Raman scattering: From bulk to nano. *Chemical Reviews* **117**, 5070–5094 (2017).

301. Olmos, V. *et al.* Assessment of Tissue-Specific Multifactor Effects in Environmental – Omics Studies of Heterogeneous Biological Samples: Combining Hyperspectral Image Information and Chemometrics. *Talanta* (2018). doi:10.1016/j.talanta.2018.10.029

302. Olmos, V. *et al.* Combining hyperspectral imaging and chemometrics to assess and interpret the effects of environmental stressors on zebrafish eye images at tissue level. *Journal of Biophotonics* **11**, e201700089 (2018).

303. Kann, B., Offerhaus, H. L., Windbergs, M. & Otto, C. Raman microscopy for cellular investigations - From single cell imaging to drug carrier uptake visualization. *Advanced Drug Delivery Reviews* **89**, 71–90 (2015).

304. Puppels, G. J., Garritsen, H. S. P., Kummer, J. A. & Greve, J. Carotenoids located in human lymphocyte subpopulations and natural killer cells by Raman microspectroscopy. *Cytometry* **14**, 251–256 (1993).

305. Lampert, J. M. *et al.* Provitamin A conversion to retinal via the β,β-carotene-15, 15′-oxygenase (bcox) is essential for pattern formation and differentiation during zebrafish embryogenesis. *Development* **130**, 2173–2186 (2003).

306. Johnson, S. L., Nguyen, A. N. & Lister, J. A. mitfa is required at multiple stages of melanocyte differentiation but not to establish the melanocyte stem cell. *Developmental biology* **350**, 405–13 (2011).

307. Nord, H., Dennhag, N., Muck, J. & Von Hofsten, J. Pax7 is required for establishment of the xanthophore lineage in zebrafish embryos. *Molecular Biology of the Cell* **27**, 1853–1862 (2016).

308. Perz-Edwards, A., Hardison, N. L. & Linney, E. Retinoic Acid-Mediated Gene Expression in Transgenic Reporter Zebrafish. (2001). doi:10.1006/dbio.2000.9979

309. Wallace, K. N. & Pack, M. Unique and conserved aspects of gut development in

zebrafish. *Developmental Biology* **255**, 12–29 (2003).

310. Ng, A. N. Y. *et al.* Formation of the digestive system in zebrafish: III. Intestinal epithelium morphogenesis. *Developmental Biology* **286**, 114–135 (2005).

311. Bergholt, M. S. *et al.* Raman spectroscopy reveals new insights into the zonal organization of native and tissue-engineered articular cartilage. *ACS Central Science* **2**, 885–895 (2016).

312. Kaminaka, S., Ito, T., Yamazaki, H., Kohda, E. & Hamaguchi, H. O. Near-infrared multichannel Raman spectroscopy toward real-time in vivo cancer diagnosis. *Journal of Raman Spectroscopy* **33**, 498–502 (2002).

313. Huang, Z. *et al.* Near-infrared Raman spectroscopy for optical diagnosis of lung cancer. *International Journal of Cancer* **107**, 1047–1052 (2003).

314. Lakshmi, R. J. *et al.* Tissue Raman Spectroscopy for the Study of Radiation Damage: Brain Irradiation of Mice. *Radiation Research* **157**, 175–182 (2002).

315. Czamara, K. *et al.* Raman spectroscopy of lipids: A review. *Journal of Raman Spectroscopy* **46**, 4–20 (2015).

316. Cheng, W.-T., Liu, M.-T., Liu, H.-N. & Lin, S.-Y. Micro-Raman spectroscopy used to identify and grade human skin pilomatrixoma. *Microscopy research and technique* **68**, 75–9 (2005).

317. Stone, N., Kendall, C., Shepherd, N., Crow, P. & Barr, H. Near-infrared Raman spectroscopy for the classification of epithelial pre-cancers and cancers. *Journal of Raman Spectroscopy* **33**, 564–573 (2002).

318. Stone, N., Kendall, C., Smith, J., Crow, P. & Barr, H. Raman spectroscopy for identification of epithelial cancers. *Faraday Discussions* **126**, 141–157 (2004).

319. Bergholt, M. S. *et al.* Correlated heterospectral lipidomics for biomolecular profiling of remyelination in multiple sclerosis. *ACS Central Science* **4**, 39–51 (2018).

320. Stöckel, S. *et al.* Raman spectroscopic identification of Mycobacterium tuberculosis. *Journal of Biophotonics* **10**, 727–734 (2017).

321. Mahadevan-Jansen, A. & Richards-Kortum, R. Raman spectroscopy for cancer

detection: a review. *Annual International Conference of the IEEE Engineering in Medicine and Biology - Proceedings* **6**, 2722–2728 (1997).

322. Kumar, S., Gopinathan, R., Chandra, G. K., Umapathy, S. & Saini, D. K. Rapid detection of bacterial infection and viability assessment with high specificity and sensitivity using Raman microspectroscopy. *Analytical and Bioanalytical Chemistry* **412**, 2505–2516 (2020).

323. Marrakchi, H., Lanéelle, M. A. & Daffé, M. Mycolic acids: Structures, biosynthesis, and beyond. *Chemistry and Biology* **21**, 67–85 (2014).

324. Fenaroli, F. *et al.* Enhanced permeability and retention-like extravasation of nanoparticles from the vasculature into tuberculosis granulomas in zebrafish and mouse models. *ACS Nano* **12**, 8646–8661 (2018).

325. Barisch, C., Paschke, P., Hagedorn, M., Maniak, M. & Soldati, T. Lipid droplet dynamics at early stages of Mycobacterium marinum infection in Dictyostelium. *Cellular Microbiology* **17**, 1332–1349 (2015).

326. Stöckel, S., Stanca, A. S., Helbig, J., Rösch, P. & Popp, J. Raman spectroscopic monitoring of the growth of pigmented and non-pigmented mycobacteria. *Analytical and Bioanalytical Chemistry* **407**, 8919–8923 (2015).

327. Volkman, H. E. *et al.* Tuberculous granuloma formation is enhanced by a Mycobacterium virulence determinant. *PLoS Biology* **2**, (2004).

328. Oehlers, S. H. *et al.* Interception of host angiogenic signalling limits mycobacterial growth. *Nature* **517**, 612–615 (2015).

329. Russell, D. G. Mycobacterium tuberculosis and the intimate discourse of a chronic infection. *Immunological Reviews* **240**, 252–268 (2011).

330. Czamara, K. *et al.* Unsaturated lipid bodies as a hallmark of inflammation studied by Raman 2D and 3D microscopy. *Scientific Reports* **7**, 40889 (2017).

331. Sarmah, S. & Marrs, J. A. Zebrafish as a Vertebrate Model System to Evaluate Effects of Environmental Toxicants on Cardiac Development and Function. *International Journal of Molecular Sciences* **17**, (2016).

332. Nascimento, J. M. P. & Dias, J. M. B. Vertex component analysis: A fast algorithm to

unmix hyperspectral data. *IEEE Transactions on Geoscience and Remote Sensing* **43**, 898–910 (2005).

333. Sukumar, N., Tan, S., Aldridge, B. B. & Russell, D. G. Exploitation of Mycobacterium tuberculosis Reporter Strains to Probe the Impact of Vaccination at Sites of Infection. *PLoS Pathogens* **10**, (2014).

334. Bergholt, M. S. *et al.* Correlated heterospectral lipidomics for biomolecular profiling of remyelination in multiple sclerosis. *ACS Central Science* **4**, 39–51 (2018).

335. Freudiger, C. W. *et al.* Label-Free Biomedical Imaging with High Sensitivity by Stimulated Raman Scattering Microscopy. *Science* **322**, 1857–1861 (2008).

336. Cheng, J.-X. & Xie, X. S. *Coherent Raman Scattering Microscopy.* (CRC Press, 2016).

337. Lei, M., Winterhalder, M., Selm, R. & Zumbusch, A. Video-rate wide-field coherent anti-Stokes Raman scattering microscopy with collinear nonphase-matching illumination. *Journal of Biomedical Optics* **16**, 021102 (2011).

338. Saar, B. G. *et al.* Video-rate molecular imaging in vivo with stimulated Raman scattering. *Science* **330**, 1368–1370 (2010).

339. Lu, F. K. *et al.* Label-free DNA imaging in vivo with stimulated Raman scattering microscopy. *Proceedings of the National Academy of Sciences of the United States of America* **112**, 11624–11629 (2015).

340. Evans, C. L. *et al.* Chemical imaging of tissue in vivo with video-rate coherent anti-Stokes Raman scattering microscopy. *Proceedings of the National Academy of Sciences of the United States of America* **102**, 16807 (2005).

341. Sen, C. K. Human Wounds and Its Burden: An Updated Compendium of Estimates. *Advances in Wound Care* **8**, 39–48 (2019).

342. Witherel, C. E., Gurevich, D., Collin, J. D., Martin, P. & Spiller, K. L. Host-Biomaterial Interactions in Zebrafish. *ACS Biomaterials Science and Engineering* **4**, 1233–1240 (2018).

343. Morris, J. L. *et al.* Live imaging of collagen deposition during skin development and repair in a collagen I - GFP fusion transgenic zebrafish line. *Developmental biology* **441**, 4–11 (2018).

344. Mahalwar, P., Walderich, B., Singh, A. P. & Volhard, C. N. Local reorganization of xanthophores fine-tunes and colors the striped pattern of zebrafish. *Science* **345**, 1362–1364 (2014).

345. Lawson, N. D. & Weinstein, B. M. In Vivo Imaging of Embryonic Vascular Development Using Transgenic Zebrafish. **318**, 307–318 (2002).

346. Rougeot, J. *et al.* RNA sequencing of FACS-sorted immune cell populations from zebrafish infection models to identify cell specific responses to intracellular pathogens. *Methods in Molecular Biology* **1197**, 261–274 (2014).